

# DEVELOPMENT OF NANOSCALE MAGNETIC SYSTEMS FOR SPIN WAVE PROPAGATION

*Thesis submitted for the degree of*  
DOCTOR OF PHILOSOPHY (TECHNOLOGY)

*in*  
NANOTECHNOLOGY

*by*  
DHEERAJ KUMAR

CENTER FOR RESEARCH IN NANOSCIENCE  
AND NANOTECHNOLOGY  
UNIVERSITY OF CALCUTTA  
2014

*Dedicated to Nanaji, whose stories I am made of . . .*

# Acknowledgements

I would like to begin by expressing my sincere gratitude to my guide and mentor, Prof. Anjan Barman for giving me the wonderful opportunity to work under his supervision. It was a great pleasure and honour to conduct research under his guidance in a competitive and yet friendly environment. I had backgrounds in mechanical engineering, fabrication and software development. He first introduced me to the realms of solid state physics, nanotechnology and magnonics. He gave me enough time to learn the ropes at my own pace without sacrificing my prior knowledge. This helped me qualify the national eligibility test in physical sciences, which eventually lead to my fellowship.

When I joined his fledgeling team as a doctoral candidate on 14<sup>th</sup> September, 2009, we essentially started from empty laboratory spaces. It is due to his incredible skills as a scientist and group leader that we were able to expand so rapidly and eventually ended up with publications in several prestigious peer-reviewed journals. Our labs now have strong funding and state of the art equipment. We can now perform in-house sample fabrication with several sputtering, lithography and chemical synthesis techniques. Experimental facilities include MOKE, TR-MOKE, VNA-FMR and BLS setups which he basically built himself to probe magnetization dynamics in different ways. A host of computers are dedicated to simulate problems and analyse results.

Under his wise tutelage, I also learned several skills directly related to the publication and presentation of ones output, which are necessary to be successful as an independent scientist. Like many of his students, I strove to inherit all the attributes of good scientist from him. He also encouraged me to leverage my diverse background and use the tools that I possessed to come up with new techniques and ideas. I hope to repay a fraction of this massive debt by building upon these learnings and sharing them with my own batch of students some day to become a part of the grand *guru-shishya* tradition. Apart from demonstrating what it takes to build a laboratory, he also trained all his students in its proper maintenance. He always motivated me to work hard and think independently. He provided me with several collaborative research opportunities so that I may also learn to make myself useful as a part of a team and contribute to the generation of new knowledge from a whole new platform. He gave me a lot of autonomous control over the manner in which I was to overcome my challenges. To cherish and enhance that kind of trust in me has been my strongest source of motivation during my life as a doctoral researcher.

I am also thankful to Dr. Saswati Barman for initiating me in the ways of micromagnetic simulations and magnetic vortex dynamics. She helped me in developing our own Landau-Lifshitz-Gilbert equation solver in MATLAB. The prompt completion of this deliverable was key in my transition from a software developer to a researcher.

Next, I would like to thank my colleges and collaborators. The first names among those are that of Dr. Jarosław Kłos and his team leader Dr. Maciej Krawczyk. They developed the plane wave method to obtain the dispersion relation of spin-waves in magnonic crystals;

while I calculated the same using complete micromagnetic simulations. Agreements and disagreements between our results have granted us new insights into the dynamics of spin-waves. I would also like to acknowledge Dr. Oleksandr Dmytriiev, who carefully observed some of my initial results and provided very helpful inputs. Dr. Sabareesan Ponraj helped me with technicalities involving the preparation of a manuscript itself. He along with Weiwei Wang and Dr. Hans Fanghor did simulations using Nmag and also shared their knowledge of the finite element method.

Bivas Rana helped me set up my life in Kolkata. Semanti Pal is a fierce researcher and a wonderful human being who also helped me learn OOMMF. They, along with Bipul Kumar Mahato and Ruma Mandal are some of the experimentalists in our group who tested my numerical tools and validated them experimentally while generating new knowledge on their own. Dr. Michael Donahue helped me understand the inner workings of OOMMF. Susmita Saha, Dr. Arabinda Haldar and Dr. Pinkai Laha helped me in sample fabrication and TR-MOKE measurements. I also received training in advanced fabrication procedures from groups led by Profs. P. S. Anil Kumar and Yoshi-Chika Otani at IISc Bangalore and RIKEN, respectively. Discussions with Milan Agrawal, Profs. Abhihit Mookerjee and Partha Guha also proved to be valuable.

I would also like to acknowledge the moral support from my mother Mrs. Usha Rakesh and sisters Dr. Deepti Sharma and Ms. Tripti Sharma. Unlike my father, they showed great restraint and hardly ever bothered me with the annoying question about when will all this be over! I understand that all their actions, including those of my father's, were guided by my best interests at their hearts. Deepti's decision to pursue doctoral research had also encouraged mine. Her advice also came in handy on different occasions. Tripti is studying the law. She advised me — free of charge, of course — on how to apply for a patent. I must also thank my wife Prachi, for her exceptional moral support.

Finally, I thank the S. N. Bose National Centre for Basic Sciences for giving me an opportunity to work here. The common research facilities under the Technical Cell were very helpful for initial characterization of my samples. Thanks to Council of Scientific and Industrial Research for providing me with the Senior Research Fellowship. I must thank various funding agencies including the Departments of Science and Technology and Information Technology (Government of India) and the European Union's Seventh Framework Programme for their financial support of my research work.

Dheeraj Kumar,  
S. N. Bose National Centre for Basic Sciences,  
Salt Lake, Kolkata, India.

# Patent and Publications

**Patent Title:** *A Spin Wave Waveguide with Bandgaps in the Microwave and Submillimeter Wave Frequency Bands*

**Inventors:** *Mr. Dheeraj Kumar and Prof. Anjan Barman*

**Country of Application:** *India*

**Status:** *Applied for* (September 2013)

**This thesis is based upon the following peer-reviewed publications and manuscripts:**

1. Numerical calculation of spin wave dispersions in magnetic nanostructures  
**D. Kumar**, O. Dmytriiev, S. Ponraj and A. Barman  
*J. Phys. D: Appl. Phys.* **45**, 015001 (2012).
2. Effect of magnetization pinning on the spectrum of spin waves in magnonic antidot waveguides  
J. W. Kłos, **D. Kumar**, J. Romero-Vivas, H. Fangohr, M. Franchin, M. Krawczyk and A. Barman  
*Phys. Rev. B* **86**, 184433 (2012).
3. Proposal for a Standard Micromagnetic Problem: Spin Wave Dispersion in a Magnonic Waveguide  
G. Venkat, **D. Kumar**, M. Franchin, O. Dmytriiev, M. Mruczkiewicz, H. Fangohr, A. Barman, M. Krawczyk and A. Prabhakar  
*IEEE Trans. Magn.* **49**, 015001 (2013).
4. Effect of hole shape on spin-wave band structure in one-dimensional magnonic antidot waveguide  
**D. Kumar**, P. Sabareesan, W. Wang and H. Fangohr and A. Barman  
*J. Appl. Phys.* **114**, 023910 (2013).
5. Magnonic Band Engineering by Intrinsic and Extrinsic Mirror Symmetry Breaking in Antidot Spin-Wave Waveguides  
J. W. Kłos,\* **D. Kumar**,\* M. Krawczyk and A. Barman  
*Sci. Rep.* **3**, 2444 (2013).
6. Influence of structural changes in a periodic antidot waveguide on the spin-wave spectra  
J. W. Kłos,\* **D. Kumar**,\* M. Krawczyk and A. Barman

---

*Phys. Rev. B* **89**, 014406 (2014)

7. Magnonic Band Structure, Complete Bandgap and Collective Spin Wave Excitation in Nanoscale Two-Dimensional Magnonic Crystals  
**D. Kumar**,\* J. W. Kłos,\* M. Krawczyk and A. Barman  
*J. Appl. Phys.* **115**, 043917 (2014)
8. Magnetic Vortex Based Transistor Operations  
**D. Kumar**, S. Barman and A. Barman  
*Sci. Rep.* **4**, 4108 (2014).
9. Development of Nanoscale Systems for Spin-Wave Propagation  
**D. Kumar** and A. Barman *To be Submitted*.

## The following co-authored publications are not included in this thesis:

1. Detection of Picosecond Magnetization Dynamics of 50 nm Magnetic Dots down to the Single Dot Regime  
B. Rana, **D. Kumar**, S. Barman, S. Pal, Y. Fukuma, Y. Otani and A. Barman  
*ACS Nano* **5**, 9559 (2011).
2. Optically Induced Tunable Magnetization Dynamics in Nanoscale Co Antidot Lattices  
R. Mandal, S. Saha, **D. Kumar**, S. Barman, S. Pal, K. Das, A. K. Raychaudhuri, Y. Fukuma, Y. Otani and A. Barman  
*ACS Nano* **6**, 3397 (2012).
3. Anisotropy in collective precessional dynamics in arrays of Ni<sub>80</sub>Fe<sub>20</sub> nanoelements  
B. Rana, **D. Kumar**, S. Barman, S. Pal, R. Mandal, Y. Fukuma, Y. Otani, S. Sugimoto and A. Barman  
*J. App. Phys.* **111**, 07D503 (2012).
4. Tunable Magnonic Spectra in Two-Dimensional Magnonic Crystals with Variable Lattice Symmetry  
S. Saha, R. Mandal, S. Barman, **D. Kumar**, B. Rana, Y. Fukuma, S. Sugimoto, Y. Otani and A. Barman  
*Adv. Funct. Mater.* **23**, 2378 (2013).
5. Configurational anisotropic spin waves in cross-shaped Ni<sub>80</sub>Fe<sub>20</sub> nanoelements  
B. K. Mahato, B. Rana, R. Mandal, **D. Kumar**, S. Barman, Y. Fukuma, Y. Otani and A. Barman  
*Appl. Phys. Lett.* **102**, 192402 (2013).

---

\*These authors contributed equally to the work.

6. Micromagnetic study of size-dependent picosecond dynamics in single nanomagnets  
S. Pal, **D. Kumar**, and A. Barman  
*J. Phys. D: Appl. Phys.* **44**, 105002 (2011).

# Abstract

It has been proposed that spin-waves, particularly those with frequencies in microwave and submillimetre wave bands, can be used for information transmission and processing. Having shorter wavelengths as compared to electromagnetic waves of the same frequency, spin-wave based devices hold the potential to aid the miniaturization of microwave communication. Designs have been proposed which use nanoscale magnetic systems to create elements which can function as attenuators, filters, phase-shifters, interferometers and logic gates. Here, we study the magnetization dynamics of spin-wave dispersion and magnetic vortex gyration. Both phenomenon are related and have their characteristic frequencies in the microwave frequency band. The nanoscale systems considered here are ferromagnetic thin films, uniform waveguides, magnonic crystals (spatially modulated magnetic systems) and magnetic vortices. Effects like magnetization pinning and mirror symmetry breaking, which alter the spin-wave dispersion characteristic call for greater spatial resolution and precision in fabrication. Thus, we summarize with what needs to be done and the future directions the research needs to take in order to make nanoscale devices technically feasible.

The spectrum of spin-waves propagating in magnetic systems is important from both fundamental and applied points of views. Propagating spin-waves in magnonic crystals will form the building blocks of future microwave data processing and communication. While magnonic modes and band gaps can help in the formulation of filters and attenuators, understanding other phenomena like spin-wave reflection, refraction and interference will help in designing magnonic circuit elements like logic gates and diodes.

The Landau-Lifshitz-Gilbert (LLG) equation has been used in this work to simulate the spin dynamics in different nanoscale magnetic systems. This equation was solved mainly using the finite difference method based Object-Oriented Micromagnetic Framework (OOMMF) or the finite element method based Nmag. In addition to using some existing software packages, we also developed our own LLG equation solver (which can also take spin-transfer torque terms into account) using MATLAB programming. The combined packages of simulation and post-processing has been named DotMag. DotMag can simulate spin dynamics in two-dimensional systems and can analyse results for any kind of nanoscale system — even those solved using third party packages, such as OOMMF. The results obtained from the newly developed software have been inspected for any magnonic bands and bandgaps using multi-domain discrete Fourier transform. Various issues related to the numerical calculations like aliasing, spectral leakage and scalloping loss have been addressed in Chap. 3. The tools prepared for analysing these magnonic conductors will also allow for the visualization of propagation and power and phase distribution of the spin-wave over the entire region of interest. These tools will be generically designed, so as to accommodate any kind of magnonic conductor.

The newly developed package DotMag, was used for the calculations of magnonic band structures of one- and two-dimensional periodic arrays of dots, anti-dots (holes created in

---

continuous magnetic medium) and filled antidots (the holes are now filled with a different magnetic medium). Influence of different structural and material parameters over the spin-wave band structure was studied in these cases. The results obtained using the micromagnetic simulations were also compared with those obtained from the plane wave method (PWM) and any differences were examined. Iso-frequency lines, which are magnonic analogues of the electronic Fermi surfaces were also calculated in the case of two-dimensional antidot arrays. With the knowledge obtained from above we investigated magnonic waveguides embedded with regular and filled antidots to design magnonic filters of tunable bandwidth and bandgaps. Some of the numerically examined magnonic crystals have been fabricated by using different lithography techniques. The low wavevector magnonic modes in some of these magnonic crystals were experimentally investigated by using our TR-MOKE experimental setup.

In Chap. 5, we study the spin-wave spectra in magnonic antidot waveguides (MAWs) versus the surface anisotropy at the ferromagnet/air interface. The MAWs under investigation have the form of a thin stripe of permalloy with a single row of periodically arranged antidots in the middle. The introduction of a magnetization pinning at the edges of the permalloy stripe and the edges of antidots is found to modify quantitatively the spin-wave spectrum. This effect is shown to be necessary for magnonic gaps to open in the considered systems. Our study demonstrates that the surface anisotropy can be crucial in the practical applications of MAWs and related structures and in the interpretation of experimental results in one- and two-dimensional magnonic crystals. We used three different theoretical methods *i.e.* PWM, finite difference method and finite element method to validate the results. We showed that PWM in the present formulation assumes pinned magnetization while in micromagnetic simulations special care must be taken to introduce pinning.

In Chap. 6, we show that structural changes breaking the mirror symmetry of a MAW can close the magnonic bandgaps. But, the effect of these intrinsic symmetry breaking factors can be compensated by a properly adjusted asymmetric external bias magnetic field, *i.e.*, by an extrinsic factor. This allows for the recovery of the magnonic bandgaps occurring in the ideal symmetric structure. The described methods can be used for developing parallel models for recovering bandgaps closed due to an intrinsic defect, *e.g.* a fabrication defect. The theoretical model developed here is particular to the field of magnonics, a rapidly emerging field combining spin dynamics and spintronics. However, the underlying principle of this development is squarely based upon the translational and mirror symmetries associated with the crystal structure. Thus, we believe that this idea of correcting an intrinsic defect by extrinsic means, should be applicable to spin-waves in both exchange and dipolar interaction regimes, as well as to electron, electromagnetic and acoustic waves in general.

In Chap. 7, we present the possibility of tuning the spin-wave band structure, particularly the bandgaps in a nanoscale MAW by varying the shape of the antidots. The effects of changing the shape of the antidots on the spin-wave dispersion relation in a waveguide have been carefully monitored. We interpret the observed variations by analysing the equilibrium magnetic configuration and the magnonic power and phase distribution profiles during spin-wave dynamics. The inhomogeneity in the exchange fields at the antidot boundaries within the waveguide is found to play a crucial role in controlling the band structure at the discussed length scales. The observations recorded here will be important for future developments of magnetic antidot based magnonic crystals and waveguides.

---

In Chap. 8, we demonstrate that the magnonic band structure, including the band gap for a MAW, can be significantly tuned by a relatively weak modulation of its structural parameters. The calculations were performed with consideration of both the exchange and dipolar interactions. For the exchange dominated regime, we discuss, in details, the impact of the changes of the lattice constant, size, and shape of the antidots on the spin-wave spectra. We have shown that a precise choice of these parameters is crucial for achieving desired properties of the antidot waveguides, *i.e.*, a large group velocity and filtering properties due to existence of magnonic band gaps. We discuss different mechanisms of magnonic gap opening resulting from Bragg scattering or anticrossing of modes. We have shown that the dipolar interactions start to assert their role in the spin-wave spectrum when the waveguide is scaled up, but even for a period of few hundreds of nanometres, the magnonic band structure preserves qualitatively the properties found in the exchange dominating regime. The obtained results are important for future development of magnonic crystal based devices.

In Chap. 9, we present the observation of a complete bandgap and collective spin-wave excitation in two-dimensional magnonic crystals comprised of arrays of nanoscale antidots and nanodots, respectively. Considering that the frequencies dealt with here fall in the microwave band, these findings can be used for the development of suitable magnonic metamaterials and spin-wave based signal processing. We also present the application of a numerical procedure, to compute the dispersion relations of spin-waves for any high symmetry direction in the first Brillouin zone. The results obtained from this procedure has been reproduced and verified by the well-established PWM for an antidot lattice, when magnetization dynamics at antidot boundaries is pinned. The micromagnetic simulation based method can also be used to obtain iso-frequency contours of spin-waves. Iso-frequency contours are analogous of the Fermi surfaces and hence, they have the potential to radicalise our understanding of spin-wave dynamics. The physical origin of bands, partial and full magnonic bandgaps has been explained by plotting the spatial distribution of spin-wave energy spectral density. Although, unfettered by rigid assumptions and approximations, which afflict most analytical methods used in the study of spin-wave dispersion, micromagnetic simulations tend to be computationally demanding. Thus, the observation of collective spin-wave excitation in the case of nanodot arrays, which can obviate the need to perform simulations may, also prove to be valuable.

DotMag was developed with the ability to excite vortex core gyration by using external magnetic field and spin transfer torque. Magnetic vortex dynamics was investigated in the cases of isolated and coupled vortices. Transducer and transistor like operations were demonstrated based on these results. Transistors constitute the backbone of modern day electronics. Since their advent, researchers have been seeking ways to make smaller and more efficient transistors. In Chap. 12, we demonstrate a sustained amplification of magnetic vortex core gyration in coupled two and three vortices by controlling their relative core polarities. This amplification is mediated by a cascade of antivortex solitons travelling through the dynamic stray field. We further demonstrated that the amplification can be controlled by switching the polarity of the middle vortex in a three vortex sequence and the gain can be controlled by the input signal amplitude. An attempt to show fan-out operation yielded gain for one of the symmetrically placed branches which can be reversed by switching the core polarities of all of the vortices in the network. The above observations promote the magnetic vortices as suitable candidates to work as stable bipolar junction transistors (BJT).



# Contents

|   |              |
|---|--------------|
| <b>Acknowledgements</b>   | <b>iii</b>   |
| <b>Patent and Publications</b>                                      | <b>v</b>     |
| <b>Abstract</b>   | <b>viii</b>  |
| <b>List of Abbreviations</b>  | <b>xvi</b>   |
| <b>List of Symbols</b>  | <b>xxiii</b> |
| <b>Material Parameters Used During Simulations</b>                  | <b>xx</b>    |
| <b>List of Tables</b>   | <b>xxi</b>   |
| <b>List of Figures</b>  | <b>xxii</b>  |
| <b>1. Introductions</b>   | <b>1</b>     |
| 1.1. Spin–Waves . . . . .   | 3            |
| 1.2. Magnetic Vortices . . . . .                                    | 7            |
| <b>2. Theoretical Background</b>                                    | <b>11</b>    |
| 2.1. Ferromagnetism . . . . .                                       | 11           |
| 2.2. Magnetic Energies . . . . .                                    | 14           |
| 2.2.1. Zeeman Energy . . . . .                                      | 14           |
| 2.2.2. Exchange Energy . . . . .                                    | 14           |
| 2.2.3. Magnetostatic Self–Energy . . . . .                          | 15           |
| 2.2.4. Magnetocrystalline Anisotropy Energy . . . . .               | 16           |
| 2.3. Magnetization Dynamics . . . . .                               | 17           |
| 2.3.1. Brown’s Equations . . . . .                                  | 17           |
| 2.3.2. Landau–Lifshitz–Gilbert Equations . . . . .                  | 18           |
| 2.3.3. Ferromagnetic Resonance and The Kittel Formula . . . . .     | 20           |
| 2.3.4. Laser Pulse Induced Ultrafast Demagnetization . . . . .      | 23           |
| 2.4. Magnonics . . . . .  | 24           |
| 2.4.1. Exchange Dominated SWs in Thin Films . . . . .               | 24           |
| 2.4.2. Dipole Dominated SWs in Thin Films . . . . .                 | 25           |
| 2.4.3. Effect of Lateral Confinement on SW Band Structure . . . . . | 27           |
| 2.4.4. Magnonic Crystals (MCs) . . . . .                            | 30           |
| 2.4.5. Magnonic Devices . . . . .                                   | 30           |

|   |            |
|---|------------|
| 2.5. Magnetic Vortex Dynamics . . . . .   | 32         |
| 2.5.1. Polarity Switching . . . . .   | 33         |
| 2.5.2. Vortex Core Gyration . . . . .   | 34         |
| <b>3. Methods</b>   | <b>38</b>  |
| 3.1. Micromagnetic Simulation . . . . .   | 40         |
| 3.2. FDM and OOMMF . . . . .  | 41         |
| 3.2.1. Numerical Approximations of Magnetic Energies . . . . .                                    | 42         |
| 3.2.2. Boundary Conditions . . . . .  | 45         |
| 3.2.3. Solving The LLG Equation in OOMMF . . . . .  | 46         |
| 3.3. FEM and Nmag . . . . .   | 48         |
| 3.3.1. FEM Meshing . . . . .  | 48         |
| 3.3.2. Solving The LLG Equation using Nmag . . . . .  | 49         |
| 3.4. Plane Wave Method (PWM) . . . . .  | 50         |
| 3.5. Fabrication Techniques . . . . .   | 52         |
| 3.5.1. Thin-Film deposition . . . . .   | 52         |
| 3.5.2. Lithography . . . . .  | 53         |
| 3.6. Sample Characterization . . . . .  | 55         |
| <b>4. Thin-Films, Waveguides and One-Dimensional Magnonic Crystals</b>                            | <b>57</b>  |
| 4.1. Method . . . . .   | 59         |
| 4.2. Results and Discussion . . . . .   | 59         |
| 4.3. Conclusion . . . . .   | 72         |
| <b>5. Free and Pinned Boundary Condition in a Magnonic Antidot Waveguide</b>                      | <b>74</b>  |
| 5.1. Waveguide Structure and the Calculation Methods . . . . .                                    | 75         |
| 5.1.1. Micromagnetic Simulation . . . . .   | 76         |
| 5.1.2. Plane Wave Method for a Magnonic Antidot Waveguide . . . . .                               | 78         |
| 5.2. The effect of pinning on the magnonic spectrum . . . . .                                     | 81         |
| 5.3. Conclusions . . . . .  | 87         |
| <b>6. Manipulation of Intrinsic and Extrinsic Mirror Symmetry in a Magnonic Antidot Waveguide</b> | <b>88</b>  |
| 6.1. Methods . . . . .  | 89         |
| 6.2. Results . . . . .  | 89         |
| 6.2.1. Magnonic Band Structure in Symmetric and Asymmetric MAW . . . . .                          | 89         |
| 6.2.2. Compensation of the Effect of an Intrinsic Symmetry breaking . . . . .                     | 95         |
| 6.3. Discussion . . . . .   | 99         |
| <b>7. Effect of Antidot Shape on Spin-Wave dispersion in a Magnonic Antidot Waveguide</b>         | <b>102</b> |
| 7.1. MAW and The Numerical Method . . . . .   | 103        |
| 7.1.1. MAW Structural and Material Parameters . . . . .   | 103        |
| 7.1.2. Micromagnetic Simulations . . . . .  | 103        |
| 7.2. Results and Observations . . . . .   | 105        |
| 7.3. Conclusions . . . . .  | 110        |

|   |            |
|---|------------|
| <b>8. Effects of Other Structural Parameters</b>  | <b>112</b> |
| 8.1. The Waveguide Structure and the Calculation Methods . . . . .                              | 114        |
| 8.2. The Influence of Structural Changes in the MAW on the SW Band Structure                    | 115        |
| 8.2.1. The Influence of Antidot Size . . . . .  | 116        |
| 8.2.2. The Influence of Lattice Period . . . . .  | 119        |
| 8.2.3. The Influence of Antidot Shape . . . . .   | 122        |
| 8.2.4. The Influence of Size Factor . . . . .   | 124        |
| 8.3. Conclusions . . . . .  | 126        |
| <b>9. Two-Dimensional Magnonic Crystals</b>   | <b>129</b> |
| 9.1. Method . . . . .   | 131        |
| 9.1.1. Magnonic crystal lattice and material parameters . . . . .                               | 131        |
| 9.1.2. Micromagnetic simulations and the plane wave method . . . . .                            | 131        |
| 9.2. Results and Discussions . . . . .  | 135        |
| 9.3. Conclusions . . . . .  | 143        |
| <b>10. Bandgaps in The Submillimetre Frequency Range in a Magnonic Antidot Waveguide</b>        | <b>145</b> |
| 10.1. Precessing Vector Fourier Transform (PVFT) . . . . .                                      | 145        |
| 10.2. Increased Amplitude . . . . .   | 147        |
| 10.3. Reduced Aliasing . . . . .  | 147        |
| <b>11. Experimentation Involving Magnonic Antidot Waveguides</b>                                | <b>151</b> |
| 11.1. MAW Samples . . . . .   | 151        |
| 11.2. Magneto-Optic Kerr Effect (MOKE) . . . . .  | 153        |
| 11.2.1. Description of The Pump-Probe Optical Setup . . . . .                                   | 154        |
| 11.3. Results and Discussion . . . . .  | 156        |
| 11.3.1. TR-MOKE Measurements from the Ni <sub>80</sub> Fe <sub>20</sub> Antidot Waveguide . . . | 156        |
| 11.3.2. Dependence of SW Spectrum on the Lattice Parameters . . . . .                           | 159        |
| 11.3.3. Bias Field Dependence . . . . .   | 162        |
| 11.4. Conclusions . . . . .   | 165        |
| <b>12. Coupled Magnetic Vortices for All-Magnetic Transistor Operations</b>                     | <b>166</b> |
| 12.1. Methods . . . . .   | 167        |
| 12.2. Results and Discussion . . . . .  | 168        |
| 12.2.1. Isolated Magnetic Vortex . . . . .  | 169        |
| 12.2.2. Coupled Magnetic Vortices Pair . . . . .  | 170        |
| 12.2.3. Magnetic Vortex Transistor (MVT) . . . . .  | 175        |
| 12.2.4. Fan-Out . . . . .   | 178        |
| 12.3. Conclusions . . . . .   | 179        |
| <b>13. Conclusions</b>  | <b>182</b> |
| 13.1. Summary . . . . .   | 182        |
| 13.2. Future Scope . . . . .  | 186        |

---

|   |            |
|---|------------|
| <b>A. Appendix</b>                                | <b>189</b> |
| A.1. Supplementary Note for Chap. 12 . . . . .    | 189        |
| A.2. Supplementary Figures for Chap. 12 . . . . . | 190        |
| <b>Bibliography</b>                               | <b>194</b> |

# List of Abbreviations

|      |  |
|------|--|
| 1D   | : One-Dimensional.                         |
| 2D   | : Two-Dimensional.                         |
| 3D   | : Three-Dimensional.                       |
| ADL  | : AntiDot Lattice.                         |
| BV   | : Backward Volume.                         |
| BZ   | : Brillouin Zone.                          |
| CAD  | : Computer Aided Design.                   |
| CCD  | : Charged Coupled Diode.                   |
| CMOS | : Complementary Metal-Oxide-Semiconductor. |
| CW   | : Clockwise.                               |
| CCW  | : Counter-Clockwise.                       |
| Co   | : Cobalt.                                  |
| DE   | : Damon-Eshbach.                           |
| DFT  | : Discrete Fourier Transform.              |
| ESD  | : Energy Spectral Density.                 |
| FDM  | : Finite Difference Method.                |
| FEM  | : Finite Element Method.                   |
| FFT  | : Fast Fourier Transform.                  |
| FIB  | : Focused Ion Beam.                        |
| FV   | : Forward Volume.                          |
| LLG  | : Landau-Lifshitz-Gilbert.                 |
| MAW  | : Magnonic Antidot Waveguide.              |
| MC   | : Magnonic Crystal.                        |

---

|         |   |
|---------|---|
| MMA     | : Methyl MethAcrylate.                          |
| MRAM    | : Magnetic Random Access Memory.                |
| MS      | : Micromagnetic Simulation.                     |
| OBD     | : Optical Bridge Detector.                      |
| ODE     | : Ordinary Differential Equation.               |
| OOMMF   | : Object Oriented MicroMagnetic Framework.      |
| PBC     | : Periodic Boundary Condition.                  |
| PPDP    | : Power and Phase Distribution Profile.         |
| PMMA    | : PolyMethyl MethAcrylate.                      |
| PWM     | : Plane Wave Method.                            |
| PVFT    | : Precessing Vector Fourier Transform.          |
| Py      | : Permalloy ( $\text{Ni}_{80}\text{Fe}_{20}$ ). |
| SEM     | : Scanning Electron Microscopy.                 |
| SHG     | : Second Harmonic Generator.                    |
| STT     | : Spin-Transfer Torque.                         |
| SW      | : Spin-Wave.                                    |
| TR-MOKE | : Time-Resolved Magneto-Optic Kerr Effect.      |
| YIG     | : Yttrium Iron Garnet.                          |
| w.r.t.  | : with respect to.                              |

# List of Commonly Used Symbols\*†

|                                    |  |
|------------------------------------|--|
| $\Gamma$                           | : Centre of the Brillouin zone.          |
| $\mu_B$                            | : Bohr magneton.                         |
| $\alpha$                           | : Gilbert damping.                       |
| $\gamma,  \bar{\gamma} ,  \gamma $ | : Gyromagnetic ratio.                    |
| $\mu_0$                            | : Magnetic permeability of free space.   |
| $\mu_B$                            | : Bohr magneton.                         |
| $\theta^f$                         | : Phase of SWs.                          |
| $\omega$                           | : SW angular frequency.                  |
| $A$                                | : Exchange coefficient.                  |
| $\mathbf{H}_{\text{anis}}$         | : Anisotropy field.                      |
| $\mathbf{H}_{\text{bias}}$         | : Bias field.                            |
| $\mathbf{H}_{\text{dem}}$          | : Demagnetizing field.                   |
| $\mathbf{H}_{\text{eff}}$          | : Effective field.                       |
| $\mathbf{H}_{\text{exch}}$         | : Exchange field.                        |
| $\mathbf{H}_{\text{ext}}$          | : External field.                        |
| $\mathbf{H}_{\text{sig}}$          | : Excitation signal.                     |
| $J$                                | : Total angular momentum quantum number. |
| $K_1, K_2, K'_1, K'_2$             | : Magneto–crystalline anisotropy.        |
| $\mathbf{M}$                       | : Magnetization.                         |
| $M_s$                              | : Saturation magnetization.              |
| $\mathbf{m}$                       | : $\mathbf{M}/M_s$ .                     |
| $S^f$                              | : Energy spectral density of SWs.        |

---

\*These symbols are used to mean the following, unless stated otherwise in a chapter.

†Magnitude of vector quantities has been represented by the italicized non–boldface version of its symbol.

|              |   |
|--------------|---|
| $f$          | : SW frequency.                           |
| $h; \hbar$   | : Plank constant; Reduced Plank constant. |
| $\mathbf{k}$ | : SW wavevector.                          |
| $k_B$        | : Boltzmann constant.                     |
| $k_x$        | : $x$ -component of SW wavevector.        |
| $k_y$        | : $y$ -component of SW wavevector.        |
| $k_z$        | : $z$ -component of SW wavevector.        |
| $t$          | : Time.                                   |
| $u$          | : Film or waveguide thickness.            |
| $w$          | : Width of waveguide or sub-waveguide.    |
| $x$          | : $x$ -coordinate.                        |
| $y$          | : $y$ -coordinate.                        |
| $z$          | : $z$ -coordinate.                        |

# Material Parameters Used During Simulations\*

| Material | $M_s(10^6)$ A/m | $A(10^{-12})$ J/m | $K1(10^3)$ J/m <sup>3</sup> | $\alpha$  |
|----------|-----------------|-------------------|-----------------------------|-----------|
| Co       | 1.4             | 30                | 520                         | $10^{-4}$ |
| Py       | 0.8             | 13                | 0                           | $10^{-4}$ |

---

\*Gyromagnetic ratio  $|\bar{\gamma}| = 2.21 \times 10^5$  m A<sup>-1</sup> s<sup>-1</sup> is used in all cases. Gilbert damping  $\alpha = 0.9$  or  $0.95$  is used to develop the steady state before starting the magnetization dynamics; which is observed at low values of  $10^{-4}$  to obtain sharper peaks in the frequency domain. Where specified, more realistic values of  $\alpha = 0.008$  or  $0.01$  is used.

# List of Tables

|   |     |
|---|-----|
| 2.1. Magnetocrystalline anisotropy . . . . .              | 17  |
| 3.1. Micromagnetic simulators . . . . .                   | 40  |
| 9.1. SW bandgaps in a 2D ADL . . . . .                    | 139 |
| 11.1. Samples for TR-MOKE experiment . . . . .            | 152 |
| 11.2. SW peaks with changing lattice parameters . . . . . | 161 |

# List of Figures

|   |     |
|---|-----|
| 1.1. (Colour) Time scales of magnetization dynamics . . . . .                           | 2   |
| 1.2. (Colour) Spin-wave . . . . .   | 4   |
| 1.3. (Colour) Magnetic vortex . . . . .   | 8   |
| 2.1. Macroscopic model . . . . .  | 21  |
| 2.2. Perpendicular standing SW mode . . . . .   | 25  |
| 2.3. Magnetostatic SW modes in a film . . . . .   | 26  |
| 2.4. (Colour) SW dispersion in a uniform waveguide . . . . .                            | 28  |
| 2.5. (Colour) BV SWs in a uniform waveguide . . . . .                                   | 29  |
| 2.6. A generic magnonic device . . . . .  | 31  |
| 2.7. (Colour) Magnetic vortex core reversal . . . . .                                   | 33  |
| 3.1. (Colour) Modelling in FDM . . . . .  | 41  |
| 3.2. Delaunay triangulation algorithm . . . . .   | 49  |
| 3.3. (Colour) Thin-film deposition . . . . .  | 52  |
| 3.4. (Colour) Optical and e-beam lithography . . . . .                                  | 53  |
| 3.5. Scanning Electron Microscope . . . . .   | 56  |
| 4.1. (Colour) SW dispersion relations in an uniform waveguide . . . . .                 | 61  |
| 4.2. SW dispersion relations calculation algorithm . . . . .                            | 62  |
| 4.3. (Colour) Effect of windowing functions . . . . .                                   | 63  |
| 4.4. (Colour) Effect of excitation signal . . . . .                                     | 65  |
| 4.5. (Colour) SWs in a thin-film . . . . .  | 66  |
| 4.6. (Colour) SW dispersion in a MAW . . . . .  | 68  |
| 4.7. (Colour) SW dispersion in a bi-component MAW . . . . .                             | 69  |
| 4.8. (Colour) Effect of number of antidot rows on SW dispersion in a MAW . . . . .      | 71  |
| 4.9. (Colour) SW power and phase distribution in a MAW . . . . .                        | 72  |
| 4.10. (Colour) SW power and phase distribution in a MAW with 3 rows . . . . .           | 73  |
| 5.1. (Colour) MAW structure . . . . .   | 76  |
| 5.2. (Colour) SW dispersion in a MAW: unpinned . . . . .                                | 82  |
| 5.3. (Colour) SW dispersion in a MAW: pinned . . . . .                                  | 84  |
| 6.1. (Colour) Antidot lattice waveguide under investigation . . . . .                   | 90  |
| 6.2. (Colour) Intrinsic mirror symmetry breaking: antidot row . . . . .                 | 91  |
| 6.3. (Colour) Symmetry breaking calibration . . . . .                                   | 93  |
| 6.4. (Colour) Extrinsic mirror symmetry breaking: bias field . . . . .                  | 94  |
| 6.5. (Colour) Extrinsic compensation of intrinsic mirror symmetry breaking . . . . .    | 98  |
| 6.6. (Colour) Mirror symmetry breaking and compensation: hole shape. vs. bias . . . . . | 100 |

|       |  |     |
|-------|--|-----|
| 7.1.  | MAW: shape of antidots . . . . .   | 103 |
| 7.2.  | (Colour) SW dispersion in a MAW: antidot shape . . . . .                   | 106 |
| 7.3.  | (Colour) SW ESD and Phase: hole shape . . . . .                            | 107 |
| 7.4.  | (Colour) Exchange and demagnetization field profiles: hole shape . . . . . | 109 |
| 8.1.  | (Colour) MAW structure . . . . .   | 114 |
| 8.2.  | (Colour) SW dispersion in MAW: antidot size . . . . .                      | 118 |
| 8.3.  | (Colour) SW dispersion in MAW: lattice constant . . . . .                  | 121 |
| 8.4.  | (Colour) SW dispersion in MAW: antidot shape . . . . .                     | 123 |
| 8.5.  | (Colour) SW dispersion in MAW: scale . . . . .                             | 125 |
| 9.1.  | (Colour) Two-dimensional antidot lattice . . . . .                         | 132 |
| 9.2.  | (Colour) SW dispersion in a 2D ADL . . . . .                               | 136 |
| 9.3.  | (Colour) SW dispersion in a 2D ADL: new approach . . . . .                 | 138 |
| 9.4.  | (Colour) SW dispersion in a 2D ADL: ESD and phase . . . . .                | 140 |
| 9.5.  | (Colour) SW dispersion in a 2D dot lattice: BV to DE transition . . . . .  | 142 |
| 10.1. | Mapping of precessing vectors into the complex plane . . . . .             | 146 |
| 10.2. | PVFT: amplitude gain . . . . .   | 147 |
| 10.3. | (Colour) PVFT: reduced aliasing in the case of a 2D ADL . . . . .          | 148 |
| 10.4. | (Colour) PVFT: reduced aliasing in the case of a MAW . . . . .             | 149 |
| 11.1. | Fabricated MAW samples . . . . .   | 152 |
| 11.2. | Kerr rotation and ellipticity . . . . .                                    | 153 |
| 11.3. | (Colour) A schematic diagram of TR-MOKE microscope . . . . .               | 154 |
| 11.4. | BV and DE SW modes in a fabricated MAW sample . . . . .                    | 158 |
| 11.5. | (Colour) Power and phase distribution . . . . .                            | 160 |
| 11.6. | Lattice dependence of SW spectrum in a MAW . . . . .                       | 161 |
| 11.7. | Field dependence of SW spectrum in MAW . . . . .                           | 163 |
| 11.8. | (Colour) Curve fitting of experimentally observed SW modes . . . . .       | 164 |
| 12.1. | (Colour) Isolated vortex and coupled vortex pair. . . . .                  | 169 |
| 12.2. | (Colour) Gyration amplification. . . . .                                   | 171 |
| 12.3. | (Colour) Gyration amplification: Stray field distribution . . . . .        | 172 |
| 12.4. | (Colour) Magnetic vortex transistor: ESD . . . . .                         | 175 |
| 12.5. | (Colour) Magnetic vortex transistor: stray field . . . . .                 | 177 |
| 12.6. | (Colour) Fan-out . . . . .   | 179 |
| A.1.  | Isolated vortex core gyration . . . . .                                    | 191 |
| A.2.  | Coupled vortices: effect of cell size . . . . .                            | 192 |

# 1. Introductions

Magnetization dynamics at nanoscale had been predicted to be characterized by a few interesting phenomena, which are deemed useful for practical applications such as information transmission, processing and storage. For example, the theorization of some key aspects of spin-waves (SWs) occurred over fifty years ago.<sup>1,2</sup> Recent advances in fabrication techniques have allowed for the examination of such phenomena on micro- and nanoscale. As SWs of microwave frequency have considerably lower wavelengths (in comparison to light), the potential to miniaturize microwave communication appears to be the guiding motivation of most of the recent studies. SWs can be more dispersive than sound or light waves and have a band structure which typically starts at a certain non-zero minimum frequency. SW dispersion is also anisotropic in most cases. The ability to alter the response of nanoscale magnetic structures simply by controlling the external field has also attracted a lot of attention.<sup>3,4</sup> The characteristic time scales  $\tau$ , of different manifestations of magnetization dynamics can be obtained using the Heisenberg relation  $\tau = h/E$ , where  $h$  is the Planck constant and  $E$  is the involved interaction energy.<sup>5</sup> This has been presented in Fig. 1.1.

As seen from Fig. 1.1, the exchange interaction, which favours the parallel alignment of spins in a ferromagnet, has a characteristic time-scale between one and ten femtoseconds. The effects of spin-orbit coupling and spin-transfer torque (STT) are apparent under a picosecond. Laser induced ultrafast demagnetization can typically be obtained within a few hundred femtoseconds.<sup>6</sup> The precession of magnetization<sup>7</sup> and its (Gilbert) damping<sup>8</sup> feature a timespan of one picosecond to tens of nanoseconds (see Fig. 1.1). SWs have the similar characteristic time-scales depending upon the strength of the damping. The phenomena of magnetic vortex core gyration<sup>9</sup> has a characteristic timespan of one nanosecond to tens of nanoseconds. The movement of magnetic domain walls, on the other hand, occurs in a

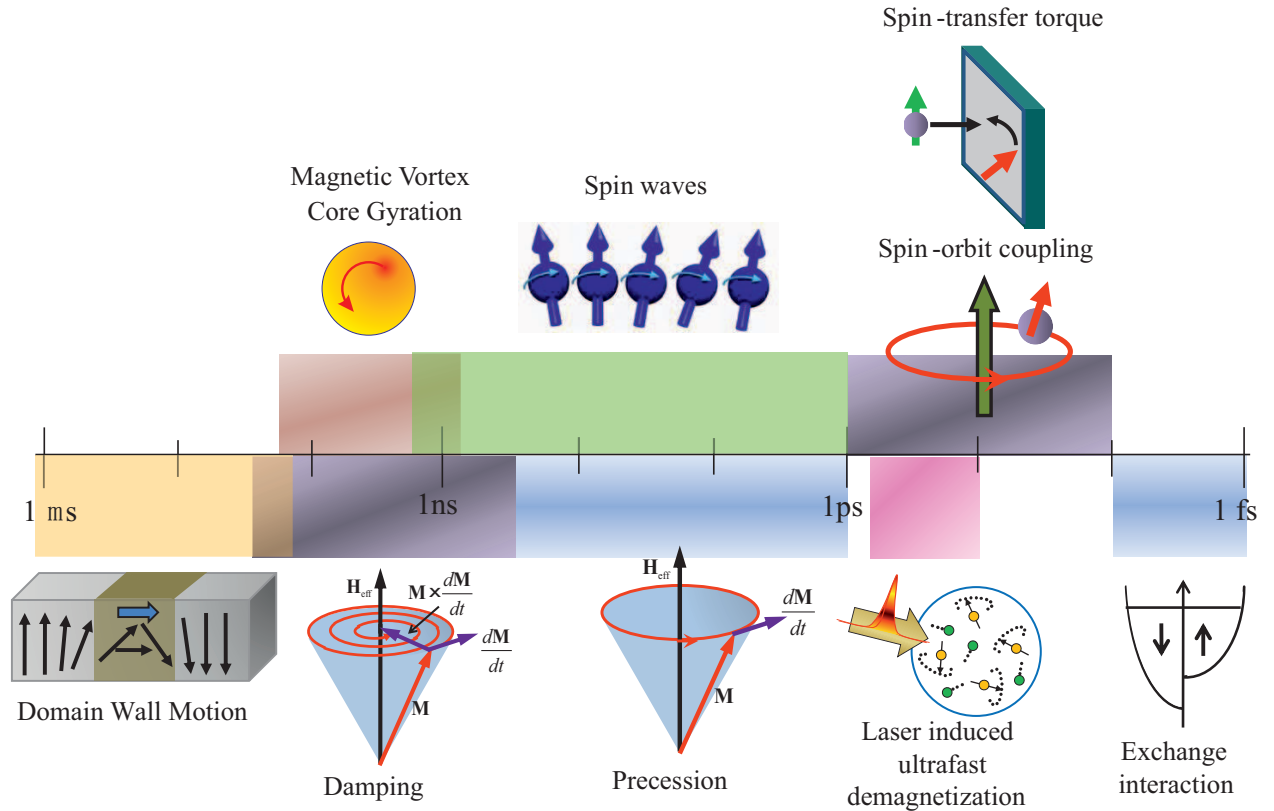


Figure 1.1.: Characteristic time scales for different manifestations of magnetization dynamics. Source: Ref. 5.

time-scale above 10 ns.

The focus of this thesis is to study SWs and magnetic vortex dynamics in nanoscale systems. As seen from Fig. 1.1,<sup>6</sup> these two roughly span the microwave and the submillimetre wave frequency bands. These two forms of magnetization dynamics are also very closely related in theory. Nanoscale magnetic systems exhibit interesting phenomena, such as, giant magnetoresistance,<sup>10,11</sup> giant Faraday rotation<sup>12</sup> and high out-of-plane magnetic anisotropy.<sup>13,14</sup> Current nanofabrication techniques give us the ability to create systems with artificial periodic modulation with high spatial resolution. SW propagating through such artificial mediums feature a characteristic spectrum complete with bands and *bandgaps* – forbidden regions in frequency domain. To this end, SW dynamics has been studied in nanoscale ferromagnetic systems such as thin-films, uniform and patterned waveguides, and nanodot and antidot arrays. *Antidots* are holes in planer ferromagnetic structures. Bi-component waveguides, where the antidots are replaced with another ferromagnet, have also been considered. Dynamics of magnetic vortices, which can also be used for the generation of

SWs<sup>15</sup> along with very efficient signal transmission and logical operations, have been studied in isolated and dipole coupled ferromagnetic nanodisks.

## 1.1. Spin–Waves

If the local magnetization  $\mathbf{M}$  of a ferromagnet gets misaligned with the effective field  $\mathbf{H}_{\text{eff}}$ , it experiences a torque leading to its precession. The precessing magnetization vector also changes its surrounding exchange and dipolar fields and spreads the information of the original misalignment of effective field to its neighbourhood. Owing to spin–orbit coupling and several other factors (like spin diffusion, magnon–phonon interaction, etc.<sup>16</sup>) the precession slowly gets damped. The processes of magnetization precession and its damping can be modelled using the Landau–Lifshitz–Gilbert (LLG) equation. Since the LLG equation describes the magnetization dynamics in terms of incremental changes in the magnetization vector, they can model any given systems as long as the involved parameters, such as the saturation magnetization, do not vary greatly during the dynamics. Thus, phenomena like SW dynamics and magnetic vortex gyration, which occur above one picosecond in time–scale and one nanometre in length–scale can be described accurately by the LLG equation.<sup>5</sup> Theoretical details of this equation has been presented in sub–Sec. 2.3.2.

The Gilbert damping is preferred over the *Bloch–Bloembergen damping*<sup>17</sup> description while dealing with ferromagnets, as the former keeps the amplitude of magnetization constant with time.<sup>18</sup> Non–Gilbert type magnetization relaxation can also be introduced by magnon–magnon scattering<sup>19,20</sup> or spin–polarized current.<sup>21</sup> In this work, we focus only on the Gilbert type damping. In frequency domain analysis of various magnetization dynamics, damping manifests itself as line–width. As it causes the information in a signal to loose coherence, damping is considered undesirable in most cases. Some recently published literature<sup>22,23</sup> seeks to lower this damping by working with different types of materials. Long range coherence of SW edge modes has also been theorized in an insulating ferromagnet<sup>24</sup> and other nanoscale systems.<sup>25</sup>

The largest contributor to  $\mathbf{H}_{\text{eff}}$  is typically the bias field  $\mathbf{H}_{\text{bias}}$ , while the SW is usually produced during a simulation by using the excitation signal  $\mathbf{H}_{\text{sig}}$ . To study the nature of

SWs generated with different bias directions, it is sometimes desirable to avoid the anisotropy field  $\mathbf{H}_{\text{anis}}$  by using materials like permalloy (Py:  $\text{Ni}_{80}\text{Fe}_{20}$ ) which have negligible magnetocrystalline anisotropy. Typically, a high bias field of strength ( $> 1$  T) is used to completely saturate the Py medium. A high value of  $\alpha \geq 0.9$  is used at the beginning of any simulations; so that the magnetic ground state may be achieved quickly. Later,  $\alpha$  is reduced to an artificially low value of  $10^{-4}$ ; so that a better resolution may be obtained in the frequency domain during a Fourier analysis. Any deviations from these parameters will be explicitly stated.

When the information of the any misalignment between the effective magnetic field and the magnetization starts to propagate as a collective excitation, SWs are said to be generated.<sup>1,26–28</sup> SWs can also be produced by STT from spin polarized current.<sup>29</sup> Figure 1.2 depicts this wave as a green curve being traced by one of the dynamical components of magnetization  $\mathbf{M}$ . As in the case of photonic or phononic waves, SWs too are capable of carrying information in the form of energy and momentum.

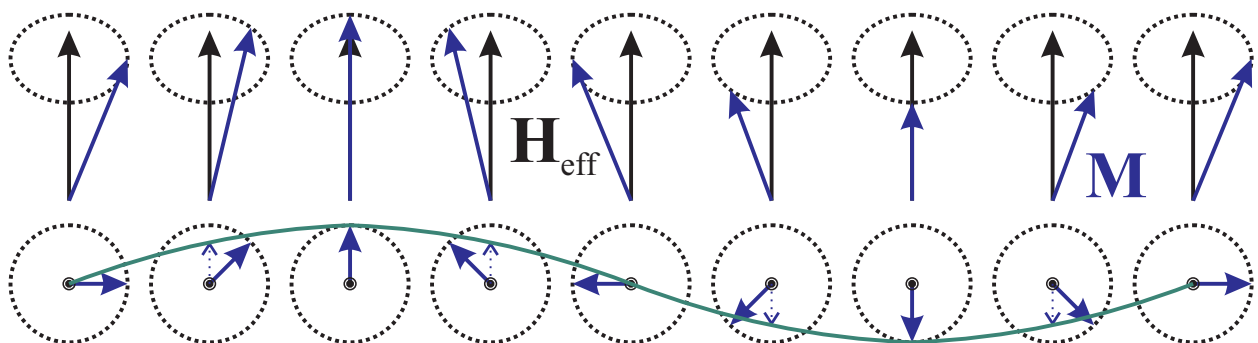


Figure 1.2.: (Top panel) Precession of blue magnetization  $\mathbf{M}$  vector around the black effective field  $\mathbf{H}_{\text{eff}}$  vector. Here the spins are arranged in an one-dimensional chain with discrete translational symmetry. (Bottom panel) Top view of the precessional dynamics showing an imaginary green wave-like curve being traced by one of the components of  $\mathbf{M}$ .

*Magnons* were theorized<sup>2,30</sup> as the quasi-particles associated with the quantization of SWs. Like photons or phonons, magnons too are classified as bosons.<sup>31–33</sup> The same, however, is not the case with electrons. Nevertheless, several techniques developed to study electrons, photons or phonons as information carriers can also be used in the case of magnons. Compared with light or sound waves, the dispersion relation in the case of SWs can be much easily controlled by controlling an extrinsic parameter — the external field,<sup>4</sup> even while the

SW dynamics is in progress.<sup>3</sup> This introduces the most significant advantage that a SW based system can have over its electronic, photonic or phononic analogues.

*Magnonic crystals*<sup>34–39</sup> (MCs) are metamaterials typically created by spatially modulating the magnetic parameters such as saturation magnetization,  $M_s$  or exchange coefficient,  $A$ <sup>40–42</sup> of a known material and where SWs are the transmission waves. MCs can be regarded as the magnonic analogues of photonic and phononic crystals. Knowledge of SW dispersion within such structures is necessary for their design and operation. An MC can be realized by a combination of periodic modulation of structural and material parameters of a magnetic material and a control over the external bias magnetic field.<sup>40–42</sup> This creates a periodic magnetic potential within an MC, which scatters the SWs eventually yielding a characteristic dispersion relation comprising of stop and pass bands. Most MCs that form the topic of current research in magnonics are either 1D<sup>43,44</sup> or 2D<sup>45–50</sup> as they are easier to fabricate on a wafer when compared to 3D MCs. Nevertheless, few theoretical reports on the study of dispersion of SWs in 3D MCs have been made.<sup>2,51,52</sup> Magnetic antidots arrays, which support higher group velocities (as compared to MCs based on dot arrays), have emerged as an important system of MCs; and a thorough investigation of high frequency magnetization dynamics in them have been reported in the literature.<sup>50,53–59</sup> Recently, the first MCs made by arranging two ferromagnetic materials with nanoscale discrete translational symmetry (bi-component MCs) have been fabricated<sup>49</sup> and bandgaps in their SW spectrum was experimentally verified.<sup>60–62</sup> Tunability of SW spectra based on the lattice symmetry in a 2D lattice of nanodots has also been reported.<sup>63,64</sup> 2D antidots lattices, formed by periodic array of holes in a ferromagnetic film, can be fabricated much easily. These systems have been intensively studied in recent years on different length-scales as well.<sup>65,66</sup>

For antidot lattices with large spatial periodicity,<sup>66</sup> the inhomogeneity of the internal magnetic field is decisive for the formation of the magnonic band structure.<sup>67</sup> With the decreasing period of antidot lattice the Brillouin zone (BZ) border will move to larger wave-vectors and the exchange interactions at some point will start to play a primary role in the formation of magnonic band structure.<sup>68</sup> Thus, based on the nature of this dependence SWs can be classified as *dipole-dominated* and *exchange-dominated*, respectively. Dipole-dominated SWs have wavelengths much greater than  $\lambda_{\text{ex}}$ , where  $\lambda_{\text{ex}} = \sqrt{2A/(\mu_0 M_s^2)}$  is

the characteristic exchange length of the ferromagnetic medium. Typically, the wavelength of dipole–dominated SWs is in the order of a few microns. On the contrary, exchange–dominated SWs have wavelengths of the order of  $\lambda_{\text{ex}}$ . This value is commonly of the order of 5 nanometres. SWs with intermediate wavevector values are called *dipole–exchange* SWs.

*Magnonics*<sup>37,38,69–71</sup> is an emerging sub–field of solid state physics, which deals with the study of SWs and related aspects of magnetization dynamics. Magnonics is mainly aimed at exploiting the properties of SWs for technological applications in the fields of microwave systems, metamaterials for electromagnetic waves, spintronics, and other magnonic devices using SWs for information communication. Compared to microwave technology, the other three fields are relatively new and in their nascent stage.<sup>69,72–75</sup> Signal processing in electronic devices relies on the electronic band structure of semiconductors. Recent developments in silicon photonics, such as the cascaded Raman laser,<sup>76</sup> also exploit the discovery of suitable bands and bandgaps. Thus, one cannot proceed with the design or development of nanoscale *magnonic devices*<sup>77,78</sup> without the study SW band structure. The possibility of tailoring metallic magnetic materials with nanoscale precision provides a tool for miniaturization and shaping the dispersion of high–frequency SWs. Apart from magnonic crystals, waveguides,<sup>79</sup> SW interferometers<sup>80–82</sup> and phase shifters<sup>83</sup> are some of the important components of magnonic devices. Like photonic devices, magnonic devices too promise a lower power consumption compared to today’s electronic devices. However, once an electronic or photonic device is designed, not much can be changed to alter its characteristics during operation. This, however is not the case with SW based devices whose characteristics can be changed extrinsically by the control of  $\mathbf{H}_{\text{bias}}$ .<sup>3,4</sup> Further, structured SW waveguides<sup>84–86</sup> have recently attracted considerable attention due to their selective transmission of microwave bands in the micro– and nano–scales and their potential applications in on–chip microwave signal processing and communication.

Prototypes of basic magnonic devices have already been demonstrated to be promising for technological applications,<sup>3,69,70,73,87</sup> but the scaling down of magnonic elements to tens of nanometres in size and tens to hundreds of GHz of operating frequencies<sup>88–91</sup> are still a challenge. Waveguides for SWs are deemed to be of vital importance in most magnonic devices.<sup>69</sup> Various forms of waveguides, such as, flat stripes having filtering properties due

to periodically modulated width<sup>85</sup> or based on a (missing) row defect in 2D MCs have been studied.<sup>38,55,92–97</sup> But so far, experiments are only done for SWs in the frequency range up to a few gigahertz. Owing to the recent advances in fabrication techniques, it has become feasible to fabricate structures with resolution better than 10 nm. For example, the spot size during focused ion beam lithography can go below 10 nm with low ( $\approx 30$  pA) ion current.<sup>50,98–100</sup> To predict properties of magnonic devices at nanometre length scale, more basic research needs to be conducted. Therefore, theoretical investigation of the SW waveguides and MCs operating in the range of tens to hundreds of GHz is a frontier field of research.

Another topic of technological importance deals with the generation and detection of SWs on nanoscale. The interactions of magnons with electrons, photons and phonons have been exploited to generate and detect SWs. SWs can be produced by spin torque nano-oscillators<sup>101,102</sup> or spin-polarized current<sup>103</sup> or by using phenomenon such as spin-Hall effect<sup>104</sup> or spin-Seebeck effect<sup>105–108</sup> and they can be detected using the inverse spin-Hall effect.<sup>109</sup> SWs can also be generated by certain magnon-soliton interactions.<sup>15</sup> A time-resolved magneto-optic Kerr effect (TR-MOKE) experimental setup uses high energy photons to excite SWs<sup>110–114</sup> and low energy photons to detect them.<sup>115–117</sup> Any time-resolved measurement done on SWs should have a temporal resolution below one picosecond to account for SWs upto 500 GHz. Short bursts of terahertz SWs have been also optically excited in ferromagnetic<sup>118,119</sup> and anti-ferromagnetic<sup>120,121</sup> mediums, testifying to the quantum nature of magnons. A vector network analyzer<sup>122,123</sup> can be used to directly detect the SW spectra while a Brillouin light scattering setup<sup>111,124,125</sup> can be used to experimentally examine the SW dispersion relation in wavevector domain as well.

## 1.2. Magnetic Vortices

Micro- and nanoscale ferromagnetic disks can support a non-trivial spin configuration called a magnetic vortex,<sup>126,127</sup> which is another kind of magnetic system studied here with the view point of information processing. Magnetic vortices can find applications in magnetic data storage, magnetic random access memory,<sup>128–131</sup> magnetic logic circuitry,<sup>132</sup> information processing devices<sup>132</sup> or the detection of impurities in a magnetic material.<sup>133</sup> Often the

magnetization aligns itself along the boundaries of laterally confined geometries in order to minimize the energy stored in the stray field. This can lead to an anti-parallel arrangement of magnetization close to the centre of the geometry. Thus, in ferromagnetic circular nanodisks, the exchange interaction pushes the magnetization at the centre of the disk out of plane: either up or down. The sense of flux closed magnetization structure — clockwise (CW) or counter-clockwise (CCW) — represents the *chirality* of the vortex.<sup>134</sup> The part of the vortex with out of plane component is called its core which can support either ‘up’ or ‘down’ *polarity*.<sup>135</sup> The chirality and the polarity of the magnetic vortex can be seen in Fig. 1.3.<sup>127</sup>

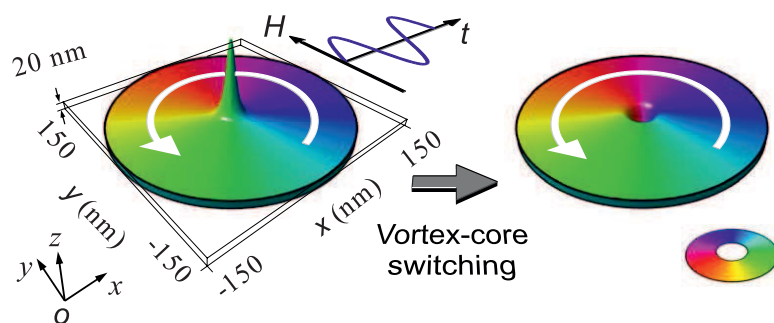


Figure 1.3.: Colour coded cyclic arrangement of magnetization in a magnetic vortex. The spikes in middle of the geometry represent the vortex core, which can be switched by applying an in-plane rotating magnetic field. Source: Ref. 127.

Apart from waveguides and MCs, micro- and nanomagnetic disks and rings are also useful in signal processing as they cover the sub-GHz regime, which is usually inaccessible by SWs. Resonating vortices, for example can be phase locked using SWs.<sup>136</sup> As seen in Fig. 1.3, magnetic vortex cores can be switched from ‘up’ to ‘down’ by the application of an external magnetic field. This polarity reversal can also be used for SW generation.<sup>15</sup> It can also be brought to gyration<sup>137,138</sup> by the application of the magnetic fields and spin polarized currents.<sup>128,139–143</sup> External magnetic fields and spin polarized currents couple to the magnetic moments of the vortex core and drive it away from the equilibrium position. In addition to these external forces, the displaced vortex core experiences an internal force arising from the demagnetizing field of the non-equilibrium magnetization pattern. This force attempts to restore the core to its equilibrium position, thus aiding the gyrotropic motion. For large amplitude excitation, the internal force increases nonlinearly and this results into a non linear vortex core gyration, and vortex core switching occurs along with creation and annihilation.

lation of new vortex and antivortex.<sup>144,145</sup> For small amplitude excitation, the internal force increases linearly and the vortex core motion remains in the linear regime.<sup>146</sup> Apart from saturation magnetization, the natural gyration frequency of a magnetic vortex also depends on the aspect ratio (the ratio of disk's diameter and thickness) of the ferromagnetic disk.<sup>147</sup>

The presence of polarity dependent rotational asymmetry makes them very attractive candidates for studying the interaction between the local magnetization and externally applied magnetic fields or spin polarized currents.<sup>139,148–157</sup> The magnetization dynamics resulting in the gyrotropic vortex core motion can also be described by the LLG equation<sup>8,158</sup> (see sub-Sec. 2.3.2). In the linear regime, the vortex core equation of motion can be derived from the Thiele's equation.<sup>146</sup> The CW or CCW sense of vortex core gyration direction is solely controlled by its polarity. In the linear regime, vortex core can be described by a harmonic oscillator model.<sup>159</sup> Consequently, magnetostatically coupled vortex gyration can be considered as coupled oscillators. Therefore, one expects mutual energy transfer and a consistent phase relation between the gyrating vortices.<sup>160,161</sup> Logic operations based on magnetic vortex state networks have been demonstrated experimentally via the vortex gyration mediated information signal transfer mechanism.<sup>162</sup>

Subsequently, the mutual transfer of energy between magnetostatically coupled vortices where one of the vortices is locally excited is extremely important for microwave communication and logic operations. In this regard, the parameters like the signal transport rate and efficiency are the key factors in determining the device performance. Vortex gyration transfer rate and energy attenuation coefficients have been calculated by analytical method and micromagnetic simulations.<sup>163</sup> Stimulated vortex gyration based energy transfer between spatially separated dipolar coupled magnetic disks has been observed by time resolved soft x-ray microscopy.<sup>155</sup> The rate of energy transfer is found to be determined by the frequency splitting caused by the dipolar interaction between the vortices.<sup>162</sup>

This energy transfer efficiency may depend on several factors such as the frequency of the exciting field pulse as compared to the gyration frequency of the vortex core, the amplitude and nature of the exciting pulse, the distance between the vortices and their relative polarity. Until recently,<sup>155</sup> the energy transfer efficiency was found to be well below 100%<sup>160,161</sup> and no amplification has been reported thus far. It has also been reported that the interaction

strength between coupled vortices is maximum when their core polarities are opposite,<sup>155</sup> although, higher interaction strength is not the sufficient condition for higher transfer efficiency. For higher amplitude input, the vortex motion enters the non-linear regime and vortex core switching occurs; making it impossible to increase and maintain a large amplitude output and a constant phase relation between gyrotropic motion of both the vortices. On the other hand, if the input signal is very weak and the frequency is close to the gyration frequency of the vortex core, the amplitude of the response gradually increases indicating that the core switching may occur at some point, which is not desirable for device application.

In Chap. 2, we introduce the background theory on which the new contributions presented in this thesis are based. Some state of the art prior to this work has also been presented here. In Chap. 3, we introduce parts of the scientific method employed during this work. Basics of the numerical methods have been presented in Chap. 4. Here we show how to obtain the SW spectra in different kinds of nanoscale magnetic systems. In Chap. 5, we study the effect free or pinned boundary conditions may have on the SW dispersion relation of a magnonic antidot waveguide (MAW) — a magnetic waveguide like structure with a row of holes (or antidots) milled along their central axis. We noticed that bandgaps can be opened in the same system if pinned boundary conditions are used without changing any material or geometrical parameters. From Chaps. 6 to 8, we consider the effects of different geometrical parameters of a MAW over its characteristic SW dispersion. Among other things, we also establish that bandgaps which collapse due to a loss of physical mirror symmetry can be recovered by using an asymmetric bias field. We extend the numerical methods to analyse the SW dispersion in 2D MCs in Chap. 9. In Chap. 10, another enhancement of the numerical method is introduced which nullifies the aliasing associated with the Fourier transforms of real valued data. As a result, we could confirm the existence of bandgaps in submillimetre frequency band in the case of a MAW. The dependence of SW spectra on lattice and bias field has been experimentally examined in Chap. 11. Polarity dependent asymmetric gain in the gyrotropic modes of magnetostatically coupled magnetic vortices has been presented in Chap. 12. Based on this observation, we also demonstrate how the operational states of a conventional transistor may be obtained using a chain of magnetic vortices. We summarize the observation made during this work in Chap. 13.

## 2. Theoretical Background

### 2.1. Ferromagnetism

A material placed within a *magnetic field*  $\mathbf{H}$ , may develop a non-zero magnetic moment. Magnetic moment per unit volume is termed as *magnetization* and is conventionally represented by the symbol  $\mathbf{M}$ . *Magnetic susceptibility*  $\chi$  is defined as the ratio of magnetization  $\mathbf{M}$  to the magnetic field  $\mathbf{H}$ :

$$\mathbf{M} \equiv \chi \mathbf{H}. \quad (2.1)$$

The dependence of magnetic susceptibility  $\chi$ , on field  $\mathbf{H}$  determines the *magnetic ordering* of the material. On the basis of this criteria a material can be classified as diamagnetic, paramagnetic, ferromagnetic, antiferromagnetic or ferrimagnetic. *Langevin's classical theory of diamagnetism* uses the electron's orbital angular momentum to adequately explain why the diamagnetic susceptibility  $\chi_d$  (typically of the order of  $10^{-6}$  cm<sup>3</sup>/mol), is always negative and independent of changes to temperature or magnetic field  $\mathbf{H}$ . If the material has  $N$  atoms per unit volume and each atom contains  $Z$  electrons, then the diamagnetic susceptibility  $\chi_d$  is given as

$$\chi_d = -\frac{Ne^2}{6mc^2} \sum_{i=1}^Z \langle r^2 \rangle r_i. \quad (2.2)$$

Here,  $m$  is the mass of an electron and  $c$  is the speed of light.

*Curie's law* for paramagnetism uses a quantum mechanical model to explain why the susceptibility in a paramagnetic material  $\chi_p$ , is independent of the magnetic field and varies inversely with temperature  $T$ . If  $g$  represents the Landé g-factor, the paramagnetic susceptibility is given as

$$\chi_p = \frac{C}{T}, \quad (2.3)$$

where

$$C = \frac{Ng^2J(J+1)\mu_B^2}{3k_B}. \quad (2.4)$$

The ferromagnetic susceptibility  $\chi_f$  is similarly given by the following *Curie–Weiss law*:

$$\chi_f = \frac{C}{T - WC} = \frac{C}{T - T_c}, \quad (2.5)$$

where  $T_c = WC$  is called the *Curie temperature* below which, all ferromagnetic materials demonstrate spontaneous magnetization. In order to derive the Curie–Weiss law (Eq. (2.5)), Weiss assumed an average molecular field of the form  $\mathbf{H} + W\mathbf{M}$ , where  $W$  is known as the *Weiss constant*. The Heisenberg theory establishes that this molecular field comes from the quantum mechanical *exchange interaction*. Pauli's exclusion principle dictates that the two electronic wavefunctions of a hydrogen molecule must combine antisymmetrically. Using separation of variables, the wavefunction  $\psi(r_i, s_i)$  of an electron can be expanded as

$$\psi(r_i, s_i) = \rho(r_i) \sigma(s_i), \quad (2.6)$$

where  $\rho$  and  $\sigma$  are functions of electron's position  $r_i$  and spin  $s_i$ , respectively. Now, the antisymmetric wavefunctions can be expressed as either

$$\psi_S = \rho_{sym}(r_1, r_2) \sigma_{anti}(s_1, s_2), \text{ or} \quad (2.7)$$

$$\psi_T = \rho_{anti}(r_1, r_2) \sigma_{sym}(s_1, s_2). \quad (2.8)$$

Here,  $\psi_S$  and  $\psi_T$  represent the *singlet* and the *triplet* states, respectively. They can be expanded as

$$\psi_S = A[\rho_a(r_1)\rho_b(r_2) + \rho_a(r_2)\rho_b(r_1)][\sigma_\alpha(s_1)\sigma_\beta(s_2) - \sigma_\alpha(s_2)\sigma_\beta(s_1)], \text{ and} \quad (2.9)$$

$$\psi_T = B[\rho_a(r_1)\rho_b(r_2) - \rho_a(r_2)\rho_b(r_1)] \begin{bmatrix} \sigma_\alpha(s_1)\sigma_\alpha(s_2) \\ \sigma_\alpha(s_1)\sigma_\beta(s_2) + \sigma_\alpha(s_2)\sigma_\beta(s_1) \\ \sigma_\beta(s_1)\sigma_\beta(s_1) \end{bmatrix}. \quad (2.10)$$

Spins are antiparallel in the singlet state with a total spin quantum number  $S = 0$ . How-

ever, in the triplet state, the total spin quantum number  $S = 1$  allows for a degeneracy of  $(2S + 1) = 3$  states. The energies for singlet ( $E_S$ ) and triplet ( $E_T$ ) states can be written as

$$E_S = A^2(K_{12} + J_{12}), \text{ and} \quad (2.11)$$

$$E_T = B^2(K_{12} - J_{12}). \quad (2.12)$$

Here,  $K_{12}$  and  $J_{12}$  denote the Coulomb interaction and *exchange integral*, respectively. They can be expressed by the following two integrals:

$$K_{12} = \int \rho_a^*(r_1) \rho_b^*(r_2) \mathcal{H}_{12} \rho_a(r_1) \rho_b(r_2) d\tau_1 d\tau_2, \text{ and} \quad (2.13)$$

$$J_{12} = \int \rho_a^*(r_1) \rho_b^*(r_2) \mathcal{H}_{12} \rho_a(r_2) \rho_b(r_1) d\tau_1 d\tau_2. \quad (2.14)$$

Here  $\mathcal{H}_{12} = e^2/r_{ab} + e^2/r_{12} - e^2/r_{1b} - e^2/r_{a2} : r_{ij} = |r_i - r_j|$ , is the Hamiltonian for electrons 1 and 2 in a hydrogen molecule with nuclei  $a$  and  $b$ .

A positive  $J_{12}$  favours the triplet state – and the parallel arrangement of spins – as  $E_T$  decreases. This is the case with ferromagnets, where the interatomic spacing  $r_{ab}$  is larger as compared to the radii of the  $d$  and  $f$  electronic orbitals.  $J_{12}$  becomes negative in *antiferromagnetic* materials leading to an antiparallel arrangement of neighbouring spins. This results in a zero net magnetism. In the case of *ferrimagnets* the antiparallel magnetic moments do not have the same magnitude. This is due to the presence of two sublattices hosting two types of ions with differing magnetic moments. This bestows ferrimagnets with some net magnetization at low temperatures. Analogous to the Curie temperature for ferromagnets, there exists a *Néel temperature* for antiferromagnets and ferrimagnets above which the thermal energy overcomes the energy of the magnetic ordering and a paramagnetic behaviour unfolds.

In this work, we deal with ferromagnetic materials like permalloy (Py:  $\text{Ni}_{80}\text{Fe}_{20}$ ) and cobalt (Co) only (the description of the hydrogen molecule has been used for the sake of simplicity). Hence, the term ‘magnetic material’ is used interchangeably with ‘ferromagnetic material’.

## 2.2. Magnetic Energies

Different components of the effective field  $\mathbf{H}_{\text{eff}}$ , is the vector sum of the external field, the demagnetizing field and the magnetocrystalline anisotropy field. Each of these components of the effective field  $\mathbf{H}_{\text{eff}}$ , contribute to the total magnetic energy  $E_{\text{tot}}$  of the system:

$$E_{\text{tot}} = E_Z + E_e + E_d + E_K, \quad (2.15)$$

where  $E_Z$ ,  $E_e$ ,  $E_d$  and  $E_K$  are the Zeeman energy, the exchange energy, the magnetostatic self-energy and the magnetocrystalline anisotropy energy, respectively. These different energy terms and their dependence on magnetization  $\mathbf{M}$  are discussed in the following subsections. Other magnetic energies, such as magnetostriction can be considered in Eq. (2.15) as well. However, they are outside the scope of this work.

### 2.2.1. Zeeman Energy

*Zeeman energy*  $E_Z$ , is the energy which originates from the interaction of external magnetic field  $\mathbf{H}_{\text{ext}}$  (which itself can be described as the sum of the bias magnetic field  $\mathbf{H}_{\text{bias}}$  and any applied signal  $\mathbf{H}_{\text{sig}}$ ), with magnetization  $\mathbf{M}$ . It can be expressed as follows:

$$E_Z = -\mu_0 \int \mathbf{M} \cdot \mathbf{H}_{\text{ext}} dV. \quad (2.16)$$

Here,  $V$  is the volume of the magnetic material. The external field is generally specified explicitly. The Zeeman energy is minimized when magnetization is parallel to the external field.

### 2.2.2. Exchange Energy

Exchange energy is the main cause of ferromagnetism (see Sec. 2.1). Assuming an isotropic exchange interaction, the Heisenberg Hamiltonian for exchange energy  $E_e$  can be evaluated as<sup>164</sup>

$$E_e = -2 \sum_{ij} (J_e \mathbf{S}_i \cdot \mathbf{S}_j), \quad (2.17)$$

where  $J_e$  is the isotropic exchange integral and  $\mathbf{S}_i$  and  $\mathbf{S}_j$  are total spins at neighbouring sites  $i$  and  $j$ . We can replace the summation with an integral to rewrite Eq. (2.17) for a continuous geometry as

$$E_e = A \int (\nabla \mathbf{m})^2 dV, \quad (2.18)$$

where  $\mathbf{m} = \mathbf{M}/M_s$  is the ratio of magnetization to the saturation magnetization,  $(\nabla \mathbf{m})^2$  is a shorthand for  $(\nabla m_x)^2 + (\nabla m_y)^2 + (\nabla m_z)^2$ .  $A$  is the *exchange coefficient* given by

$$A = A_{ij} = \frac{2J_e S^2}{\Delta_{ij}}, \quad (2.19)$$

where  $\Delta_{ij}$  is separation between neighbouring sites  $i$  and  $j$ . Isotropy is assumed with  $A = A_{ij}$ . For ferromagnets such as nickel, permalloy ( $\text{Ni}_{80}\text{Fe}_{20}$ ), iron and cobalt, the typical values of the exchange coefficient are<sup>6</sup>  $9 \times 10^{-12}$  J/m,  $13 \times 10^{-12}$  J/m,  $21 \times 10^{-12}$  J/m and  $30 \times 10^{-12}$  J/m, respectively.

### 2.2.3. Magnetostatic Self-Energy

The Maxwell's equations for a ferromagnet can be written as<sup>6</sup>

$$\nabla \times \mathbf{H}_{\text{dem}} = 0, \text{ and} \quad (2.20)$$

$$\nabla \cdot \mathbf{B} = 0. \quad (2.21)$$

Here,  $\mathbf{H}_{\text{dem}}$  is the demagnetizing field. Using  $\mathbf{B} = \mu_0 (\mathbf{H}_{\text{dem}} + \mathbf{M})$  and the fact that curl of a gradient is zero, we can now deduce

$$\mathbf{H}_{\text{dem}} = -\nabla U_{\text{dem}}, \text{ and} \quad (2.22)$$

$$\nabla \cdot \mathbf{H}_{\text{dem}} = -\nabla \cdot \mathbf{M}. \quad (2.23)$$

Thus, we arrive at

$$\nabla^2 U_{\text{dem}} = \nabla \cdot \mathbf{M}. \quad (2.24)$$

Here,  $U_{\text{dem}}$  is a scalar potential corresponding to the demagnetizing field  $\mathbf{H}_{\text{dem}}$ .

The component of  $\mathbf{H}_{\text{dem}}$  parallel to the ferromagnet's surface  $S$  needs to be continuous

near  $S$ . Similar constraint is obeyed by the component of  $\mathbf{B}$  which is normal to the surface  $S$ . Apart from these boundary conditions, far away from the ferromagnet, we also have  $U_{\text{dem}} \rightarrow 0$ . Equation (2.24) can be solved analytically with these boundary conditions to obtain<sup>165,166</sup>

$$U_{\text{dem}}(\mathbf{r}) = \frac{1}{4\pi} \left( - \int_{V'} \frac{\nabla' \cdot \mathbf{M}(\mathbf{r}')}{|\mathbf{r} - \mathbf{r}'|} dV' + \oint_{S'} \frac{\hat{\mathbf{n}} \cdot \mathbf{M}(\mathbf{r}')}{|\mathbf{r} - \mathbf{r}'|} dS' \right), \quad (2.25)$$

where  $V'$  represents the volume of the ferromagnet bounded by surface  $S'$ . Thus, from Eqs. 2.22 and 2.25, we get

$$\mathbf{H}_{\text{dem}}(\mathbf{r}) = \frac{1}{4\pi} \left( - \int_{V'} \frac{(\mathbf{r} - \mathbf{r}') \nabla' \cdot \mathbf{M}(\mathbf{r}')}{|\mathbf{r} - \mathbf{r}'|^3} dV' + \oint_{S'} \frac{(\mathbf{r} - \mathbf{r}') \hat{\mathbf{n}} \cdot \mathbf{M}(\mathbf{r}')}{|\mathbf{r} - \mathbf{r}'|^3} dS' \right). \quad (2.26)$$

Knowing  $\mathbf{H}_{\text{dem}}$  from Eq. (2.26), the magnetostatic self-energy  $E_d$  can now be calculated as

$$E_d = -\frac{\mu_0}{2} \int_V (\mathbf{H}_{\text{dem}} \cdot \mathbf{M}) dV. \quad (2.27)$$

#### 2.2.4. Magnetocrystalline Anisotropy Energy

Spin-orbit coupling in a crystal structure can force the electronic spins to favour some crystallographic directions more than others. Thus, depending upon the crystal structure of a ferromagnet, certain directions may be preferred by the magnetization vector  $\mathbf{M}$ . The magnetocrystalline anisotropy energy is minimum if  $\mathbf{M}$  points along these crystallographic axes. They are defined as *easy axes*. *Hard axis* is the crystallographic direction along which, it is very difficult for the magnetization vector to align itself as doing so would result in a high magnetocrystalline anisotropy energy  $E_K$ . It is conventional to express such *uniaxial anisotropy* as a polynomial of sines of the angle  $\theta$  made by magnetization  $\mathbf{M}$  with the easy axis:<sup>164</sup>

$$E_K = K_1 \sin^2 \theta + K_2 \sin^4 \theta, \quad (2.28)$$

where, the *anisotropy constants*  $K_1$  and  $K_2$  (typically  $K_1 \gg K_2$ ) change with temperature. If  $K_1 < 0$ , the easy axis lies in plane — known as the *easy plane* — perpendicular to a predefined crystallographic direction.

Similar to the uniaxial anisotropy, the *cubic anisotropy* can be expressed in terms of

Table 2.1.: Magnetocrystalline anisotropy for some common ferromagnets. Source: Ref. 6.

| Metal | Crystal Structure | Easy axis    | Hard axis     | $K_1$ or $K'_1$<br>(J/m <sup>3</sup> ) | $K_2$ or $K'_2$<br>(J/m <sup>3</sup> ) |
|-------|-------------------|--------------|---------------|--|--|
| Py    | <i>fcc</i>        | —            | —             | —                                      | —                                      |
| Ni    | <i>fcc</i>        | [111]        | [110], [100]  | $-5.0 \times 10^3$                     | —                                      |
| Fe    | <i>bcc</i>        | [100], [110] | [111]         | $4.6 \times 10^4$                      | $1.5 \times 10^4$                      |
| Co    | <i>hcp</i>        | <b>c</b> *   | <b>a, b</b> * | $4.1 \times 10^5$                      | $1 \times 10^5$                        |

cosines  $\alpha_1$ ,  $\alpha_2$  and  $\alpha_3$  of the angular direction of magnetization w.r.t. the edges of the cubic crystal:<sup>164</sup>

$$E_K = K'_1 (\alpha_1^2 \alpha_2^2 + \alpha_2^2 \alpha_3^2 + \alpha_3^2 \alpha_1^2) + K'_2 \alpha_1^2 \alpha_2^2 \alpha_3^2. \quad (2.29)$$

Ni and Fe exhibit cubic anisotropy, while (*hcp*) Co features uniaxial anisotropy. Py does not have a significant magnetocrystalline anisotropy. Thus, it is ideally suited for cases where one wishes to examine the magnetization dynamics without considering the effects of magnetocrystalline anisotropy. The values of  $K_1$  (or  $K'_1$ ) and  $K_2$  (or  $K'_2$ ) for some common ferromagnets are presented in Tab. 2.1.

## 2.3. Magnetization Dynamics

### 2.3.1. Brown's Equations

Let us recall the Eq. (2.15):

$$E_{\text{tot}} = E_Z + E_e + E_d + E_K.$$

Assuming uniaxial anisotropy, we can now substitute the terms on the right hand side of the above equation by using Eqs. (2.16), (2.18), (2.27) and (2.28) to obtain:

$$E_{\text{tot}} = \int_V \left( -\mu_0 \mathbf{M} \cdot \mathbf{H}_{\text{ext}} + A (\nabla \mathbf{m})^2 - \frac{\mu_0}{2} \mathbf{M} \cdot \mathbf{H}_{\text{dem}} + K_1 \sin^2 \theta \right) dV. \quad (2.30)$$

---

\***a**, **b** and **c** are the basis vectors of the *hcp* lattice.

The value of total energy  $E_{\text{tot}}$ , near its minima should not change with minor variations in the magnetization:

$$\frac{\delta E_{\text{tot}}}{\delta \mathbf{M}} = 0. \quad (2.31)$$

With that assumption we get the following *Brown's equations*:<sup>167</sup>

$$\mathbf{m} \times \left( 2A\nabla^2 \mathbf{m} + \mu_0 M_s (\mathbf{H}_{\text{ext}} + \mathbf{H}_{\text{dem}}) + 2K_1 \cos \theta \hat{\mathbf{c}} \right) = 0, \text{ or} \quad (2.32)$$

$$\mathbf{M} \times \left( \lambda_{\text{ex}}^2 \nabla^2 \mathbf{m} + \mathbf{H}_{\text{ext}} + \mathbf{H}_{\text{dem}} + \frac{2K_1}{\mu_0 M_s} \cos \theta \hat{\mathbf{c}} \right) = 0. \quad (2.33)$$

Here,  $\hat{\mathbf{c}}$  is the unit vector along the easy axis and  $\lambda_{\text{ex}}^2$  is the ratio of the exchange coefficient  $A$  to the stray field energy constant  $\mu_0 M_s^2/2$ .  $\lambda_{\text{ex}}$  is called the *exchange length* below which the exchange field is believed to play a greater role in magnetization dynamics when compared to the demagnetizing field.

As the cross product of magnetization with another term in Eq. (2.33) is zero, both of them must be collinear. So we define the effective field as:

$$\mathbf{H}_{\text{eff}} = \overbrace{\lambda_{\text{ex}}^2 \nabla^2 \mathbf{m}}^{\mathbf{H}_{\text{exch}}} + \mathbf{H}_{\text{ext}} + \mathbf{H}_{\text{dem}} + \overbrace{\frac{2K_1}{\mu_0 M_s} \cos \theta \hat{\mathbf{c}}}_{\mathbf{H}_{\text{anis}}}. \quad (2.34)$$

Here  $\mathbf{H}_{\text{exch}}$  and  $\mathbf{H}_{\text{anis}}$  are the exchange and anisotropy fields, respectively.

If the torque  $\mathbf{M} \times \mathbf{H}_{\text{eff}}$  is not zero then magnetization  $\mathbf{M}$  will keep precessing about the effective field  $\mathbf{H}_{\text{eff}}$  until the dynamics gets damped out. The same is discussed in the next sub-section.

### 2.3.2. Landau–Lifshitz–Gilbert Equations

The Hamiltonian  $\mathcal{H}$  for a spin observable  $\mathbf{S}$  in the presence of a magnetic flux density  $\mathbf{B}$  is given by

$$\mathcal{H} = -g\mu_B \mathbf{S} \cdot \mathbf{B}/\hbar, \quad (2.35)$$

where  $\mu_B$  is the Bohr magneton and  $\hbar$  is the reduced Plank constant. The time rate of change the spin observable  $\mathbf{S}$ , can be expressed in terms of its commutation with the Hamiltonian

as:<sup>6</sup>

$$i\hbar \frac{d}{dt} \langle \mathbf{S} \rangle = [\mathbf{S}, \mathcal{H}]. \quad (2.36)$$

As per the commutation rule between different components of the spin operator, we have

$$[S_x, S_y] = i\hbar \epsilon_{xyz} S_z. \quad (2.37)$$

From Eqs. (2.35), (2.36) and (2.37), we get

$$\frac{d}{dt} \langle \mathbf{S} \rangle = \frac{g\mu_B}{\hbar} \mathbf{S} \times \mathbf{B}. \quad (2.38)$$

Using Eq. (2.38), Landau & Lifshitz<sup>7</sup> suggested:

$$\frac{d\mathbf{M}}{dt} = -|\gamma| \mathbf{M} \times \mathbf{H}_{\text{eff}}, \quad (2.39)$$

where  $|\gamma|$  is known as the *gyromagnetic ratio* and the local effective field  $\mathbf{H}_{\text{eff}}$  is defined by Eq. (2.34). Equation (2.39) is known as the *Landau–Lifshitz equation*. It describes the precession of magnetization  $\mathbf{M}$  in the presence of an effective field  $\mathbf{H}_{\text{eff}}$ .

This precession is gradually damped by dissipative processes such as spin–orbit coupling, spin diffusion, magnon–phonon interaction or misalignment of atomic spins.<sup>16</sup> Gilbert modified Eq. (2.39) to account for this damping by introducing a phenomenological damping term:

$$\frac{d\mathbf{M}}{dt} = -|\gamma| \mathbf{M} \times \mathbf{H}_{\text{eff}} + \frac{\alpha}{M_s} \mathbf{M} \times \frac{d\mathbf{M}}{dt}. \quad (2.40)$$

Here, the Gilbert damping constant  $\alpha > 0$  needs to be determined by careful experimentation. For transition metals  $\alpha \ll 1$ . Its respective values for nickel, iron, cobalt and permalloy ( $\text{Ni}_{80}\text{Fe}_{20}$ ) are 0.064, 0.0019, 0.011 and 0.008.<sup>168–170</sup> Equation (2.40) is known as the *Gilbert*

equation. Upon replacing  $d\mathbf{M}/dt$  on the right-hand-side of Eq. (2.40) with itself, we get

$$\begin{aligned}
\frac{d\mathbf{M}}{dt} &= -|\gamma| \mathbf{M} \times \mathbf{H}_{\text{eff}} + \frac{\alpha}{M_s} \mathbf{M} \times \left( -|\gamma| \mathbf{M} \times \mathbf{H}_{\text{eff}} + \frac{\alpha}{M_s} \mathbf{M} \times \frac{d\mathbf{M}}{dt} \right) \\
&= -|\gamma| \mathbf{M} \times \mathbf{H}_{\text{eff}} - \frac{\alpha |\gamma|}{M_s} \mathbf{M} \times (\mathbf{M} \times \mathbf{H}_{\text{eff}}) - \alpha^2 \frac{d\mathbf{M}}{dt} \\
\implies (1 + \alpha^2) \frac{d\mathbf{M}}{dt} &= -|\gamma| \mathbf{M} \times \mathbf{H}_{\text{eff}} - \frac{\alpha |\gamma|}{M_s} \mathbf{M} \times (\mathbf{M} \times \mathbf{H}_{\text{eff}}) \\
\implies \frac{d\mathbf{M}}{dt} &= -|\bar{\gamma}| \mathbf{M} \times \mathbf{H}_{\text{eff}} - \frac{\alpha |\bar{\gamma}|}{M_s} \mathbf{M} \times (\mathbf{M} \times \mathbf{H}_{\text{eff}}) \tag{2.41}
\end{aligned}$$

Equation (2.41) is known as the *Landau–Lifshitz–Gilbert (LLG) equation* and is equivalent to the Gilbert equation under the relation  $|\gamma| = (1 + \alpha^2) |\bar{\gamma}|$ .  $|\gamma|$  and  $|\bar{\gamma}|$  are known as Gilbert and Landau–Lifshitz gyromagnetic ratios, respectively. Since,  $\alpha \ll 1$  in most cases considered here, we can sometimes assume  $|\gamma| \approx |\bar{\gamma}|$ . In most cases, an analytical solution is not possible and a numerical approach is adopted by using micromagnetic solvers (see Tab. 3.1). As the time derivative appears on only one side of the LLG Eq. (2.41), it is preferred over the Gilbert Eq. (2.40).<sup>171</sup>

### 2.3.3. Ferromagnetic Resonance and The Kittel Formula

As per the LLG Eq. (2.41), the frequency  $\omega$  with which the magnetization vector  $\mathbf{M}$  (of a continuous ferromagnet) precesses around the effective field  $\mathbf{H}_{\text{eff}}$  can be approximated by  $\omega \approx |\bar{\gamma}| H_{\text{eff}}$ . If a small signal  $\mathbf{H}_{\text{sig}}$ , varying with the same frequency  $\omega$ , is applied orthogonally to the external bias field then a resonance occurs and the magnetization dynamics starts to draw power from the signal. This is known as the *ferromagnetic resonance*.

In the absence of any external field, Eq. (2.23) could have been used to determine  $\mathbf{H}_{\text{dem}}$  for a uniformly magnetized ferromagnet of infinite size. The macrospin model deals with uniformly magnetized ferromagnets. Magnetization tends to align itself parallel to the surfaces of ferromagnetic body. The effects of this shape anisotropy is significantly pronounced in the case of nanoscale systems such as thin films or nanowires. This is also why the experimentally reported precession frequencies<sup>172</sup> were two to four times higher than that predicted by the macrospin model.<sup>173</sup>

Consider a uniformly magnetized ferromagnetic slab depicted in Fig. 2.1 (a) with a face

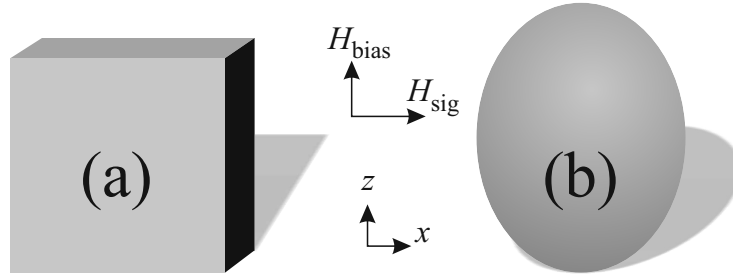


Figure 2.1.: Uniformly magnetized ferromagnetic (a) slab and (b) ellipsoid.

at  $y = 0$ . Let the applied external field  $\mathbf{H}_{\text{ext}}$  be given by

$$\mathbf{H}_{\text{ext}} = (H_{\text{sig}}, 0, H_{\text{bias}}), \quad (2.42)$$

where  $H_{\text{sig}}$  is the microwave frequency signal and  $H_{\text{bias}}$  is the external bias field. Exploiting the continuity of the normal component  $B_y$  of magnetic flux density  $\mathbf{B}$ , one can write  $H_y = -M_y$ . Thus, the effective field  $\mathbf{H}_{\text{eff}}$  of  $(H_{\text{sig}}, -M_z, H_{\text{bias}})$  should be used for calculation of the resonant frequency with the LLG Eq. (2.41). The exchange field does not affect the ferromagnetic resonance frequency.<sup>173</sup> Ignoring the damping in Eq. (2.41), we get:

$$\begin{aligned} \frac{dM_x}{dt} &= -|\bar{\gamma}| (M_y H_z - H_y M_z) \\ &= -|\bar{\gamma}| (M_z + H_z) M_y \\ &= -|\bar{\gamma}| B_z M_y / \mu_0, \end{aligned} \quad (2.43)$$

$$\begin{aligned} \frac{dM_y}{dt} &= -|\bar{\gamma}| (M_z H_x - H_z M_x) \\ &= |\bar{\gamma}| M_x H_{\text{bias}}, \text{ and} \end{aligned} \quad (2.44)$$

$$\frac{dM_z}{dt} \approx 0. \quad (2.45)$$

Equation (2.44) is obtained with the assumption that the signal amplitude is sufficiently small. From Eqs. (2.43) and (2.44), we can now write

$$\frac{d^2 M_x}{dt^2} = -|\bar{\gamma}|^2 B_z H_{\text{bias}} M_x / \mu_0. \quad (2.46)$$

Solving the above equation, we get the ferromagnetic resonant frequency of

$$\omega = |\bar{\gamma}| \sqrt{B_z H_{\text{bias}} / \mu_0}, \quad (2.47)$$

which agrees well with the experimentally observed value. Thus, it is important to consider the effect of demagnetization while interpreting any results involving ferromagnetic resonance at the nanoscale.

The demagnetizing field  $\mathbf{H}_{\text{dem}}$ , can be expressed using an inner product of magnetization  $\mathbf{M}$  with the *demagnetizing tensor*  $\overleftrightarrow{\mathbf{N}}$ :<sup>174</sup>

$$\mathbf{H}_{\text{dem}} = -\overleftrightarrow{\mathbf{N}} \cdot \mathbf{M}. \quad (2.48)$$

Here  $\overleftrightarrow{\mathbf{N}}$  is a second rank symmetric tensor with unit trace:<sup>166</sup>

$$\overleftrightarrow{\mathbf{N}} = \begin{bmatrix} N_{xx} & N_{xy} & N_{xz} \\ N_{xy} & N_{yy} & N_{yz} \\ N_{xz} & N_{yz} & N_{zz} \end{bmatrix} : N_{xx} + N_{yy} + N_{zz} = 1. \quad (2.49)$$

Equation (2.49) can be used to obtain the  $\omega$  at which the ferromagnetic resonance (of a uniformly magnetized body with uniform demagnetization) will occur:<sup>27</sup>

$$\omega = \left\{ (\omega_H + |\bar{\gamma}| N_{xx} M_s) (\omega_H + |\bar{\gamma}| N_{yy} M_s) - |\bar{\gamma}|^2 N_{xy}^2 M_s^2 \right\}^{1/2}, \quad (2.50)$$

where we assume  $M_z \approx M_s$  and

$$\omega_H = |\bar{\gamma}| (H_{\text{bias}} - N_{zz} M_s). \quad (2.51)$$

Equation (2.50) can be used when  $z$ -axis points in the direction of bias magnetic field. If needed, an analogous tensor  $\overleftrightarrow{\mathbf{N}}_{\text{anis}}$ , which can be defined for magnetocrystalline anisotropy field should also be used along with the demagnetizing tensor  $\overleftrightarrow{\mathbf{N}}$ .

As shown in Fig. 2.1 (b), if the principal axes of an ellipsoidal ferromagnet are aligned with the coordinate axes, only the diagonal components of tensor  $\overleftrightarrow{\mathbf{N}}$  remain non-zero. This

gives a resonant frequency for a generic ellipsoidal ferromagnet as

$$\omega = |\bar{\gamma}| \sqrt{(H_{\text{bias}} + (N_{xx} - N_{zz}) M_s) (H_{\text{bias}} + (N_{yy} - N_{zz}) M_s)}. \quad (2.52)$$

Equation (2.52) is known as the *Kittel formula*.<sup>173</sup>

### 2.3.4. Laser Pulse Induced Ultrafast Demagnetization

One type of magnetization dynamics that is not completely described by the LLG equation is an ultrafast demagnetization process which can be triggered by a femtosecond laser pulse.<sup>175</sup> As seen in Fig. 1.1, this happens within a picosecond. But, how is the magnetization quenched so quickly while conserving the net angular momentum<sup>176</sup>? Photons from the laser pulse interact with the spin degrees of freedom of electrons while non-linearly modifying their own angular momentum. *Hot electrons*, with temperature up to  $10^3$  K,<sup>177</sup> are then created due to electron–electron scattering.<sup>178</sup> This is followed by electron–magnon interaction mediated thermalization of spin population.<sup>179,180</sup> This causes the loss of phase memory of electronic wavefunctions w.r.t. the excitation, eventually leading to the ultrafast demagnetization. The exact mechanism of this process is the subject of hot debate,<sup>181–184</sup> but most scientists believe that a phonon mediated spin–flip scattering plays an important role.<sup>113,176,178,185–187</sup>

Some time after the ultrafast demagnetization, the spins begin to relax in two time scales. The faster relaxation time scale of a few picoseconds is the result of electrons and spins exchanging energy with the lattice by the electron–phonon interaction. A *three temperature model*<sup>175,188</sup> involving electrons, spins and phonons has been proposed to describe this process. As the magnetocrystalline anisotropy field changed with rapidly changing temperature of phonons, it works as a trigger to initialize the precession of magnetization around the local effective field. The longer relaxation time scale of hundreds of picoseconds results due to the diffusion of electron and lattice heat.<sup>189,190</sup> Relaxation dynamics in both these time scales can be modelled by the LLG equation.

## 2.4. Magnonics

Like other physical waves, SWs exhibit phenomena like resonance,<sup>172,173</sup> reflection and refraction,<sup>191–196</sup> dispersion,<sup>197</sup> interference and diffraction,<sup>80,198–201</sup> tunnelling,<sup>202,203</sup> Doppler effect<sup>204–206</sup> and formation of envelop solitons.<sup>207–209</sup> Magnons, the quanta of SWs, have been identified as bosons.<sup>2,30</sup> Bose–Einstein condensation of magnons has also been observed in different magnetic systems.<sup>31,32,210</sup> Magnonics is the study of various aspects of SWs — both classical and quantum mechanical.<sup>38,69,70</sup> In the following sub–sections, we first introduce the theory of SW dynamics in terms of its dispersion relation in different kinds of nanoscale magnetic systems, then we discuss how magnonics as field of study has been developed so far.

### 2.4.1. Exchange Dominated SWs in Thin Films

SWs are called exchange dominated if their wavenumber  $k \gg 1/\lambda_{\text{ex}}$ . It has been demonstrated that the spectrum of exchange dominated SWs can be tuned by controlling the exchange field.<sup>68</sup> SW dispersion relation  $\omega(k)$  for a 1D chain of ferromagnetic sites of spin  $S$  and distance  $a$  apart has been calculated as<sup>211</sup>

$$\omega = 4JS(1 - \cos ka) / \hbar, \quad (2.53)$$

where  $k$  is the SW wavevector. In the long wavelength limit ( $ka \ll 1$ ), Eq. (2.53) reduces to

$$\omega = (2JSa^2/\hbar) k^2. \quad (2.54)$$

As the presence of boundaries or surfaces in a magnetic medium alters the exchange field in their immediate neighbourhood, the dispersion relation of exchange dominated SWs is generally regarded to be isotropic within a bulk magnetic medium. In the case of thin films, SWs obey the following dispersion relation<sup>212</sup>

$$f(k) - f(0) = |\bar{\gamma}| M_s \lambda_{\text{ex}}^2 k^2. \quad (2.55)$$

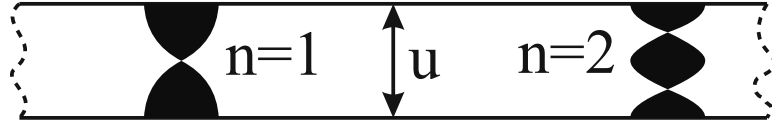


Figure 2.2.: Profile of perpendicular standing SW mode with  $n = 1$  and  $2$  nodes in a thin film with antinodes at the surfaces.

Exchange dominated SWs, which propagate normal to the surface of a thin film, form a standing wave with quantized wavenumber  $k = \pi n/u$ , where  $n$  is the number of nodes in the mode profile and  $u$  is the thickness of the thin film. These are known as *perpendicular standing SWs*. A mode profile with one and two nodes is sketched in Fig. 2.2 such that the magnetization dynamics at surface is completely unpinned.<sup>213</sup>

### 2.4.2. Dipole Dominated SWs in Thin Films

The behaviour of SWs becomes *dipole dominated* if their wavenumber  $k \ll 1/\lambda_{\text{ex}}$ . It means that the band structure of a dipole dominated SW can be controlled by manipulating the demagnetizing field. Dipole dominated SWs are also known as *magnetostatic waves*. Unlike the exchange dominated SWs, the dispersion relation of magnetostatic waves depends heavily upon the relative orientation of the film, the effective magnetic field  $\mathbf{H}_{\text{eff}}$  and the SW wavevector  $\mathbf{k}$ . The orientation of  $\mathbf{H}_{\text{eff}}$  can change during SW dynamics. In the context of this sub-section we consider only the orientation that  $\mathbf{H}_{\text{eff}}$  had during the steady state ( $d\mathbf{M}/dt = 0$ ).

When  $\mathbf{H}_{\text{eff}}$  (and magnetization) is normal to the surface of the thin film and the SW's propagation direction is in the plane of the film ( $\mathbf{k} \perp \mathbf{H}_{\text{bias}}$ ), the spin wave (SW) mode is called *forward volume (FV) magnetostatic mode*. If  $\mathbf{H}_{\text{eff}}$  is in the plane of the thin film then the conditions  $\mathbf{k} \parallel \mathbf{H}_{\text{eff}}$  and  $\mathbf{k} \perp \mathbf{H}_{\text{eff}}$  give rise to *backward volume (BV)* and surface — or *Damon–Eshbach (DE)* SWs, respectively. The dispersion relation of SWs in these different configurations is given as<sup>79,214</sup>

$$f^2 = \begin{cases} f_0 \left( f_0 + f_M \frac{1-e^{-ku}}{ku} \right) & \text{(BV),} \\ f_0 \left( f_0 + f_M \left( 1 - \frac{1-e^{-ku}}{ku} \right) \right) & \text{(FV),} \\ f_0 (f_0 + f_M) + \frac{f_M^2}{4} (1 - e^{-2ku}) & \text{(DE),} \end{cases} \quad (2.56)$$

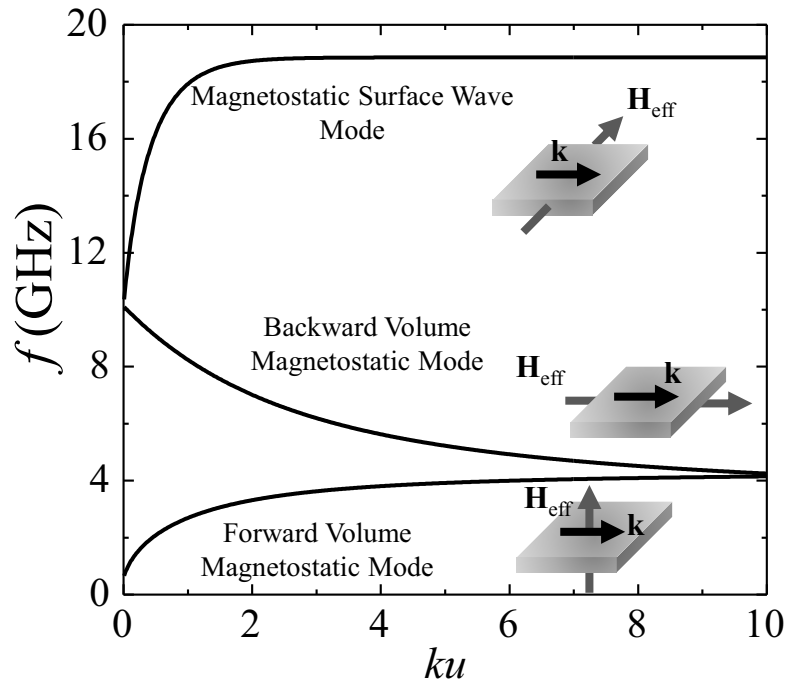


Figure 2.3.: Dispersion relation of magnetostatic SW modes in a film for different relative orientations of wavevector  $\mathbf{k}$  and effective field  $\mathbf{H}_{\text{eff}}$  in the steady state ( $d\mathbf{M}/dt = 0$ ).

where  $f_M = |\bar{\gamma}| M_s$  and

$$f_0 = \begin{cases} |\bar{\gamma}| H_{\text{bias}} & \text{BV and DE;} \\ |\bar{\gamma}| (H_{\text{bias}} - M_s) & \text{FV.} \end{cases} \quad (2.57)$$

The forms of these dispersion relations are shown in Fig. 2.3. For  $k \rightarrow 0$ , Eq. (2.56) converges to describe the Kittel modes of ferromagnetic resonance as presented here in sub-Sec. 2.3.3. BV modes are characterized by anti-parallel phase and group velocities. This character is evident till the angle  $\phi$  between the in-plane  $\mathbf{H}_{\text{eff}}$  and SW wavevector  $\mathbf{k}$  increases from 0 to a critical value  $\phi_c = \tan^{-1} \sqrt{H_{\text{bias}}/M_s}$ . Here  $H_{\text{bias}}$  is the magnitude of the applied bias field. The power of DE modes decay exponentially away from the surface.<sup>6</sup> The associated penetration depth  $\delta$ , is zero for  $\phi = \phi_c$  and increases with increasing  $\phi$ :  $\phi_c \leq \phi \leq \pi/2$ . Dispersion relation for SWs for a more general relative orientation of wavevector and effective field has been covered by Kalinikos and Slavin.<sup>214</sup>

For  $k\lambda_{\text{ex}} \gg 1$ , Eq. (2.56) converges to a value independent of  $k$ . Thus, if we take only

the dipolar field into account, all SWs will have negligible group velocity for larger values of  $k\lambda_{\text{ex}}$ . If  $k\lambda_{\text{ex}} \approx 1$ , the SWs are classified as dipole–exchange SWs. We can obtain the dispersion relation in that case by substituting  $f_0$  with  $f_{\text{ex}} = f_0 + k^2\lambda_{\text{ex}}^2 f_{\text{M}}$  in Eq. (2.56).

### 2.4.3. Effect of Lateral Confinement on SW Band Structure

In this sub–section\* we discuss the SW dispersion in laterally confined uniform waveguides while taking both dipolar and exchange fields into consideration and ignoring any magnetocrystalline anisotropy. Rewriting Eq. (2.56) after replacing  $f_0$  with  $f_{\text{ex}} = f_0 + k^2\lambda_{\text{ex}}^2 f_{\text{M}}$ , we get the relation:

$$f^2 = \begin{cases} f_{\text{ex}} \left( f_{\text{ex}} + f_{\text{M}} \frac{1-e^{-ku}}{ku} \right) & \text{(BV),} \\ f_{\text{ex}} \left( f_{\text{ex}} + f_{\text{M}} \left( 1 - \frac{1-e^{-ku}}{ku} \right) \right) & \text{(FV),} \\ f_{\text{ex}} (f_{\text{ex}} + f_{\text{M}}) + \frac{f_{\text{M}}^2}{4} (1 - e^{-2ku}) & \text{(DE).} \end{cases} \quad (2.58)$$

Let the two components  $k_x$  and  $k_y$  of wavevector  $\mathbf{k}$  point along length and width of the waveguide, respectively; such that  $\mathbf{k} \cdot \mathbf{k} = k^2 = k_x^2 + k_y^2$ . Here, a uniform magnetization across the thickness of the waveguide has been assumed.<sup>79</sup> Broken continuous translational symmetry near the edges of the waveguides impose the following quantization along the width  $w$  of the waveguide:<sup>215</sup>

$$k_y = (n + 1) \pi / w_{\text{eff}}, \quad n = 0, 1, 2, \dots \quad (2.59)$$

Here,

$$w_{\text{eff}} = \frac{wd}{d-2}, \quad (2.60)$$

$$d = \frac{2\pi}{p(1-2\ln(p))}, \quad (2.61)$$

$$p = \frac{u}{w} \ll 1. \quad (2.62)$$

Different values of  $n$ , which denotes the number of lateral nodal lines in SW mode profile,

---

\*This sub–section are based on Venkat *et al.*<sup>79</sup>

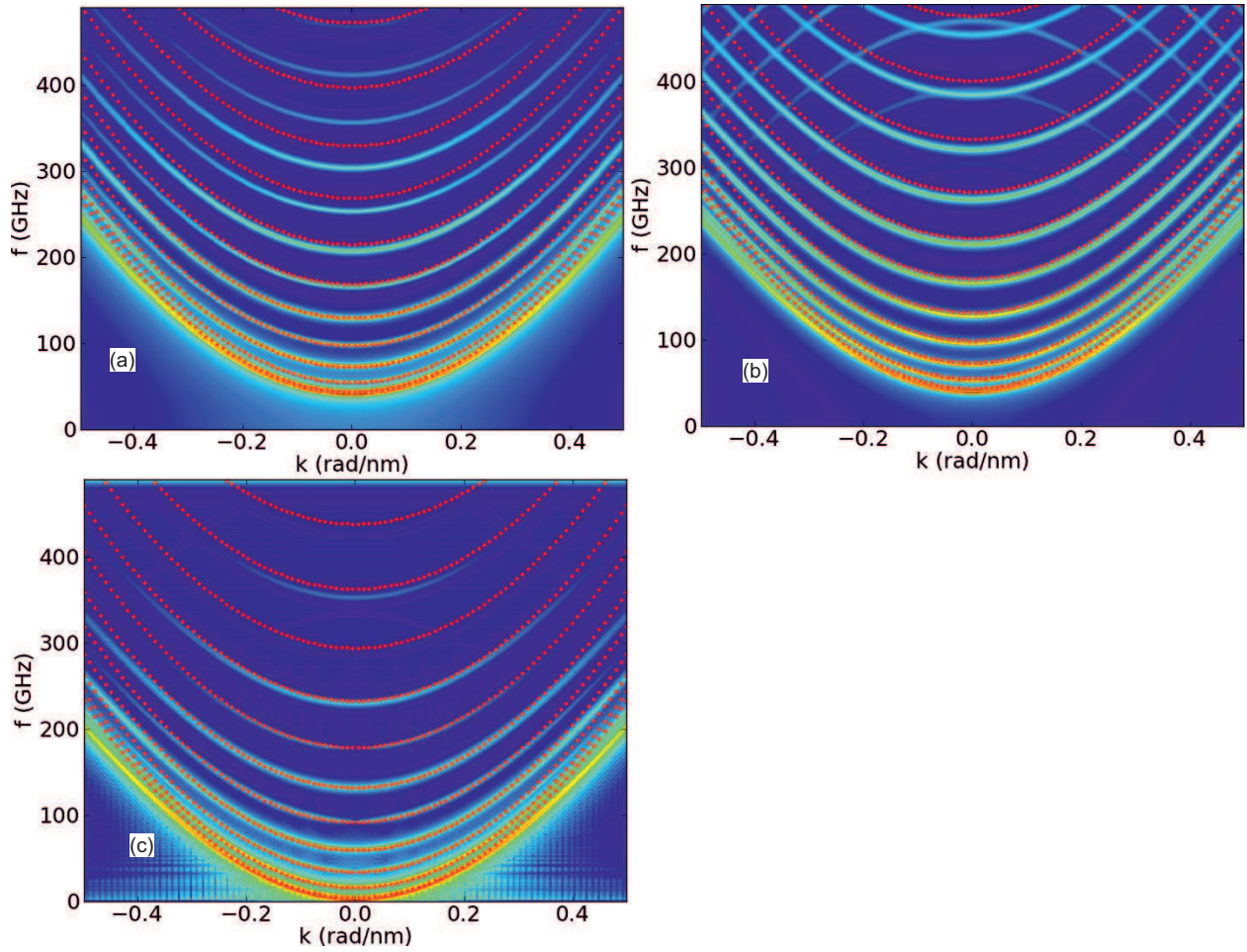


Figure 2.4.: Frequency – wavevector dispersion calculated under a bias field strength  $\mu_0 H_{\text{bias}}$  of 1.01 T from numerical (solid lines) and analytical (dotted lines; see Eq. (2.58)) methods for (a) BV, (b) DE and (c) FV configurations. (d) Dimensions of the geometry under considerations with relative orientation of the bias field. Source: Ref. 79.

yield different modes for the same configuration as shown by the dotted lines in Fig. 2.4. SW dispersion relations for BV, DE and FV arrangements in the case of a 50 nm wide and 1 nm thick uniform Py waveguide under a bias field strength  $\mu_0 H_{\text{bias}}$  of 1.01 T,<sup>79</sup> are shown in Fig. 2.4 (a), (b) and (c), respectively. It can be noticed that dotted lines calculated using Eq. (2.58) agree well with those calculated using micromagnetic simulations (MSs) for lower values of frequency and wavevector. For larger values of  $k_x$  the simulated branches of SW dispersion relation start to bend due to creation of false Brillouin zone boundaries during FDM related discretization of the waveguide.

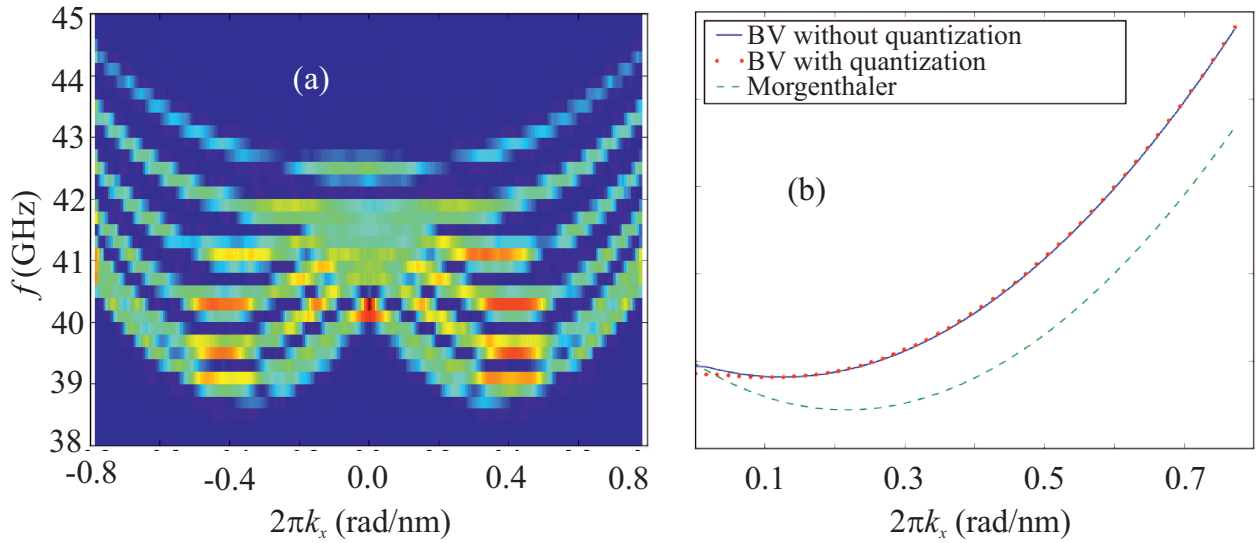


Figure 2.5.: Dispersion relation of SWs of the case presented in Fig. 2.4 (a), recalculated with exchange coefficient  $A = 2.515 \times 10^{-13}$  J/m using (a) MSs and (b) analytical models (as noted in the legend). Source: Ref. 79.

For higher order bands, the simulated results underestimate the frequency values. It can also be noted that the opposite sign of phase and group velocity, which is the hallmark of BV configuration is not observed in Fig. 2.4 (a). The effect of exchange field, which gives a parabolic shape to dispersion curves, is too dominant to allow that phenomenon. Thus, the case presented in Fig. 2.4 (a) is recalculated with a reduced exchange coefficient  $A = 2.515 \times 10^{-13}$  J/m. The results obtained using MSs are presented in Fig. 2.5 (a). This can be compared to results obtained using the analytical expression for BV configuration as given by Eq. (2.58), with and without the quantization specified by Eq. (2.59). Another model, which assumes comparable exchange and dipole interaction was presented by Morgenthaler<sup>216</sup> as

$$f^2 = f_{\text{ex}} \left( f_{\text{ex}} + f_{\text{M}} \frac{k_y^2 + k_z^2}{k_x^2 + k_y^2 + k_z^2} \right), \quad (2.63)$$

where for the first mode,  $k_z$  can be obtained from  $k_x = k_z \tan(k_z u)$ . As seen from Fig. 2.5, this result most closely reproduces the first mode that is yielded by simulations.

The differences between simulated and analytical results presented here demonstrate that some finite size effects are not captured by analytical expressions. More complex nanoscale systems will be discussed in dedicated chapters, and there, we will need to rely more heavily

on results obtained from complete simulations instead of analytical models. Before continuing that study, let us now get an overview of technological aspects of magnonics.

#### 2.4.4. Magnonic Crystals (MCs)

Using lithography techniques and nanofabrication, material can be removed from a uniform waveguide to create patterned waveguides<sup>85</sup> with discrete translational symmetry. This leads to a periodic variation in total energy  $E_{\text{tot}}$  as well. As  $E_{\text{tot}}$  depends upon both magnetization  $\mathbf{M}$  and effective magnetic field  $\mathbf{H}_{\text{eff}}$ , its variation can also be controlled by controlling  $\mathbf{H}_{\text{eff}}$ .<sup>3</sup> Similar to how Bloch theorem may be used in terms of electronic or photonic crystals,<sup>38</sup> a theory for calculation of SW dispersion in magnonic crystals has also been developed.<sup>51,217</sup> MSs can also be used to calculate SW dispersion in MCs. These methods have been discussed in some detail in Chap. 3. Patterned waveguides are essentially 1D MCs. The dependence of SW dispersion in an 1D antidot waveguide on various factors is also studied in the following chapters. We also discuss 2D MCs in Chap. 9. Let us now consider how elements like magnonic waveguides and crystals function as active and passive components of magnonics devices.

#### 2.4.5. Magnonic Devices

Magnonic devices – which aim to use SW for information processing – have attracted the attention of the research community due to the following potential advantages over their electronic and photonic counterparts:<sup>69</sup>

- Easy manipulation of device characteristics by controlling the bias magnetic field  $\mathbf{H}_{\text{bias}}$ .
- Magnetic nano-elements are also non-volatile memory elements, thus facilitating their easy integration with current technological ecosystem, e.g., magneto-optical disks and read heads in MRAMs.
- In microwave and submillimetre ranges, SWs have considerably lower wavenumbers, which can be used for miniaturization of certain devices.

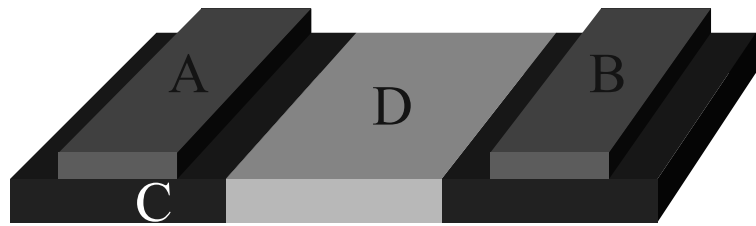


Figure 2.6.: A schematic of magnetostatic SW based generic magnonic device. Input and output antennae, waveguide and device’s functional medium are marked as A, B, C and D, respectively. Source: Ref. 69.

A schematic of a typical magnonic device is presented in Fig. 2.6. Here, A and B are SW source and detector antennae. C is an uniform waveguide which conducts SWs as it is, and D is the functional medium such as an MC which manipulates the information contained in SWs. This assembly is usually micron sized and used with magnetostatic SWs. Ferrites, such as YIG, are typically used for waveguide C, because they tend to have very low SW damping and thus allow the signal to carry for longer ( $\approx 1$  mm) distances. Magnetic parameters may or may not be homogeneous in D. In the former case, it becomes uniform and similar to C. By controlling the external magnetic field and material parameters, D can be made to function<sup>69</sup> as a *phase shifter*, an *amplifier*, a *frequency mixer*, a *filter* or a *generator* of short trains of magnetostatic SWs.

The functional region D can also divide the SW signal into two parts and recombine them after a phase-shift, either constructively or destructively to mimic a Mach-Zehnder-type *interferometer*<sup>38</sup> for SWs. Apart from *logical switches* this can also be used to *transduce* an electric signal to a magnonic one.<sup>5</sup> Even the NAND (an universal gate) functionality has now been demonstrated.<sup>82</sup>

Although, YIG has a very low (SW) damping,<sup>70</sup> their films are difficult to grow on silicon and Py, as a ferromagnet, is better suited for integration with current silicon based technologies.<sup>38</sup> It has also been projected<sup>74</sup> that the number of operations per unit area per unit time (throughput) of magnonic logic can outperform CMOS logic by more than three orders of magnitude.

## 2.5. Magnetic Vortex Dynamics

The core of a magnetic vortex is marked by out of plane magnetization. The radius of this core,  $r_{\text{core}}$ , depends largely on the exchange length  $\lambda_{\text{ex}}$ , and the film thickness  $u$  as<sup>16</sup>

$$r_{\text{core}} = 0.68\lambda_{\text{ex}}\sqrt[3]{u/\lambda_{\text{ex}}} \quad (2.64)$$

For vortices formed in circular nanodisks, the out of plane component of magnetization  $m_z$  can point either up or down at the centre. Based on this polarity  $p$  of the vortex (core) can be assigned a value 1 or  $-1$ . Immediately around core  $m_z$  takes the sign of  $-m_z$  ( $r = 0$ ), before taking near zero values. This gives the magnetic vortex core its ‘halo’ or ‘dip’. Multiple analytical models<sup>218–220</sup> have been offered to describe the profile of magnetization within its core, however the experimentally observed halo,<sup>134</sup> has so far only been reproduced by MSs<sup>221</sup> and the generalized trial function introduced by Hubert and Schäfer.<sup>174</sup> This halo plays a key role in ultrafast vortex dynamics.<sup>16</sup> Apart from polarity, another attribute of a magnetic vortex is known as chirality  $c$ , which, depending upon the curl of magnetization around the edge of vortex can either be 1 (CCW) or  $-1$  (CW).

If  $\varphi = \tan^{-1}(m_y/m_x)$ , the *winding number*  $n$  of a vortex with boundary  $S$  is defined as

$$n \equiv \frac{1}{2\pi} \oint_S \frac{d\varphi}{dS} \quad (2.65)$$

The winding number is 1 for a vortex and  $-1$  for an *antivortex*.<sup>16</sup> A non-zero winding number provides topological stability to vortices and antivortices,<sup>222</sup> imposing a rule regarding the conservation of winding number unless a high torque is applied to undo it.<sup>223,224</sup> This also implies that the formation of a vortex must occur simultaneously with the formation of an antivortex, unless the vortex core nucleation occur on the boundary  $S$ . *Skyrmion number* (also called Pontryagin index)  $q$ ,<sup>225</sup> is another conserved topological index, which is defined as<sup>226</sup>

$$q \equiv pn/2. \quad (2.66)$$

This means that vortex–antivortex annihilation can be spontaneous only if the pair has the same polarity. Otherwise, it must be mediated by a singularity like a Bloch point,<sup>227</sup>

where change in magnetization direction is marked by the presence or a region with vanishing magnetization. Energy released in such vortex–antivortex annihilation leads to SW generation.<sup>228</sup>

### 2.5.1. Polarity Switching

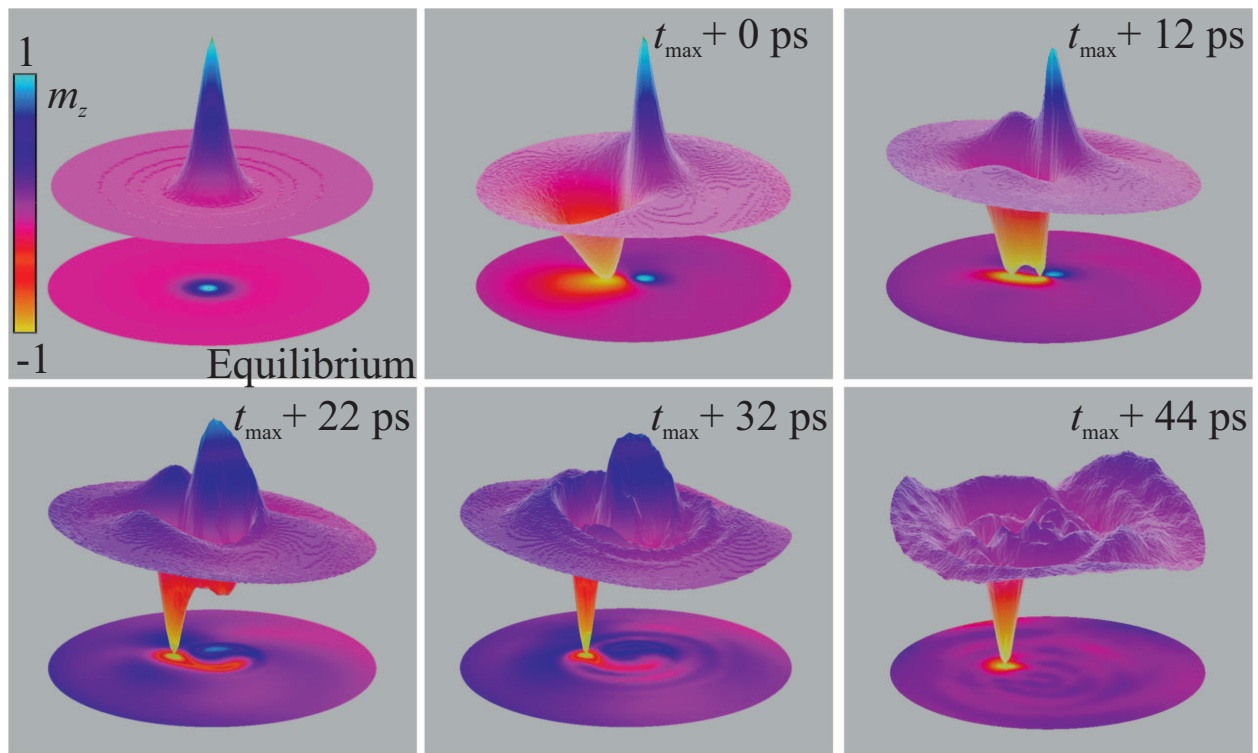


Figure 2.7.: Time evolution of  $z$ -component of magnetization in a magnetic vortex undergoing a core reversal. Source: Ref. 16.

Creation and annihilation of vortex–antivortex pairs also mediate *polarity switching* — a process where the polarity  $p$  changes to  $-p$ .<sup>15</sup> A time evolution of this core reversal, which lasts about 40 ps has been shown in Fig. 2.7.<sup>16,229</sup> Here, a circular nanodisk of radius 100 nm and thickness 20 nm are used with material parameters of Py assuming a damping  $\alpha = 0.01$  and surface anisotropy  $K_S = 0.1$  mJ/m<sup>2</sup>. An in-plane Gaussian signal of 60 ps duration and a maxima of 80 mT at time  $t_{\max}$ .

A production of vortex–antivortex pair, seen at  $t_{\max} + 12$  ps in Fig. 2.7, is believed to be mediating the polarity reversal.<sup>128</sup> While the energy from the signal is being absorbed, the winding and skyrmion numbers before and after this pair production remain conserved. Next,

the new antivortex annihilates with the old vortex, leaving the new vortex with opposite polarity intact. However, here the skyrmion number changes from  $1/2$  to  $-1/2$ . This, is marked by a release of energy in the form of SWs. Apart from the generation of SWs, the use of polarity switching in data storage has also been envisioned.<sup>128,230</sup>

### 2.5.2. Vortex Core Gyration

If the excitation signal, either in the form of a spin-polarized current or a changing magnetic field, is sufficiently small, it induces a translation of the vortex core around its equilibrium position. This is referred to as *magnetic vortex core gyration*. In the steady state — when the velocity of the core  $\mathbf{v}$  does not change in magnitude, and if the shape of the magnetic structure is not altered greatly, the following Thiele's equation<sup>146,174,231</sup> describes this gyration:

$$\mathbf{F}_{\text{ext}} + \mathbf{G} \times \mathbf{v} + \alpha \overleftrightarrow{\mathbf{D}} \cdot \mathbf{v} = 0, \quad (2.67)$$

where  $\mathbf{G}$  is the *gyrotropic vector* and  $\overleftrightarrow{\mathbf{D}}$  is the net *dissipation tensor*. Using spherical polar co-ordinates where  $\theta$  and  $\phi$  are the polar and azimuthal angles, these quantities can be expressed as<sup>16</sup>

$$\mathbf{G} = -\frac{\mu_0 M_s}{|\gamma|} \int (\sin \theta \nabla \theta \times \nabla \phi) dV, \text{ and} \quad (2.68)$$

$$\overleftrightarrow{\mathbf{D}} = -\frac{\mu_0 M_s}{|\gamma|} \int (\nabla \theta \nabla \theta + \sin^2 \theta \nabla \phi \nabla \phi). \quad (2.69)$$

For a magnetic vortex in a nanodisk, the above equations can be rewritten as<sup>149,232,233</sup>

$$\begin{aligned} \mathbf{G} &= -2 \frac{\pi \mu_0 u M_s}{|\gamma|} n p \hat{\mathbf{z}} \\ &= -G p \hat{\mathbf{z}} : G > 0 \end{aligned} \quad (2.70)$$

$$\begin{aligned} \overleftrightarrow{\mathbf{D}} &= \begin{bmatrix} D_{xx} & D_{xy} \\ D_{yx} & D_{yy} \end{bmatrix} \\ &= \begin{bmatrix} D & 0 \\ 0 & D \end{bmatrix}, \end{aligned} \quad (2.71)$$

where

$$D = -\frac{\pi\mu_0 u M_s}{|\gamma|} \ln \frac{R}{r_{\text{core}}}. \quad (2.72)$$

Here  $R$  is the radius of the nanodisk.

### Gyrotropic Frequency

If the vortex core is away from the centre of the nanodisk, a demagnetizing field is created, which attempts to restore the core's position  $\mathbf{r}$  to the centre of the disk, resulting in a force

$$\mathbf{F}_{\text{ms}} \equiv -\kappa \mathbf{r}, \quad (2.73)$$

where the positive constant  $\kappa$  is given by<sup>137,234</sup>

$$\kappa = \pi \frac{\mu_0 M_s^2 u}{\chi_0}, \quad (2.74)$$

where, the initial susceptibility  $\chi_0$ , can be obtained from the relation

$$\frac{1}{\chi_0} = \frac{2u}{R} \left[ \ln \left( \frac{8R}{u} \right) - \frac{1}{2} \right] : \frac{u}{R} \ll 1. \quad (2.75)$$

Taking this into account while ignoring damping and any external forces, Eq. (2.67) changes to

$$-\kappa \mathbf{r} + \mathbf{G} \times \mathbf{v} = 0 \quad (2.76)$$

$$\implies -\kappa \mathbf{r} - G p \hat{\mathbf{z}} \times (2\pi f_0 p \hat{\mathbf{z}} \times \mathbf{r}) = 0 \quad (2.77)$$

$$\implies f_0 = \frac{|\gamma| M_s}{4\pi \chi_0} \left( \because \mathbf{r} \perp \hat{\mathbf{z}} \ \& \ p^2 = 1 \right). \quad (2.78)$$

Equation (2.78) systematically overestimates<sup>137</sup> the gyration frequency  $f_0$ , because the rigid vortex model<sup>149</sup> used here, predicts the development of additional surface charges at the edge of nanodisk, attributing greater energy to the dynamics. By imposing a boundary condition which prohibits the development of surface charges we get<sup>137,153</sup>

$$f_0 = \frac{|\gamma| M_s}{9\pi \chi_0}, \quad (2.79)$$

where

$$\frac{1}{\chi_0} = \frac{9.98u}{R}: \frac{u}{R} \ll 1. \quad (2.80)$$

The frequency of vortex core gyration as predicted by Eq. (2.79) has been verified by simulation<sup>137</sup> and also experimental results<sup>147,235</sup> using a Py (where damping is low). It can be seen from Eq. (2.79), that the gyrotropic frequency of a vortex in a nanodisk only depends upon its aspect ratio and the saturation magnetization of the material used.

### External Forces on The Vortex Core

Let us rewrite Thiele's Eq. (2.67), taking the restoring force  $\mathbf{F}_{\text{ms}}$  from Eq. (2.73):

$$\mathbf{F}_{\text{ext}} - \kappa \mathbf{r} + \mathbf{G} \times \mathbf{v} + \alpha \overleftrightarrow{\mathbf{D}} \cdot \mathbf{v} = 0. \quad (2.81)$$

At equilibrium  $\mathbf{r} = 0$  and  $\mathbf{v} = 0$ . Thus, a non-zero  $\mathbf{F}_{\text{ext}}$  is required to trigger the dynamics. This force is usually provided by an external magnetic field or by spin-transfer torque (STT). Force experienced due to an external magnetic field  $\mathbf{H}_{\text{ext}}$  is given by<sup>151</sup>  $\mu (\hat{\mathbf{z}} \times \mathbf{H}_{\text{ext}})$  where (assuming no side charges<sup>153</sup>), factor<sup>145</sup>  $\mu = 2\pi M_s R u c / 3$ . We can see that this force depends upon the chirality  $c$  of the vortex. Thus, the initial response to an applied magnetic field is mainly controlled by the chirality of the vortex.

STT can contribute to both gyrotropic and dissipative forces. In the presence of spin-polarized current where the drift velocity of the electrons is  $\mathbf{u}$ , the Thiele's equation changes to the following form:<sup>236-239</sup>

$$-\kappa \mathbf{r} + \mathbf{G} \times (\mathbf{v} - \mathbf{u}) + \overleftrightarrow{\mathbf{D}} \cdot (\alpha \mathbf{v} - \beta \mathbf{u}) = 0. \quad (2.82)$$

Here, the dimensionless factor  $\beta$  (typically of the order of  $10^{-2}$ )<sup>236</sup> is a measure of non-adiabaticity of the spin-current. When  $\alpha \approx \beta$  and  $\mathbf{r} \approx 0$ , we get  $\mathbf{v} \approx \mathbf{u}$ . Thus, the initial displacement of vortex core is along the direction of the electrons' drift velocity, and unlike the initial displacement from the external field, it is independent of the vortex chirality.<sup>239</sup> This can be useful as chirality of vortex is difficult to manipulate.<sup>240,241</sup>

In a network of  $N$  interacting vortices, the force  $\mathbf{F}_{\text{ext}}^i$  on the  $i^{\text{th}}$  vortex is given by

$$\mathbf{F}_{\text{ext}}^i = -\frac{\delta W(\mathbf{r}_1, \mathbf{r}_2, \mathbf{r}_3, \dots, \mathbf{r}_N)}{\delta \mathbf{r}_i} \quad (2.83)$$

After an initial disturbance which can be triggered either by an external field or by dint of STT, the equation of motion (assuming no external forces and negligible damping) can be described by Eq. (2.76). We can also see from Eq. (2.70) that  $\mathbf{G}$  depends on the polarity of the vortex (or antivortex). Thus the sense of rotation of the vortex core is controlled by polarity of the vortex. It has also been observed that an excitation signal rotating CCW (or CW) induces a greater gyration of the vortex core when the polarity is up (or down).<sup>152</sup> Further, polarity dependent logical operations<sup>162</sup> and high signal transfer efficiency<sup>155</sup> has also been reported. In Chap. 12, we note that an asymmetric amplification of gyration can be obtained when signal is transferred from one vortex to another by carefully controlling the relative polarities of the interacting vortices. This can be used to mimic the states of a conventional electronic transistor.

## 3. Methods

The scientific method followed in this thesis can be outlined in terms of the following steps:

- **Problem design:** To study the phenomena of SW dispersion in nanoscale systems, we first design the system. Then we agree upon either a geometrical or a material design parameter of the system which is theorized to affect SW dispersion.
- **Simulation:** Once the design of the system is finalized, we perform simulations to predict the nature of dependence of SW dispersion on the considered design parameter. Typically, the FDM based OOMMF is used for this purpose as it yields sufficiently accurate results in a manageable time frame.
- **Analysis of simulation data:** The simulation data is in the form of magnetization as a function of space and time where both space and time coordinates are evenly spaced. Discrete Fourier transform (DFT) is performed on this data, to obtain the energy spectral density (ESD) in different real and inverse domains. This gives us valuable information about the magnetization dynamics, such as, SW dispersion relation, iso-frequency lines or the eigenfrequency of vortex gyration.
- **Fabrication:** If the simulated results contain something of interest, we may want to verify the finding experimentally. In order to do that we first fabricate the simulated system as per the design. Fabrication can be done by using different synthesis or lithography techniques. Although, significant advancements have been made recently in this area, it is still difficult to fabricate huge arrays with features involving deep nanoscale precision. As it will be discussed in the following chapters, some aspects of the magnetization dynamics, such as SW dispersion, can tolerate some fabrication defects.<sup>242</sup> On the other hand, given finite amount of computational resources, it is also

---

impossible to simulate systems exactly as they are fabricated. Some, techniques like the use of periodic boundary condition (PBC)<sup>243,244</sup> have helped abridge this divide between simulated and fabricated systems, but there is still a lot of ground to be covered.

- **Characterization:** Some imaging techniques, such as scanning electron microscopy (SEM), are needed to verify if the fabricated sample is in good condition. This step is similar to quality inspection of a manufactured part or device. Any samples featuring systematic defects are rejected at this point. Magnetic parameters, which are also measured at this point, should be in good agreement with known values.
- **Experimentation:** Experimental techniques, such as Time Resolved–Magneto–Optic Kerr Effect (TR–MOKE) is used to directly observe the magnetization dynamics. The experimental technique should be chosen carefully to allow the study of the effects of geometrical or material parameter as determined during the problem design.
- **Analysis of experimental data:** Experimental data may also need to be analysed in order to obtain the characteristic response in different cases of the designed problem.
- **Conclusion:** A close agreement between simulated and experimental results validate our finding. These results may also be compared with existing theoretical models discussed in Chap. 2. If no analytical models exist at this point, a new one may be proposed. These results are now disseminated through a conference presentation, a journal publication or a patent application.

The effort described in this thesis is largely focused on problem design, simulation and analysis. The methods of simulation, fabrication and characterization are covered in further detail in the following sections of this chapter. Analysis techniques are described in dedicated chapters as they have evolved over time. A summary of the analysis techniques in its generic form is presented in the concluding chapter. Experimental techniques, which are used to validate some basic findings presented here are discussed in Chap. 11. As, some aspects of the numerical techniques were developed during the course of this work itself, it has been validated by using a comparison with the well established plane wave method (PWM). The underlying theory of the PWM has been discussed in Sec. 3.4.

### 3.1. Micromagnetic Simulation

Most analytical methods, like the PWM<sup>51</sup> or the dynamical matrix method,<sup>245</sup> often make simplifying assumptions of perfection (*e.g.* a perfect MC) or linearity (linear dynamics) to solve the magnetization dynamics. Simplifying boundary conditions<sup>213</sup> are also used sometimes to make the task easier. Nevertheless, analytical methods are used very widely to treat simple systems for obtaining qualitative results as they are considerably faster and more scalable with system geometry when compared to simulation based computational methods. In contrast, computer simulations can be performed for real world finite systems or infinite ideal MCs (by the use of periodic boundary conditions<sup>243,244</sup>). They also yield more accurate and experimentally realizable results. Both, analytical and computational methods solve the LLG Eq. (2.41) recalled below:

$$\frac{d\mathbf{M}}{dt} = -|\bar{\gamma}|\mathbf{M} \times \mathbf{H}_{\text{eff}} - \frac{\alpha|\bar{\gamma}|}{M_s}\mathbf{M} \times (\mathbf{M} \times \mathbf{H}_{\text{eff}}).$$

The advantage of writing the LLG equation as an ordinary differential equation (ODE) in time, while abstracting the spatial derivatives in the components of effective magnetic field  $\mathbf{H}_{\text{eff}}$ , is the ease with which standard ODE solving algorithm, such as one of the Runge–Kutta type algorithms, may now be used.

Table 3.1.: Micromagnetic simulators. Source: Ref. 5.

| Name          | Developers                       | Open Source | Method |
|---------------|----------------------------------|-------------|--------|
| LLG Simulator | M. R. Scheinfein                 | Paid        | FDM    |
| MAGPAR        | W. Scholtz                       | Free        | FEM    |
| MicroMagus    | D. V. Berkov<br>and N. L. Gorn   | Paid        | FDM    |
| Nmag          | H. Fangohr<br>and T. Fischbacher | Free        | FEM    |
| OOMMF         | M. Donahue<br>and D. Porter      | Free        | FDM    |

Micromagnetic simulators<sup>246</sup> solve Eq. (2.41) with the help of the finite difference method (FDM) or the finite element method (FEM). The later of the two yields more precise results at the cost of greater computational resources in most cases.<sup>247</sup> OOMMF and Nmag are open source and very widely used by different groups around the world. Table 3.1<sup>5</sup> lists popular

micromagnetic simulation (MS) platforms commonly used for the purpose of simulating SW dynamics.

## 3.2. FDM and OOMMF

While modelling the sample geometry FDM based solvers, such as OOMMF uses cuboidal discretization cells where the cuboids (or cells) have the same dimensions. This is shown in Fig. 3.1<sup>248</sup> for the case of a semi-circular disk. Some disagreement, in the form of steps, can be seen. This produces some errors while estimating the magnetization dynamics which can be reduced by using smaller cell sizes.

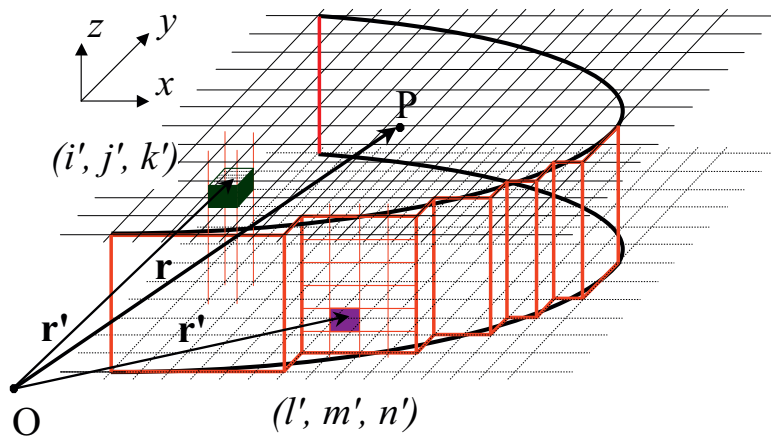


Figure 3.1.: A semi-circular disk modelled in terms of cuboidal regions. The straight red lines and the curved black lines mark the physical and numerical boundaries of the geometry. Source: Ref. 248.

Let us now recall Eq. (2.34):

$$\mathbf{H}_{\text{eff}} = \mathbf{H}_{\text{ext}} + \mathbf{H}_{\text{exch}} + \mathbf{H}_{\text{dem}} + \mathbf{H}_{\text{anis}}.$$

Thus, the effective field can be calculated as the sum of fields corresponding to different energies as described in Sec. 2.2. Alternatively, one can calculate the total energy first and find out the effective field as its functional derivative w.r.t. magnetization:<sup>249</sup>

$$\mathbf{H}_{\text{eff}} = -\frac{\delta e_{\text{tot}}}{\mu_0 \delta \mathbf{M}}. \quad (3.1)$$

Here  $e_{\text{tot}}$  is the total energy density. This energy based approach is used by OOMMF. Let us now discuss how different energy terms described in Sec. 2.2 can be approximated for a discretized sample.

### 3.2.1. Numerical Approximations of Magnetic Energies

Let a geometry be discretized into  $N$  cuboidal cells with  $\mathbf{r}_i$  and  $V_i$  denoting the position (of centre) and volume of the  $i^{\text{th}}$  cell. Then, the Zeeman energy can be approximated as

$$E_Z \approx -\mu_0 \sum_{i=1}^N \mathbf{M}(\mathbf{r}_i) \cdot \mathbf{H}_{\text{ext}}(\mathbf{r}_i) V_i. \quad (3.2)$$

The maximum error with this approximation is of the order of<sup>248</sup>  $\nabla^2 V$ , where  $\nabla$  is the maximum cell dimension and  $V$  is the total volume of the geometry.

While computing the exchange energy numerically, one can approximate Eq. (2.18) in the following manner:<sup>250</sup>

$$E_{\text{exch}} \approx - \sum_{i=1}^N V_i \sum_{j \in \{N(i)\}} A_{ij} \frac{\mathbf{m}(\mathbf{r}_i) \cdot (\mathbf{m}(\mathbf{r}_j) - \mathbf{m}(\mathbf{r}_i))}{|\mathbf{r}_j - \mathbf{r}_i|^2}, \quad (3.3)$$

where  $\{N(i)\}$  is the set of sites in the neighbourhood of site  $i$ . The corresponding exchange field may be approximated as

$$\mathbf{H}_{\text{exch}}(\mathbf{r}_i) = \lambda_{\text{ex}}^2(\mathbf{r}_i) \sum_{j \in \{N(i)\}} \frac{(\mathbf{m}(\mathbf{r}_j) - \mathbf{m}(\mathbf{r}_i))}{|\mathbf{r}_j - \mathbf{r}_i|^2}. \quad (3.4)$$

Here too, the error is  $O\nabla^2 = O|\mathbf{r}_j - \mathbf{r}_i|^2$ . Equation (3.3) can be simplified using the fact that  $\mathbf{m}(\mathbf{r}_i) \cdot \mathbf{m}(\mathbf{r}_i) = 1$ . However, that may degrade numerical precision if  $\mathbf{m}(\mathbf{r}_i)$  is almost parallel to  $\mathbf{m}(\mathbf{r}_j)$ .<sup>251</sup> If the cell size is too big, larger angles between  $\mathbf{m}(\mathbf{r}_i)$  and  $\mathbf{m}(\mathbf{r}_j)$  may lead to issues like collapse of Néel walls<sup>248,252</sup> or artificial pinning hindering the motion of Bloch points.<sup>253</sup> As discussed in sub-Sec. 2.5.1, Bloch points play an important role in polarity switching. These issues can be overcome by reducing the size of cuboids used for discretization of the geometry.<sup>248</sup>

The anisotropy energy given by Eq. (2.28) can be approximated as following:<sup>248</sup>

$$E_K \approx \begin{cases} -\sum_{i=1}^N K_1(\mathbf{r}_i) (\mathbf{m}(\mathbf{r}_i) \cdot \hat{\mathbf{u}}(\mathbf{r}_i))^2 V_i & \text{(Uniaxial)} \\ \sum_{i=1}^N [K_1(\mathbf{r}_i) (m_x^2(\mathbf{r}_i) m_y^2(\mathbf{r}_i) + m_y^2(\mathbf{r}_i) m_z^2(\mathbf{r}_i) + m_x^2(\mathbf{r}_i) m_z^2(\mathbf{r}_i)) \\ + K_2 m_x^2(\mathbf{r}_i) m_y^2(\mathbf{r}_i) m_z^2(\mathbf{r}_i)] V_i & \text{(Cubic)} \end{cases} \quad (3.5)$$

If  $K_1$  is positive,  $\hat{\mathbf{u}}$  is an unit vector in the direction of easy axis. Otherwise, it is normal to the easy plane. In the case of cubic anisotropy, the crystal axes need to be oriented parallel to the coordinate axes. Here too, the error in numerical approximation is  $O(\nabla^2)$ . The corresponding field equations can be written as

$$\mathbf{H}_{\text{anis}}(\mathbf{r}_i) = \begin{cases} (\mathbf{m}(\mathbf{r}_i) \cdot \hat{\mathbf{u}}(\mathbf{r}_i)) \frac{2K_1}{\mu_0 M_s} \hat{\mathbf{u}}(\mathbf{r}_i) & \text{(Uniaxial)} \\ -\frac{2\overleftrightarrow{\mathbf{N}}^K(\mathbf{r}_i) \cdot \mathbf{m}(\mathbf{r}_i)}{\mu_0 M_s} & \text{(Cubic)} \end{cases} \quad (3.6)$$

Here,  $\overleftrightarrow{\mathbf{N}}^K$  is a tensor with diagonal entries only:

$$\overleftrightarrow{\mathbf{N}}^K(\mathbf{r}_i) = \begin{bmatrix} N_{11}^K(\mathbf{r}_i) & 0 & 0 \\ 0 & N_{22}^K(\mathbf{r}_i) & 0 \\ 0 & 0 & N_{33}^K(\mathbf{r}_i) \end{bmatrix}, \quad (3.7)$$

such that:

$$N_{11}^K(\mathbf{r}_i) = K_1(\mathbf{r}_i) (m_y^2(\mathbf{r}_i) + m_z^2(\mathbf{r}_i)) + K_2(\mathbf{r}_i) m_y^2(\mathbf{r}_i) \cdot m_z^2(\mathbf{r}_i), \quad (3.8)$$

$$N_{22}^K(\mathbf{r}_i) = K_1(\mathbf{r}_i) (m_x^2(\mathbf{r}_i) + m_z^2(\mathbf{r}_i)) + K_2(\mathbf{r}_i) m_x^2(\mathbf{r}_i) \cdot m_z^2(\mathbf{r}_i), \quad (3.9)$$

$$N_{33}^K(\mathbf{r}_i) = K_1(\mathbf{r}_i) (m_x^2(\mathbf{r}_i) + m_y^2(\mathbf{r}_i)) + K_2(\mathbf{r}_i) m_x^2(\mathbf{r}_i) \cdot m_y^2(\mathbf{r}_i). \quad (3.10)$$

The demagnetizing energy and the corresponding field terms can be approximated as

$$E_d \approx \frac{\mu_0}{2} \sum_{i=1}^N V_i \mathbf{M}(\mathbf{r}_i) \cdot \sum_{j=1}^N \overleftrightarrow{\mathbf{N}}(\mathbf{r}_i - \mathbf{r}_j) \cdot \mathbf{M}(\mathbf{r}_j), \text{ and} \quad (3.11)$$

$$\mathbf{H}_{\text{dem}}(\mathbf{r}_i) \approx \sum_{j=1}^N \overleftrightarrow{\mathbf{N}}(\mathbf{r}_i - \mathbf{r}_j) \cdot \mathbf{M}(\mathbf{r}_j), \quad (3.12)$$

respectively. Here  $\overleftrightarrow{\mathbf{N}}$  is the discrete analogue of the demagnetizing tensor introduced in Eq. (2.49), whose components can be calculated using

$$4\pi dV N_{ij}(\mathbf{r}) = 8f(\mathbf{r}) - 4 \sum_{\mathbf{s} \in \{A\}} f(\mathbf{s}) + 2 \sum_{\mathbf{s} \in \{B\}} f(\mathbf{s}) - 2 \sum_{\mathbf{s} \in \{C\}} f(\mathbf{s}). \quad (3.13)$$

Here  $dV = dx dy dz$  is the volume of the cuboid with its centroid at  $(\mathbf{r}) = (x, y, z)$ , and  $i \in \{x, y, z\}$  and  $j \in \{x, y, z\}$ , and  $\{A\}$ ,  $\{B\}$  and  $\{C\}$  are sets of position vectors in neighbourhood of  $\mathbf{r}$ , such that

$$\{A\} = \{(x \pm dx, y, z), (x, y \pm dy, z), (x, y, z \pm dz)\}, \quad (3.14)$$

$$\{B\} = \{(x \pm dx, y \pm dy, z), (x, y \pm dy, z \pm dz), (x \pm dx, y, z \pm dz)\}, \quad (3.15)$$

$$\{C\} = \{(x \pm dx, y \pm dy, z \pm dz)\}. \quad (3.16)$$

For diagonal ( $N_{ii}$ ) and off-diagonal ( $N_{ij}$ ) terms of  $\overleftrightarrow{\mathbf{N}}$ , the function  $f(\mathbf{r}) = f(x, y, z)$  in Eq. (3.13) can be expressed as<sup>248</sup>

$$f(x, y, z) = \begin{cases} \frac{1}{2}y(z^2 - x^2) \sinh^{-1}\left(\frac{y}{\sqrt{x^2+z^2}}\right) \\ \quad + \frac{1}{2}z(y^2 - x^2) \sinh^{-1}\left(\frac{z}{\sqrt{x^2+y^2}}\right) \\ \quad - xyz \tan^{-1}\left(\frac{yz}{xr}\right) \\ \quad + (2x^2 - y^2 - z^2)r/6 & : i = j = x. \\ xyz \sinh^{-1}\left(\frac{z}{\sqrt{y^2+z^2}}\right) \\ \quad + \frac{1}{6}y(3z^2 - y^2) \sinh^{-1}\left(\frac{x}{\sqrt{y^2+z^2}}\right) \\ \quad + \frac{1}{6}x(3z^2 - x^2) \sinh^{-1}\left(\frac{y}{\sqrt{x^2+z^2}}\right) \\ \quad - \frac{1}{2}y^2z \tan^{-1}\left(\frac{xz}{yr}\right) - \frac{1}{2}x^2z \tan^{-1}\left(\frac{yz}{xr}\right) \\ \quad - \frac{1}{6}z^3 \tan^{-1}\left(\frac{xy}{zr}\right) - xyr/3 & : i \neq j \neq z \neq i. \end{cases}$$

Here  $\sinh^{-1}(l) = \log(l + \sqrt{1+l^2})$ .

Equation (3.12) essentially defines demagnetizing field  $\mathbf{H}_{\text{dem}}$  as the discrete convolution of demagnetizing tensor  $\overleftrightarrow{\mathbf{N}}$ , with magnetization  $\mathbf{M}$ . This can allow for efficient computation

of the field using fast Fourier transform (FFT) techniques.<sup>254</sup>

Once energy or field terms are computed numerically w.r.t. to position  $\mathbf{r}$ , we can now find the  $\mathbf{H}_{\text{eff}}$  as the sum of its constituents and proceed with solving the LLG ODE w.r.t. time while giving due considerations to initial and boundary conditions.

### 3.2.2. Boundary Conditions

Differential equation require some boundary and initial conditions to obtain a unique solution. In the case of the LLG equation, the initial condition is typically supplied in the problem design as  $\mathbf{M}(\mathbf{r}, t = 0)$ . This is a relaxed state of magnetization before a signal is provided to trigger the dynamics.

The general form of boundary conditions \* (in addition to the Maxwell boundary conditions at external faces of the ferromagnetic plane of thickness  $u$ , proposed by Guslienko and Slavin<sup>255</sup> takes into account both dipolar pinning and pinning induced by uniaxial surface anisotropy:

$$\mathbf{M} \times \left( \lambda_{\text{ex}}^2 \frac{\partial \mathbf{M}}{\partial \hat{\mathbf{n}}} + \frac{2K_S}{\mu_0 M_s^2} (\mathbf{M} \cdot \hat{\mathbf{n}}_a) \hat{\mathbf{n}}_a + u \mathbf{H}_{\text{dem}} \right) = 0, \quad (3.17)$$

where  $\frac{\partial \mathbf{M}}{\partial \hat{\mathbf{n}}}$  is the directional derivative of magnetization at the boundary. The uniaxial surface anisotropy is defined by its strength  $K_S$  and orientation  $\hat{\mathbf{n}}_a$ .  $\mathbf{H}_{\text{dem}}$  depends on the thickness  $u$  and in-plane sizes  $R$  of the system (e.g., stripe width). It was shown<sup>255</sup> that for small systems ( $\sqrt{Ru} < \lambda_{\text{ex}}$ ) the magnetization pinning can be achieved only in the presence of strong surface anisotropy. Therefore, in the exchange limit the Rado–Weertman boundary condition,<sup>256</sup> which simply neglects the dipolar pinning, is sufficient.

Note that the surface anisotropy field (second term in the brackets in Eq. (3.17)) depends monotonously on  $K_S$ . As a result, the logarithmic derivative of the components of dynamical magnetization  $\left(\frac{\partial m_i}{\partial \hat{\mathbf{n}}}\right)/m_i$  ( $i$  indicates the Cartesian components of  $\mathbf{m}$ ) taken on the side faces of the waveguide also has monotonous dependence on  $K_S$  in the regime of linear dynamics<sup>255</sup> and approaches the values  $\pm\infty$  – *pinned boundary conditions* – and 0 – *unpinned boundary conditions* – for high and low values of  $K_S$ , respectively. Once we have our boundary conditions in order, we can proceed to solve the LLG ODE.

---

\*Parts of this sub-section is based on Klos *et al.* Phys. Rev. B **86**, 184433 (2012).

Sometimes, a problem may require us to model geometries where one (*e.g.* a wave-guide) or two (*e.g.* a 2D MC) dimensions are infinite. If these systems possess translational symmetry, 1D or 2D periodic boundary condition (PBC) may be used. In OOMMF these boundary conditions are presently enabled by employing some publicly written extensions.<sup>243,244</sup> Under periodic boundary conditions the exchange and demagnetizing fields are calculated with the following in mind:

$$\mathbf{H}_{\text{exch}}(\mathbf{r}) = \begin{cases} \mathbf{H}_{\text{exch}}(\mathbf{r} + \mathbf{a}_1) & \text{(1D PBC)} \\ \mathbf{H}_{\text{exch}}(\mathbf{r} + \mathbf{a}_1 + \mathbf{a}_2) & \text{(2D PBC)} \end{cases} \quad (3.18)$$

$$\mathbf{H}_{\text{dem}}(\mathbf{r}) = \begin{cases} \mathbf{H}_{\text{dem}}(\mathbf{r} + \mathbf{a}_1) & \text{(1D PBC)} \\ \mathbf{H}_{\text{dem}}(\mathbf{r} + \mathbf{a}_1 + \mathbf{a}_2) & \text{(2D PBC)} \end{cases} \quad (3.19)$$

Here  $\mathbf{a}_1$  and  $\mathbf{a}_2$  represent the periodicity in mutually orthogonal directions.

### 3.2.3. Solving The LLG Equation in OOMMF

In this work, the 4th order Runge–Kutta method has been used to solve the LLG equation as an ODE in time.

#### 4th order Runge–Kutta method

Let magnetization be known at time  $t_1$  as  $\mathbf{M}(\mathbf{r}, t_1)$  or  $\mathbf{M}_1(\mathbf{r})$ . Since different magnetic energies, depend upon magnetization and the external field  $\mathbf{H}_{\text{ext}}(\mathbf{r}, t_1)$ , the effective magnetic field can be expressed as a function of magnetization, position and time as

$$\mathbf{H}_{\text{eff}}(\mathbf{r}, t) = \mathbf{h}(\mathbf{M}, \mathbf{r}, t). \quad (3.20)$$

Thus the LLG equation can be rewritten as

$$\begin{aligned} \frac{d\mathbf{M}}{dt} &= -|\bar{\gamma}|\mathbf{M} \times \mathbf{H}_{\text{eff}} - \frac{\alpha|\bar{\gamma}|}{M_s}\mathbf{M} \times (\mathbf{M} \times \mathbf{H}_{\text{eff}}) \\ &= -|\bar{\gamma}|\mathbf{M} \times \mathbf{h}(\mathbf{M}, \mathbf{r}, t) - \frac{\alpha|\bar{\gamma}|}{M_s}\mathbf{M} \times (\mathbf{M} \times \mathbf{h}(\mathbf{M}, \mathbf{r}, t)) \\ &= \mathbf{f}(\mathbf{M}, \mathbf{r}, t). \end{aligned} \quad (3.21)$$

So for  $i^{\text{th}}$  cuboid with centroid at  $\mathbf{r}_i$ , we can write

$$\left. \frac{d\mathbf{M}}{dt} \right|_{\mathbf{r}=\mathbf{r}_i} = \mathbf{f}(\mathbf{M}, \mathbf{r} = \mathbf{r}_i, t) = \mathbf{f}_i(\mathbf{M}, t). \quad (3.22)$$

Here, the rate of change of magnetization at site  $i$  is being described by a vector function  $\mathbf{f}_i$ .

Let us now define  $\mathbf{k}_{i1}$ ,  $\mathbf{k}_{i2}$ ,  $\mathbf{k}_{i3}$  and  $\mathbf{k}_{i4}$  as following:

$$\mathbf{k}_{i1} = \mathbf{f}_i(\mathbf{M}_1, t_1), \quad (3.23a)$$

$$\mathbf{k}_{i2} = \mathbf{f}_i\left(\mathbf{M}_1 + \frac{h}{2}\mathbf{k}_{i1}, t_1 + \frac{h}{2}\right), \quad (3.23b)$$

$$\mathbf{k}_{i3} = \mathbf{f}_i\left(\mathbf{M}_1 + \frac{h}{2}\mathbf{k}_{i2}, t_1 + \frac{h}{2}\right), \text{ and} \quad (3.23c)$$

$$\mathbf{k}_{i4} = \mathbf{f}_i(\mathbf{M}_1 + h\mathbf{k}_{i3}, t_1 + h). \quad (3.23d)$$

Now, we can obtain  $\mathbf{M}(\mathbf{r}, t_2) = \mathbf{M}_2$ , where time step  $h = t_2 - t_1$  as

$$\mathbf{M}(\mathbf{r}, t_2)|_{\mathbf{r}=\mathbf{r}_i} = \mathbf{M}(\mathbf{r}, t_1)|_{\mathbf{r}=\mathbf{r}_i} + \frac{h}{6}(\mathbf{k}_{i1} + 2\mathbf{k}_{i2} + 2\mathbf{k}_{i3} + \mathbf{k}_{i4}). \quad (3.24)$$

Thus we can find how magnetization changes as time goes from  $t_1$  to  $t_2$  in a time step  $h$  for each position  $\mathbf{r}_i$ . Now, let  $\mathbf{M}'(\mathbf{r}, t_2)$  be calculated using Eqs. 3.23 and 3.24 with two equal time steps of  $h' = h/2$ . Thus the error  $\epsilon(\mathbf{r}, t_2)$  going from  $t_1$  to  $t_2$  in one step can be defined as

$$\epsilon(\mathbf{r}, t_2) = \frac{h}{2} |\mathbf{f}(\mathbf{M}', \mathbf{r}, t_2) - \mathbf{f}(\mathbf{M}, \mathbf{r}, t_2)|. \quad (3.25)$$

For a step to be successful,  $\max(\epsilon)$  should be less than a given value, which can be made smaller and smaller to get more and more accurate results. However this will cause simulations to run for longer periods of time. Thus, once a physical output parameter appears to converge, it is no longer necessary to further reduce these error limits. In simulations performed during this work convergence was tested based on the dimensions of cuboid. Limits of time steps  $h$  was decided based on the time-scale of underlying magnetization dynamics (*e.g.* 1 ps for SW dynamics and 10 ps for a vortex core's gyration). OOMMF allows the users to decide these limits for themselves.

### 3.3. FEM and Nmag

FEM based Nmag uses an adaptive tetrahedral mesh of varying edge lengths. Nmag yields more accurate results by sacrificing significant computational time and resources. Thus, OOMMF was the preferred platform of doing simulations in this work. Nmag has also been used on one occasion for the purpose of a comparative analysis where high accuracy was necessary. Most of the results produced here were validated against those yielded by the PWM.

#### 3.3.1. FEM Meshing

In FDM a geometrical body is modelled as a set of packed cuboids. In the case of FEM tetrahedrons are used instead of cuboids. It makes the modelling much more accurate. In some cases it can also save computational resources by avoiding empty areas. Here we describe the *Delaunay triangulation algorithm*<sup>257</sup> which is popular due to its efficiency and robustness.

To start the mesh generation a set of distinct forming points  $\{P\} = \{p_1, p_2, p_3, \dots, p_N\}$  is randomly selected in the space of the geometry to be modelled. A *Voronoi region*  $\{V(p_i)\}$  is defined as the set of points in space which are closer to  $p_i$  than any other point  $p_j \in \{P\}$ . Points which belong to two Voronoi regions  $\{V(p_i)\}$  and  $\{V(p_j)\}$  ( $p_i, p_j \in \{P\}$ ) form the boundaries of the regions. Forming points whose Voronoi regions share a common boundary can be connected together to form the edges of a tetrahedral structure such that the circumsphere of any tetrahedron does not enclose any forming point. The edges of the tetrahedrons should be small enough to resolve magnetic domains such as a Bloch point. If that is not the case, or if the forming points do not approximate the finer features of the geometry, additional forming points need to be included in  $\{P\}$  and the process of triangulation needs to be repeated. This algorithm is also presented in Fig. 3.2 for a planer system where tetrahedrons are replaced by triangles and circumspheres are replaced by circumcircles. Forming points and their respective Voronoi regions are seen in 2D space in Fig. 3.2 (a). A mesh of triangles is created using the forming points, such that their circumcircles do not include any forming points. If a new forming point has to be introduced

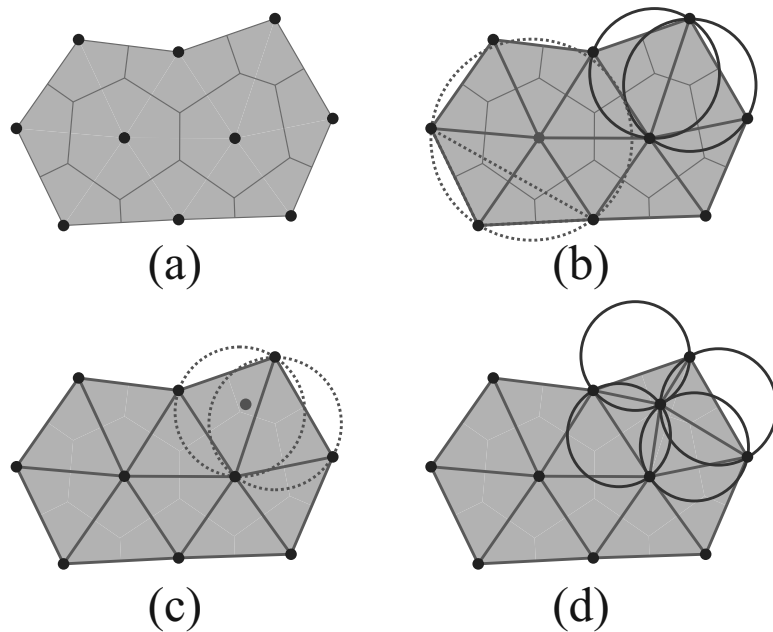


Figure 3.2.: (a) Forming points and their Voronoi regions. (b) A mesh of triangles using the forming points as vertices. Triangles whose circumcircle encompass any forming points are rejected. (c) A new forming point is introduced near an unacceptably long edge. This causes the rejection of two triangles whose circumcircles include the new forming point. (d) New smaller triangles are created whose circumcircles don't encompass any forming points. Source: Ref. 16.

to avoid an unacceptably long edge, new triangles are created to redefine the mesh.

### 3.3.2. Solving The LLG Equation using Nmag

Nmag can work with meshes produced by freewares such as Netgen. Once a mesh of tetrahedrons and their vertices are available, Galerkin discretization<sup>258</sup> is used to approximate the magnetization and effective magnetic fields. This is conceptually similar to the approximation process described in sub-Sec. 3.2.1. Following, this approximation of magnetization and effective field one can proceed to solve the LLG equation by implementing an algorithm of differential equation solution.

### 3.4. Plane Wave Method (PWM)

The PWM considers linear approximation of the LLG equation\*. The magnetization dynamics is treated in the form of harmonic time precession of the magnetization with the angular frequency  $\omega$ , expressed by the dynamical components of magnetization vector:  $m_x(\mathbf{r}, t) = m_x(\mathbf{r})e^{i\omega t}$  and  $m_y(\mathbf{r}, t) = m_y(\mathbf{r})e^{i\omega t}$ . The dynamics of magnetization in the direction of bias field is neglected, i.e. we assume  $M_z(\mathbf{r}, t) \approx M_s$ . As a result the linearised LLG equations have a form of two linear differential equations for the precession amplitudes:  $m_x(\mathbf{r})$  and  $m_y(\mathbf{r})$ . The amplitudes  $m_x(\mathbf{r})$  and  $m_y(\mathbf{r})$  can be transformed to the reciprocal space with the use of Bloch theorem. This allows to convert the linearized Landau-Lifshitz equations into the algebraic eigenvalue problem:

$$\begin{pmatrix} \{m_x(\mathbf{G})\} \\ \{m_y(\mathbf{G})\} \end{pmatrix} \hat{M} = \frac{i\omega}{\gamma\mu_0 H_0} \begin{pmatrix} \{m_x(\mathbf{G})\} \\ \{m_y(\mathbf{G})\} \end{pmatrix} \quad (3.26)$$

by Fourier transformation of material parameters ( $M_s$ ,  $\lambda_{\text{ex}}$ ) and the periodic factor of Bloch functions, where  $\{m_x(\mathbf{G})\}$  and  $\{m_y(\mathbf{G})\}$  denote the vectors with the set of Fourier coefficients for periodic parts of Bloch functions. The matrix  $\hat{M}$  of the eigenvalue problem can be written in a block-matrix form:

$$\hat{M} = \begin{pmatrix} \hat{M}^{xx} & \hat{M}^{xy} \\ \hat{M}^{yx} & \hat{M}^{yy} \end{pmatrix}. \quad (3.27)$$

The submatrices in (3.27) are defined as follows:

$$\hat{M}_{ij}^{xx} = -\hat{M}_{ij}^{yy} = -i \frac{k_y + G_{y,j}}{H_0 |\mathbf{k} + \mathbf{G}_j|} S(\mathbf{k} + \mathbf{G}_j) M_s (\mathbf{G}_i - \mathbf{G}_j), \quad (3.28)$$

---

\*This section is based on parts of Klos *et al.* Phys. Rev. B **89**, 014406 (2014).

$$\begin{aligned}
\hat{M}_{ij}^{xy} &= \delta_{ij} + \sum_l \frac{(\mathbf{k} + \mathbf{G}_j) \cdot (\mathbf{k} + \mathbf{G}_l)}{H_0} \lambda_{\text{ex}}^2(\mathbf{G}_l - \mathbf{G}_j) M_s(\mathbf{G}_i - \mathbf{G}_l) \\
&+ \frac{(k_y + G_{y,j})^2}{H_0 |\mathbf{k} + \mathbf{G}_j|^2} (1 - C(\mathbf{k} + \mathbf{G}_j)) M_s(\mathbf{G}_i - \mathbf{G}_j) \\
&- \frac{(G_{z,i} - G_{z,j})^2}{H_0 |\mathbf{G}_i - \mathbf{G}_j|^2} M_s(\mathbf{G}_i - \mathbf{G}_j) (1 - C(\mathbf{G}_i - \mathbf{G}_j)), \tag{3.29}
\end{aligned}$$

$$\begin{aligned}
\hat{M}_{ij}^{yx} &= -\delta_{ij} - \sum_l \frac{(\mathbf{k} + \mathbf{G}_j) \cdot (\mathbf{k} + \mathbf{G}_l)}{H_0} \lambda_{\text{ex}}^2(\mathbf{G}_l - \mathbf{G}_j) M_s(\mathbf{G}_i - \mathbf{G}_l) \\
&- \frac{1}{H_0} C(\mathbf{k} + \mathbf{G}_j) M_s(\mathbf{G}_i - \mathbf{G}_j) \\
&+ \frac{(G_{z,i} - G_{z,j})^2}{H_0 |\mathbf{G}_i - \mathbf{G}_j|^2} M_s(\mathbf{G}_i - \mathbf{G}_j) (1 - C(\mathbf{G}_i - \mathbf{G}_j)), \tag{3.30}
\end{aligned}$$

where indexes  $i, j, l$  of reciprocal lattice vectors  $\mathbf{G}_i$  are integers.  $M_s(\mathbf{G}_i)$  and  $\lambda_{\text{ex}}^2(\mathbf{G}_i)$  are the Fourier coefficients associated with the saturation magnetization and exchange constant, respectively. The additional functions used in the equations above are defined as follows:

$$\begin{aligned}
S(\mathbf{k}) &= \sinh(|\mathbf{k}|u/2) e^{-|\mathbf{k}|u/2}; \\
C(\mathbf{k}) &= \cosh(|\mathbf{k}|u/2) e^{-|\mathbf{k}|u/2}, \tag{3.31}
\end{aligned}$$

where  $u$  denotes the thickness of the 1D or 2D magnonic crystal.

In order to use PWM for 1D structure one has to make the structure artificially periodic along the direction perpendicular to the waveguide axis. Here, the supercell method can be used, which exploits the fact that the properties of the confined system are equivalent to the properties of the set of its non-interacting copies. In Eqs. (3.28), (3.29), and (3.30) we have already used 2D wave vectors  $\mathbf{k}$  and reciprocal lattice vectors  $\mathbf{G}$  in the  $(x, y)$  space, which refers to the infinite sequence of parallel waveguides separated by an artificial material.<sup>213</sup> In 1D nanoscale waveguides, calculations are performed for  $y$  component of the wavevector equal 0, i.e. the direction of propagation of SWs is limited to the axis of the waveguide.

## 3.5. Fabrication Techniques

### 3.5.1. Thin-Film deposition

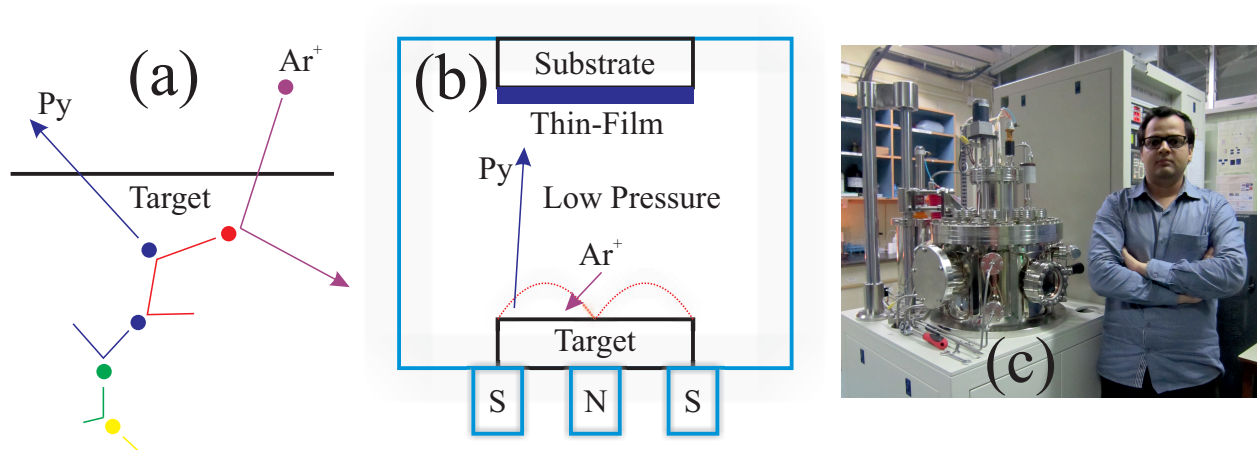


Figure 3.3.: (a) Incoming  $\text{Ar}^+$  ion collides with atoms in the target. A sputtered atom is released upon a cascade of collisions. (b) A sketch of sputtering vacuum chamber showing dashed field lines. (c) My picture with a sputtering setup at the S. N. Bose National Centre for Basic Sciences, Kolkata.

The first step in fabrication is to deposit a thin layer of a magnetic material such as Py over a (typically silicon) substrate. This is accomplished by *sputter deposition*. *Sputtering* is a process where fast moving ions cause an ejection atoms from a *target*. These atoms from the target can be caught by the substrate allowing the thin-film to increase its thickness with time. The incoming  $\text{Ar}^+$  ion triggers a cascade of collisions within the target as shown in Fig. 3.3 (a). Atoms are only able to leave the surface of the target if they have more energy than the surface binding energy. Dashed field lines in Fig. 3.3 (b) denote the electric and magnetic fields generated by a magnetron. This helps trap the argon plasma, which is sustained at a very low pressure of  $\approx 10$  mTorr, close to the target. The neutral atom leaving the surface is not affected by these fields. Atoms arriving to settle at the substrate increase the deposited film's thickness. A sputtering setup at the S. N. Bose National Centre for Basic Sciences is shown in Fig. 3.3 (c). Sometimes the use of multiple targets is considered desirable so that a thin dielectric layer may be placed over the magnetic thin-film. This will help prevent the oxidation of the thin film layer.

### 3.5.2. Lithography

Material can be removed from different locations in a deposited thin film using lithography techniques such as photolithography, e-beam lithography and focused ion beam (FIB) milling. The resolution of the lithography process depends upon the energy of the particles (or quasi-particles) being used. Thus, photolithography should be used to etch micron sized vast regions, while FIB milling should be used where resolution is below 50 nm. Anything in between those limits may be handled using e-beam lithography. A schematic diagram showing optical and e-beam lithography is presented in Fig. 3.4.<sup>6</sup>

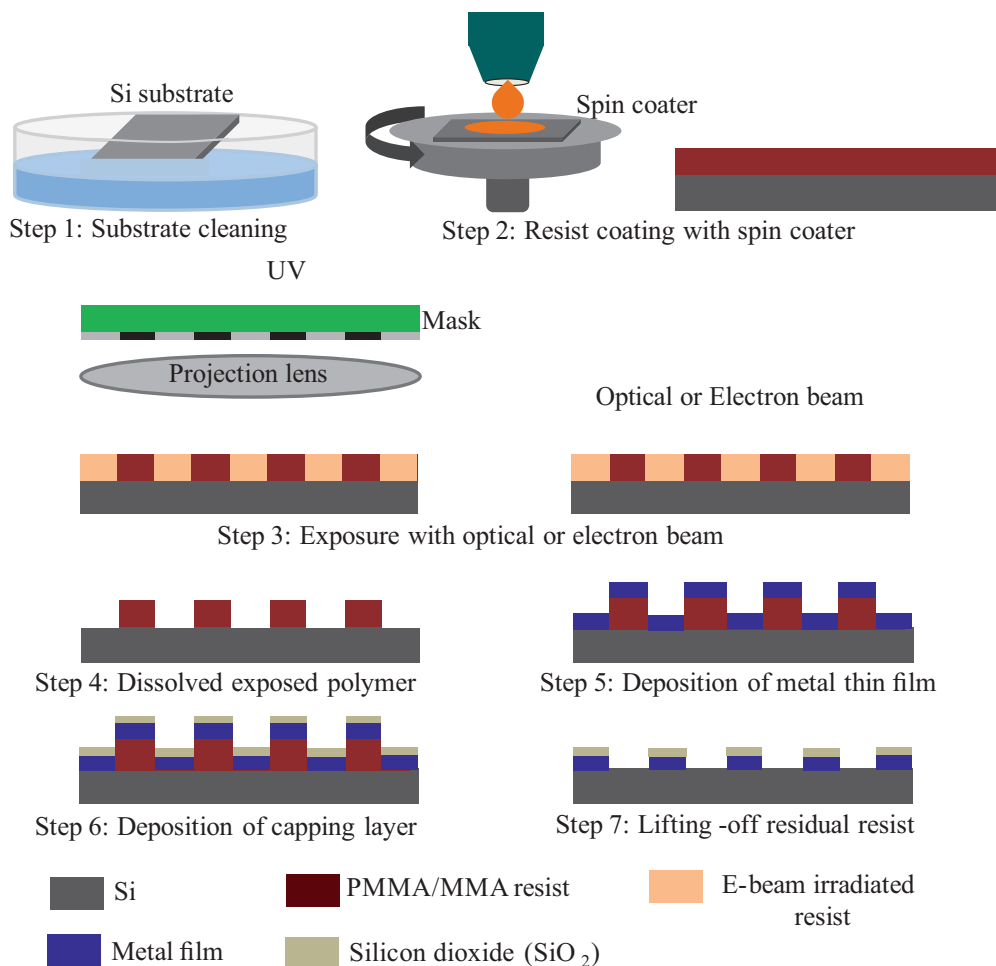


Figure 3.4.: Step-wise description of optical and e-beam lithography. Source: Ref. 6.

A photo-mask, which may be designed using computer aided design (CAD), containing a desired pattern. This facilitates the parallel growth of the micro-structures. In the case of e-beam or FIB lithography, the focus of etching needs to be controlled and moved from one

spot to another during the lithography process.

The first step in optical lithography is cleaning of the Si(100) substrate by removing any organic or inorganic materials from its surface. This is done by submerging the substrate in an ultrasonic bath of acetone and water (20 mins each), respectively. The substrate is then dried with dry N<sub>2</sub> from a nitrogen gun. Then a spin coater is used to coat the surface of the substrate with a uniform layer of positive photoresist dissolved in an organic solvent. The thickness of the photoresist layer depends upon the its viscosity and the spinning speed of the spin coater. These parameters needs to calibrated to obtain a layer of desired thickness. A photo-mask containing the patterns to be fabricated is then placed on top of the substrate. A projection lens is used as shown in Fig. 3.4 to ensure a proper exposure of the coated substrate. This exposure causes the the polymer chains in the resist to break, which is then put into distilled water at room temperature, rinsed for 60 s and dried using dry the nitrogen gun. Next, the substrate is submerged into MIBK:IPA (1:3) (methyl isobutyl ketone : isopropyl alcohol) solution and rinsed for another 30 s. Finally, the substrate is submerged into acetone and rinsed (for 60 s) and dried again. This step causes the two dimensional pattern of the photo-mask to appear as a three dimensional structure on the substrate. Now a film of Py can be deposited as described in sub-Sec. 3.5.1. Finally, the film deposited on the resist can be lifted-off using a stripper solution along with the resist leaving only the desired Py structure onto the Si surface.

High energy electrons are generated by accelerating a beam of electrons across a high voltage. The cleaning process is similar in optical and e-beam lithography. The spin coating is then done to produce a bilayer of polymethyl methacrylate (PMMA) and methyl methacrylate (MMA). The thickness of individual layers is controlled by calibration. As the PMMA layer develops faster than the MMA layer, the resulting overhung structure gives an undercut edge profile (of the resist) after development. A scanning electron microscope (SEM) can now be used to expose the resist with focused electrons. The pattern of this exposure can be controlled using a CAD software. The beam current and dose time are typically of the order of 100 pA and 1 $\mu$ s, receptively. The exposed resist is then dissolved using developer solutions. A required 3D structure of the unexposed resists now survives on the substrate. A ferromagnetic layer can now be deposited as described in sub-Sec. 3.5.1. The lift-off to

remove the unexposed resist (along with the film deposited over it) can now be done using stripper solutions. FIB milling, where heavier gallium ions are used instead of electrons can now be used to create even finer nanostructures after this point. The steps of cleaning, spin-coating, development and lift-off are similar to what is described before in the cases of optical and e-beam lithography techniques.

### 3.6. Sample Characterization

Even with all the recent advancements in nanofabrication, there are often numerous defects in the fabricated nanoscale samples. Any sample with serious systematic defects can not be used for experimentation. Due to the finite spot size of optical, electron or ion beams, deformations like rounded corners of the square dots or holes are always found. Inaccurate calibration of spin-coating, development of lift-off steps can also result in severe defects. A slow cooling of sputter deposited Py thin film can develop an inhomogeneous distribution of iron and nickel. During FIB milling gallium ion can get redeposited around the edges of the geometry which has just been removed. This can lead to pinning of magnetization dynamics at these edges.<sup>213</sup> Apart from these fabrication related defects, mechanical defects may also appear due to poor handling or storage of the samples. The oxidation and contamination of the magnetic sample is mitigated by coating the sample with a non-reactive dielectric substances like glass or  $\text{Al}_2\text{O}_3$ .

Once all the steps of fabrication are properly calibrated, and the sample is handled and stored carefully, even then one should examine the samples to verify that it is in good condition to start experimentation. SEM imaging was used in this work to observed the structure of the fabricated systems. A schematic of scanning electron microscope is presented in Fig. 3.5.<sup>6</sup> The sample is mounted on a small specimen stage by using a double-sided carbon tape. The sample's surface should be electrically conductive grounded to prevent any accumulation of electrostatic charge. A stream of electrons, or an electron beam, is emitted either from an electron gun fitted with a tungsten filament cathode (thermionic) or from a field emission cathode. The later method produces narrower electron beam leading to a superior spatial resolution. The energy of the electrons in eV can typically vary from

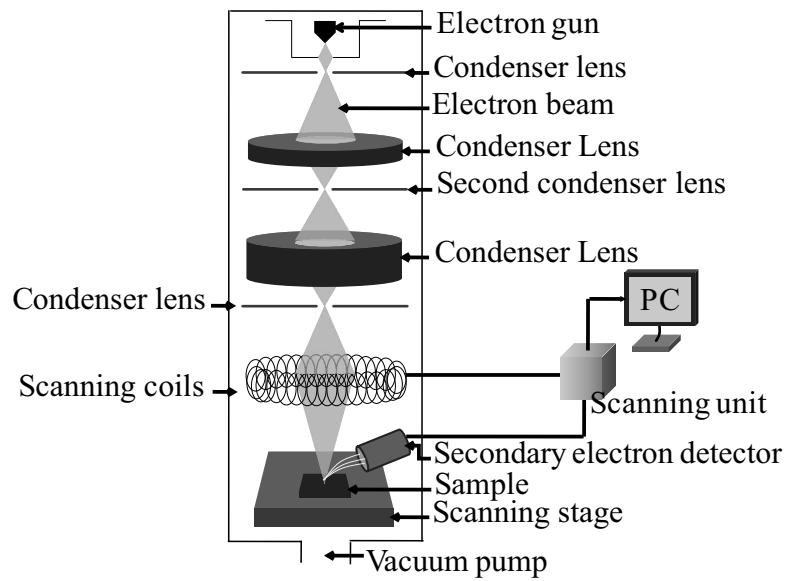


Figure 3.5.: Schematic of scanning electron microscope. Source: Ref. 6.

two to five orders of magnitude. After emission, the electrons are further accelerated by applying a voltage. The beam passes through a series of electromagnetic *condenser lenses* (see Fig. 3.5), which alter the spot size of the beam. An electromagnetic scanning coil, which can scan a rectangular region in a raster fashion, finally focuses the beam in the plane of the sample.<sup>6</sup> Upon an inelastic collision with the atoms in the sample, the energetic scanning electrons produce *secondary electrons*. The relative intensities of scanning and secondary electrons is then compared to generate the surface topography and morphology of samples.

# 4. Thin–Films, Waveguides and One–Dimensional Magnonic Crystals

\*The spectrum of spin–waves (SWs) propagating in magnetic systems is important from both fundamental and applied points of view. Propagating SWs in spatially modulated magnetic systems, namely the magnonic crystals,<sup>3,69</sup> will form the building blocks for future microwave data communication. Recently, much effort has been made in understanding and tailoring the magnonic band structures (frequency versus wavevector) in various magnonic crystals with nanoscale features. The numerical simulation method is particularly important because this can be effectively used to design the desired magnonic band structures before starting the expensive nanofabrication methods. However, conventional micromagnetic simulators provide only the space–time data by solving the Landau-Lifshitz-Gilbert equation (LLG equation)<sup>7,8</sup> and meaningful conversion of that data to frequency and wavevector domains<sup>259,260</sup> poses several computational challenges. Object Oriented Micromagnetic Framework (OOMMF)<sup>250</sup> exploits the finite difference method to calculate magnetization dynamics.

The dispersion curves obtained by a 2D discrete Fourier transform (DFT)<sup>261</sup> of the space–time data obtained from micromagnetic simulations may contain artefacts. These mainly include lack of resolution in the frequency or wavevector domain, aliasing, spectral leakage and scalloping loss. These artefacts render the resultant dispersion diagram, unreadable. Discretization of continuous magnetic objects also leads to the appearance of an artificial period and as a result to the formation of an artificial band where the spectrum should

---

\*This chapter is based upon Kumar *et al.* *J. Phys. D: Appl. Phys.* **45**, 015001 (2012).

---

be continuous.<sup>259,260</sup> The effect of most of these problems can be reduced by sampling the magnetization over a larger sample size or over a longer period of time. Range in frequency and wavevector domains can be increased by sampling the magnetization at a higher sampling rate in time and space domains, respectively. But, these measures will soon consume the available computational resources without providing much clarity to the obtained results. In this chapter we aim to document and standardize a sequence of steps that help in obtaining better results without compromising on the speed or extent of the numerical analysis. The improvement in quality, made by these methods, is established by a numerical comparison, which is further verified by the manual observation of the obtained dispersion diagrams. The presented method can also be used to compute the dispersion of SWs in different kinds of magnonic conductors,<sup>5</sup> which form a rich family of spatially modulated magnetic structures or artificial lattices designed to control the spectrum of SWs. Based on their geometry these magnonic conductors can be classified as one (1D), two (2D) or three dimensional (3D) and based on their continuity they can be either continuous waveguides or magnonic crystals (discrete arrays of dots or antidots). Magnonic crystals can also be made of more than one magnetic material, which allows us to classify them on the basis of homogeneity (as homogeneous and heterogeneous). While processing the results from a 3D magnonic crystal, the limited computational resources force us to use slower forms of computer memory.

In the following sections we explain how dispersion curves of SWs can be obtained by a 2D DFT of magnetization data which, in turn, is the output of a finite difference based ordinary differential equation (ODE) solver, such as OOMMF. We further discuss the shortcomings of this method and demonstrate how various techniques can be used to mitigate them. Material parameters of Py are used for the results shown here. Heavy damping is used to reach the state of saturated magnetization sooner under a constant bias. We have further applied the newly developed numerical technique to a range of magnonic media including magnetic nanostripes, magnetic nanowires and thin film elements. We have further calculated the dispersion curves for simple magnonic crystals with 1D and quasi-2D arrangements of periodic antidot arrays in permalloy thin films, which opens up allowed and forbidden magnonic bands.

## 4.1. Method

OOMMF produces the output data in several files where each file corresponds to a particular instance of simulation time and contains the information of magnetization distribution over the entire magnetic object. Being a finite difference method based ODE solver, OOMMF divides a magnetic object into an artificial periodic array of rectangular cuboids. The region of space, where no magnetic material is present, is assumed to have zero saturation magnetization. Subroutines were written to read the data into three four-dimensional matrices (one matrix for each component of magnetization), namely  $M^i(t, x, y, z)$ ,  $M^j(t, x, y, z)$  and  $M^k(t, x, y, z)$ . The variables  $t$ ,  $x$ ,  $y$  and  $z$  represent discrete equally spaced values of time and space. A dynamic component of magnetization (in our case orthogonal to the external bias field as we consider fully saturated samples) should be selected for the purpose of dispersion analysis. If  $M^k(t, x, y, z)$  is one such component, we set  $M_{x_m, y_n}^k(t, z) = M^k(t, x_m, y_n, z)$  to obtain a 2D matrix of the magnetization component,  $M^k$  at  $x = x_m$ , and  $y = y_n$ . The coordinate system should be appropriately rotated if the direction of propagation of spin-wave is neither of  $x$ ,  $y$  or  $z$ . A 2D DFT can now be performed on this matrix to obtain the output  $\tilde{M}_{x_m, y_n}^k(f, k_z) = F(M_{x_m, y_n}^k(t, z))$ . The magnitude of this output corresponds to the magnitude of the corresponding Fourier components. If we take some particular frequency  $f$ , the corresponding wavevector  $k_z$  can be found by finding the high values of the Fourier component magnitudes for this particular frequency  $f$ . In order to visualize the dispersion curve we record a colour-weighted 3D plot (or a colour weighted scatter plot) of  $P_{x_m, y_n}(f, k_z) \propto \log_{10} |\tilde{M}_{x_m, y_n}^k(f, k_z)|$  versus  $f$  and  $k_z$ . Thus, as seen in Fig. 4.1, when viewed from the top, the colour scale represents the Fourier power on a proportional decibel scale. Let the sum of  $|\tilde{M}_{x_m, y_n}^k(f, k_z)|^2$  over all values of  $x_m$  and  $y_n$  be represented by  $|\tilde{M}^k(f, k_z)|^2$  then  $P(f, k_z) \propto \log_{10} |\tilde{M}^k(f, k_z)|$  will contain information of all the modes present in the magnetic medium for the chosen direction, namely  $z$ .

## 4.2. Results and Discussion

As evident from Fig. 4.1 (a), there are several issues with the results obtained by the method described above. Introducing the Hanning window function has clearly improved the contrast

as seen in Fig. 4.1 (b). Since using a window function already reduces the scalloping loss, zero padding, as shown in Fig. 4.1 (c), does not affect the end result significantly in this case. However, it is still useful in improving the computational performance as described later in this section. Sinc excitation signal controls aliasing. This is better demonstrated in the case of a nano-wire, as described later in this chapter, where the range of observation (in frequency and wavevector domains) is higher than that in Fig. 4.1 (d). We now enumerate the major issues and establish some techniques to overcome them. Figure 4.2 depicts this entire procedure schematically.

High resolving powers in both frequency and wavevector domains are often desirable for studying the fine structures of the dispersion curves. The difference between two consecutive values of frequency (resolution in frequency) equals  $1/t$ , where  $t$  is the duration of observation, and resolution in the wavevector domain equals  $1/l$ , where  $l$  is the length of the sample. If a dynamic phenomenon finishes too rapidly, possibly due to very high damping, it would be impossible to have a good frequency resolution. Similarly, if the size of the magnetic medium is very small then we will obtain bad resolution in the wavevector domain. Resolving power in frequency and wavevector domains can, respectively, be improved by running the dynamics for a longer duration and by using longer samples in the direction of SW propagation.

Since we deal with the LLG equation within a continuum micromagnetic framework, phenomena associated with time-scale faster than 1 ps and length scale below 1 nm are beyond the scope of this framework. This gives upper bounds (Nyquist frequency) of range in both frequency and wavevector domains as 500 GHz and  $5 \times 10^8 \text{ m}^{-1}$  (or 3.141 rad/nm), respectively. Higher rates cost more memory for the same desired resolution. Unless necessary, these rates may be kept as low as possible. For exchange interaction to be effective, the size of the rectangular cuboid should be less than the exchange length of the magnetic material. The rate of sampling of magnetization in time should be high enough to capture the precessional motion correctly. Hence, it should not be less than one ‘snapshot’ per 10 ps in most cases. Fourier expansion for the  $N$  element sequence  $x_n$  may be written as

$$\tilde{X}_k = \sum_{n=0}^{N-1} x_n e^{\frac{-2\pi i k n}{N}}. \quad (4.1)$$

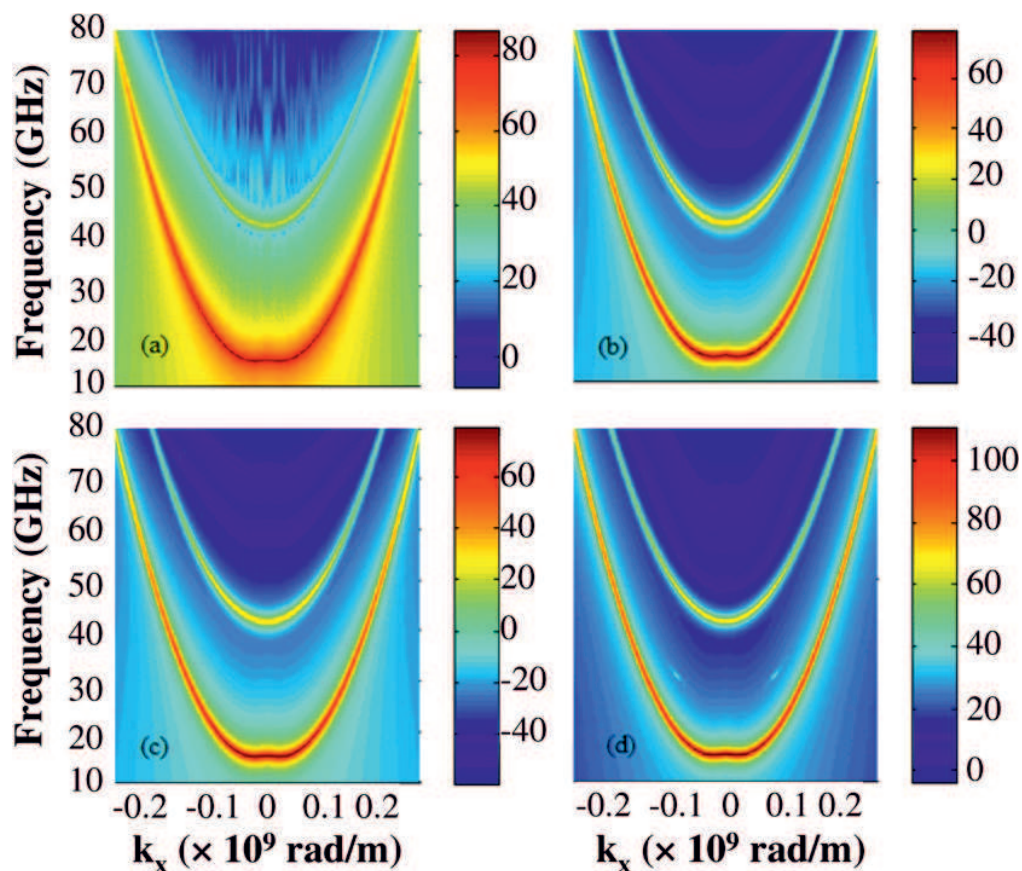


Figure 4.1.: Dispersion along a  $5 \mu\text{m}$  long and  $30 \text{ nm}$  wide permalloy waveguide with thickness =  $10 \text{ nm}$ . Bias field  $\mu_0 H_{\text{bias}} = 0.05 \text{ T}$  is applied along the length of the waveguide. The dispersion in (a) uses a rectangular window; (b) introduces a Hanning window; (c) adds zero padding and (d) uses a sinc excitation signal as opposed to a Gaussian excitation signal used in (a)-(c). Source: Ref. 262.

For a propagating wave  $\tilde{X}_0$  may be ignored as it represents the amplitude of a wave with no frequency (or no wavevector depending upon the dimension used for the Fourier expansion). Ideally  $\tilde{X}_0$  should be zero for a propagating wave, but often, in the case of a DFT, it has a finite value due to the lack of resolving power and aliasing. Moreover, the initial magnetization distribution of a magnetic medium may contain some demagnetized regions. High bias fields may be used to minimize these regions. Furthermore, for the purpose of dispersion analysis, the initial magnetization state should be subtracted from the entire time domain response. This subtraction makes it easier to visualize the propagation of spin waves but it will not affect the resultant dispersion curves.

Spectral leakage<sup>263</sup> is another issue associated with DFT, which needs to be taken care of. If power is being delivered at a certain frequency (and wavevector) and that frequency

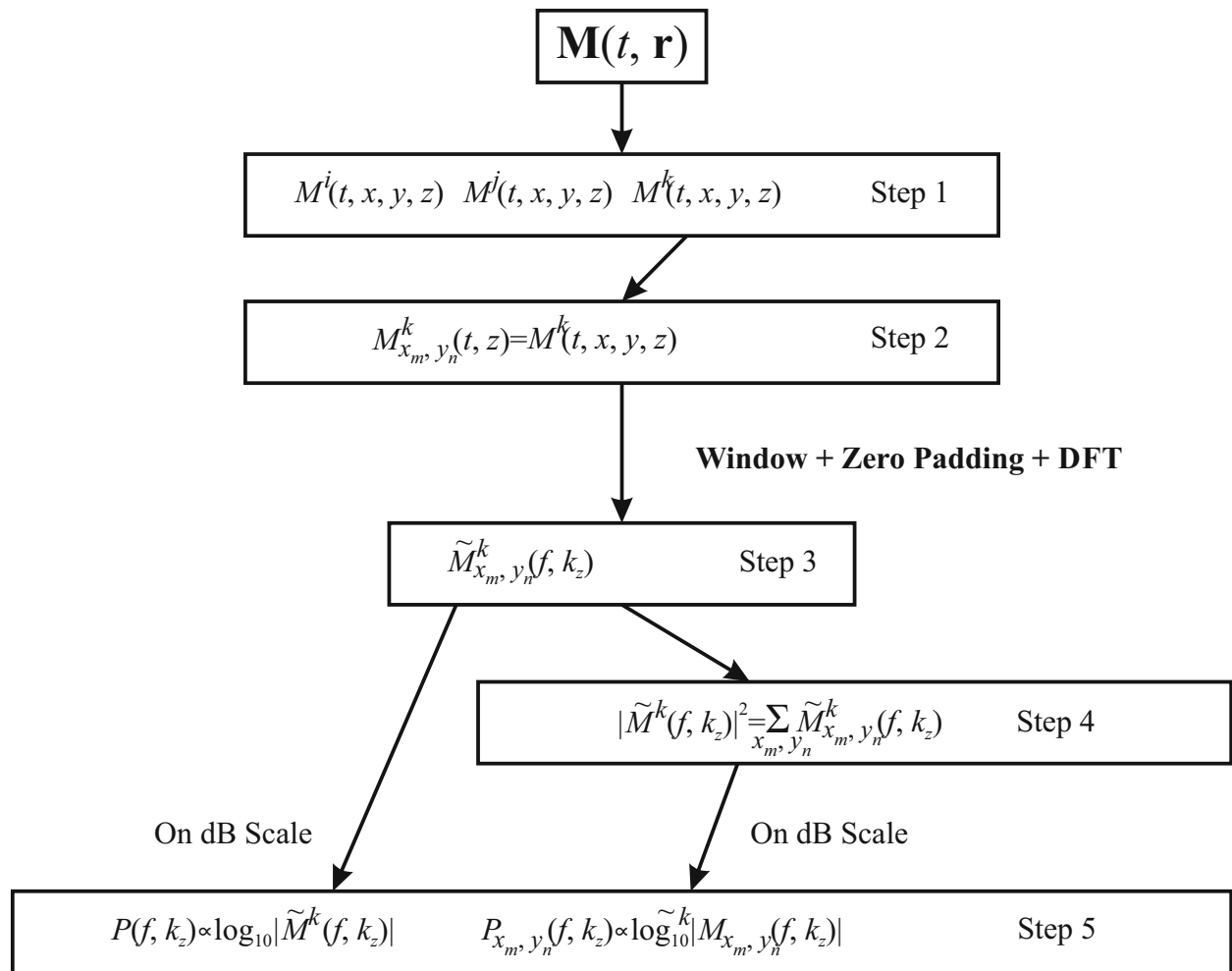


Figure 4.2.: Representation of steps involved in obtaining the dispersion curve for SWs in given magnetic objects. Source: Ref. 262.

(or wavevector) value is missing on the DFT output scale, that power is represented by amplitudes over the entire spectrum. These amplitudes are proportional to a sinc function,  $\text{sinc}(Dn)$  whose parameter  $Dn$  is the difference in number of cycles in time (or space) domain and number of sampling points (in the same dimension). The effect of spectral leakage becomes especially evident when power is represented on a proportional decibel scale. This can be controlled using a window function. Apart from controlling spectral leakage, most window functions help in mitigating aliasing. A 2D window function is needed for a 2D DFT. Two 1D window functions (one for each dimension) are multiplied for this purpose.

A common side effect of using a window function is the broadening of the central peak. Several window functions were compared based on this criterion. A  $5 \mu\text{m}$  long 1D Py

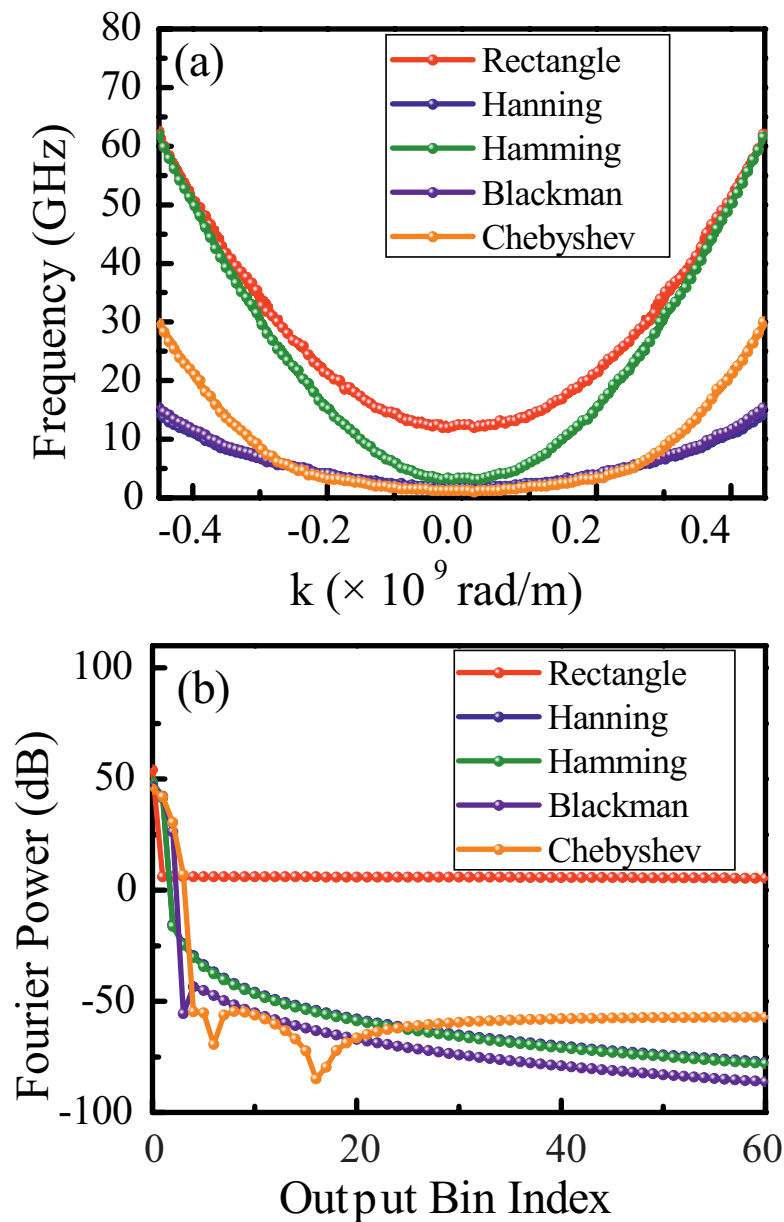


Figure 4.3.: (a) Comparison of mode widths for some window functions. A loss of power of 100 dB for a given value of wavevector was considered as mode cut-off limit. (b) Form of some window functions in frequency domain. As designed, the Chebyshev window maintains a main lobe to side lobe difference of 100 dB here. This is why a very high cut-off value of 100 dB is used in (a). This high cut-off value has led to high numerical mode widths. With good colour contrast visually discernable widths are much lower. Source: Ref. 262.

nanowire with a square cross section of side 9 nm was used for this purpose. Figure 4.3 (a) shows a plot of this width in frequency domain as a function of the wavevector for a few of these window functions. Another way of comparison between window functions is to

compare the difference between the main lobe and side lobes as a function of their position, as shown in Fig. 4.3 (b). For the Chebyshev window this difference can be better controlled. However, when this window is used, a higher difference results in further broadening of the central lobe. This broadening is especially pronounced for a low resolving power. Also, a higher assigned difference in frequency (or wavevector) domain causes a spike at both ends of this window.<sup>264</sup> This should not be a problem if the values of magnetization component under consideration at the beginning and end of simulation have near zero values. Hence, the Chebyshev window is found to be very useful when the numbers of sampling points in space and time domains are high and the duration of simulation has allowed damping to decrease the considered magnetization component to zero.

Due to the nature of DFT, amplitudes beyond the Nyquist frequency are represented at false frequency values. One of the ways these amplitudes can be identified is by sampling at different rates and checking whether they have changed their positions on the axis. Another way to avoid this problem is to ensure that the excitation signal does not supply any power beyond a certain frequency (which is lower than the Nyquist frequency). This can be done by using a signal which varies as a sinc function in both space and time domains (as Fourier transform of a sinc is a rectangle function). In the case of a magnonic crystal (e.g. a 2D array of dots), the sinc signal in space acts upon regions of finite and zero saturation magnetization. A sinc signal should still be considered if the effect of aliasing in the wavevector domain is too pronounced (for example, due to a low number of sampling points in space). A localized excitation signal may be used otherwise. This use can also be mandated by problem design. The resultant aliasing can then be controlled by sampling the magnetization at different spatial frequencies and identifying the amplitudes, which have moved on the wavevector axis.

Data sampled over a finite interval of space or time effectively uses a rectangular window function. This causes a drop in power from one frequency (or wavevector) value to the next. This is termed as scalloping loss. This loss can be reduced by the use of a non-rectangular window. For example, the scalloping loss, from lobe centre to half-way down the lobe centre, for a Hanning window is 1.45 dB, while that for a rectangular window is 4 dB. Scalloping loss can be further reduced by using zero padding<sup>263</sup> which effectively increases the number of

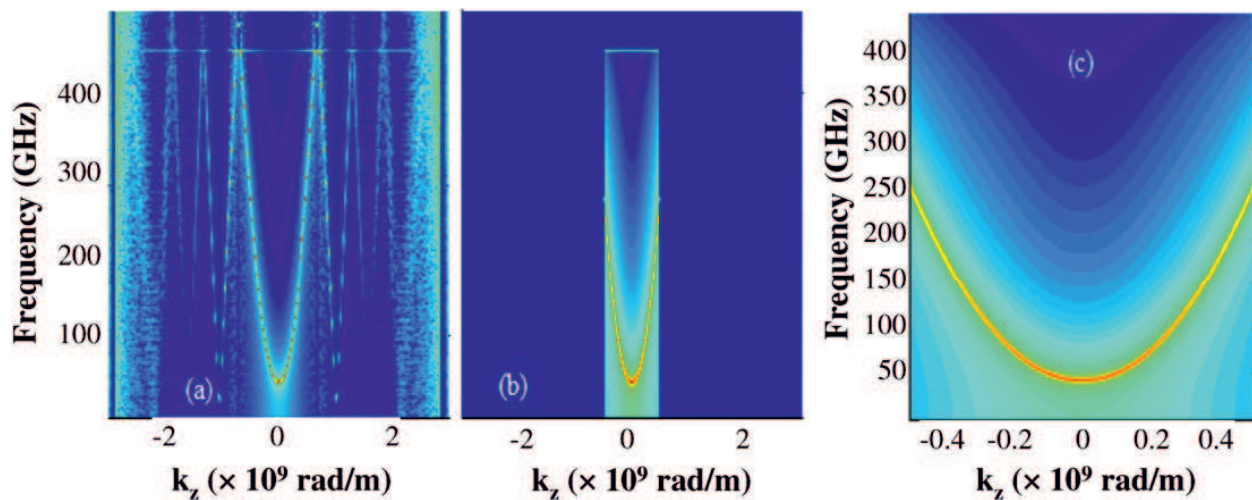


Figure 4.4.: Dispersion in a 1D nanowire of square cross section of side 9 nm with bias field,  $\mu_0 H_{\text{bias}} = 1.01$  T: (a)  $k_{\text{cut}} = 3$  rad/nm, (b)  $k_{\text{cut}} = 0.5$  rad/nm and (c) ‘powered’ region of dispersion. A linear colour map is used to represent power from 400 to -200 dB. Source: Ref. 262.

output targets (or ‘bins’) on the frequency (or wavevector) axis. Zero padding can also take advantage of some fast Fourier transform (FFT) algorithms<sup>261,265</sup> by ensuring that the length of data is an integral power of a prime number for delivering better computational speed. The window function is applied before zero padding because doing the reverse gives incorrect result as a part of window function would be multiplied by padded zeros. Zero padding does not improve the resolving power in the sense that the width of the mode remains the same on the frequency or wavevector axis. It also consumes memory. Therefore, it may be preferable to wait till the magnetization values are damped naturally to zero, rather than to artificially pad the data with zeroes, as waiting would also increase the resolving power in the frequency domain without consuming any extra memory which is not already required for zero padding.

Figure 4.4 shows the dispersion of SWs in a 5  $\mu\text{m}$  long 1D nanowire with a square cross section of edge 9 nm. Excitation signal is proportional to  $\sin(2\pi f_{\text{cut}} t') / (2\pi f_{\text{cut}} t')$ . Here  $t'$  represents time and  $f_{\text{cut}}$  is the parametric frequency of the signal, beyond which it carries no power. A similar cut-off value, say  $k_{\text{cut}}$ , can be set in the wavevector domain by making the signal proportional to  $\sin(2\pi k_{\text{cut}} x) / (2\pi k_{\text{cut}} x)$ .  $f_{\text{cut}}$  and  $k_{\text{cut}}$  cannot be more than the Nyquist frequency (or wavevector) values in their respective domains. For the purpose of simulation, material parameters of Py were used along with a cell size of 1 nm. Figure 4.4 (a) shows the dispersion when a signal with  $f_{\text{cut}} = 450$  GHz and  $k_{\text{cut}} = 3$  rad/nm was

used. Figure 4.4 (b) was produced with  $k_{\text{cut}} = 0.5$  rad/nm. A sudden drop in power beyond the cut-off values may be noted. Figure 4.4 (c) shows this ‘powered’ region of dispersion, which has a much better clarity and sharper width as opposed to what is observed in Fig. 4.4 (a).

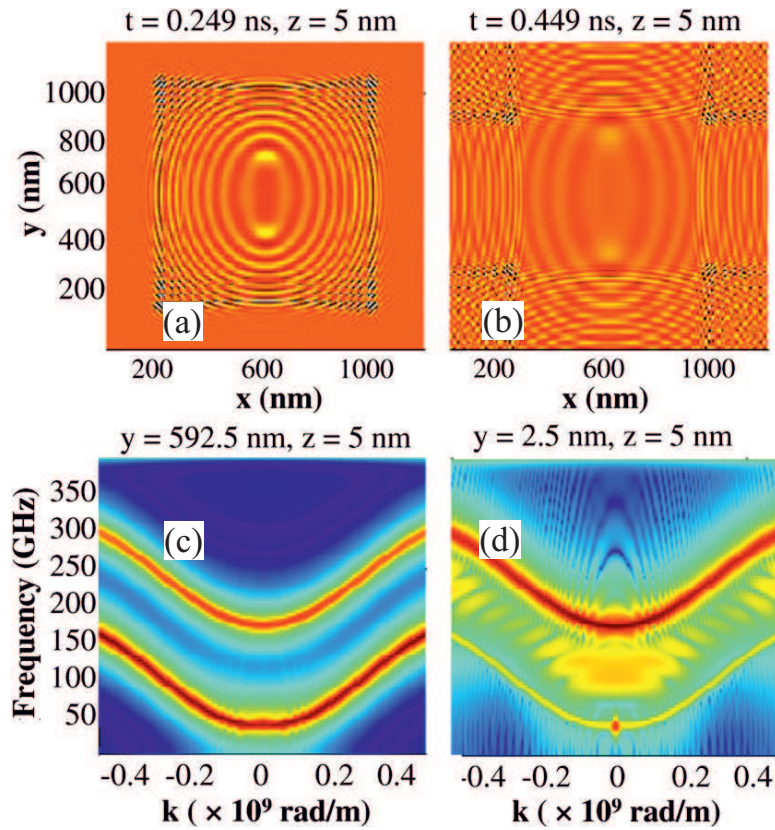


Figure 4.5.: Spin wave propagation in a confined Py thin film element of dimensions  $1.2 \mu\text{m} \times 1.2 \mu\text{m} \times 10$  nm at (a)  $t = 249$  ps and (b)  $t = 449$  ps for  $\mu_0 H_{\text{bias}} = 1.01$  T applied along the horizontal edge of the Py element. Dispersion curves (c) along the horizontal edge ( $y = 2.5$  nm) and (d) at the centre ( $y = 592.5$  nm) of the Py element. Source: Ref. 262.

Figures 4.5 (a) and (b) show the snapshots of the SWs with time in a confined Py thin film element of dimensions  $1.2 \mu\text{m} \times 1.2 \mu\text{m} \times 10$  nm. A bias field  $\mu_0 H_{\text{bias}} = 1.01$  T was applied parallel to the horizontal edge of the element to saturate the magnetization along the direction. Figures 4.5 (c) and (d), respectively, show the dispersion of SWs along the centre ( $y = 592.5$  nm) and along the edge ( $y = 2.5$  nm) of this element. The dynamics is excited by a sinc signal in the time domain, which is spatially localized at the centre of the element so that the SWs can propagate uniformly within the  $x - y$  plane. Two prominent dispersion

curves are observed in the former case, while a single curve is prominent in the latter. The lowest branch corresponds to the uniform magnetization dynamics ( $n = 0$ ) across the width of the magnetic element while the upper one corresponds to the quantization ( $n = 1$  or half-wavelength) across the width of the element. Due to the dynamic boundary conditions<sup>255</sup> the lowest branch is barely excited when we consider the direction along the horizontal edge of the element as one can see from Fig. 4.5 (d). The spin wave wave-front takes an elliptical shape due to the dependence of group velocity on the angle between wavevector and the direction of static magnetization (bias magnetic field).

Propagating SWs in continuous magnetic media show continuous dispersion of frequency as a function of wavevector. Formation of periodic modulation of the magnetic medium results in opening of band gaps at the Brillouin zone (BZ) boundary. Magnetic antidot lattices serve the purpose due to the creation of discontinuity at the magnetic material and air interface or at a different magnetic material filling the antidots.<sup>55,56,105,242,266,267</sup> In the following, we apply the described numerical techniques to calculate the dispersion curves of magnonic crystals made up of 1D and 2D arrangements of magnetic antidots in permalloy thin films. Cuboidal cells of edge 3 nm are used during the simulation for magnonic crystals examined in this chapter. Figures 4.6 (a) and (b) show the static magnetic configurations of a 1D array of square antidots with edge and separation of 12 nm carved into a permalloy strip with width = 24 nm, length = 2.4  $\mu\text{m}$  and thickness = 3 nm. A bias magnetic field ( $\mu_0 H_{\text{bias}}$ ) of 1.01 T was applied (a) along the length and (b) across the width of the sample so that the dispersions of SWs in the backward volume magnetostatic spin-wave (BV) configuration<sup>268</sup> and magnetostatic surface wave or Damon–Eshbach (DE) configuration<sup>269</sup> are obtained. Figures 4.6 (c) through (d) show the computed dispersion curves of SWs with wavevector for this sample. The confinement along the width of the permalloy strip, on which the square antidots are imprinted, will cause a number of symmetric and anti-symmetric modes for all allowed values of the wavevectors. The spatial modulation of magnetic parameters due to the introduction of the square antidots introduces a band spectrum and we investigate the effect of that on the symmetric and anti-symmetric modes in the resultant dispersion curves.

In Fig. 4.6 (c), we show the excitation of only the symmetric modes in the 1D array of antidots, while in Fig. 4.6 (d) both symmetric and anti-symmetric modes are excited

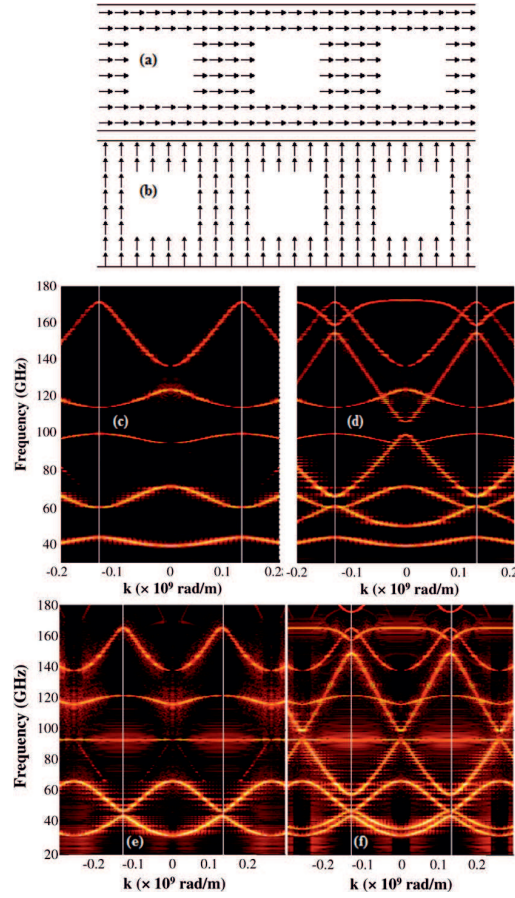


Figure 4.6.: Static magnetic configurations (in-plane) of the central portion of the simulated sample with the bias field,  $\mu_0 H_{\text{bias}} = 1.01$  T, applied (a) along the length and (b) across the width of the sample. The sample is a permalloy strip with width = 24 nm, length = 2.4  $\mu\text{m}$ , thickness = 3 nm and with 1D array of square antidots carved in it. The antidots are square in shape and have both width and separation of 12 nm. Simulation of SW dispersion of (b) symmetric mode only and (c) both symmetric and anti-symmetric modes for the BV configuration. (e) Symmetric only and (f) both symmetric and anti-symmetric modes in DE configuration are also shown. The vertical white lines mark the boundaries of the BZ which has a total width of 0.2618 rad/nm. Source: Ref. 262.

in the same sample. The anti-symmetric modes can be excited if the applied signal is anti-symmetric across the width of the crystal. The anti-symmetric modes do not interact with symmetric modes<sup>270,271</sup> and four new branches are created in the observed frequency range of dispersion curves. We have further calculated the dispersion of a bi-component medium to demonstrate the effects of variation of the periodic potential in the magnonic medium as a result of the inclusion of a second ferromagnetic medium within the antidot regions. Figure 4.7 (a) and (b) show the static magnetic configurations of a bi-component

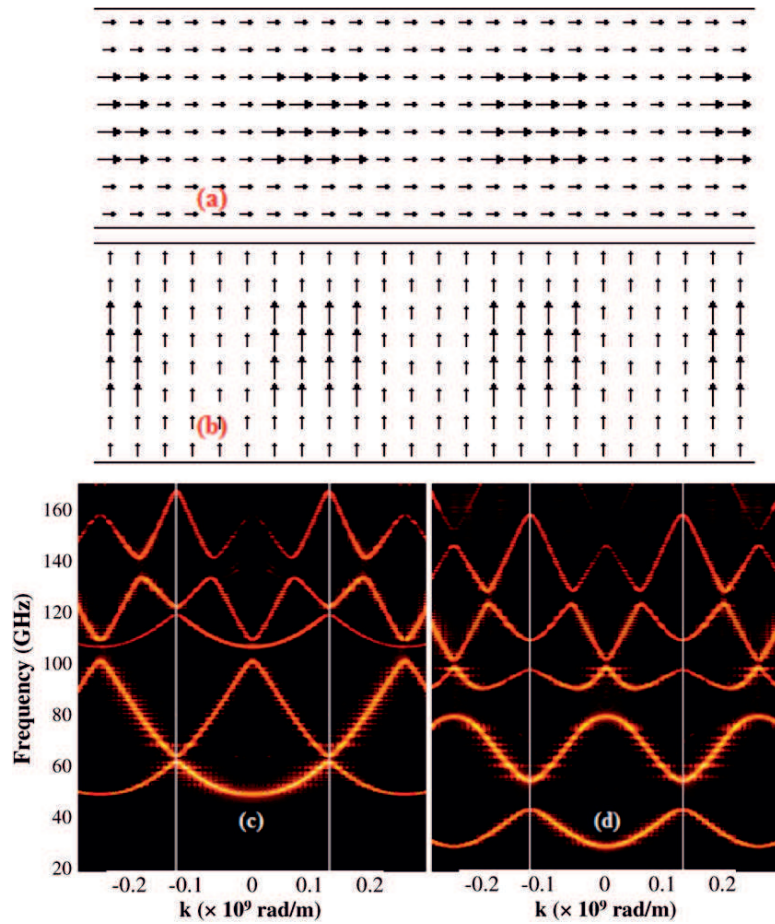


Figure 4.7.: Static magnetic configurations (in-plane) of the central portion of the simulated sample with the bias field,  $\mu_0 H_{\text{bias}} = 1.01$  T, applied (a) along the length and (b) across the width of the sample. The sample is a bi-component medium with 1D array of square-shaped Co inclusions in a permalloy strip with width = 24 nm, length =  $2.4 \mu\text{m}$  and thickness = 3 nm. The sides of Co squares are 12 nm and the edge-to-edge separations between the two squares is 12 nm. Simulated dispersion of symmetric modes in the above samples with the bias field applied (c) along the length and (d) across the width of the sample. The vertical white lines mark the boundaries of the BZ which has a total width of 0.2618 rad/nm. Source: Ref. 262.

medium with 1D array of square-shaped Co ( $K = 520 \times 10^3 \text{ J/m}^3$ ,  $M_s = 1400 \times 10^3 \text{ A/m}$ ,  $A = 30 \times 10^{-12} \text{ J/m}$ ,  $|\bar{\gamma}| = 2.21 \times 10^5 \text{ rad s}^{-1} \text{ T}^{-1}$ ) inclusions in a permalloy strip with width = 24 nm, length =  $2.4 \mu\text{m}$  and thickness = 3 nm. The edge and separation of Co squares are 12 nm. The static magnetic field  $\mu_0 H_{\text{bias}} = 1.01$  T is applied (a) along the length and (b) across the width of the simulated samples. Figures 4.7 (c) and (d) show the dispersion of symmetric modes in this medium for the bias field geometries of (a) and (b), respectively.

The band gaps in Fig. 4.7 (c) are considerably reduced as compared with those in Fig. 4.6 (c) due to the reduction in the difference between the values of the magnetic parameters in the bi-component medium as compared with the unfilled antidots. Similarly, with the exception of first band gap the others are significantly smaller in Fig. 4.7 (d) when compared with the modes in Fig. 4.6 (e). For the long permalloy strip the shape anisotropy is along the length of the sample and hence the application of bias field across the width causes a reduction in the effective field and consequently a downward shift in the overall frequencies in the dispersion curves is observed. In the DE (Fig. 4.7 (d)) geometry the curvature of dispersion (and the corresponding group velocities) and band gaps are significantly different from that in the BV geometry (Fig. 4.7 (c)) due to the difference in the initial magnetization state as a result of the competition between the Zeeman, demagnetization and magnetocrystalline anisotropy energies in two different materials in the bi-component magnonic crystal.

We now extend our calculation of dispersion curves to three rows of 1D arrays of antidots (quasi-2D antidot arrays). The introduction of quasi-periodicity across the width of the magnonic crystal and the dipolar interactions between the different rows of antidot arrays cause significant modifications in the dispersion curves. In Fig. 4.8, we show the dispersion curves of the quasi-2D antidot arrays with length = 2.4  $\mu\text{m}$ , width = 72 nm and thickness = 3 nm. The bias field  $\mu_0 H_{\text{bias}} = 1.01$  T was applied along the (a) length and (b) across the width of the magnonic crystal. A comparison of Figs. 4.6 (c) and (e) with Figs. 4.8(c) and (d) reveals that the latter show band intersection and very rich dispersion patterns. The two lowest frequency branches of dispersion in Fig. 4.8 (c) have the same curvatures, signifying the same group velocity but different phase velocities. However, the group velocities of the two lowest dispersion branches in Fig. 4.8 (d) are different. The higher frequency branch also has a lower spectral power.

Figures. 4.9 (b) and (c) show the spatial distribution of the power and phase of magnetization for specific frequency values on different branches of the dispersion curves for the 1D array of antidots as shown by the white dotted lines in Fig. 4.9 (a). The power and phase distribution information are obtained by fixing one of the spatial co-ordinates in  $M^k(t, x, y, z)$  and performing a DFT with respect to time domain. The bias field was applied along the length of the 1D antidot array. The mode corresponding to  $f = 39.99$

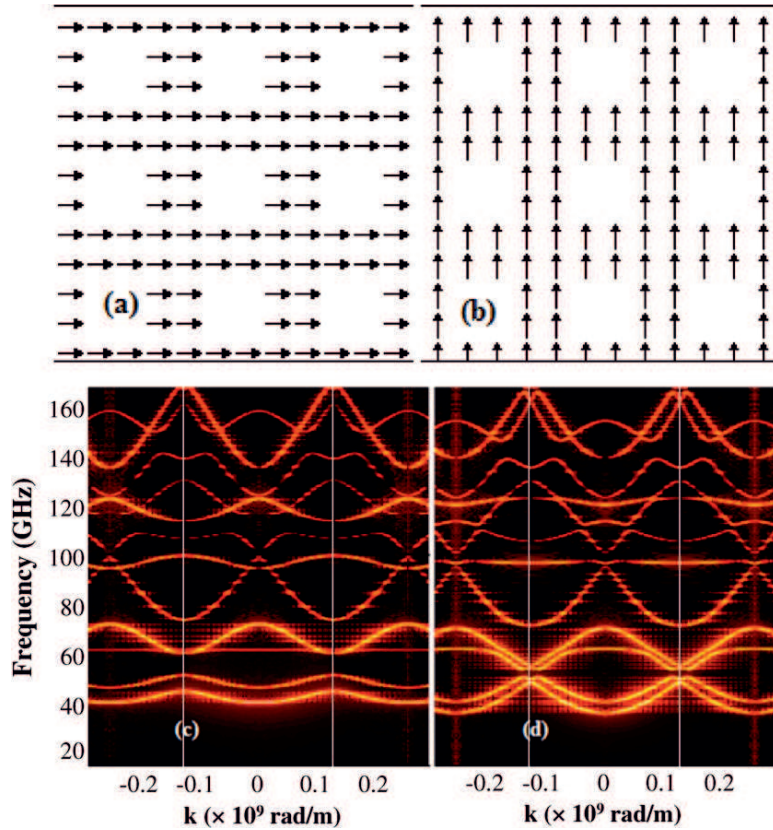


Figure 4.8.: Static magnetic configurations (in-plane) of the central portion of the simulated sample with the bias field,  $\mu_0 H_{\text{bias}} = 1.01$  T, applied (a) along the length and (b) across the width of the sample. The sample is a permalloy strip with width =  $72$  nm, length =  $2.4$   $\mu\text{m}$ , thickness =  $3$  nm and with three rows of 1D array of square antidots imprinted in it. The antidots are square in shape and have both width and separation of  $12$  nm. Simulated dispersion of symmetric modes in the above samples with the bias field applied (c) along the length and (d) across the width of the sample. Source: Ref. 262.

GHz (Fig. 4.9 (b)) belongs to the lowest band (band index  $n = 1$ ) and propagates with uniform phase along the length of the array. The mode at  $f = 60.84$  GHz (Fig. 4.9 (c)) belongs to the band with  $n = 2$  and propagates with regions around alternating antidots oscillating out-of-phase. Figure 4.10 shows the spatial distribution of power and phase of the quasi-2D array of antidots. The four branches of dispersion are highlighted in Fig. 4.10 (a). The power and phase distributions of the lowest ( $n = 1$ ) and highest branches ( $n = 4$ ) of the quasi-2D array are similar to the  $n = 1$  and  $n = 2$  bands, respectively, for the 1D case, as shown in Figs. 4.10 (b) and (e). The power and phase distributions for the two middle branches ( $n = 2$  and  $3$ ) are shown near the BZ boundary where dispersion becomes flat

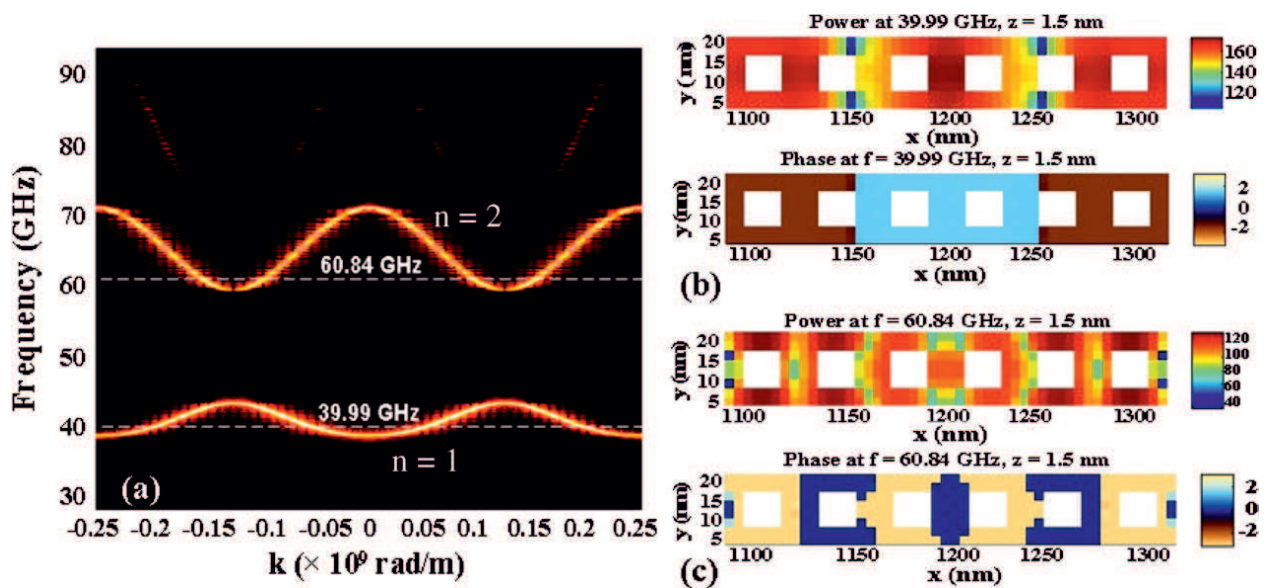


Figure 4.9.: (a) Selected part of the dispersion image, as shown in Fig. 4.6 (c), showing the frequencies at which the spatial distribution of power and phase of SWs is shown. The power and phase corresponding to modes at (b)  $f = 39.99$  GHz and (c)  $f = 60.84$  GHz. The excitation was done at the centre of the array ( $x = 1200$  nm) and only a small part of the array is shown for visual clarity. A bias field of 1.01 T is applied along the length of the array. Source: Ref. 262.

and the group velocity close to zero. The power and amplitude distributions are distinctly different from the propagating modes, as shown in Figs. 4.10 (b) and (e).

### 4.3. Conclusion

In this chapter, we have reported a technique, which can be employed to obtain dispersion of SWs in different kinds of magnetic micro- and nanostructures with high numerical contrast and clarity. The use of DFT windows and sinc functions to control the spectral leakage and aliasing is highlighted. The examples of dispersion calculations for magnetic nanostripes, magnetic nanowires and confined thin film elements are shown to validate the method. We then employed the described technique to calculate the dispersion curves on 1D and quasi-2D magnonic crystals based upon magnetic antidot arrays in BV and DE configurations. The effect of inclusion of a second magnetic component in 1D arrays of antidot lattice on the dispersion curves is also demonstrated. The dispersion curves obtained using this technique can be used in conjunction with analytical modelling to form guiding principles

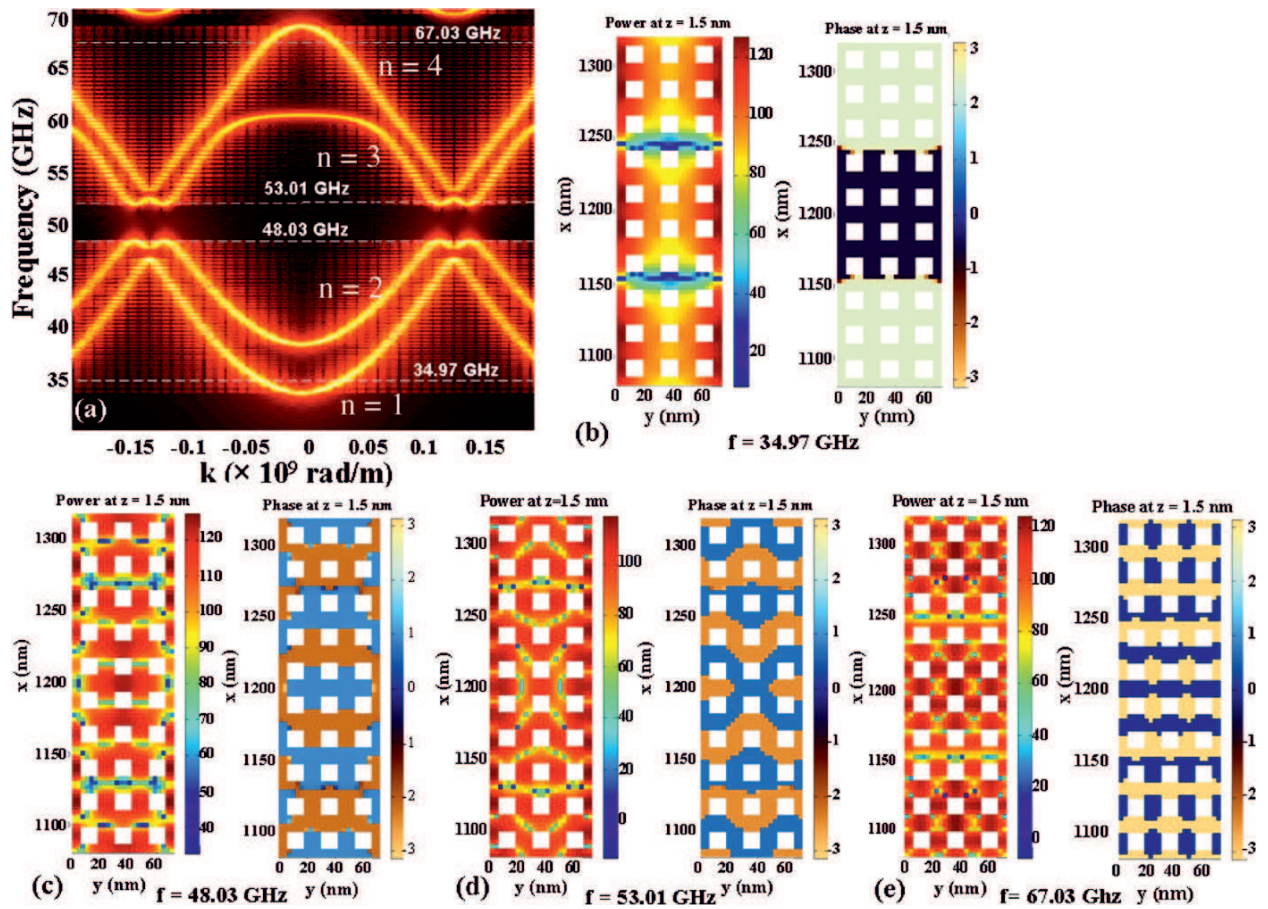


Figure 4.10.: (a) Selected part of the dispersion image, as shown in Fig. 4.8 (d), showing the frequencies at which the spatial distribution of power and phase of SWs is shown. The power and phase corresponding to modes at (b)  $f = 34.97$  GHz, (c)  $f = 48.03$  GHz, (d)  $f = 53.01$  GHz and (e)  $f = 67.03$  GHz. The excitation was done at the centre of the array ( $x = 1200$  nm) and only a small part of the array is shown for visual clarity. A bias field of 1.01 T is applied along the width of the array. Source: Ref. 262.

in investigating and controlling the details of magnonic band structures in different kinds of magnonic crystals.

# 5. Free and Pinned Boundary Condition in a Magnonic Antidot Waveguide

\*In this chapter we focus on the boundary conditions imposed on the dynamic components of the magnetization vector and their effect on the spectrum of SWs in magnonic waveguides. These boundary conditions are additional to the electromagnetic ones, which describe the degree of freedom of the magnetization vector at the edges of the ferromagnetic material. The effect of the boundary conditions on the spectrum of SWs in uniform thin films has been investigated broadly.<sup>215,272,273</sup> However, no such research has been conducted so far in antidot lattices, in which the interfaces with air play an important role in the formation of magnonic bands.<sup>274,275</sup> Only free boundary conditions are assumed in the vast majority of papers dealing with periodic waveguides. Thus, there is a gap in the research, which we attempt to fill in with this study.

In this chapter we study the magnonic band structure in waveguides, a basic element of any magnonic device.<sup>93,95</sup> Waveguides for exchange SWs have been recently investigated theoretically with the use of micromagnetic simulations;<sup>84,259,267</sup> periodic waveguides have been demonstrated to have filter properties due to the folding effect and the opening of magnonic gaps in the SW spectrum.<sup>5,94</sup> Here we investigate a periodically modulated waveguide with a series of antidots in the centre. Aware of the fact that the periodicity of the waveguide can be realized in many different ways—by width or shape corrugation, or by applying a specific magnetic field<sup>5,94,267</sup> — we are confident that the fundamental features of this quasi-1D pe-

---

\*This chapter is based upon Kłos *et al.* *Phys. Rev. B* **86**, 184433 (2012).

riodic system are conserved and the conclusions drawn for the model considered will be of general nature.

We show that a magnetization pinning introduced at the edges of the waveguide can significantly change its SW spectrum. To cross-check our results we perform calculations based on different methods: micromagnetic simulations and the plane wave method (PWM). These techniques have already been successfully used for the interpretation of experimental data obtained for systems of various geometry in the formulation used here.

We show that the pinning is intrinsic for PWM at the interface of magnetic/nonmagnetic material. For micromagnetic calculations the magnetic moments are not forced to be pinned by default. We introduce pinning by placing on the interface a thin layer for which the dynamics of magnetization is frozen (with the amplitude of precession set to zero).

The chapter is organized as follows. In Sec. 5.1 we describe the structure under investigation and the calculation methods used. In Sec. 5.2 we explain the effects that the boundary conditions imposed on the dynamic magnetization components at the edges of the ferromagnetic material have on the magnonic spectrum. Our results are summarized in the closing Sec. 5.3.

## 5.1. Waveguide Structure and the Calculation Methods

The magnonic waveguide under consideration is shown in Fig. 5.1. It has the form of a thin and infinitely long permalloy stripe with a single row of square holes disposed periodically along the central line. A bias magnetic field is applied along the stripe and assumed to be strong enough ( $H_{\text{bias}} = 1$  T) to saturate the sample. The material parameters of Py were used in all calculations.

We use three methods of calculating the dispersion of SWs in the permalloy MAW: the finite difference method, the finite element method and the PWM, with OOMMF,<sup>250</sup> Nmag<sup>276</sup> and a home-developed Fortran code, respectively.

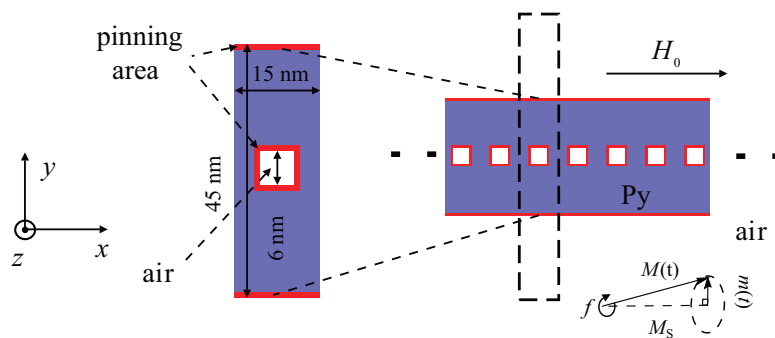


Figure 5.1.: Magnonic antidot waveguide under investigation: a 3 nm thick and 45 nm wide infinite Py stripe with a periodic series of 6 nm  $\times$  6 nm square antidots disposed centrally along the  $x$ -axis with a period of  $a = 15$  nm. Bias magnetic field  $\mu_0 H_{\text{bias}} = 1.01$  T is oriented along the  $x$ -axis. The 1.5 nm wide red lines at the Py/air interfaces mark the regions in which pinning is assumed in the OOMMF calculations. The dashed box shows the supercell size used in PWM calculations. Source: Ref. 213.

### 5.1.1. Micromagnetic Simulation

The micromagnetic simulations (OOMMF, Nmag) are performed in two steps. The magnetic ground state is obtained first. We let the magnetization evolve in the presence of damping to reach the static equilibrium orientation. In the next step, with damping neglected ( $\alpha = 0$ ), a small pulse of magnetic field was applied as given by Eq. (5.1) with a small amplitude (which guarantees the linear regime of spin dynamics). After recording the magnetization in each mesh point for each time step, Fourier transformation is performed in the time and space domains to obtain the SW dispersion, i.e., the wave-vector dependence of the SW frequency.<sup>260,262</sup>

The excitation signal used to study the dynamics is of the form

$$h_z(t, x, y) = h_z^0 \text{sinc}\{2\pi f_{\text{cut}}(t - t_0)\} \times \text{sinc}\left\{k_{\text{cut}}\left(x - \frac{1}{2}x_{\text{max}}\right)\right\} \times \sum_{n=1}^N \sin\left(n\pi \frac{y}{y_{\text{max}}}\right), \quad (5.1)$$

where the sinc function is taken in the form  $\text{sinc}(\theta) = \sin(\theta)/\theta$ . The strength of the signal is defined by  $\mu_0 h_z^0 = 5$  mT. The parameter  $f_{\text{cut}} = 490$  GHz sets the upper limit of frequencies of SWs excited by the sinc like pulse. An offset  $t_0 = 50$  ps was given to avoid the high spikes close to the  $f_{\text{cut}}$  in the frequency domain of the signal. The  $k_{\text{cut}}$  is a wave number cut-off defined later. The symbols  $x_{\text{max}} = 3 \mu\text{m}$  and  $y_{\text{max}} = 15$  nm denote the sizes of the sample.

The summation in Eq. (5.1) was done for  $N = 30$  subdivisions.

The benefits for using such a signal and the procedure to obtain the desired dispersion relation are described in Sec. 4.2. In the case of an antidot lattice the effect of convolution of the periodic array of holes will be observed in the wave-vector domain. A wavevector cut-off  $k_{\text{cut}}$ , which is an odd multiple of half the Brillouin zone (BZ) length (here  $3\pi/a$ ), may be used to mitigate this effect. Also, in order to generate both symmetric and antisymmetric wave fronts a suitable dependence (which, here, is a sum of symmetric and antisymmetric excitations along the width) on  $y$  has been applied to the signal.

The OOMMF simulations are performed with 1D periodic boundary conditions<sup>243</sup> applied along the  $x$ - axis. A 1.5 nm mesh is used in these simulations. The correctness of the assumed discretization was verified by comparing the results with those of simulations using a 0.5 nm mesh.

The micromagnetic simulations do not assume by default any torque acting on the external interfaces (numerical calculations are limited to the magnetic medium only). Therefore, the spins are precessing freely on the systems boundaries with dipolar effects taken fully into account.

We can force the pinning in all mesh cells located on the interfaces between magnetic and non-magnetic materials (see the red-coloured pinning area in Fig. 5.1). It can be done by freezing the magnetization dynamics  $\frac{\partial}{\partial t}\mathbf{M}(\mathbf{r}, t) = 0$  with initial conditions  $M_z(\mathbf{r}, t = 0) = 0$  and  $M_y(r, t = 0) = 0$  at the beginning of the second stage of calculation when the system managed to reach the ground state. From the LLG equation, it follows that the initial condition for  $z$  and  $y$  components of magnetization will be sustained, if the conditions  $M_y(r, t = 0) = 0$  and  $M_z(r, t = 0) = 0$  are set in the pinned layer. We checked that for the strong external field that we used ( $\mu_0 H_{\text{bias}} = 1.01$  T) the magnetization in the ground state is uniform and parallel to the direction of  $\mathbf{H}_{\text{bias}}$  even in the vicinity of the interfaces.

Because of the use of the finite difference method in OOMMF simulations, space is discretized into small cuboids. Nmag uses the finite element method, in which, in contrast, the modelled object is discretized on a tetrahedral mesh. In general, this allows for better modelling of arbitrarily shaped objects, but for the considered antidot waveguide, this does not provide an advantage because our simulating object consists basically of orthogonal

walls. For the mesh creation, we use the open source generator “NETGEN”. When creating the unstructured mesh, care must be taken in providing the software with a proper value of the maximum-mesh size parameter. Only when this value is small enough is it possible to calculate the exchange and magnetostatic fields with reasonable accuracy. Unfortunately, as the maximum mesh- size parameter decreases, the number of tetrahedral elements increases, making the computing time and memory demands increase as well. One way to partially overcome this problem is to use an adaptive mesh with the smaller cell sizes in the vicinity of antidot edges. We must select a value below the exchange length, which in the case of permalloy is 5.1 nm. Therefore, we selected a maximum size of 4.5 nm for the edge length of all tetrahedra to achieve accurate results. However, the average edge length was about 2.5 nm with standard deviation equal to 0.6 nm. It was decided not to use periodic boundary conditions in Nmag simulations but instead use a finite segment of this waveguide of length 1.8 micrometer, containing 120 repetitions of the unit cell. The waveguide is surrounded by non-magnetic material, which does not have to be discretized. This is because Nmag used a hybrid finite elements/boundary elements method to calculate the magnetostatic contribution.

The steps to obtain the dispersion relation are the same as in OOMMF. As a first step, a high value of the Gilbert damping parameter is chosen and the system is evolved under the external field to find the energy-minimizing configuration of the system. This state is used as the starting point during the second part. Now damping is neglected and the system is excited with a pulse containing a broad frequency range. Using the Fourier transform, the resonating values of  $(k, \omega)$  are obtained as local maxima. These values constitute the dispersion diagram.

### 5.1.2. Plane Wave Method for a Magnonic Antidot Waveguide

PWM has been discussed in some detail in Sec. 3.4. Here we revisit the method while elaborating its application in the case of a 1D MAW. In the PWM, periodic Bloch conditions are applied both along the MAW axis and in the direction perpendicular to this axis. An artificial periodicity in the  $y$  direction creates a periodic series of non-interacting copies of the original waveguide — this is the supercell approach.<sup>277</sup> We used the supercell marked

in Fig. 5.1 by dashed line. The assumed periods are 15 nm (antidot period) and 100 nm (artificial supercell) along the  $x$  and  $y$  axes, respectively.

The antidots and spacer areas were filled with artificial material characterized by a high value of volume anisotropy field and an extremely low value of magnetization saturation that squeezed the magnetization dynamics in this region (effect of the low magnetization saturation) and shifted the frequencies of spurious modes appearing in the results into a very high-frequency range (impact of the high volume anisotropy field). Note that according to the Landau-Lifshitz equation the increase of the effective field in the artificial material (as a result of big volume anisotropy) will also decrease the amplitudes of dynamical magnetization if one wants to keep the SW frequency constant. We have made sure that the assumed 65 nm waveguide spacing is sufficient to neglect the interactions between adjacent copies. We plotted the dispersion relation in the  $\Gamma - Y$  direction (i.e., for a propagation direction perpendicular to the waveguide's axis). The branches that we obtained were flat which confirmed the localization of SWs in the  $Y$  direction and the lack of crosstalks between adjacent copies of waveguides. We also checked the amplitude of SWs in the spacers separating waveguides, which occurred to be cancelled. The cancelling of spin dynamics in the air gaps (spacers and antidot areas) results in magnetization pinning at the interface with magnetic material. In order to simulate the system of planar geometry with partially pinned magnetization on the interfaces with non-magnetic material one can artificially change the in-plane sizes of the system from  $R$  to effective  $R_{\text{eff}}$  to achieve a non-zero value of dynamical magnetization when the position  $r$  coincides with  $R$ .<sup>215</sup> We used this procedure to perform PWM calculations in the dipolar-exchange regime for 2D antidot lattices.<sup>57</sup>

We are considering the magnetization dynamics without damping in the linear approximation only. We are assuming that the magnetization precesses around X-axis in a cone with small angle (as it is presented in Fig. 5.1). Under this assumption we can write:

$$\begin{aligned} M_x(\mathbf{r}) &\approx M_s, \\ M_y(\mathbf{r}, t) &= m_y(\mathbf{r})e^{i\omega t}, \\ M_z(\mathbf{r}, t) &= m_z(\mathbf{r})e^{i\omega t}. \end{aligned} \tag{5.2}$$

The exchange term can be expressed as:<sup>27</sup>

$$\mathbf{H}_{\text{exch}} = \nabla \lambda_{\text{ex}}^2 \nabla \mathbf{M}(\mathbf{r}, t), \quad (5.3)$$

which directly deviates from the Heisenberg model.<sup>278</sup>

To describe demagnetizing field for periodic slab of finite thickness we used the ideas proposed by Kaczér and Murtinová<sup>279</sup> and then developed in Ref. 280 where each component of (static  $\mathbf{H}_{\text{dem}}(\mathbf{r})$  and dynamic  $\mathbf{h}_{dm}(\mathbf{r}, t)$ ) demagnetizing field is depending, in general, on the spatial distribution of all component of magnetization. The components of the static and dynamic demagnetizing fields within the linear approximation taken into account are

$$H_{dm,x}(\mathbf{r}) = - \sum_{\mathbf{G}} M_s(\mathbf{G}) \left( \frac{G_x}{G} \right)^2 (1 - C(z, G)) e^{-i(\mathbf{G} \cdot \mathbf{r}_{\parallel})}, \quad (5.4)$$

$$h_{dm,z}(\mathbf{r}, t) = \sum_{\mathbf{G}} \left[ -m_z(\mathbf{G}) C(z, |\mathbf{G} + \mathbf{k}|) + i m_y(\mathbf{G}) \frac{|k_y + G_y|}{|\mathbf{G} + \mathbf{k}|} S(z, |\mathbf{G} + \mathbf{k}|) \right] e^{i\omega t} e^{-i((\mathbf{G} + \mathbf{k}) \cdot \mathbf{r}_{\parallel})}, \quad (5.5)$$

$$h_{dm,x}(\mathbf{r}, t) = \sum_{\mathbf{G}} \left[ -m_y(\mathbf{G}) \frac{(k_y + G_y)^2}{|\mathbf{G} + \mathbf{k}|^2} (1 - C(z, |\mathbf{G} + \mathbf{k}|)) + i m_z(\mathbf{G}) \frac{|k_y + G_y|}{|\mathbf{G} + \mathbf{k}|} S(z, |\mathbf{G} + \mathbf{k}|) \right] e^{i\omega t} e^{-i((\mathbf{G} + \mathbf{k}) \cdot \mathbf{r}_{\parallel})}, \quad (5.6)$$

where  $\mathbf{G} = [G_x, G_y]$  and  $\mathbf{r}_{\parallel} = [x, y]$  are 2D reciprocal lattice vector and position vector in real space. The symbols:  $M_s(\mathbf{G})$  and  $m_{\alpha}(\mathbf{G})$  denote the coefficient of Fourier expansion for magnetization saturation  $M_s(\mathbf{r}_{\parallel}) = \sum_{\mathbf{G}} \mathbf{M}(\mathbf{G}) e^{-i(\mathbf{G} \cdot \mathbf{r}_{\parallel})}$  and periodic part of Bloch functions:  $m_{\alpha}(\mathbf{r}_{\parallel}) = m_{\alpha}(\mathbf{G}) \sum_{\mathbf{G}} \mathbf{M}(\mathbf{G}) e^{-i((\mathbf{G} + \mathbf{k}) \cdot \mathbf{r}_{\parallel})}$ , where  $\alpha = y, z$  and  $\mathbf{k}$  is a wavevector. The functions  $C(z, \kappa)$  and  $S(z, \kappa)$  are defined as:

$$C(z, \kappa) = \frac{\sinh(z\kappa)}{\sinh(c\kappa) + \sinh(c\kappa)}, \quad (5.7)$$

$$S(z, \kappa) = \frac{\cosh(z\kappa)}{\sinh(c\kappa) + \sinh(c\kappa)}, \quad (5.8)$$

where  $2c$  is the thickness of MAW (in  $z$ -direction). The demagnetizing fields do not change a lot across the slab except the regions in the close vicinity of the external surfaces (note that the structure is uniform in  $z$ -direction). Therefore we assumed that all fields:  $\mathbf{H}_{\text{dem}}(\mathbf{r}_{\parallel})$

and  $\mathbf{h}_{dm}(\mathbf{r}_{\parallel}, t)$  are independent on  $z$ -coordinate by taking its values from the centre of the slab. This simplification allowed us to consider the system as 2D one.

In the linearisation procedure we took advantage from the assumption:  $m_{\alpha}(\mathbf{r}) \ll M_s$ ,  $\alpha = y, z$  and dropped all small terms with precession frequency higher than  $\omega$ . Then after applying the Fourier transformation we were able to convert the linearised differential equations for  $m_y(\mathbf{r}), m_z(\mathbf{r})$  into the set of algebraic equation in the form of eigenproblem with  $m_y(\mathbf{G}), m_z(\mathbf{G})$  as eigenvectors and  $\omega$  playing the role of eigenfrequency.

We checked that the sufficient convergence for the presented dispersion plots (Fig. 5.3) is achieved for  $11 \times 91$  plane waves propagating in  $x$  and  $y$  direction, respectively (described by different  $x$  and  $y$  components of reciprocal vectors  $\mathbf{G}$ ). The details of the PWM, its supercell formulation, and the application of this technique are available in the literature.<sup>51,57,277,280</sup>

## 5.2. The effect of pinning on the magnonic spectrum

Figure 5.2 (a) shows the magnonic band structure obtained in the OOMMF simulations. The SW spectrum is very rich, with a clear evidence of periodicity and folding effects. Three repetitions of the Brillouin zone (BZ), delimited by vertical solid lines, are considered. Free boundary conditions for the dynamic components of the magnetization vector (unpinned magnetization) at the edges of Py were used in these calculations. The lack of pinning is confirmed by the mods profiles (bottom of Fig. 5.2) computed with OOMMF (not shown) and Nmag where the non-zero values of  $|m_z|^2$  at the air/Py interfaces are observed. Very similar SW dispersion (Fig. 5.2 (b)) were obtained also in the Nmag simulations. Surprisingly, the results obtained by the PWM are different. The PWM spectra are shown in Fig. 5.3 (red dashed lines). The bands are seen to be shifted up in the frequency scale, and the modes seem less numerous.

In search of explanation of this discrepancy we calculated the profiles of the dynamic components of the magnetization vector in the PWM. The coloured maps in Fig. 5.3, bottom, represent the modulus  $|m_z|^2$  of the  $z$  component for a number of lowest-frequency modes; blue and red correspond to low and high values of  $|m_z|^2$ , respectively. In all the modes in question the magnetization is pinned at the Py/air interfaces (thin white lines). Therefore,

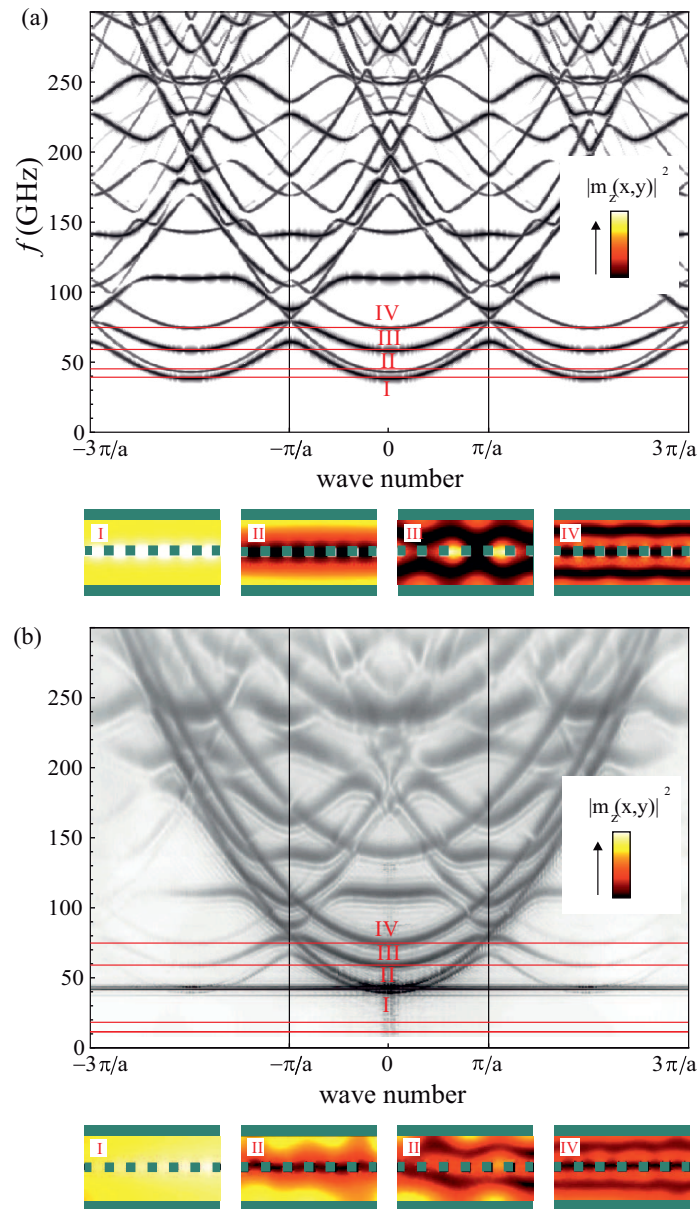


Figure 5.2.: Dispersion of SWs in the MAW presented in Fig. 5.1, as calculated with (a) OOMMF and (b) Nmag. The vertical lines delimit the first Brillouin zone. The magnetization is assumed to precess freely at the Py/air interface, i.e., unpinned magnetization. Bottom in (a) and (b): maps of  $|m_z(x,y)|^2$  for the different values of frequency (I to IV) calculated with (a) OOMMF and (b) Nmag. Note that each distribution of  $|m_z(x,y)|^2$  obtained by micromagnetic calculations contains contributions of the eigenmodes differing in the wave numbers. Source: Ref. 213.

we suspect that the main reason for the discrepancy between the results of PWM and the micromagnetic simulation are the different boundary conditions applied in these two methods.

Unfortunately, no extension of the PWM method has been developed yet to allow for unpinned magnetization at the interfaces with non-magnetic material. We can extend the micromagnetic simulations, though, imposing various boundary conditions on the dynamic components of the magnetization vector  $\mathbf{M}$ . The procedure described in the previous section allows one to achieve  $\mathbf{m} = 0$  (i.e., pinning of the magnetization  $\mathbf{M}$ ) at the interfaces with nonmagnetic material. Figure 5.3, top panel, shows the results of the OOMMF simulations (grey lines) and, superimposed, the PWM data. The agreement between the OOMMF and PWM results is satisfactory now, and the effect of the pinning on the magnonic spectrum of the MAW can be explained in detail.

The changes in the SW spectrum resulting from the introduction of pinning are relatively simple in uniform thin films. The main difference is the occurrence of an extra mode, uniform across the film thickness, in the case of unpinned surfaces; surface-localized modes (surface SWs) can occur, too.<sup>273,281</sup> The frequencies of the higher modes for pinned and unpinned surfaces are quite similar. As we have shown already, the changes in a MAW are more significant and complex. Many additional modes are seen to occur in the MAW spectrum calculated for unpinned magnetization (see Fig. 5.2) compared to those obtained in the pinned case (see Fig. 5.3). Due to the pinning in the row of antidots some modes existing in an unpinned system (the modes with high amplitude of  $|m_z|^2$  in the centre of the MAW — see modes I and III in Fig. 5.2) can appear in a pinned system. The pinning in the centre of the MAW reduces the degrees of freedom of the SWs and practically divides the waveguide into two parallel sub-waveguides weakly coupled through the barrier formed by the antidot series. This is due to the small edge-to-edge distance between neighbouring antidots, which results in a minor crosstalk between the SWs propagating in the two sub-waveguides. The confinement of the modes increases their separation on the frequency scale in the case of an MAW with pinned magnetization. Moreover, due to the minor interaction between the sub-waveguides, the eigenstates are almost degenerate for frequencies up to 200 GHz in a wide wave number range.

In the absence of pinning, SWs spread freely over the whole width of the waveguide. This is

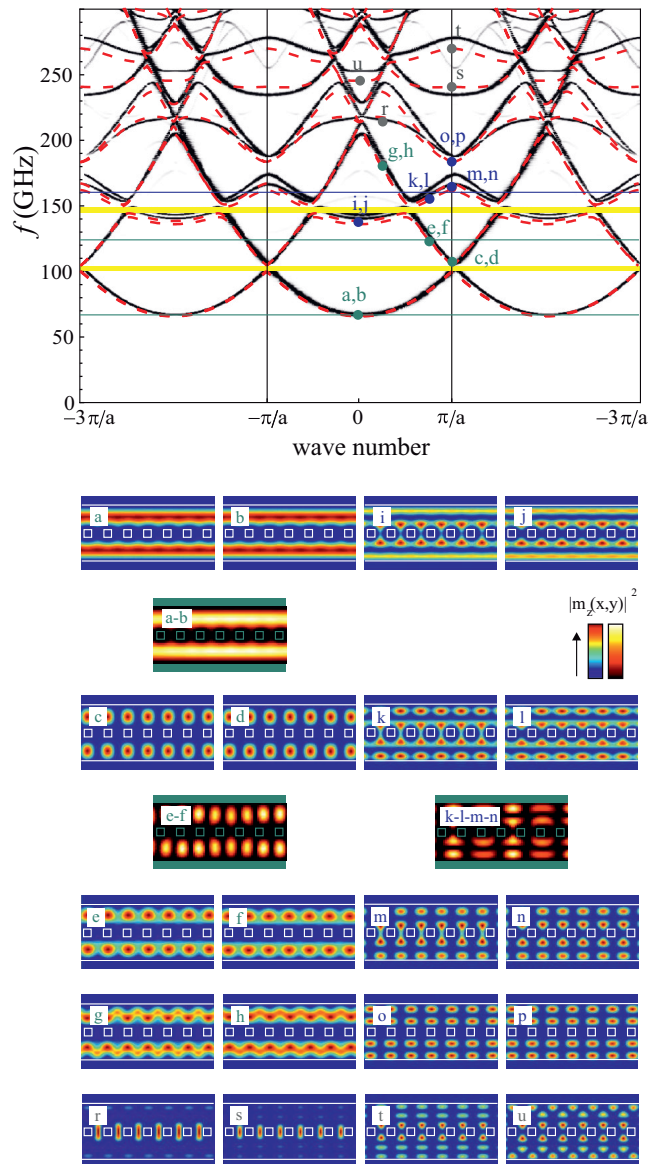


Figure 5.3.: Dispersion of SWs in the MAW presented in Fig. 5.1, as calculated with OOMMF with dynamic magnetization pinned at the Py/air interfaces (grey lines). PWM results are plotted with red dashed lines. Yellow bars represent the magnonic bandgaps (in OOMMF calculations). Bottom: maps of  $|m_z|^2$  at points (a) to (u) in the plot above. Green (a–h) and blue (i–p) labels refer to modes originating from the first and second dispersion parabolas, respectively, of each isolated sub-waveguide at the right and left of the central row of antidots. Brown labels denote high-frequency modes localized in the row of antidots. The maps plotted in full colours scale and hot colours scale present the results calculated with OOMMF and Nmag, respectively. The horizontal colour lines in the dispersion plot mark the contributions from different Bloch bands to the OOMMF profiles. Source: Ref. 213.

why the unpinned modes are distributed more densely on the frequency scale. The dispersion branches of some unpinned modes are reminiscent of the continuous parabolas in Fig. 5.2. In the low-frequency range this behaviour is seen in every alternative band, i.e., the 2nd, 4th, and 6th bands from the BZ centre, where a nodal line should appear in the centre of the MAW. The lower amplitude of the SWs in the centre of the MAW results in a negligible impact of the antidot series on the spin dynamics. The effect of the antidot series on the spin dynamics is similarly small in (1) the dispersion branches of unpinned modes with a nodal line in the centre of the MAW [see Fig. 5.2 (c)] and (2) all the dispersion branches of pinned modes. In spite of this, their frequencies are not equal due to the different boundary conditions at the external edges of the MAW. Therefore, no frequency agreement can be expected between the unpinned and pinned modes in wires of the same width.

Another important property of the magnonic band structure of MAWs found in our study is that the magnetization pinning at the edges of the MAW results in the opening of magnonic gaps (yellow bars in Fig. 5.3). This means that even MAWs with as little as 5% air can be used as filters with stop and pass bands. As the first magnonic gap occurs at the border of the BZ, its opening is clearly related to the periodicity of the MAW. However, the second gap (between the 4th and 5th bands) is seen to open inside the BZ. This indicates a different origin of this gap.

The second gap results from the anticrossing between two pairs of modes: modes with no nodal line within each sub-waveguide and modes with a nodal line in each half of the MAW. In other words, the anticrossing occurs between two parabolas (connected with the lower and higher harmonics across the MAW width) of the SW dispersion crossing due to folding to the first BZ.

It is worth noting that the closing of the gaps in the system with unpinned magnetization is due to the presence of additional bands (1st, 3rd, 5th, ...) corresponding to modes with a significant magnetization amplitude in the centre of the MAW [see Figs. 5.3 (a) and 5.3 (b), first and third mode]. These modes are, in fact, more affected by antidots and more separated from each other than the modes with a nodal line in the centre of the MAW, but their presence makes the spectrum of the unpinned system denser and results in more effective bands overlapping.

The relatively small width of the gaps in the system with pinned magnetization is due to the less effective impact of antidots on modes with low value of dynamical magnetization in the centre of the MAW.

The above discussion applies to the low-frequency range, in which the mode quantization is related to the confinement of SWs between one edge of the waveguide and the central row of antidots. In the high-energy range the following effects can interfere with this simple mechanism: (1) SWs can be localized between antidots in the central region of the MAW; (2) the crosstalk can be much more efficient in the case of short SWs, which can easily “leak out” from one sub-waveguide to the other.

Let us discuss in detail the profiles of the dynamic magnetization component  $|m_z|^2$  presented in the bottom panel of Fig. 5.3. Three types of modes can be distinguished by profile: (1) modes (a—h) originating from the first mode of each sub-waveguide (no nodal line inside each sub-waveguide); (2) modes (i—p) related to the second mode in the completely isolated sub-waveguides (one nodal line in the MAW); (3) modes (r—u), which are high-frequency excitations localized mostly between antidots in the centre of the MAW. The modes are plotted for different BZ points, indicated in the top panel of Fig. 5.3. The modes in the centre of the BZ have no nodal line perpendicular to the MAW axis, while the modes at the edge of the BZ only have one such line in each BZ. At intermediate points the non-zero amplitude oscillates more smoothly along the MAW axis.

In the low-frequency range the SW modes show the following characteristics: (1) modes occur in pairs with in phase and out-of-phase correlation between excitations in the two sub-waveguides; (2) the frequency difference between the modes in each pair increases with growing frequency; (3) the mode splitting can be suppressed (even for relatively high frequencies) in every second pair of modes at the edge of the BZ, where the nodal line between antidots blocks the crosstalk between sub-waveguides (cf. modes o, p to m, n).

In order to verify the mode profiles calculated using PWM we plotted also some profiles with the aid of micromagnetic simulation (OOMMF). They are presented in Fig. 5.3 in a hot colours scale and their frequencies are marked by horizontal lines to show from which bands they collect the contributions. The labels a, b, e, f, and k, l, m, n present what kind of mixture of Bloch states (calculated using PWM) exist in the profiles calculated with the

aid of OOMMF.

Helpful for practical realizations of MAWs is the insensitivity of the magnonic gaps to the shape of the antidots until its filling fraction and mirror symmetry of MAW is unchanged. On such a small scale, with a feature size of a few nanometres, the shape can be expected to play a minor role. The situation will be different in the magnetostatic regime, *i.e.*, for smaller wave vectors and larger antidot periods where the demagnetizing field is strongly shape dependent and can affect the SW spectrum in the low-frequency regime.<sup>63</sup>

### 5.3. Conclusions

We have shown that the boundary conditions for the dynamic components of the magnetization vector at ferromagnetic material/air interfaces are of much importance for the SW spectra in nanoscale magnonic antidot waveguides. Our results demonstrate that the magnetization pinning facilitates the opening of magnonic gaps in magnonic antidot waveguides with air filling fraction even as low as 5%. This indicates an additional functionality of these types of waveguides as filters with tunable stop and pass bands. Also, our results show that the pinning will be an important factor to be considered in the interpretation of experimental data obtained for antidot lattices or designing new devices in which the antidot arrangement is periodic in nanoscale. The pinning or unpinning at the interfaces is usually related to the surface magnetic anisotropy, determined by the shape of the atomic orbitals modified at the interfaces by the surrounding material and the reconstruction or relaxation processes. Thus the surface anisotropy can depend on many factors, such as the interface structure on the atomic or nanometre scale, the strain, the crystallographic structure, or the chemical composition.<sup>282</sup> In two-dimensional systems the investigation of these effects can be regarded as an extension of the research in magnetic bilayers and multilayers, which were in focus at the time of the discovery of the giant magneto-resistance effect. We have also shown that peculiar properties of computational methods often used in the calculations are related to specific boundary conditions for dynamical components of magnetization implicitly assumed in each method.

# 6. Manipulation of Intrinsic and Extrinsic Mirror Symmetry in a Magnonic Antidot Waveguide

\*Recently, micromagnetic simulations (MSs) were used to show that periodic waveguides have filter properties due to the opening of magnonic gaps in the SW spectrum at high frequencies.<sup>5,84,267</sup> In this chapter we investigate the influence of the fundamental property of symmetry on the magnonic band structure. We study how loss of mirror symmetry within an one-dimensional nanoscale magnonic antidot waveguide (MAW) may affect the magnonic bandgap. When this symmetry exists then based on their profiles with respect to the central longitudinal axis, the SW spectra can be separated into two groups: symmetric modes and anti-symmetric modes. The breaking of the mirror symmetry will automatically make the classification impossible. We will study two types of the symmetry breaking mechanisms: categorizing them as intrinsic and extrinsic. To demonstrate the generality of the methods discussed here, we have considered two intrinsic factors and two different kinds of field profiles: stepped or ramped (extrinsic factors). The intrinsic factors discussed here are the shape of the antidots and their positions within the MAW. The question is: how do these changes influence the magnonic spectra and the existing bandgaps? Also, how “big” the symmetry breaking needs to be in order to close the gaps? The answers to these questions are very important for the applications of nanoscale SW waveguides in magnonic signal processing and also from the point of view of the basic research, as it concerns fundamental properties of a diverse group of systems. We address these questions

---

\*This chapter is based upon Kłos *et al. Sci. Rep.* **3**, 02444 (2013).

in this article and go even further in terms of magnonic band engineering. We will study the possibility of compensating the changes introduced by the structural modifications in the magnonic spectra by modifying the bias magnetic field. We will demonstrate how collapsed bandgaps in asymmetric waveguides can be restored by the application of the asymmetric bias magnetic field. The extent of this restoration is also studied.

## 6.1. Methods

The calculations of the magnonic band structure are performed with the finite difference method MS and the PWM, with OOMMF<sup>250</sup> and a Fortran code developed by us, respectively. Both methods solve the Landau-Lifshitz-Gilbert (LLG) equation. The damping is neglected in PWM calculations and included in MS ( $\alpha = 10^{-4}$ ). The effective magnetic field  $\mathbf{H}_{\text{eff}}$  here consists of the bias magnetic field  $\mathbf{H}_{\text{bias}} = (H_0, 0, 0)$ , demagnetizing field and exchange field. The pinned dynamical components of the magnetization vector were assumed at Py/air interfaces in calculations with both methods. The pinning in OOMMF was introduced by fixing magnetization vector in all cells of the discretization mesh, which border the antidots, *i.e.*, for the width 0.5 nm along  $y$  axis. (In MS the discrete mesh size of  $1.5 \times 0.5 \times 3$  nm along  $x$ ,  $y$  and  $z$  axis, respectively, were used. The MS were performed for 4 ns. In the PWM we use 961 plane waves.) Further details on obtaining the SW dispersion relations by analysing the results of MSs are discussed in Sec. 4.1. In the PWM the pinning is applied exactly at the edges of Py. Due to small thickness of the MAW, uniform SW profile across the thickness is assumed. Both methods were already used in the calculations of the SW dynamics and proved to give correct results.<sup>57,58,213,262</sup>

## 6.2. Results

### 6.2.1. Magnonic Band Structure in Symmetric and Asymmetric MAW

We study the symmetric and asymmetric magnonic waveguides based on the antidot lattice structure shown in Fig. 6.1. It has the form of a thin (thickness  $u = 3$  nm) and infinitely long

permalloy ( $\text{Ni}_{80}\text{Fe}_{20}$ ) stripe with a single row of square holes ( $s = 6$  nm antidots) disposed periodically along the central line. The stripe width and the lattice constant are fixed at  $2 \times w + s = 45$  nm and  $a = 15$  nm, respectively. The row of holes is placed at the distance  $w = 19.5$  nm from the top (and bottom) edge of the stripe in the case of the symmetric MAW. A bias magnetic field, strong enough to saturate the sample ( $\mu_0 H_0 = 1$  T), is applied along the length of the stripe. The material parameters of Py were assumed in calculations.

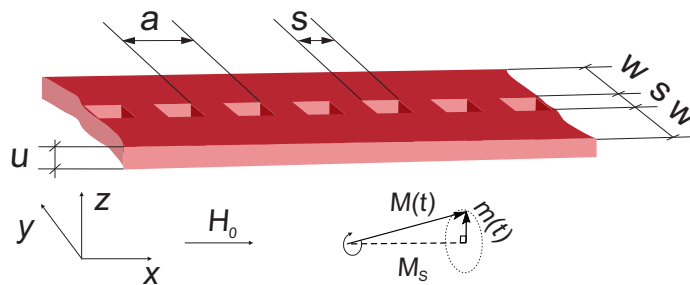


Figure 6.1.: Antidot lattice waveguide under investigation:  $u = 3$  nm thick and  $2w + s = 45$  nm wide (infinitely long) Py stripe with a periodic series of square antidots (of edge  $s = 6$  nm) disposed along the waveguide with a period of  $a = 15$  nm. The row of antidots divides the waveguide into two sub-waveguides of width  $w = 19.5$  nm each. Bias magnetic field  $\mu_0 H_0 = 1$  T is oriented along the waveguide, ( $x$ -axis). Source: Ref. 4.

We start our investigation with the symmetric MAW (Fig. 6.1).<sup>213</sup> The dispersion relations of SWs in the symmetric MAW is shown in Fig. 6.2. The results of the OOMMF simulations are shown in Fig. 6.2 (a) and of the PWM in Fig. 6.2c (black solid lines). The agreement between results from these two methods is satisfactory. The presence of two magnonic bandgaps (of about 4 GHz each) is evident and they are marked in yellow. The origins of these two bandgaps were found to be different. The first one opens at the BZ boundary due to the Bragg reflection of SWs, while the second gap opens up within the BZ.<sup>213</sup> It was shown that this splitting of the bands within the BZ is due to the anti-crossing between two families of modes,<sup>84</sup> those with and without a nodal line in the upper and lower parts of the MAW (see the first row of profiles in the bottom panel of Fig. 6.2). We showed in Sec. 5.2<sup>213</sup> that the pinning at the edges of Py (at the waveguide edges and at edges of antidots) is crucial for the existence of these magnonic gaps.

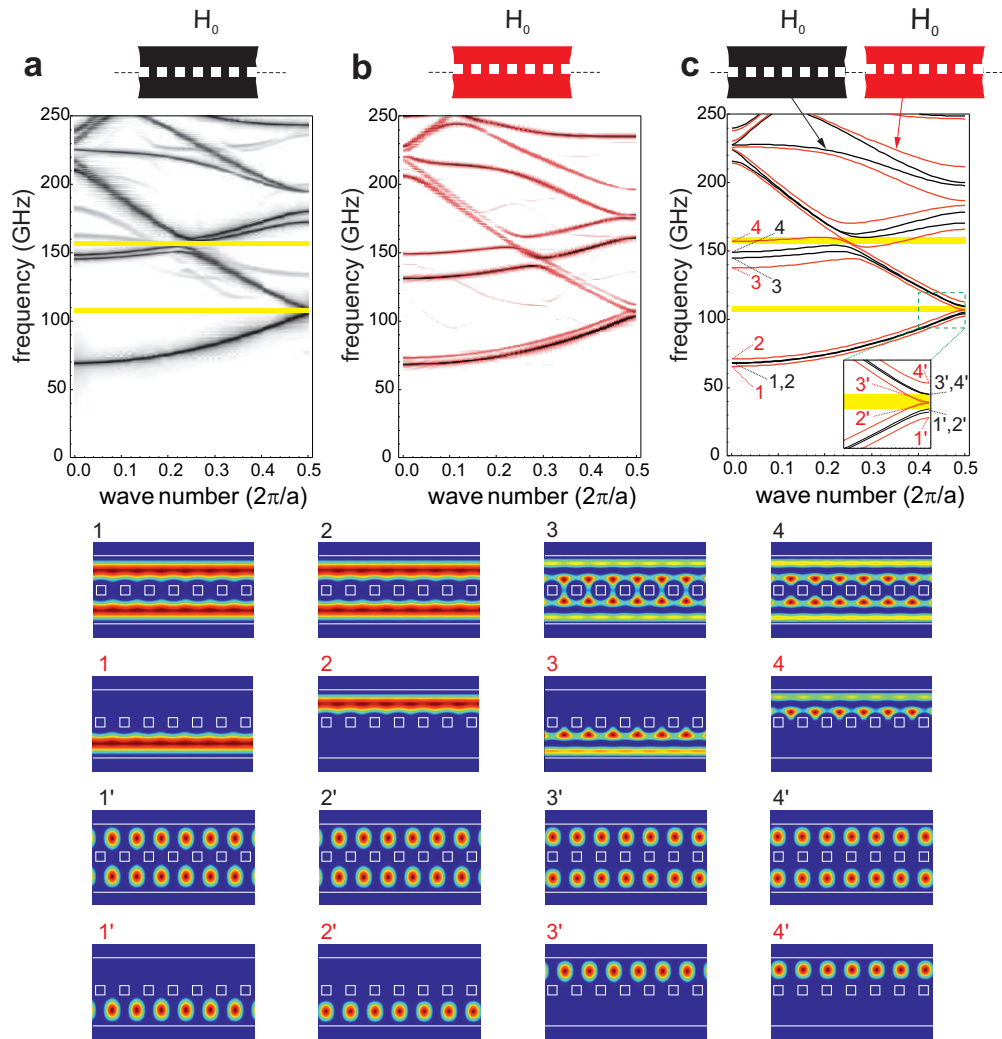


Figure 6.2.: Magnonic band structures of MAWs (shown in insets above the main figures where the thin dashed lines mark the middle of the MAW) calculated with OOMMF in (a) and (b), and with PWM in (c). The band structures for the symmetric MAW are shown in a) and in c) with black solid lines. The results for MAW with upward shifted antidots row are shown in (b) and (c) with red lines calculated with OOMMF ( $\Delta w = 1$  nm) and PWM ( $\Delta w = 0.9$  nm), respectively. In the bottom panel, the squared amplitudes of the dynamical magnetization  $|m_z|^2$  for first four modes in the center (first and second row) and boundary (third and fourth row) of the BZ is calculated with PWM—cf. (c) are shown for symmetric (first and third row) and asymmetric (second and fourth row) MAW. Source: Ref. 4.

The structure investigated above has a mirror symmetry with respect to the central axis of the MAW. Thus, the 1<sup>st</sup> and the 3<sup>rd</sup> modes are symmetric while the 2<sup>nd</sup> and the 4<sup>th</sup> are antisymmetric. The frequencies of first two modes (symmetric and antisymmetric one) are

degenerate in the entire wavevector regime and their maps of square of the amplitude of these modes are identical (see the first and third rows of profiles for BZ center and border in the bottom panel of Fig. 6.2). The degeneracy of symmetric and antisymmetric oscillations in the waveguide points at very weak coupling of oscillations localized in the upper and the lower parts of the MAW (in the two equivalent sub-waveguides, Fig. 6.1). The shift of the row of antidots from the central line will break the mirror symmetry of the MAW. If this shift is in  $+y$  direction, the upper and lower sub-waveguides will become narrower and wider, respectively. Frequencies of modes localized in the two sub-waveguides will split, with one mode shifted up and the other shifted down on the frequency scale. The dispersion relations of SWs in asymmetric MAWs, obtained by shifting the row of antidots by  $\Delta w = 1$  nm and 0.9 nm upward, calculated using OOMMF and PWM, are presented in Figs. 6.2 (b) and (c) (red lines), respectively. (In OOMMF slightly larger value of  $\Delta w$  were used because of the limitations of the discretization mesh and time needed for simulations.)

We see that a shift of the antidots row (along the width of MAW) by only 2% of  $2w + s$  is enough to close both magnonic gaps. At the BZ center, the first (second) mode center has an amplitude concentrated in the wider (narrower) part of the MAW of width  $w + \Delta w$  ( $w - \Delta w$ ) (see profiles in the second row in Fig. 6.2 at the bottom). The modes 3' and 4' at the BZ boundary originate from modes 1' and 2', respectively due to the folding from the neighboring BZ. Therefore, their profiles of amplitudes are quite similar. Typically, lower frequency modes are concentrated in wider regions of space. It means that two lower (higher) modes must be concentrated in wider (narrower) MAW. Note that, the oscillations of the magnetization amplitude for the modes at the BZ boundary are related to the shifting of the phase of the Bloch waves with the period of the lattice. When  $\Delta w = 0$ , modes 1' and 2' are concentrated in relatively larger regions (between the antidots) in the two sub-waveguides when compared to the coverage of modes 3' and 4' (directly above or below the antidots). However, when the mirror symmetry is lost ( $\Delta w \neq 0$ ), 1' and 3' cover the larger regions between the antidots while 2' and 4' are limited to the smaller regions directly above or below the antidots in the two sub-waveguides. Further, 3' and 4' are on a narrower sub-waveguide as compared to 1' and 2'. This makes the spatial distribution of 2' and 3' comparable in shape and expanse. Thus these two modes have similar frequencies at the BZ

boundary which, in turn, leads to the collapse of the first magnonic bandgap. A very similar mechanism is responsible for the closing of the second gap as well; even though the origin of this gap is different and the respective changes of frequencies of the third and the fourth bands are larger. As we mentioned before, the second gap appears at the anti-crossing of the modes with different quantization across the width of MAW. The modes 3' and 4' have no horizontal nodal line inside of each sub-waveguides whereas the modes 3 and 4 have one for each part of the MAW.

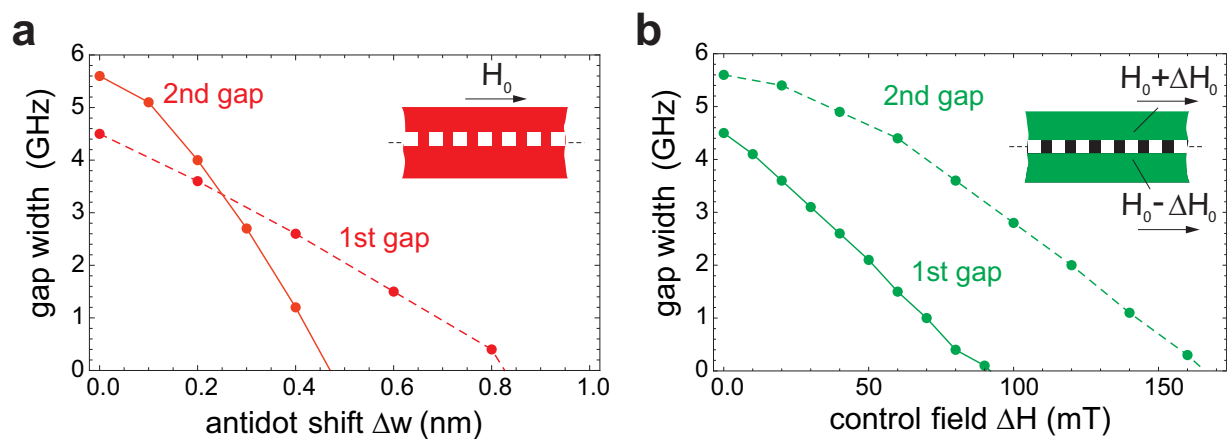


Figure 6.3.: Width of magnonic gaps in the considered MAW as a function of (a) the shift of the antidots row  $\Delta w$ , and (b) an additional asymmetric bias magnetic field  $\Delta H_0$  in the symmetric MAW. The  $\Delta H_0$  increases the bias magnetic field in the upper half of the MAW (to  $H_0 + \Delta H_0$ ) and decreases the bias magnetic field in the lower half of the MAW (to  $H_0 - \Delta H_0$ ). Source: Ref. 4.

The bandgap widths as a function of  $\Delta w$  are shown in Fig. 6.3 (a). The width decreases monotonously with increasing  $\Delta w$ . The slope for the second gap is larger leading to its complete collapse at  $\Delta w = 0.45$  nm, while the first gap exists up to 0.8 nm. We note that the shift of the antidots row does not change the translational periodicity in the structure. Thus the observation of magnonic bandgap closing shown in Fig. 6.3 (a) is purely related to the loss of the mirror symmetry of MAW and associated movement of different modes.

We now demonstrate that breaking the mirror symmetry by extrinsic means can also lead to splitting of the bands and closing of magnonic gaps. In Fig. 6.4 we show PWM results (dashed green lines) with the additional magnetic field  $\Delta H_0$  ( $\mu_0 \Delta H_0 = 180$  mT) applied (a) parallel and (b) antiparallel to the original bias  $H_0$ , in the upper part of the symmetric MAW. The black solid lines mark the magnonic band structure for the homogeneous magnetic field,

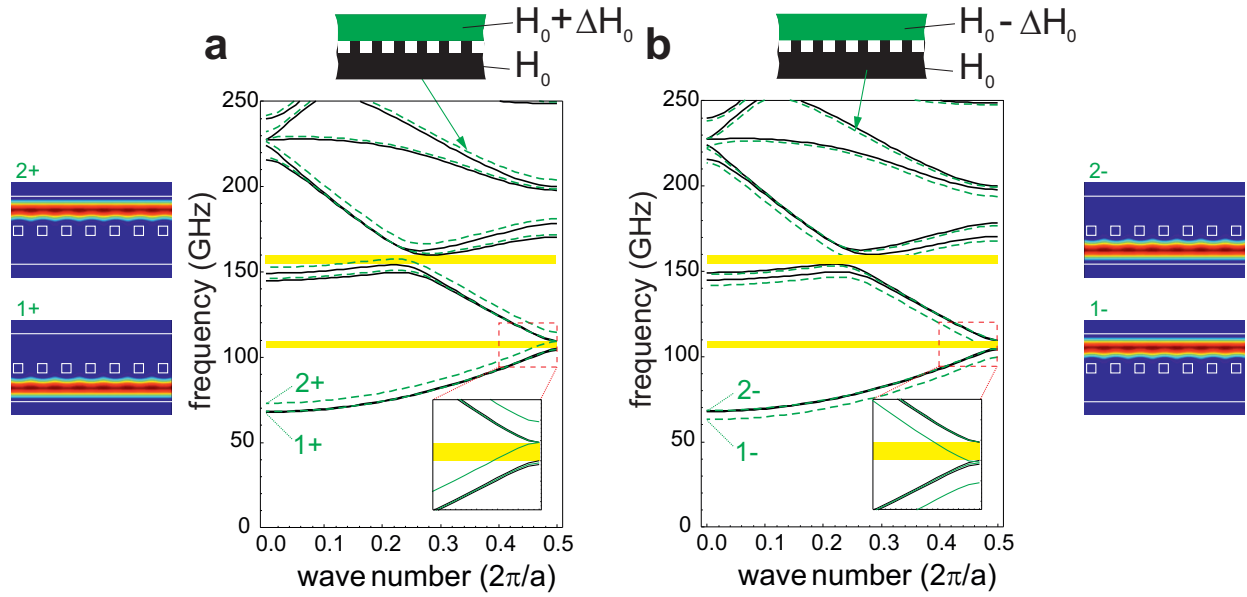


Figure 6.4.: Magnonic band structure of the MAW (presented in Fig. 6.1) calculated with PWM for asymmetric bias magnetic field (green dashed lines). The additional magnetic field of  $\mu_0\Delta H_0 = 180$  mT is applied in the upper part of the MAW (a) parallel and (b) antiparallel to the direction of the bias field  $H_0$ . The magnonic band structure for the symmetric MAW with homogeneous bias magnetic field is shown in black solid lines in (a) and (b). The squared amplitudes  $|m_z|^2$  for the first and second modes in the BZ center are presented on both sides of the figures for the MAW with asymmetric bias magnetic fields. Source: Ref. 4.

*i.e.*, the same as in Fig. 6.2 c). The parts of the MAW where the increased or reduced bias magnetic fields were applied were 18 nm wide from the closest MAW edge. Similar results were also obtained from simulations (not shown). The parts of the MAW with changed (increased or decreased) bias magnetic field are marked with green colour in the insets of Fig. 6.4. From Fig. 6.4, we can see that the (a) increase or (b) decrease of the bias magnetic field splits frequency bands by shifting the position of some modes up or down, while other frequency modes remain unchanged. The squared amplitudes of the SWs pertaining to the first two modes (1 and 2) are calculated at the BZ centre and are shown at the left and right of Fig. 6.4. A selective population distribution, predicated upon the changed external field, is clearly evident amongst these modes. The increase (decrease) of the bias magnetic field in the upper half of the MAW increase (decrease) the frequency of the modes localized in this sub-waveguide. It is worth noting that an uniform change of the magnetic field will shift the whole spectra but preserve the bandgaps in the structure.

### 6.2.2. Compensation of the Effect of an Intrinsic Symmetry breaking

We have just shown that the magnonic spectra, especially the magnonic bandgaps for the considered MAW are sensitive towards loss of its (intrinsic or extrinsic) mirror symmetry. We now investigate if it is possible to compensate the effect of an intrinsic symmetry breaking in a MAW by an extrinsic factor. In our case it will be a compensation of the effect of the structural asymmetry on the magnonic band structure (and magnonic bandgaps) by asymmetric bias magnetic field. The answer will begin from the development of an analytical model.

We showed that the amplitudes of modes from the first four magnonic bands in asymmetric MAW concentrate mainly at the top or bottom part of the structure (see the square of the amplitude in Figs. 6.2 and 6.4). This allows for a qualitative explanation of the observed changes in magnonic band structure by a model of two sub-waveguides (in the upper and lower parts of the waveguide), which are weakly coupled through a row of antidots. This observation lets us also to make the estimation of a compensation of the symmetry breaking mechanisms. We will discuss first the effect of the changes of the width and bias magnetic field in a single waveguide on the dispersion relation of SWs.

In the homogeneous waveguide the solutions of the linearised LLG equation (with damping neglected) can be written in the following form:  $\mathbf{m}(x, y) = \mathbf{m}(y)e^{ik_x x}$ , where  $k_x$  is the wave-vector of the SW along the waveguide and  $\mathbf{m}(y)$  describes the dependence of the amplitude of dynamical components of the magnetization  $\mathbf{m}$  across the waveguide width (we assume the uniform magnetization across the waveguide thickness, which is much less than the width). The solutions can be estimated as:  $\mathbf{m}(y) \approx \sin(\kappa y), \cos(\kappa y)$  where the transversal component of the wave-vector  $\kappa = (n + 1)\pi/w_{\text{eff}}$  is quantized ( $n = 0, 1, 2, \dots$  counts the number of nodal lines across the waveguide width). For strong but not ideal pinning the effective width  $w_{\text{eff}} = wd/(d - 2)$  depends on the pinning parameter  $d$ , which determines the boundary conditions for magnetization and gives also a possibility to include the dipolar effects into the model.<sup>255</sup> It varies in general from 0 to  $\infty$  for the transition from unpinned to fully pinned boundary conditions. The pinning parameter  $d = 2\pi(1 - \frac{K_s}{\pi M_s^2 u}) / [\frac{u}{w}(1 - 2 \ln(\frac{u}{w}) + (\frac{\lambda_{\text{ex}}}{u})^2)]$  depends both on the material and structural parameters

( $K_s$  denotes the surface anisotropy). It accounts for both the exchange and the dipolar interactions. For  $d \approx \infty$ , as in our numerical calculations,  $n = 0$  means no nodal line in the upper or lower part of the MAW (see, Fig. 6.2; modes 1 and 2),  $n = 1$  denotes a single nodal line (see, Fig. 6.2; modes 3 and 4), etc. The dispersion relation of SWs in the waveguide can be written in the form:<sup>28,255</sup>

$$\omega = \sqrt{(\omega_0 + \omega_{\text{ex}})(\omega_0 + \omega_{\text{ex}} + \omega_{\text{dip}})}, \quad (6.1)$$

where  $\omega$  is the angular frequency of SWs.  $\omega_0 = \gamma\mu_0 H_0$ ,  $\omega_{\text{ex}} = \gamma\mu_0 M_s \frac{\lambda_{\text{ex}}^2}{w^2}(n^2\pi^2 + k_x^2 w^2)$ ,  $\omega_{\text{dip}} = \gamma\mu_0 M_s \frac{1 - \exp(-k_x u)}{k_x u}$  denote the contributions from external, exchange and dipolar fields, respectively.

The estimations of changes in SW dispersion relation resulting from the changes of  $w$  or  $H_0$  can be done by calculation of the full differential of the function  $\omega = \omega(w, H_0)$ . It will allow one to derive the relation between small changes of  $\Delta H_0$  and  $\Delta w$ , for which the desired compensation between intrinsic and extrinsic symmetry breaking is obtained, *i.e.*, when  $d\omega(w, H_0) = 0$ :

$$\frac{\mu_0 \Delta H_0}{\Delta w} \approx \frac{2\pi^2 \mu_0 M_s \lambda_{\text{ex}}^2 (n+1)^2}{w^3} \times f\left(\frac{K_s}{\pi u \mu_0 M_s^2} - 1, \frac{\lambda_{\text{ex}}}{w}, \frac{u}{w}\right). \quad (6.2)$$

This ratio, having units of T/m, describes how much extra asymmetric magnetic field needs to be added to compensate for the shift in the row of the antidots. The function:  $f(s, l, r) = [s + \frac{1}{\pi}(2\frac{l^2}{r} - 4r \ln(r))][s + \frac{1}{\pi}(r + \frac{l^2}{r} - 2r \ln(r) - s)]s^{-2}$  depends on three dimensionless parameters:  $s$ —the relative strength of the surface anisotropy,  $l$ —ratio between exchange length and the width of the waveguide and  $r$ —the aspect ratio of the waveguide. The values of  $f(s, l, r)$  with big absolute value of  $K_s$ , refer to the regime of strong pinning. Note that Eq. (6.2) does not depend on  $k_x$ , which means that it should be fulfilled for any wave-vector.

In our MAW, we have two sub-waveguides separated by the antidots row. When we shift the row of the antidots by  $\Delta w$  along positive  $y$  direction, the width of the upper sub-waveguide decreases by  $\Delta w$  and the width of the lower sub-waveguide increases by the same amount. This causes the higher and lower frequency modes to become concentrated in the narrower and wider sub-waveguide, respectively. To compensate for these changes in

the dispersion relation by a bias magnetic field we need to do the opposite. According to Eq. (6.2) we need to apply different bias magnetic fields to upper and lower sub-waveguides. The dependence of the magnonic gap width under asymmetric bias magnetic field of the step-like shape applied to the MAW; *i.e.*, in the upper part of the MAW bias magnetic field is  $H_0 + \Delta H_0$ , while in the lower part of MAW is  $H_0 - \Delta H_0$ , calculated with PWM is shown in Fig. 6.3 (b). We can see decrease in the gap widths with increasing  $\Delta H_0$ , similar to the changes observed with increasing  $\Delta w$ .

After these estimations we perform the PWM calculations. The results are presented in Fig. 6.5 (b) and (c) for  $\Delta H_0$  to recover the first and the second magnonic gaps in the asymmetric MAW (*i.e.*, when  $\Delta w = 0.9$  nm and 0.5 nm), respectively (see Fig.6.3 (a)). It is interesting that we found it possible to recover the first and the second magnonic gaps but with different values of the ratio  $\frac{\mu_0 \Delta H_0}{\Delta w}$ . The analytical values of this ratio (calculated from the Eq. (6.2)) with  $w = 18.5$  nm, *i.e.*, the distance between pinned layers used in MS) for the ideal pinning ( $f(s, l, r) = 1$ ) for the first gap (when  $n = 0$ ) and the second one ( $n = 1$ ) are 101 mT/nm and 406 mT/nm, respectively. To validate our predictions we performed MSs for  $\mu_0 \Delta H_0 = 105$  mT and  $\Delta w = 1$  nm. The simulation results are shown in Fig. 6.5 (a) with the first frequency gap opened and in good agreement with the PWM calculations shown in Fig. 6.5 (b). Although, the second bandgap is formed due to the anti-crossing of the  $n = 0$  and  $n = 1$  modes, at  $\Delta w = 0.5$  nm the splitting of the  $n = 1$  dominates (see Figs. 6.2 (b) and (c)). Hence, in order to open the second gap we have to target the shifts for the bands with a single nodal line ( $n = 1$ ) by applying the field for which  $\frac{\mu_0 \Delta H_0}{\Delta w}$  is about 4 times bigger than that for the first gap (410 mT/nm). This confirms the applicability of Eq. (6.2) with a square dependence on  $n + 1$ . The profiles of SWs (compare bottom panels of Fig. 6.2 and Fig. 6.5) further establish the restoration of amplitude distribution by extrinsic compensation. The presented results proved that the asymmetric bias magnetic field can reduce the effect of the intrinsic symmetry breaking introduced by the shifting of the position of antidots on magnonic spectra. Small differences in the extent of bandgap recovery obtained from numerical calculations and the analytical model, show that the pinning in the middle of MAW is not perfect.

Our predictions should also be applicable to MAWs where the loss of the mirror symmetry

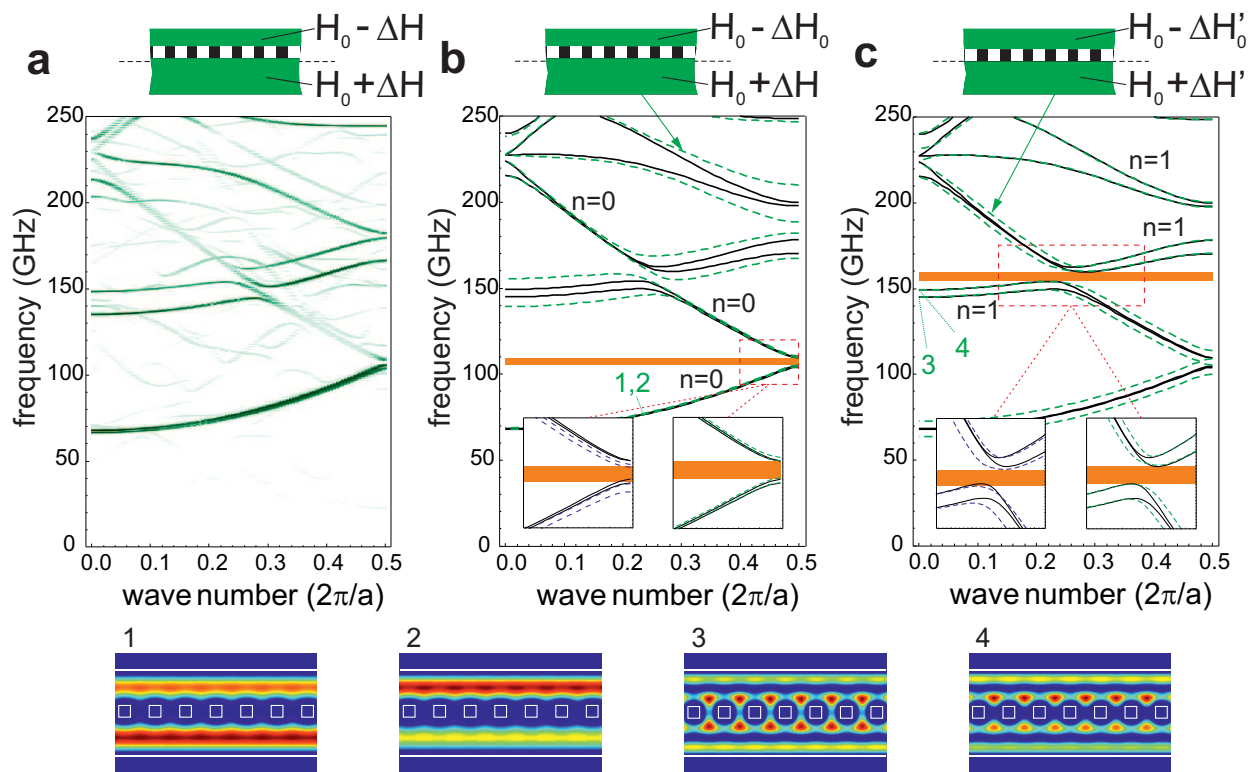


Figure 6.5.: Magnonic band structure of the MAW showing the compensation effect of an intrinsic asymmetry by an asymmetric extrinsic field. In (a) and (b) (green lines) the first gap (for the modes  $n = 0$ ) is reopened. The calculations with OOMMF (a) and PWM (b) were performed for  $\Delta w = 1$  nm and 0.9 nm, respectively, with  $\mu_0 \Delta H_0 = 105$  mT ( $\mu_0 H_0 = 1$  T). The reopening of the second gap (opened in the anti-crossing of the mode  $n = 0$  with  $n = 1$ ) is presented in (c). Calculations in (c) were done with PWM for  $\mu_0 \Delta H_0 = 205$  mT and  $\Delta w = 0.5$  nm. The left insets in (b) and (c) show enlarged results for the step-like field profile of the bias magnetic field; and the right ones show the outcomes for linear change of the magnetic field profile (ramp-like profile) across the MAW. At the bottom, profiles of SW calculated with PWM are shown. Profiles for modes 1 and 2 are calculated for the band structure in (b) and modes 3 and 4 for the band structure in (c) at the BZ centre. Source: Ref. 4.

has occurred due to a change in a different intrinsic parameter. In order to establish the same, we now perform calculations for MAW with rectangular antidots. The new MAW structure is shown at the top row of Fig. 6.6. The MAW consists of the rectangular antidot row with dimensions  $6 \text{ nm} \times 4.5 \text{ nm}$ , along the waveguide and across its width, respectively. The sub-waveguides formed on both sides of the antidots have now different width of  $w = 19.5$  and  $w + \Delta w = 21$  nm. Study of this kind of asymmetry can be of practical importance,

because such unintended defects can occur during the design or fabrication stages. The magnonic band structures calculated with PWM and OOMMF for this MAW are shown in the Fig. 6.6 (a). We can see that the mirror symmetry breaking by the decrease of antidots size across the waveguide width results in the splitting of magnonic bands and consequently the collapse of bandgaps in a manner similar to the results presented in Fig. 6.2 (b). The analytical formula Eq. (6.2) still can be used to estimate the bias magnetic field necessary to reopen magnonic bandgap in the spectra. According to Fig. 6.6 (a) we need to increase the frequency of the first and third modes without affecting the second and fourth modes. According to our models, we should be able to achieve this simply by increasing the magnetic field in the wider (21 nm wide) part of the MAW by  $\mu_0\Delta H_0 = 0.02$  T. The result of the calculations for the step-like magnetic field is shown in Fig. 6.6 (b). The first magnonic bandgap has almost the same width as for the symmetric waveguide. The results of the PWM calculations are confirmed by MSs, which are shown in Fig. 6.6 (a) and (b) as colour maps. The good agreement is found.

### 6.3. Discussion

We have shown that a small mirror symmetry breaking in MAW by the shift of the row of antidots from the waveguide axis or by an asymmetric change of their shape (*i.e.*, by changes, which leave the discrete translational symmetry of the lattice intact) can result in closing of magnonic bandgaps in the range of the spectra determined mainly by exchange interactions. We observed that the loss of symmetry causes a redistribution of the amplitude associated with different SW modes in the physical space of the MAW. This results in the movement of modes in the SW spectrum. Although, the two bandgaps observed and discussed here have different origins, their collapse is demonstrably a direct result of the loss of the mirror symmetry and the associated redistribution of SW amplitude.

Moreover, we have shown that the magnonic bandgap in the asymmetric MAW can be reopened by an asymmetric bias magnetic field of a step-like profile across the MAW width. With the help of an analytical model we were able to extract the main parameters responsible for closing the gap and its reopening by the external magnetic field. It was presented that

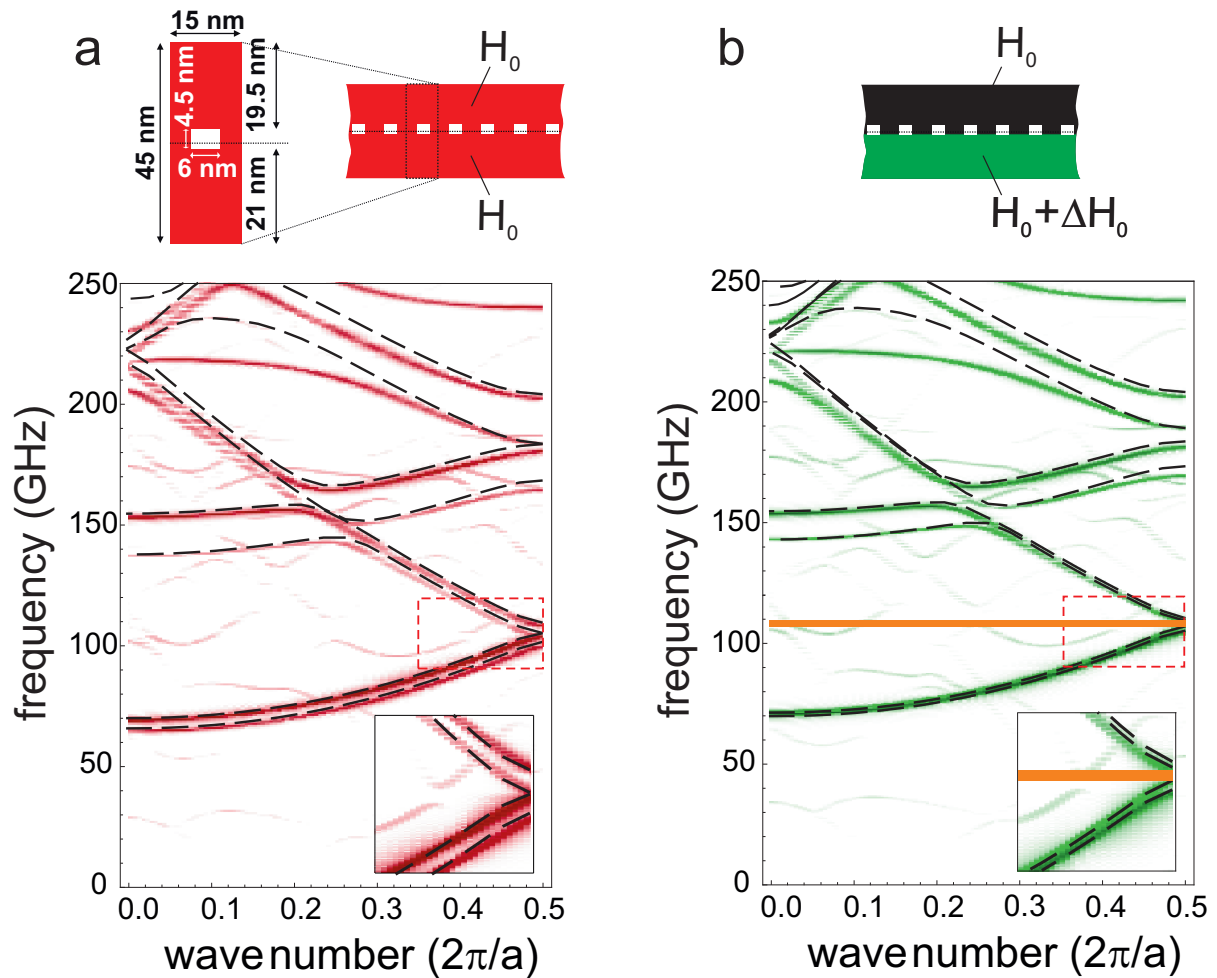


Figure 6.6.: Magnonic band structure of the MAW with rectangular antidots of dimensions  $6 \text{ nm} \times 4.5 \text{ nm}$  (shown at the top). The antidots row separate two sub-waveguides of different widths,  $19.5 \text{ nm}$  and  $21 \text{ nm}$ . The uniform bias magnetic field  $\mu_0 H_0 = 1.0 \text{ T}$  is applied parallel to the MAW axis. The dashed lines and the colour maps show the results from PWM calculations and MSs, respectively. (b) The magnonic band structure for the same MAW as in (a) but with step-like bias magnetic field with the value of  $\mu_0 H_0 = 1.0 \text{ T}$  in the narrower waveguide and  $\mu_0(H_0 + \Delta H_0) = 1.2 \text{ T}$  in the wider waveguide. The first magnonic gap marked by the coloured rectangle has reopened. Source: Ref. 4.

two magnonic bandgaps of different origins can be selectively reopened in the asymmetric waveguides by this way. It was shown here with an analytical model and also in some papers,<sup>68,213,242</sup> that the detailed shape of antidots and random defects do not play significant roles in effects studied in the manuscript. Our results can be crucial for practical realization of SW waveguides for magnonic applications in high frequencies, because precise mirror

symmetry is difficult to achieve on such small scales, leading to deviations from the ideal structure. The intrinsic and extrinsic symmetry breaking or its compensation can also be exploited to tailor the magnonic band structure or manipulate active and inactive waveguide modes, which couple to the external fields<sup>83,283</sup> in a similar way as was predicted for plasmonic metamaterials.<sup>284</sup>

The experimental proof of the compensation effect proposed here with the step-like profile of the bias magnetic field is challenging. More feasible for experimental realization will be a continuous change of the bias magnetic field. We propose to use a ramp-like profile of the magnetic field:<sup>285</sup>  $H = H_0 + 2\Delta H_0(2y + \Delta w)$ , where  $y = 0$  corresponds to the MAW center. The values of  $\Delta w$  and  $\Delta H_0$  can take the same values as for the step-like profile of magnetic field considered above. The results of PWM calculations for the  $\Delta H_0$  and  $\Delta w$  taken in the calculations presented above are shown in Fig. 6.5 in right insets. These results were also confirmed by MSs. We have found, that this kind of field acts similar to the field with step-like profile, when its value is normalized to the same average value as the step-like field for corresponding sub-waveguides (the aforementioned formula for ramp-like field meets this criteria).

The development of the analytical model presented here was made possible solely by dint of the fundamental properties of discrete translational and mirror symmetries of a crystal lattice. Thus, the main conclusions should not be limited to the particular cases investigated here and it should be possible to extend this idea to other SW waveguides, including those with larger dimensions, or to other types of waves. In the former case the inhomogeneous demagnetizing field, anisotropy of magnetostatic SW dispersion relation,<sup>286</sup> and multi-mode character of waveguides<sup>201</sup> have to be taken into account. Thus, further investigation is necessary. The compensation effects proposed here should find applications also in other systems, like electrons propagating in a periodically patterned graphene nano-ribbon by the external electric field,<sup>287–289</sup> or in photonic, plasmonic and phononic waveguides although with tailored electric and elasticity fields, respectively.

# 7. Effect of Antidot Shape on Spin–Wave dispersion in a Magnonic Antidot Waveguide

\*This chapter aims to help fill that gap in research by numerically simulating the magnonic dispersion in 1D MAW lattices with different geometric shapes of the antidots. We also study the spatial magnetization distribution for different frequencies and wavevectors of the observed dispersion modes. We further plot exchange and demagnetization fields to examine how they change with differing antidot shapes. We have used antidots, which are  $n$  sided regular convex polygons inscribed within a circumcircle of radius,

$$r_n = \sqrt{\frac{2fA}{n} \operatorname{cosec}\left(\frac{2\pi}{n}\right)}; \quad (7.1)$$

such that, the filling fraction  $f$ , the ratio of area of the hole to the area  $A$  of the unit cell, remains a constant. Micromagnetic simulations were performed for  $n = 3$  (triangular), 4 (square), 5 (pentagonal) and 6 (hexagonal antidots) in Object-Oriented Micromagnetic Framework (OOMMF).<sup>250</sup> The case of  $n = \infty$  (circular antidots) was simulated using Nmag.<sup>276</sup> This chapter is organized as follows. The geometrical structure of the waveguide and method used for calculating dispersion are described in greater detail in Sec. 7.1. Section 7.2 presents the results and analysis linking the ground state field distribution with changes in the observed SW dispersion modes. Section 7.3 contains the concluding remarks.

---

\*This chapter is based upon Kumar *et al.* *J. Appl. Phys.* **114**, 023910 (2013).

## 7.1. MAW and The Numerical Method

### 7.1.1. MAW Structural and Material Parameters

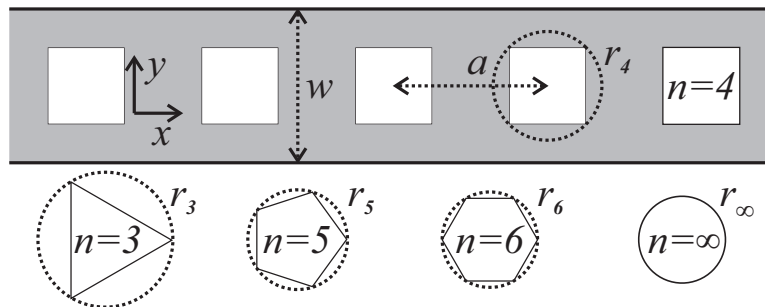


Figure 7.1.: (Top panel) A part of the 1D MAW structure showing square antidots (white holes in grey magnetic region) disposed along the central axis of the waveguide of width,  $w = 24$  nm and lattice constant,  $a = 24$  nm. The square antidots are inscribed within a circle of radius,  $r_4$ . (Bottom panel) Other examined antidot shapes inscribed within their respective imaginary circumcircles. For  $n \in \{3, 4, 5, 6, \infty\}$ ,  $r_n$  is given by Eq. (7.1), where filling fraction  $f = 0.25$  and unit cell area  $A = wa$ . Source: Ref. 68.

Figure 7.1 depicts the MAW structures under investigations. The MAWs had both width,  $w$  and lattice constant,  $a$  set to 24 nm and a length,  $l$  and thickness,  $s$  of 2.4  $\mu\text{m}$  and 3 nm in all cases. For  $f = 0.25$ ,  $A = wa$  and  $n \in \{3, 4, 5, 6, \infty\}$ , Eq. (7.1) dictates  $r_n$  as 21.06, 16.97, 15.56, 14.89 and 13.54 nm, respectively. The material parameters similar to that of permalloy (Py:  $\text{Ni}_{80}\text{Fe}_{20}$ ) were used during simulations (exchange constant,  $A = 13 \times 10^{-12}$  J/m, saturation magnetization,  $M_s = 0.8 \times 10^6$  A/m, gyromagnetic ratio,  $\bar{\gamma} = 2.21 \times 10^5$  m/As and no magnetocrystalline anisotropy).

### 7.1.2. Micromagnetic Simulations

Micromagnetic simulations<sup>246</sup> are done with the help of the finite difference method (FDM) based OOMMF (for  $n = 3, 4, 5$  and 6) or the finite element method (FEM) based Nmag (for  $n = \infty$ ). For the cell size used here, Nmag reproduces the circular shape much better than that obtained in OOMMF. The use of two different simulation packages also ensures that the established results are independent of the spatial discretization. Both these open source platforms solve the Landau-Lifshitz-Gilbert (LLG) equation.

In order to obtain the SW dispersion relations, a 2D discrete Fourier transform (DFT) was performed on the obtained results.<sup>262</sup> Before simulating the SW dynamics, a magnetic steady state was achieved by subjecting the MAWs to an external bias of 1.01 T (along the length of the waveguide) under a Gilbert damping constant,  $\alpha = 0.95$ . This high external field saturates the magnetization of MAWs. To observe sharper dispersion peaks  $\alpha$  was artificially reduced to  $10^{-4}$  during simulation of the dynamics. For simulations done in OOMMF, cuboidal cells of dimensions  $dx = dy = d = 1$  nm and  $dz = s = 3$  nm were used to span the MAWs. The resultant gridding of antidot edges which are not aligned with  $X$  or  $Y$  axes may cause the entire hole geometry to move towards one of the edges of the MAW. How this intrinsic mirror symmetry breaking affects the SW dispersion relations was described in Chap. 6.<sup>4</sup> Nmag, being FEM based, uses adaptive meshing and hence, its outputs do not suffer from this issue. However, spatial interpolation needs to be done in order to obtain magnetization values at every 1 nm interval before performing the DFT. Data was collected every  $dt = 1$  ps for both OOMMF and Nmag for a total duration of 4 ns. This gives us a sampling frequency,  $f_s = 1000$  GHz. The excitation signal,  $H_z$  is normal to the plane of the MAWs and is given by:

$$H_z = H_0 \left( \frac{\sin(2\pi f_c(t - t_0))}{2\pi f_c(t - t_0)} \right) \times \left( \frac{\sin(2\pi k_c(x - x_0))}{2\pi k_c(x - x_0)} \right) \times \left( \sum_{i=1}^{w/dy} \sin(i\pi y/w) \right). \quad (7.2)$$

Here  $\mu_0 H_0 = 6$  mT,  $f_c = 490$  GHz,  $t_0 = 1/(f_s - 2f_c) = 50$  ps,  $k_c = \pi/a$  and  $x_0 = l/2 = 1$   $\mu\text{m}$ . This form of excitation signal will excite both symmetric and antisymmetric modes of the dispersion relations in a width confined MAW. The aliasing associated with DFT is mitigated by the fact that the signal given by Eq. (7.2) carries no power beyond  $f_c$  in the frequency domain. Similarly, power in the wavevector domain is limited to the first Brillouin zone (BZ) from  $-k_c$  to  $k_c$ .

We also calculated the SW power and phase distribution profiles (PPDPs) for a given  $(k, f)$  pair of any dispersion relation. It was done by masking the obtained relation with a suitable mask in wavevector domain followed by doing an inverse Fourier transform in the same domain to yield data in physical space. For example, in order to obtain these results for  $(k, f) = (K, F)$  a mask,  $D_m$  was created to span the entire  $k$  vs.  $f$  space such that:

$$D_m(k, f) = \begin{cases} 1 & \text{if } k = \frac{2}{a}c\pi \pm K: c \text{ is an integer} \\ 0 & \text{elsewhere.} \end{cases} \quad (7.3)$$

After multiplying  $D_m$  with the obtained dispersion relations we then take an inverse Fourier transform in  $k$ -space to arrive at the desired PPDPs. This mask is designed to include power only from  $k = K$  and nullify the power present in the rest of the wavevector domain. Simply performing the inverse transform in  $k$ -space without using such a mask will allow power from the entire wavevector range to distort the results.

## 7.2. Results and Observations

The calculated dispersion relations are tabulated in Fig. 7.2. Frequency ranges from 0 to 120 GHz and wavevector  $k$  ranges from 0 to the first BZ boundary ( $\pi/a$ ) are displayed. As the bias field is kept constant at 1.01 T, a forbidden region is observed in all the cases up to the ferromagnetic resonance mode of about 39 GHz. SW of any  $k$  is not allowed in this region. Bandgap I is also present in all the cases. For triangular, square, pentagonal, hexagonal and circular antidots, its respective values are 4.3 GHz (43 GHz to 47.3 GHz), 5.6 GHz (44.1 GHz to 49.7 GHz), 4.4 GHz (44.5 GHz to 48.9 GHz), 4.4 GHz (44.8 GHz to 49.2 GHz) and 3.5 GHz (44.9 GHz to 48.4 GHz). In the case where the square antidots were tilted by  $45^\circ$  (diamond shaped antidots), bandgaps I & II were observed; and their respective values were 3.6 GHz (44.2 GHz to 47.8 GHz) and 3.5 GHz (57.8 GHz to 61.3 GHz). An additional bandgap (III) of 6.6 GHz (94 GHz to 100.6 GHz) was observed in the case of triangular antidots. Bandgaps II & III are direct but bandgap I is indirect suggesting a difference in their origin which can be studied by looking at the spatial PPDPs for the modes between which they exist.

Figure 7.3 shows the spatial SW PPDPs for the marked  $(k, f)$  values in the Fig. 7.2. Only a part of the entire MAW structures have been shown for convenience. Mode ① appears to describe the uniform mode showing insignificant power or phase variation in the medium. The power distribution profile (PoDP) of mode ②, being at the BZ boundary,

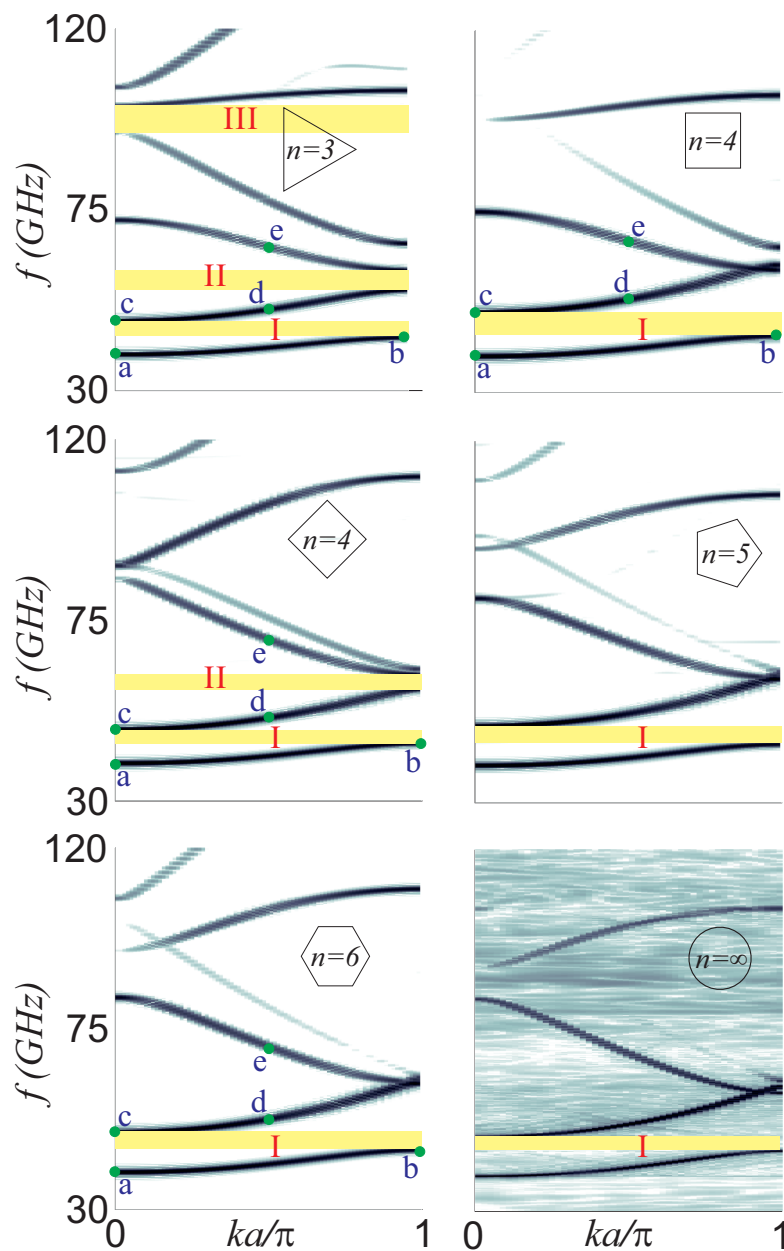


Figure 7.2.: SW dispersion results of MAW structures marked with their respective anti-dot shapes as insets. Indexed band gaps are highlighted with horizontal bars. Source: Ref. 68.

features narrow vertical nodal lines at  $x = x_0 \pm (c + 1/2)a$ ; where  $c$  is an integer. The regions joining these nodal lines are  $\pi$  radians out of phase with each other. This suggests that the positions of the phase boundaries in the phase distribution profiles (PhDP) depend on the location of the signal  $x_0$  used in Eq. (7.2). Power distribution profiles for mode © contains a horizontal nodal line right down the centre of the MAWs in all cases. The upper and lower

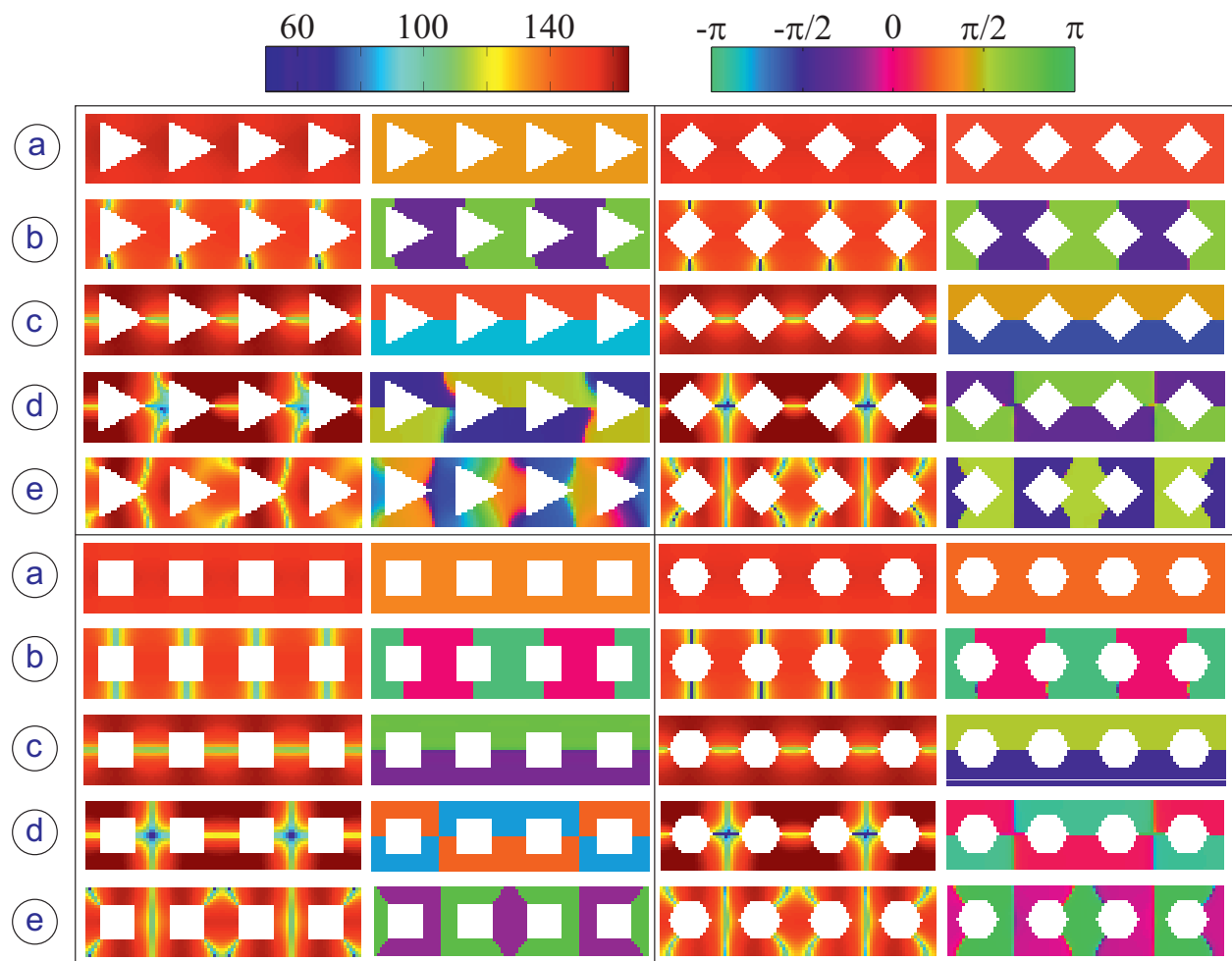


Figure 7.3.: Power (first and third column) and phase (second and fourth column) distribution profiles corresponding to marked  $(k, f)$  locations (Ⓐ to Ⓔ) in Fig. 7.2 for MAWs with triangular, diamond, square and hexagonal shaped antidots. Power is presented on an arbitrary logarithmic colour map while the phase profile representations use a cyclic colour map. Source: Ref. 68.

parts of the waveguide are again  $\pi$  radians out of phase with each other. This hints at the fact that modes Ⓐ and Ⓒ correspond to zero and first order modes along the width due to the lateral confinement of the waveguide.<sup>215</sup> Modes Ⓓ and Ⓔ are calculated at  $k = \pi/2a$  as they become nearly degenerate at the BZ boundary for square and hexagonal antidots. This degeneracy can lead one of the modes to affect the results of the other. Vertical nodal lines for both these modes are now located at  $x = x_0 \pm (2c + 1)a$ . Yet again, the position of the phase boundaries appear to be controlled by the location of the signal at  $x_0$ . The periodicity of these nodal lines  $2a$  is understandable given the location of modes (half way from BZ boundary). Slight curvature is observed in all the nodal lines for triangular

antidots. We attribute this to the lack of mirror symmetry within the hole geometry along a vertical axis. Similar curvature of nodal lines was detected for the MAW with pentagonal antidots (not shown) which also lacked such a symmetry. Belonging to the same dispersive branch of the spectrum, modes ③ and ④ share a horizontal nodal line which stems from the aforementioned lateral confinement. The observed effects of such confinement and the shape of dispersion curve to which modes ① through ④ belong reminds us of the first two (nearly) parabolic dispersion curves observed in the case of a uniform waveguide.<sup>79</sup> In contrast, mode ⑤ belongs to dispersive branch in the spectrum, which curves downwards. This branch is formed by the anti-crossing of lowest energy modes originating in the two neighbours of a BZ; and as such mode ⑤ unlike modes ① and ② does not show any horizontal nodal lines. Since the first two lowest energy branches share the same upward curvature, only indirect bandgap originating in the same BZ is possible. The third lowest energy branch of a BZ which originates in its two neighbouring BZs (aided by zone folding) has downward curvature. Thus, only a direct bandgap can be supported between this and the second lowest energy curve at the BZ boundary.

A quick visual comparison of different dispersion relations displayed in Fig. 7.2 reveals a qualitative convergence of dispersion modes starting as early as  $n = 4$  (square antidots). No new band gaps open or close. Section 5.2 discussed such similarities between results from different antidot based MAWs and how this convergence, or insensitivity towards the shape of the hole is desirable for the functioning of MAWs. However, note that when the square antidots are tilted by  $45^\circ$  (diamond shaped antidots) (see Fig. 7.2, left column middle row), one of the band gaps from  $n = 3$  case is partially restored. The computations of the exchange and the dipole field profiles (EFPs and DFPs) are done to help understand the cause for this observation. These profiles are shown in Fig. 7.4. It may be noted how the EFP around the square antidots matches to that around the hexagonal antidots. They have similar field orientations and cover similar regions in space. Maximum value of the this field is of the order of 20% of  $M_s$ . However, their demagnetizing field profiles do not match well. On the other hand, the demagnetizing field profile around the tilted square antidots matches better with the same around the hexagonal antidots (similar field orientations and elongated coverage in space and comparable maxima of the order of 50% of  $M_s$ ). Hence, the demagnetizing field or

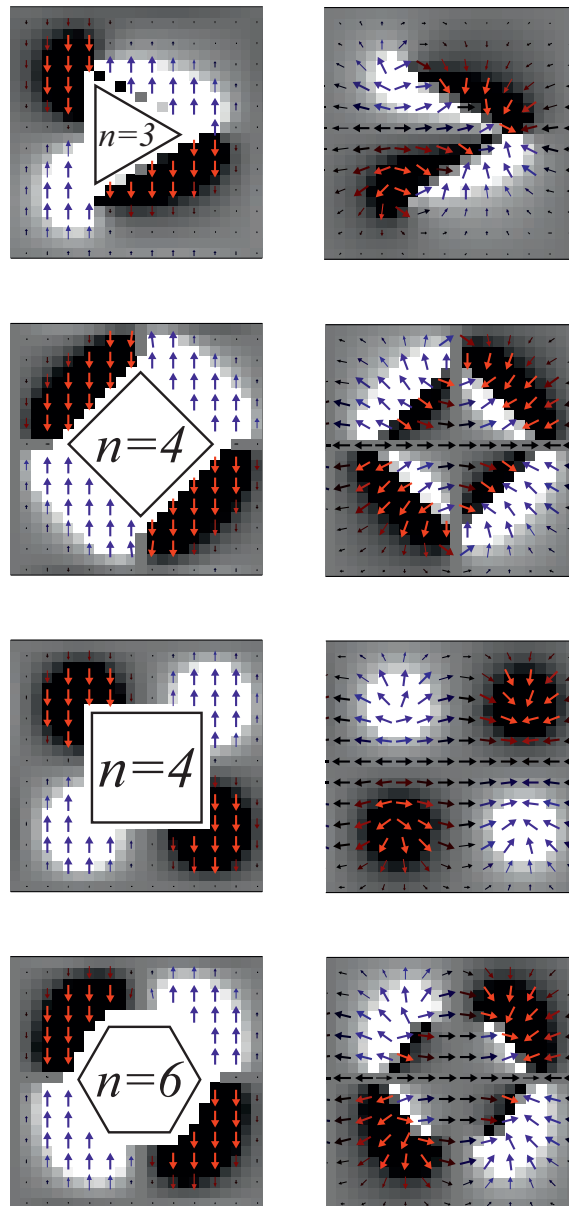


Figure 7.4.: Exchange (left column) and demagnetizing (right column) field profiles at  $t = 0$  for  $n = 3, 4$  &  $6$  (marked by insets).

its corresponding potential distribution, may not be the cause of the observed changes in the band structure. Dipole dominated SWs, which occur in much larger structural dimensions are more likely to be affected by the demagnetizing field distribution. To further test the postulate, that the dispersion in considered MAWs is largely dependent upon the exchange field distribution, the case of diamond shaped antidots was considered. It was anticipated that these antidots will produce elongated regions of inhomogeneous exchange fields (similar

to what is observed along the slanting edges of the triangular antidots) as opposed to chiefly circular ones (which is seen in the case of square antidots). Surly enough, the exchange field profiles of triangular, diamond shaped and square antidots were remarkably different from each other (as one of the edges of triangular antidot is vertical). This establishes a correlation of observed SW dispersion on their exchange instead of their demagnetizing field distribution.

Exchange energy density,  $E_{\text{exch}}(\mathbf{r}_i)$ , which contributes to the total energy  $\mathbf{M} \cdot \mathbf{H}_{\text{eff}}$ , is isotropic in a homogeneous magnetic medium with uniform exchange coefficient  $A$ . This field is calculated in OOMMF<sup>250</sup> as given below:

$$E_{\text{exch}}(\mathbf{r}_i) = A\mathbf{m}(\mathbf{r}_i) \cdot \sum_{\mathbf{r}_j} \frac{\mathbf{m}(\mathbf{r}_i) - \mathbf{m}(\mathbf{r}_j)}{|\mathbf{r}_i - \mathbf{r}_j|^2}. \quad (7.4)$$

Where  $\mathbf{r}_j$  enumerates the region in the immediate neighbourhood of  $\mathbf{r}_i$ . In the absence of SW dynamics  $\mathbf{m}(\mathbf{r}_i) - \mathbf{m}(\mathbf{r}_j) \simeq 0$  except where  $\mathbf{r}_j$  lies close to antidot boundary. Therefore, by changing its geometrical boundary, the exchange field distribution around an antidot can be changed. This can conceivably scatter exchange dominated SWs differently and alter their resultant dispersion relation.

It also needs to be considered if the simulations represent the physical reality. Particularly, how can FDM or FEM based ordinary differential equation solvers like OOMMF or Nmag, which necessarily discretize the continuous sample, calculate the isotropic exchange energy and the demagnetization energy<sup>247</sup> with good accuracy? Reference 253 concludes that the discrete representations should yield accurate results for  $\pi d/a = \pi/24 \ll 1$ . This was further confirmed by the fact that using  $d = 0.5$  nm for the MAW with tilted square antidots did not alter the exchange field distribution significantly.

### 7.3. Conclusions

We have discussed the dispersion of spin-waves in nanoscale one-dimensional magnonic antidot waveguides. In particular we have observed how an antidot's geometry can affect the said dispersion. By dint of power and phase distribution profiles of different spin-wave modes,

---

we have explored the origin of direct and indirect bandgaps that were encountered in the obtained dispersion relations. This understanding can be used, for example, to more readily design for the direct bandgaps and avoid the indirect ones. We have also studied the degree and nature of the inhomogeneity in the exchange field distribution around the edges of an antidot. Apart from offering a way to control the band structure of the exchange dominated spin-waves, we have also demonstrated their dependence on the exchange field profile around the antidots. We demonstrated that useful direct bandgaps can be opened at the same filling fraction without removing additional material during fabrication. Demagnetizing field profile, whose intensity here reached over  $0.5M_s$ , is expected to affect the dispersion relations on (thousand times) greater length scales. Without considering the changes in the exchange field distribution, the same has been established by Ref. 63 in two-dimensional magnonic crystals where the hole is filled up by another magnetic material. However, forbiddingly vast computational resources will be required to obtain those results with good frequency and wavevector domain resolutions without compromising the accuracy of the dynamics.

# 8. Effects of Other Structural Parameters

\*The periodic waveguide gives the possibility to design the selective leads which possess the filtering properties for transmitted SWs due to the presence of magnonic gaps. The position and the width of those gaps can be controlled by the structural parameters of the waveguides or by the bias magnetic field. It is also possible to design frequency dependent delay lines by exploiting the significant reduction of SW group velocity in the vicinity of magnonic gaps. The subject of periodic waveguides for SWs was extensively studied for few kinds of geometries: (i) comb-like structures and loop structures, where the SWs interference at the junctions in those branched structures is crucial for magnonic band gap opening,<sup>290</sup> (ii) the waveguides with periodically corrugated edges where the periodic change of the width is the main factor responsible for the generation of the magnonic band structure,<sup>5</sup> (iii) the ferromagnetic stripe with periodicity of the magnetization introduced by ion implantation<sup>291</sup> or (iv) periodic bias magnetic field,<sup>94</sup> and (v) SWs waveguides with periodicity introduced by a regular repetition of the bent sections where the bending induces periodic anisotropy field.<sup>292</sup> The other class of the periodic waveguides are the systems with periodically placed antidots (holes),<sup>213</sup> which is not to be challenging for fabrication even with a resolution in the range of few nanometres.<sup>50</sup>

In this chapter we numerically investigate magnonic antidot waveguide (MAW) made of permalloy (Py) with air holes (i.e., antidots) placed equidistantly along the wire in its center. The considered antidot waveguide having the width and period in nanoscale will then operate in the frequency range of few tens of GHz. Here, we use two different computational

---

\*This chapter is based upon Kłos *et al.* *Phys. Rev. B* **89**, 014406 (2014).

---

techniques, relatively fast plane wave method<sup>58,62</sup> (PWM) to perform systematic studies and extensive micromagnetic simulation<sup>5,84,94,267,293</sup> (MSs) (with the aid of OOMMF software)<sup>250</sup> to verify the obtained results. Similar MAW structures were already investigated in the previous papers showing that MAWs have interesting properties, which are relevant for technological applications.<sup>4,68,213</sup>

In Chap. 5<sup>213</sup> it was shown, that pinning of the magnetization at the edges of MAW can be an important factor which helps to open magnonic band gaps. Moreover, it was shown, that antidots occupying as small as 5% of the MAW surface area, are sufficient to open magnonic band gaps. In the Chap. 6<sup>4</sup> the influence of the intrinsic and extrinsic mirror symmetry breaking on the magnonic band gaps in MAW with pinned magnetization at edges was investigated. It was shown that small deficiencies in the symmetry of the MAW structure can result in closing magnonic band gaps but it was also demonstrated that these band gaps can be reopened by asymmetric external magnetic field. In Chap. 7<sup>68</sup> MAWs with comparable lattice periods and waveguide width were considered (25% of the area occupied by the antidots). The influence of the static demagnetizing field and non-uniformity of the exchange field on magnonic band structure in MAWs with various shapes of antidots were considered. Nevertheless, the influence of thorough and systematic structural changes in MAW on magnonic band structure have not yet been considered towards the optimization of MAW design. Thus, there is a need of the comprehensive studies which will thoroughly explain the impact of different structural parameters on the SW spectrum of MAW and reveal interesting properties of the magnonic band structures. Such studies are also of crucial importance for experimental realizations of MAWs with magnonic band gaps and their practical applications. In this chapter we study the influence of antidots size, lattice period, antidots shape and size factor on the dispersion of SWs and magnonic band gaps in nanoscale MAW.

This chapter is organized as follows. In Sec. 8.1 we describe the structure of the MAW and calculation methods in brief. Subsequently, we explain the magnonic band structure in MAW and the influence of the structural changes i.e., antidots size, lattice period, antidots shape and size factor in Sec. 8.2. Finally, we summarize our results and discuss the prospects of practical realizations.

## 8.1. The Waveguide Structure and the Calculation Methods

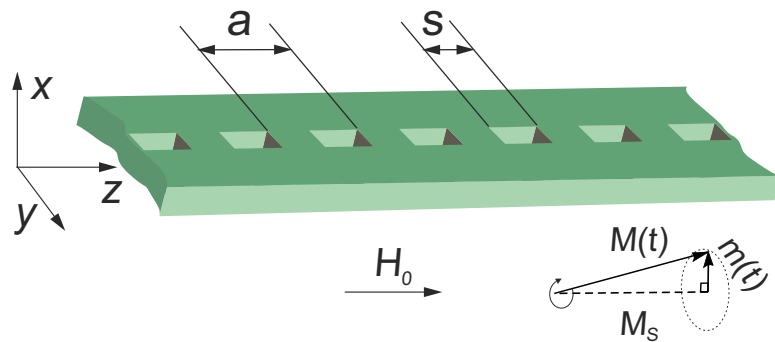


Figure 8.1.: The structure of the antidot waveguide, where the row of the equidistant square holes was placed in its center. The size  $s$  and the distance between antidots (i.e., the period of the structure  $a$ ) are 6 and 15 nm, respectively. The thickness of the waveguide is 1 nm. The sketch below the waveguide structure depicts the precession of magnetization around the direction of external magnetic field  $H_0$ . Source: Ref. 66.

We study here the symmetric magnonic waveguides based on a one-dimensional (1D) antidot lattice structure shown in Fig. 8.1. It has the form of a thin (thickness 1 nm) and infinitely long permalloy ( $\text{Ni}_{80}\text{Fe}_{20}$ ) stripe with a single row of square holes of side  $s = 6$  nm disposed periodically along the central line. The stripe width and the lattice constant are fixed at 45 nm and  $a = 15$  nm, respectively. The row of holes is placed at a distance of 19.5 nm from both top and bottom edges of the stripe. Thus, the waveguide possesses an axis of mirror symmetry down the middle of the waveguide. A bias magnetic field is applied along the stripe and it is strong enough to saturate the sample ( $\mu_0 H_0 = 1$  T) and make the magnetization collinear and equal to its saturation value even in the regions close to the sides of the waveguide and antidot edges. The material parameters of Py are assumed in calculations.

The calculations of the magnonic band structure are performed with the PWM and the finite difference method based OOMMF. Damping is neglected in PWM calculations and included in MS ( $\alpha = 0.0001$ ). The effective magnetic field  $\mathbf{H}_{\text{eff}}$  here consists of the bias magnetic field  $H_0$ , exchange field  $\mathbf{H}_{\text{exch}} = \nabla \lambda_{\text{ex}}^2 \nabla \mathbf{M}$  and demagnetizing field  $\mathbf{H}_{\text{dem}}$ . For OOMMF calculations the standard formula for dipole-dipole interaction in the lattice of

magnetic moments was used. In our PWM implementation we use Kaczer formula<sup>279</sup> for demagnetising field in planar periodic structures. The pinned dynamical components of the magnetization vector were assumed at Py/air interfaces in calculations with both methods.<sup>213</sup> The pinning in OOMMF was introduced by fixing magnetization vector in all cells bordering the Py/air interfaces\*. The boundary conditions for dynamical component of magnetization do not result from Landau-Lifshitz equation. They can result from the presence of surface anisotropy (which depends on the physical and chemical states of the surface) or from so called dipolar pinning.<sup>255,256</sup> Although we have limited our investigation to the case of pinned magnetization, the conclusions we draw will be still valid in systems with partially free magnetic moments on the external interfaces.<sup>4</sup>

The pinning at the edges of antidots forces the decay of the magnetization dynamics in the center of the MAW for small values of lattice constants  $a$  and relatively large antidot sizes  $s$ . By varying these parameters we can observe the gradual transition from the case of two weakly coupled periodic sub-waveguides (formed by each of the two semi-isolated 19.5 nm wide halves of the whole MAW) to the case of one waveguide (45 nm width, being the whole MAW) with small periodic perturbation (the further discussion with the numerical results will be presented in sub-Sec. 8.2.2). In the PWM, the pinning is exactly at the edges of Py, whereas in MS the pinning was applied in the layer of the finite thickness. This difference can slightly influence results obtained with both methods. The effect of magnetization pinning is seen in the profiles of SW dispersion relations shown in Figs. 8.2 and 8.3. Due to the small thickness of the MAW and relatively large ratio of the width to thickness of MAW, a uniform SW profile across the thickness is assumed.

## 8.2. The Influence of Structural Changes in the MAW on the SW Band Structure

The dispersion relation, i.e., frequency as a function of the wavevector,  $f(k)$ , is a periodic function with the period equal to the reciprocal lattice vector  $G = 2\pi/a$ . This dispersion

---

\*In MS the discrete mesh size of  $1.5 \times 1.5 \times 1 \text{ nm}^3$  along  $X$ ,  $Y$  and  $Z$  axis, respectively, was used. The MSs were performed for 4 ns. In the PWM we use 781, 1065, 1647 plane waves, depending on the value of the period  $a$ .

also has a mirror symmetry with respect to the point  $k = 0$ . Because of that it is enough to show  $f(k)$  only in the half of the first Brillouin zone (BZ) but for the purpose of clarity of analysis, we will present results in the full BZ.

### 8.2.1. The Influence of Antidot Size

Figure 8.2 presents the SW spectra of MAW for three different sizes  $s \times s$  of the square antidots: for  $s = 4, 6$  and  $8$  nm. We kept the period of the MAW constant ( $a = 20$  nm). For fixed period  $a$ , the increase of the antidot size makes the two sub-waveguides (formed by halves of MAW) more isolated, because it reduces the crosstalk between magnetization dynamics in these two sub-waveguides. It is noticeable both in the SW dispersion and in the profiles of the squared amplitudes of the dynamical magnetization in Fig. 8.2 (the profiles in Fig. 8.2 show the out-of-plane component of the magnetization vector). Let us compare two lowest modes for  $s = 4$  and  $8$  nm denoted in Fig. 8.2 by (a) and (b). For  $s = 4$  nm the lowest mode (a) is formed by strongly coupled SWs propagating in two sub-waveguides. This mode, as the lowest one, has no nodal line in the center of MAW and therefore the SWs are allowed to penetrate in the areas between the antidots. The antidot with larger size ( $s = 8$  nm) can however successfully extinguish the SW dynamics in the MAW center. In this case ( $s = 8$  nm) the modes (a) and (b) are almost degenerate with in-phase (a) and out-of-phase (b) SWs precession between two sub-waveguides. Their amplitudes and position of dispersion branches are almost the same. The mode (b) is however more robust to the changes in the antidot size. It is due to the fact that this mode has a nodal line in the center of the MAW, which leads to the decaying of the SW dynamics in the vicinity of the antidots row. As a result the SWs mode (b) is weakly affected by the presence of the series of antidots placed in the middle of the structure. The comparison of the maps of mode (b) for  $s = 4$  nm and for  $s = 8$  nm do not show significant differences.

It is also visible that the shrinking of the antidots size, from  $8$  nm to  $4$  nm splits the levels of modes (a) and (b) gradually. The difference between the frequencies of these modes become larger as the antidot sizes decreases. This increase of splitting between these modes can be attributed to increasing of dynamical coupling between SWs in sub-waveguides, as is discussed in the next paragraph. One can notice also the small changes in the position

for two lowest modes in the frequency scale. The lowering of frequency of the modes can be attributed to the slight increase in the effective width of each sub-waveguide with the reduction of the size of antidots.

The red dashed lines in the dispersion plots show the SW spectra for plain waveguide of width of 19.5 nm,<sup>79</sup> which corresponds to the width of single sub-waveguide with  $s = 6$  nm. The artificially introduced periodicity ( $a = 20$  nm) folds the parabolic dispersion branches (typical for exchange dominated regime) to the first BZ. In the considered frequency range (0-300 GHz) two folded-back dispersion parabolas are visible related to the mode confinement and quantization across the waveguide. By comparing MAW spectra to the spectrum of the plain sub-waveguide the following features can be noticed. (i) The MAW dispersion branches, which mimic the spectrum of the plain sub-waveguide (e.g., modes (a) and (b)) are confined mostly in the interior of the sub-waveguides of MAW, whereas modes of MAW completely distorted from the parabolic shape (e.g. modes (c) and (d)) have amplitudes concentrated at the row of antidots. (ii) When the interaction between sub-waveguides in MAW increases (for smaller antidot size), then the distortion of parabolic-like dispersion branches is more significant. This effect is stronger for higher modes. For our system already MAW modes related to the second parabola of plain sub-waveguide are strongly perturbed. We can recognize at least two features of such distortion: the splitting between the modes being even and odd with respect to the MAW center (e.g., modes (a) and (b)), the frequency down-shift (stronger for modes originating from the second parabola) resulting from the increase of the effective width of the sub-waveguides in MAW. For instance the modes (e) and (f) can be hardly identified as those related to the crossing of the folded arms of the second parabola in the BZ center (the modes have one nodal line in the center of each sub-waveguide). They are significantly shifted down as the antidots are reduced.

Due to the periodicity in the system the magnonic band gaps can be opened in the SW spectrum. If the periodicity can be regarded as a small perturbation in a plain waveguide possible bandgaps occur in three different scenarios: (i) at BZ edges – it happens for the lowest dispersion branch (originating from the first dispersion mode of the uniform waveguide), (ii) in the BZ center – as a result of the first self-crossing of the branches related to the same dispersion mode, after folding-back to the first BZ (only if there is no overlapping with higher

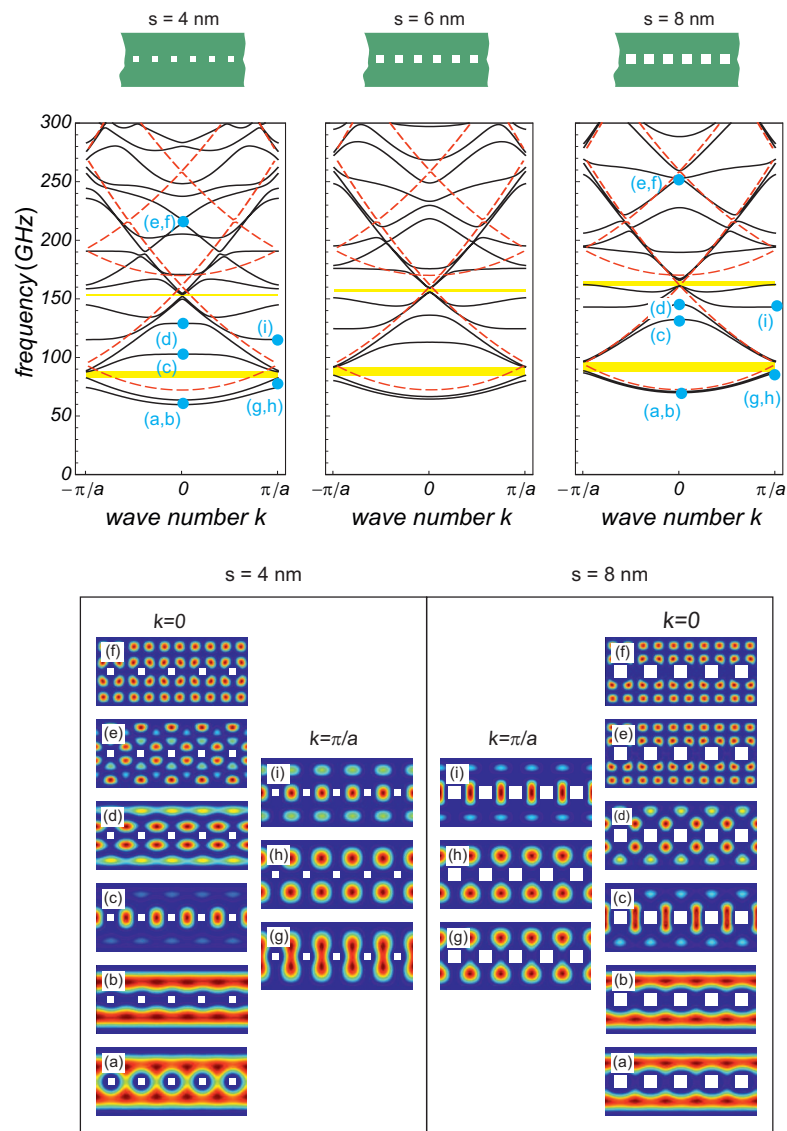


Figure 8.2.: The dependence of size of antidots on SW spectra of MAW. The inset above the central part of the figure shows the system under investigation: 1 nm thick and 45 nm wide, infinitely long Py stripe with a periodic series of square antidots of size  $s \times s$ , where  $s = 4, 6,$  and  $8$  nm, disposed along the waveguide with a period of  $a = 20$  nm. Bias magnetic field  $\mu_0 H_0 = 1$  T is oriented along the waveguide. The row of antidots divides the waveguide into two sub-waveguides. The coupling between sub-waveguides is controlled by the size of antidots with small antidots resulting in strong coupling ( $s = 4$  nm) and big antidots in weak coupling ( $s = 8$  nm). Red dashed lines show the dispersion for homogeneous waveguide of the width  $w = 19.5$  nm with artificial folding-back of the dispersion to the first BZ. The coloured maps present the squared amplitude of the out-of-plane component of dynamical magnetization for bands marked by letters from (a) to (i) in the SW spectra. Source: Ref. 66.

modes, which can be supported by the sufficiently large value of the ratio period/width), (iii) inside of the BZ – being the effect of the anti-crossing of branches related to different dispersion modes. The scenarios (i) and (ii) are related to the Bragg scattering for the spin waves differing in wave number by  $\Delta k = (2n)2\pi/a$  and  $\Delta k = (2n+1)2\pi/a$ , respectively, where  $n$  is integer number. Such simple picture of the mechanisms can be used for very weak periodic modulation, where the dispersive branches in the system can be referred to as modes of the plain waveguide, and does not exhaust all possible mechanisms of band gap formation.<sup>294–296</sup> The magnonic gaps marked by yellow bars in Fig. 8.2 are related to the first and second scenario mentioned above. The gap generated by the anti-crossing of branches related to the different dispersion parabolas of the plain sub-waveguides (i.e, the third scenario) can be observed in the first column in Fig. 8.3 (see the second gap for  $a = 15$  nm). For considered range of antidot sizes ( $s = 4, 6$  and  $8$  nm) both gaps (the first and the second one) become slightly wider with the increase in the antidot size. However, introduction of much larger antidots (when  $s \approx a$ ) will cancel the periodicity in the system and will lead to the gaps closing. This behaviour can be understood by considering two competing mechanisms. The gap will be wide when the periodicity is strong (large antidots with the inter-antidot distance comparable to the antidot sizes) and the crosstalks between sub-waveguides are small (values of the ratio  $s/a$  close to 1 allows to separate sub-waveguides). The first condition will enhance the Bragg scattering, the second one will reduce the splitting of the even and odd modes with respect to the MAW center.

### 8.2.2. The Influence of Lattice Period

Figure 8.3 shows the variation in the magnonic spectra with the lattice constant ( $a = 15, 21$  and  $30$  nm). We change the separation between the antidots keeping their size constant ( $s = 6$  nm). The increase of lattice constant  $a$  contracts the size of the BZ. We decided not to change the range of the wave number  $k$  for successive values of  $a$  in Fig. 8.3. Therefore, the dispersion plots for  $a = 15, 21$  and  $30$  nm encompass: 1,  $1\frac{1}{3}$  and 2 BZs, respectively. To, discuss the impact of the lattice constant on the MAW spectrum one has to include this additional factor. The reduction of the BZ size can affect the spectrum of the 1D periodic SW waveguide in two ways: (i) The SW spectrum contains more bands in the same

frequency range. The edges of successive BZ appear more frequently in wavevector domain and therefore the dispersion foldings at the BZ edges splits the bands more often in frequency domain. (ii) The group velocity is reduced. If the spectrum is folded back multiple times, thus the number of bands reaching the BZ edge and center (where the group velocity drops to zero) increases. Both the Bragg scattering and self-crossing of bands leads to the band repulsion and their flattening.

Because of much more complex evolution of the magnonic spectrum with changes in the lattice constant, it is more difficult to trace the variations in the origin of the bandgaps width. The shrinking of the BZ (with the increase of  $a$ ) changes the frequency position of the bandgaps opened at the BZ edges and can also result in opening or closing of gaps formed due to self-crossing or anti-crossing of dispersion branches. Nevertheless some characteristic features for this evolutions can be noticed. (i) The magnonic bandgaps are shifted down in the frequency range. It is caused by the dense folding of the dispersion branches in the narrower BZ. The reasonably strong bands overlapping, for larger values of  $a$ , can also close the bandgaps in higher frequency range [see Fig. 8.3 for  $a = 30$  nm]. (ii) There is no simple answer to what value of  $a$  is optimal for the existence of a wide magnonic bandgap. The limits of very small and very large lattice constant (with a fixed antidot size) do not support the wide bandgaps in the system. For short periods the antidots start to overlap, which cancels the periodicity and makes two sub-waveguides isolated (in terms of exchange interactions) and the bandgap closes. In the limit of large lattice constants ( $a \gg s$ ) the periodicity in the system can be treated as a small perturbation and therefore, the Bragg scattering should be weak and it leads to a gradual bandgap closing. But the localized modes with flat bands appear in the low frequency spectra [see mode (a) in Fig. 8.3 for  $a = 30$  nm] and the simple picture does not hold.

The increase of the lattice constant with the fixed size of the antidots makes the separation between the antidots larger. For  $a \gg s$ , MAW can not be treated as two weakly coupled sub-waveguides. The data presented in the right column of Fig. 8.3 shows that considered system ( $a = 30$  nm) is close to this limit. For even larger values of  $a$ , one may interpret the spectrum as a perturbation of the spectrum of the plain waveguide of width 45 nm (equals to the total width of MAW and shown in the right column of Fig. 8.3 with dashed lines),

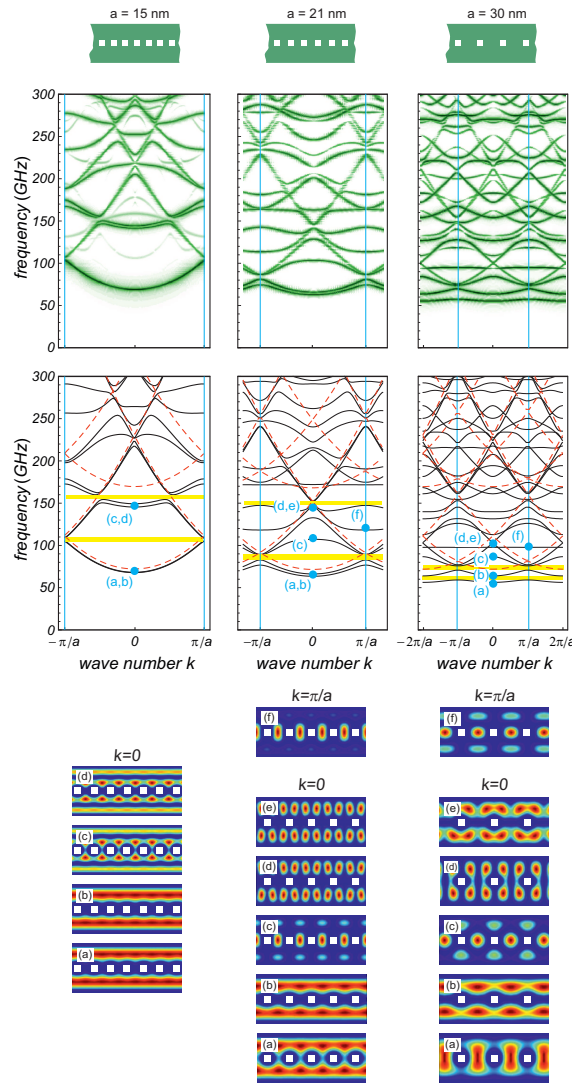


Figure 8.3.: The dependence of SW spectra of MAW on the waveguide period. The size of the antidots is kept constant  $s = 6$  nm. The increase of the period (from  $a = 15$  to 21 and 30 nm) leads to increase of the coupling between SWs in the sub-waveguides. Note the change in location of the BZ edges marked by blue vertical lines. In the first row schematic plots of the MAW are shown, in the second and third row the dispersion of SWs calculated by micromagnetic simulations (OOMMF) and PWM are presented respectively. Together with the PWM results the dispersion for homogeneous waveguides of width  $w = 19.5$  nm (for  $a = 15$  and 21 nm) and  $w = 45$  nm (for  $a = 30$  nm) with artificial folding-back of the dispersion to the first BZ is shown with dashed (red online) lines. The coloured maps on the bottom of the figure show the squared amplitude of the out-of-plane component of magnetization calculated with PWM for points of the magnonic band structure labelled by (a) - (f). Source: Ref. 66.

rather than those in two sub-waveguides. Let us discuss how the increase in the ratio  $a/s$  affects the spatial distribution of modes [bottom row in Fig. 8.3]. Two trends are evident.

(i) The modes localized at the antidots row are shifted to the lower frequency range. Modes (c) and (f) for  $a = 21$  and  $30$  nm have SW amplitudes localized between the antidots. With the increase of the period the size of these areas extend; and the SWs confined in the larger areas decrease their frequencies. (ii) The modes even with respect to the MAW center, start to leak their amplitudes to the middle of MAW. For larger values of  $a$ , the pinning at the antidot edges is not sufficient to diminish the SW power at the center of the MAW even for the lowest modes. We can observe this process by analysing the evolution of modes (a) and (b) while increasing lattice constant. For  $a = 15$  nm it is almost impossible to distinguish between the profiles of the (a) and (b) modes. When  $a = 21$  nm the power from even mode (a) starts to penetrate in the areas between the antidots. It leads to the coupling of excitation in the two sub-waveguides and splits the dispersive branches of even (a) and odd (b) modes. The lowest mode of the large considered lattice constant  $a = 30$  nm spreads its amplitude over the whole MAW width with maximum concentration in its center. Due to smoother spatial variation of the amplitude across the whole width of MAW (in comparison to the cases  $a = 15$  nm or  $a = 21$  nm) the frequency of this mode is lowered.

The second row in Fig. 8.3 presents the dispersions obtained from MS. The agreement with PWM is evident. The small discrepancies start to appear in the high frequency range where the bands calculated using OOMMF are slightly shifted down. This can be attributed to finite cell sizes used in the finite difference method based solver. The maximum difference between the positions of the bands calculated in OOMMF and PWM reaches about 5% at the top of the presented spectra.

### 8.2.3. The Influence of Antidot Shape

The effect of antidot shape on SW dispersion in MAW has been discussed in some detail for dipole dominated SWs<sup>45,63</sup> and exchange dominated SWs without pinning at Py/air interfaces.<sup>68</sup> Here, we revisit some of those findings for the completeness of this study. In order to make the systems of various antidots shape comparable, we fixed the area of the antidots independent of their shape. We compared two basic antidot shapes: the square shape and the circular shape. The results for  $a = 15$  nm,  $s = 6$  nm for square antidots and radius of 3.38 nm for circular antidots are presented in Fig. 8.4. The SW spectra for

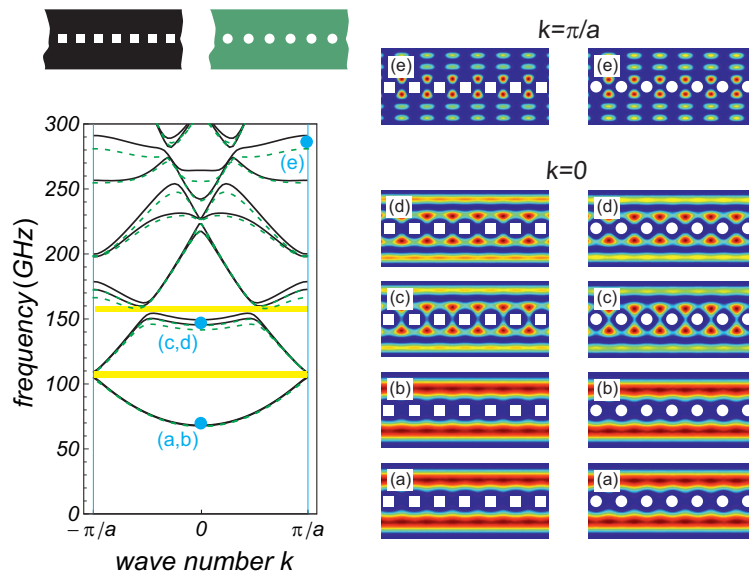


Figure 8.4.: The SW spectra for the MAW with square (black solid line) and circular (green dashed lines) antidots. The lattice constant is fixed ( $a = 15$  nm) and areas of square and circular antidots are the same ( $36$  nm<sup>2</sup>). The maps in the two columns on the right presents the out-of-plane components of dynamical magnetization for selected modes in the center and the edge of the BZ for square and circular antidots, on the left and right, respectively. Source: Ref. 66.

these two antidot shapes do not differ significantly. The branches coinciding with the first dispersion parabola [cf. the red dashed line in the left column of the Fig. 8.3] almost overlap with other. There is no discernible difference between modes (a) and (b) for both the MAWs with square and circular antidots. The levels associated with the second dispersion parabola [e.g. modes (c) and (d)] for the MAW with circular antidots are slightly lowered in reference to the corresponding modes of the MAW with square antidots. The differences in the profiles of (c) and (d) mode are also very subtle for two considered geometries. The more pronounced dissimilarity can be noticed for the modes localized at the row of antidots (e). For this case almost all SW amplitude is focused in the vicinity of the antidots. Therefore this kind of excitation is relatively sensitive to the difference in shape of antidots, which is in fact the very small change in the geometry of the whole system. Similar effects were also found for other structures investigated in this chapter, i.e., for lattice constants 21 and 30 nm, and antidots sizes of 4 and 8 nm. Antidot geometry affects the exchange and demagnetizing field distribution around itself. Thus their periodicity in an MAW provides the periodic and inhomogeneous potential necessary for the Bragg scattering and the resultant characteristic

SW spectrum. The demagnetizing field distribution is shown to play a more prominent role on larger length scales.<sup>63</sup> On the considered length scales, where we have exchange dominated SWs, the spectrum is affected only if the hole shape causes the exchange field distribution to change.<sup>68</sup> From the application point of view, perhaps the first direct magnonic bandgap and related dispersive modes are the most important in the SW spectrum. Thus we find that, for exchange dominated SWs, even if minor periodic deformations of antidot shape occur during the fabrication of an MAW, its SW spectrum will remain practically unaffected as long as the exchange field distribution is unchanged.

#### 8.2.4. The Influence of Size Factor

For the MAW of the width 45 nm discussed in the previous subsections, the exchange interaction dominates over magnetostatic interactions. It results from the small values of dynamic demagnetizing fields in comparison to exchange field for large values of wave numbers. Even the amplitudes of static demagnetizing field reach the values 0.1 T at the interfaces of Py/air perpendicular to the direction of external field, which are quite small in comparison to the value of external field 1 T and to the width of the bands [taking  $\gamma\mu_0 H_{\text{dm}}$  for comparison]. Therefore the SW dispersion manifest purely exchange behaviour with parabolic trend visible even for wave numbers close to the BZ center [see e.g., Fig. 8.4].

The models we use in calculations include both kinds of interactions: exchange and dipolar. To observe the noticeable impact of dipolar interaction on the SW dispersion, one has to scale up the structure of MAW. We magnified the MAW structure with square antidots presented in Fig. 8.4 by the factor of 6 [the width, thickness, antidots size and lattice constant were all increased 6 times]. For this structure in the first BZ we observe a negative group velocity near the BZ center for the first two bands [Fig. 8.5], i.e., the feature characteristic for the backward volume magnetostatic waves.<sup>28</sup> For larger values of the wave number, a quadratic dispersion typical for exchange interaction begin to dominate. As a result the two lowest dispersion branches have a minimum with a group velocity reaching zero away from the BZ center. The discussion of SW eigenmodes presented in the previous section has assumed the domination of exchange interactions. We have interpreted the magnonic band structure as an effect of cross-talks of two quasi-parabolic dispersion relations related to two sub-waveguides

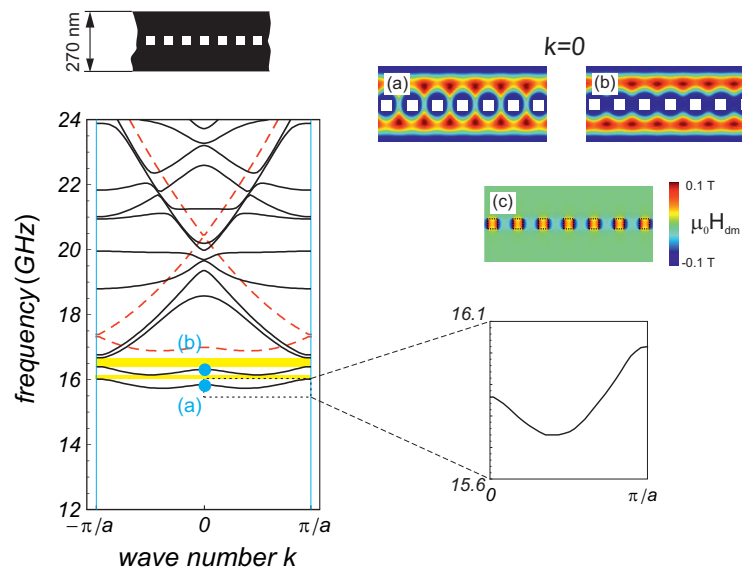


Figure 8.5.: The PWM calculations of SW spectra for the MAW magnified by the factor of 6 in reference to the structure presented in Fig. 8.4 with square holes showing the crossover of exchange and dipolar effects related to the stronger manifestation of dipolar interactions. The structural parameters are: the lattice constant:  $a = 90$  nm, antidots size:  $s = 36$  nm, thickness and width: 6 nm and 270 nm, respectively. Red dashed lines show the dispersion for homogeneous waveguide of the width 135 nm [i.e., half of the total MAW width]. The maps (a) and (b) presents the out-of-plane components of dynamical magnetization for two modes in the center of the BZ. (c) The map of the static demagnetizing field, its component along the waveguide,  $H_{dm}$ . The peaks of the static demagnetizing field are significantly smaller than the value of external magnetic field  $\mu_0 H_0 = 1$  T. Source: Ref. 66.

folded at the edges of the BZ. From Fig. 8.5 it is clear, that even in a crossover of dipolar and exchange regime, this picture can be still valid and the spectrum presented in Fig. 8.5 preserves most of the features found for exchange dominated systems [cf. Figs. 8.2, 8.3 and 8.4]. We can also link the spectrum of the MAW [black lines in Fig. 8.5] to the spectra of homogeneous sub-waveguides [red dashed lines] as well.

One of the important differences in comparison to exchange dominated systems, is the increase of the strength of interactions between two sub-waveguides. This effect is manifested by the stronger splitting of the levels of even [Fig. 8.5(a)] and odd [Fig. 8.5(b)] modes with respect to the MAW center. The increase of the coupling between these two SW excitations in different sub-waveguides can be attributed to three factors: (i) to the enhancement of long range dipolar interactions due to increased thickness of MAW, (ii) to the decrease of

the band width [resulting from the large lattice constant and consequently smaller first BZ] and thus the relative increases of the role of a non-uniformity of the static demagnetizing field [Fig. 8.5 (c)], and finally (iii) to the increase of separation between antidots, thus the lowering of frequency of quantize SWs between neighboring antidots.

The considered regime of sizes [the width of the MAW presented in Fig. 8.5 equal to 270 nm] can be realized by a much broader spectrum of fabrication techniques which make this system more interesting from experimental point of view.

### 8.3. Conclusions

We have presented in-depth theoretical study of the impact of structural changes on the spin wave spectrum of the new type of thin nanoscale magnonic waveguides with the row of antidots placed in its center. The influence of the antidots size and shape, distance between antidots and the scale factor of antidots waveguides on magnonic band structure and magnonic band gaps have been investigated. These studies allow us for the identification of main parameters and mechanisms which influence the width of magnonic band gaps in nanoscale MAW. Moreover we have described the roles of exchange and dipolar interactions in the formation of the magnonic band structure in the thin MAW with widths from tens to hundreds of nm. In summary we have found that:

- The increase of antidot size in relation to the waveguide period makes the effective pinning in the center of the waveguide stronger. By controlling the strength of this pinning one can affect the crosstalk between SWs propagating in two adjacent halves of the waveguide (sub-waveguides). The gradual degeneracy of the (a, b) modes occurs as the antidot size increases.
- When the size of antidots is small enough, or the edge to edge distance between the neighboring antidots are large enough, the SWs localized on the periodic row of antidots are observed in lower frequency range (together with the lowest dispersion branches for modes propagating in sub-waveguides)—see, e.g. modes (c) and (i) in Fig. 8.2 [and also modes (c) and (f) in Fig. 8.3].

- The magnonic gaps are expected to open at the BZ edges or BZ center (Fig. 2). The gap can be opened for the intermediate values of the wave number as well, where it is caused by the anti-crossing of the bands originating from different transverse modes in homogeneous sub waveguides cf. the modes (a,b) and (c,d) in the left panel in Fig. 8.2 [modes (a,b) and (c,d) differ in the number of horizontal nodal lines] and the second gap in this sub-figure [ $a = 15$  nm,  $s = 6$  nm].
- When the waveguide period  $a$  is fixed then the existence of magnonic band gap and change of its width and position is easier to analyse as a function of the antidot size  $s$  [Fig. 8.2], than for the opposite case,  $s$  fixed and  $a$ -varied [Fig. 8.3]. It is because a change in  $a$  alters not only the strength of the periodicity but also affects the location of BZ edges. Nevertheless, the period of the MAW, and its relation to the antidots size, are important factors which influenced magnonic band gaps and the group velocity of SW. Thus, its proper choice will be crucial for application of nanoscale MAW in magnonics, to transmit or filter SW signals.
- The shape of the antidots does not affect the SW spectrum of exchange dominated SWs unless the exchange field distribution is altered. High frequency modes, which contain power close to the row of antidots show greater sensitivity towards changes in the shape of the antidots. Thus for modes from the low frequency part of the spectra the antidots shape is not important parameter in nanoscale MAW.
- Enhancement of the size of the MAW increases the crosstalk between SWs propagating in two adjacent halves of the waveguide (sub-waveguides) and the backward volume magnetostatic wave character of dispersion relation near BZ center for these SWs is found. But still the main features the magnonic band structure in the exchange dominating systems are preserved.

Thus, we have shown that SW waveguides based on thin ferromagnetic stripes with single row of periodically spaced antidots in nanoscale are promising for magnonic applications in frequencies from few to tens of GHz. Only a single row of antidots offer enough room for manipulation of the SW spectra to design single mode waveguides or waveguides with filtering properties due to existence magnonic band gaps. The insensitivity of main part of the

magnonic spectra on the detailed shape of antidots, promises the possibility for fabrication of high frequency magnonic waveguides with the current technology.

# 9. Two–Dimensional Magnonic Crystals

\*Analogous to photonic crystals, magnonic crystals (MCs)<sup>35,69,71</sup> are magnetic meta-materials designed for the propagation of spin waves (SWs).<sup>28,37,38,297</sup> Based on their design, MCs exhibit a characteristic SW dispersion relation complete with bands and, sometimes, band gaps which can be tuned by controlling material and structural parameters as well as the strength and orientation of the bias magnetic field.<sup>45,298</sup> This phenomenon makes MCs useful as potential candidates for the design of SW based signal processing and logic devices.<sup>299</sup>

The knowledge of dispersion relation of a wave propagating through a medium is necessary to understand its transmission characteristics. Although MCs have been a subject of intense study lately,<sup>49,50,52,58,68,79,83,86,213,300</sup> reports on a time domain numerical calculation of dispersion relations of SWs propagating in two-dimensional (2D) MCs are very rare.<sup>5,97,301</sup> As other analytical methods are available, the use of time domain simulations and spatial Fourier transform to obtain the dispersion relation in a photonic or phononic crystal is rarely seen<sup>302</sup> as well. We hope to fill that gap in research with this work. The underlying principles, over which the procedure described here is used, has been discussed more generally in Chap. 4. Here too, we essentially use a micromagnetic simulator called Object Oriented Micromagnetic Framework<sup>250</sup> (OOMMF) to obtain magnetization  $\mathbf{M}$ , as a function of position  $\mathbf{r}$ , and time  $t$ . Then we use a multi-domain discrete Fourier transform to obtain the desired dispersion relation: SW power as a function of wavevector  $\mathbf{k} = (k_x, k_y)$ , and frequency  $f$ . However, while simulating the magnetization dynamics in large (ideally infinite<sup>303</sup>) 2D crystals, one can be expected to need far greater computational resources

---

\*This chapter is based upon Kumar *et al.* *J. Appl. Phys.* **115**, 043917 (2014).

than during the simulations of their one-dimensional (1D) counterparts.<sup>213</sup> Using a finite sample size may produce some spurious modes in the obtained dispersion relation.<sup>303</sup> Thus, the use of 2D periodic boundary condition<sup>244</sup> (PBC) becomes mandatory in order to obtain good numerical resolution in wavevector and frequency domains while consuming finite computational resources. Also, 2D crystals have more high symmetry directions when compared to their 1D analogues. Different techniques will be required to obtain the results for different directions in the 2D reciprocal space covering the entire irreducible part of the Brillouin zone (BZ).<sup>211</sup> Moreover, the signal which generates the waves will have to be carefully designed so that the resulting spectrum represents the physical dispersion relation of plane propagating SWs. Due to all these complications, a need to validate the results obtained here with a well established method, such as the plane wave method (PWM)<sup>51</sup> becomes very clear.

The details of MC considered here are presented in sub-Sec. 9.1.1. Simulation parameters and PWM are described further in sub-Sec. 9.1.2. OOMMF uses the finite difference method (FDM) to solve the LLG equation as an ordinary differential equation in time and space (derivatives with respect to space are hidden away in  $\mathbf{H}_{\text{eff}}$ ). PWM is based on the Bloch wave formalism. As these two methods are fundamentally different in approach, some quantitative differences in results are to be expected. The results from both the methods and their differences have been discussed in Sec. 9.2 for the antidot lattice (ADL). Due to small lattice constant, the considered system is an exchange dominated one and consequently, the differences in dispersion relations along the bias magnetic field and perpendicular to it are subtle. These differences have been explored by calculating the iso-frequency contours in the wavevector space using both MS and the PWM. The iso-frequency contours are the curves of the constant frequency plotted in the wavevector space, they are wave counterparts of the Fermi surfaces known from the theory of the solid state physics.<sup>211</sup> The iso-frequency contours are very important tool for the analysis of the wave propagation phenomena, giving a deep insight into direction and velocity of propagating, reflected and refracted waves in artificial crystals. Such type of analysis, while widely explored in photonic and phononic crystals for designing their metamaterials properties,<sup>304–306</sup> is almost absent in magnonics. Thus, developing the ability to compute these iso-frequency contours using MS can be a breakthrough in exploring magnonic metamaterials based on MC; because the MSs can be

performed without approximation limited applicability of the PWM (or other analytical methods<sup>245</sup>), and thus yields experimentally realizable results even with complex magnetic configurations.

We also plot the energy spectral density and phase distributions associated with different modes in the SW spectrum in order to understand their physical origin and explain any observed partial or complete bandgaps. Finally, we use the method described here to obtain the SW dispersion relations in the case of 2D dot array where the SW propagation is mediated by inter-dot stray magnetic field as opposed to dipole-exchange interaction in ADL. This brings about an interesting change in the spectra, which is discussed in Sec. 9.2 along with their effective properties.

## 9.1. Method

### 9.1.1. Magnonic crystal lattice and material parameters

The structure considered here is an infinitely large square array of square antidots with their ferromagnet-air interface under pinned boundary conditions.<sup>213</sup> The geometrical structure of the sample is shown in Fig. 9.1 (a). The lattice constant  $a = 30$  nm and the antidots are square holes of edge length,  $l = 12$  nm. The material parameters of permalloy (Py: Ni<sub>80</sub>Fe<sub>20</sub>) are used during simulations and in PWM calculations: exchange constant,  $A = 13 \times 10^{-12}$  J/m, saturation magnetization,  $M_s = 0.8 \times 10^6$  A/m, gyromagnetic ratio,  $\bar{\gamma} = 2.21 \times 10^5$  m/As and no magnetocrystalline anisotropy. A saturating bias magnetic field of  $\mu_0 \mathbf{H}_{\text{bias}} = 1$  T points in  $x$  direction.

### 9.1.2. Micromagnetic simulations and the plane wave method

The micromagnetic simulations involve solving the LLG equation using a finite difference method based ordinary differential equation solver; and then, Fourier transforming the obtained space and time dependent magnetization data to get SW spectral density in wavevector and frequency domains.<sup>262</sup> Cell size  $(d, d, s) = (1.5, 1.5, 3)$  nm along  $(x, y, z)$  axis was used during the FDM based simulations. The pinning in micromagnetic simulations was

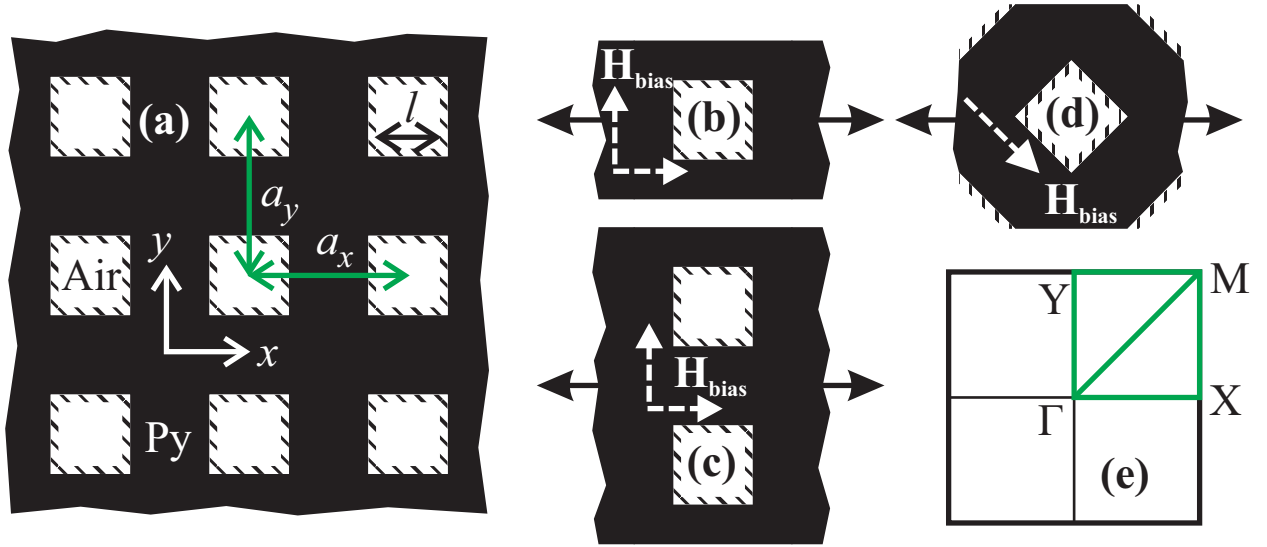


Figure 9.1.: (a) The 2D antidot lattice under consideration. A square lattice with a lattice constant  $a_x = a_y = 30$  nm is assumed for simplicity. The thickness  $s$  of the film is 3 nm. The antidots are square (white) air holes of edge  $l = 12$  nm in ferromagnetic Py (black) medium. Dynamics is pinned at the edge of holes. The pinned region is marked with a different texture. Element geometry used in micromagnetic simulations extends to over hundred repetitions in length (horizontal dark arrows in (b), (c) and (d)) for good wavenumber resolution. 2D PBC is applied over these elements to mimic the infinite geometry. White arrows in (b), (c) and (d) show the direction of bias field used for simulations of SW dispersion for BV and DE configuration. (d) shows the first BZ in the reciprocal lattice with typical symmetry point labels.

introduced by fixing magnetization vector in all cells of the discretization mesh, which border the antidots, i.e., in regions marked with different texture in Fig. 9.1. Figures 9.1 (b), (c) and (d) show parts of the elements over which 2D PBC are used to simulate the dispersion relation for different directions of the wave vector. These elements extend over 100 (up to 300) repetitions of unit cells in the horizontal direction to yield good resolution in the wavenumber domain. The 2D PBC is also implemented in order to improve the results with finite computational resources.<sup>244</sup> Figure 9.1 (e) shows the first BZ, the path in its irreducible part and typical symmetry points:  $\Gamma = (0, 0)$ ,  $X = \pi/a(1, 0)$ ,  $Y = \pi/a(0, 1)$  and  $M = \pi/a(1, 1)$ .<sup>211</sup> Note that when the bias field is in the plane, an asymmetry is expected between the two orthogonal directions of SW propagation:  $\mathbf{H}_{\text{bias}} \parallel \mathbf{k}$  (BV) and  $\mathbf{H}_{\text{bias}} \perp \mathbf{k}$  (DE).<sup>79</sup> Thus, the triangle  $\Gamma XM$  is no longer the irreducible BZ. However, in the forward volume arrangement when  $\mathbf{H}_{\text{bias}}$  is perpendicular to the plane of the 2D MC, the symmetry

is restored and dispersion is the same in the two orthogonal directions.<sup>97,307</sup> The technique described here can be used independent of the direction of  $\mathbf{H}_{\text{bias}}$ .

In order to get the results in the  $\Gamma - X$  and  $Y - M$  directions, we use different excitation signals of the form  $\mathbf{H}_{\text{sig}} = (0, 0, H_z)$ , on elements shown in Figs. 9.1 (b) and (c), respectively.  $\mathbf{H}_{\text{bias}}$  is horizontal along the  $x$  axis (dashed white arrows). Similarly, dispersion along the  $\Gamma - Y$  and  $X - M$  directions can be obtained when  $\mathbf{H}_{\text{bias}}$  is across the width of the elements (vertical arrows along  $y$  axis). Here,  $H_z = H_0 N_t N(x) n_y$  with  $\mu_0 H_0 = 5$  mT and  $N_t$ ,  $N(x)$  and  $n_y$  as given by Eqs. (9.1), (9.2) and (9.3), respectively:

$$N_t = \frac{\sin(2\pi f_c(t - t_0))}{2\pi f_c(t - t_0)}, \quad (9.1)$$

$$N(x) = \frac{\sin(k_c x)}{k_c x}, \quad (9.2)$$

$$n_y = \cos(2\pi y/y_{\text{max}}) + \sin(2\pi y/y_{\text{max}}). \quad (9.3)$$

See Eq. (7.2) for the detailed description of the terms involved in these equations. Here, the origin of coordinates is at the center of the considered geometry. It is due to  $N_t$  and  $N(x)$  that the signal contains power between  $\pm f_c$  and  $\pm k_c$  in frequency and wavevector domains respectively.<sup>262</sup>  $n_y$  should be asymmetric to ensure that both symmetric and antisymmetric modes are present in the resulting spectrum.<sup>297</sup> In Eq. (9.3),  $y$  goes from 0 to  $y_{\text{max}}$ . While computing dispersion along  $\Gamma - X$  and  $\Gamma - Y$  directions (Fig. 9.1 (b)),  $y_{\text{max}} = a$ . However, for  $Y - M$  and  $X - M$  directions (Fig. 9.1 (c)),  $y_{\text{max}} = 2a$ . Both the elements in Figs. 9.1 (b) and (c) will span the same infinite 2D geometry under a 2D PBC; except, in the later case we can control whether the dynamics in the neighboring rows will be in phase or out of phase. Thus we can fix the wavevector component  $k_y$  or  $k_x$  to 0 or  $\pi/a$  in the simulations. This is necessary to differentiate between the parallel directions  $\Gamma - X$  and  $Y - M$  or  $\Gamma - Y$  and  $X - M$ . Also,  $n_y^{mn}$  given by the expression

$$n_y^{mn} = C_m \cos(2m\pi y/y_{\text{max}}) + C_n \sin(2n\pi y/y_{\text{max}}) \quad (9.4)$$

can be used instead of  $n_y$  to selectively alter the amplitude of  $m$ -th symmetric or  $n$ -th antisymmetric mode. The freedom of choice of amplitudes  $C_m$  and  $C_n$  allows us to artificially

control the statistical temperature of the magnons in the crystal and also helps in isolating a single mode in the case of a degeneracy. We can also sum over  $m$  and  $n$  to alter multiple modes in a single dynamic simulation. We also attempt to obtain the dispersion in  $\Gamma - M$  direction by using the element shown in Fig. 9.1 (d). However, as there are two scattering centres (antidots) per cell in this arrangement, we can obtain the dispersion relations correctly only up to half of the BZ in that direction.<sup>97</sup>

Until now, we could use a signal similar to the one we did in the case of an 1D lattice.<sup>68</sup> But, this limitation forced us to come up with a new signal

$$H_z = H_0 N_t N(x) N(y) n(x) n(y), \quad (9.5)$$

which has to be used in a larger 2D lattice of  $100 \times 100$  antidot array (with the cell size  $d$  increased to 3 nm to decrease time of computations). Here,  $n(x)$  is given by:

$$n(x) = \sum_{m=1}^5 (\sin(2\pi m x/a) - \cos(2\pi m x/a)), \quad (9.6)$$

with analogous formula for  $n(y)$ . This signal is a point like source with the amplitude decay with distance as described by sinc function (in  $N(x)$  Eq. (9.2) along  $x$  axis and in similar form for  $N(y)$  for  $y$  dependence), having sharp cut-off in Fourier domain and able to excite symmetric and antisymmetric modes with respect to  $x$ - or  $y$ - axis. This signal was arrived upon largely by intuition, nevertheless, its agreement with the results obtained from PWM validates the usefulness of this signal. Spectral density, periodicity and asymmetry of the excitation signal (or source) should also be considered while developing similar techniques for other kinds of crystals (*e.g.* photonic or phononic crystals).

Three fold (one in time and two in space) Fourier transforms was needed to obtain the SW dispersion here. Magnetization was assumed to be uniform across the thickness of the film. We can now easily generalize that in the case of three-dimensional MCs, a signal of the form  $H_z = H_0 N_t N(x) N(y) N(z) n(x) n(y) n(z)$  will be required followed by a four fold discrete Fourier transform.

We have also calculated the spatial distribution of energy spectral density (ESD),  $S_f$  and

phase,  $\theta$  from the following equations:

$$S_f = |\tilde{m}(\mathbf{r}, f)|^2; \quad (9.7)$$

$$\theta = \tan^{-1} \left( \frac{\text{Im}(\tilde{m}(\mathbf{r}, f))}{\text{Re}(\tilde{m}(\mathbf{r}, f))} \right). \quad (9.8)$$

Here,  $\tilde{m}(\mathbf{r}, f)$  is the time domain Fourier transform, of a dynamical magnetization data. Unlike the new method used in Chap. 7, this gives us power from the entire wavevector domain for a selected frequency  $f$ . However, if power is present for just one particular wavevector then both methods yield qualitatively identical results.

The PWM is a spectral method in which the eigenproblem is numerically solved in the frequency and wavevector domains by the standard numerical routines. We solve here LLG equation in linear approximation without damping. The PWM calculations are performed with the assumption of the full magnetic saturation of the ADL along the bias magnetic field. As pinning during simulation will occur at the cell's center, a hole size of  $l + d$  was assumed during PWM calculations. Due to small thickness of the ADL, uniform SW profile across the thickness is assumed. The PWM in this formulation was already used in the calculations of the SW dynamics in 2D ADL and proved to give correct results.<sup>4,57,62,213</sup> The detailed description of the method can be found in Refs. 62 and 308.

## 9.2. Results and Discussions

The dispersion along the path in the first BZ shown in Fig. 9.1 (e) calculated with MSs by using the elements shown in Fig. 9.1 (b)-(d) is assembled as Fig. 9.2 (a) using solid lines. An overlay of dashed lines representing the SW dispersion relation obtained from the PWM is provided for comparison. Both these results appear to agree with each other except for the  $\Gamma - M$  direction where the numerical method was able to yield results for only half of the total BZ extent. This is because we set  $k_c$  to  $\pi/(\sqrt{2}a)$  here (the spatial periodicity is  $\sqrt{2}a$ ). Compared to the element shown in Fig. 9.1 (b), which can be used to produce results for  $\Gamma - X$  or  $\Gamma - Y$  directions, the one in Fig. 9.1 (d) features two scatter centres per unit cell. And, if we artificially increase  $k_c$  to  $\sqrt{2}\pi/a$ , both scattering centres will be activated to produce additional spurious modes.<sup>97</sup> To demonstrate the same we plot  $S_f$  (normalized

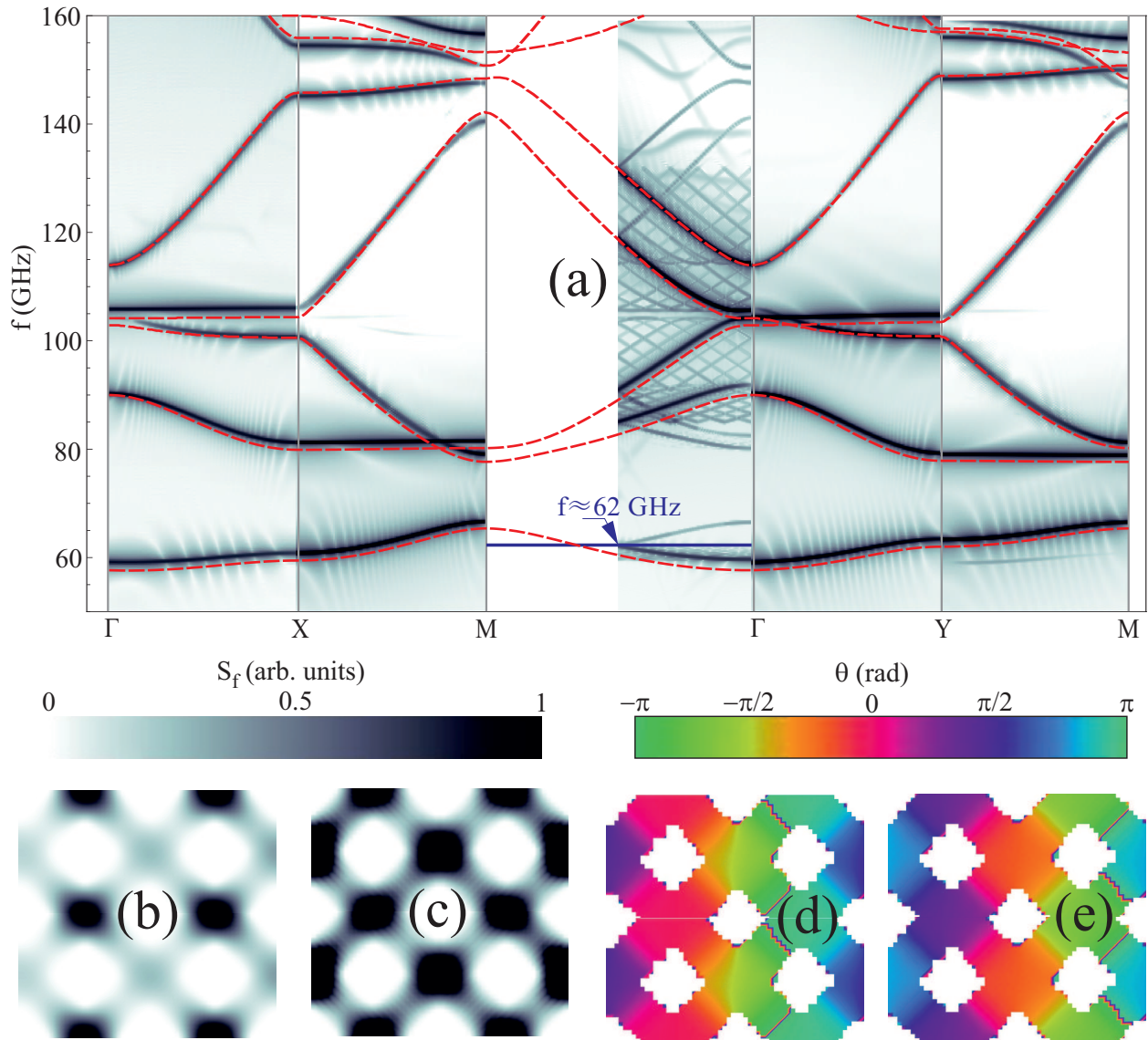


Figure 9.2.: (a) SW dispersion calculated using MSs (solid line) and PWM (dashed lines). ESD  $S_f$ , distribution for the horizontal line ( $f \approx 62$  GHz) shown in (a) in parts of the sample when the propagation direction is along  $\Gamma - M$  for (b)  $k_c = \pi/(\sqrt{2}a)$  and (c)  $k_c = \sqrt{2}\pi/a$ . Corresponding phase  $\theta$ , distribution is shown in (color online) (d) and (e), respectively.

between 0 and 1) and  $\theta$  (given by Eqs. (9.7) and (9.8), respectively), for frequency  $f \approx 62$  GHz in Figs. 9.2 (b) to (e). Note that the horizontal separation between regions of high ESD is about  $\sqrt{2}a$  in Fig. 9.2 (b) for  $k_c = \pi/(\sqrt{2}a)$ . This reduces to  $a/\sqrt{2}$  in Fig. 9.2 (c) for  $k_c = \sqrt{2}\pi/a$  when both scattering centres in the unit cell (of the element shown in Fig. 9.1 (d)) are activated at once. The phase distributions also confirm that neighbouring locations of high ESD are about  $\pi$  and  $\pi/2$  radians out of phase with each other in former

( $k_c = \pi/(\sqrt{2}a)$ ): Fig. 9.2 (d)) and later ( $k_c = \sqrt{2}\pi/a$ : Fig. 9.2 (e)) cases, respectively. Apart from incomplete result for the  $\Gamma - M$  direction, we can also see that the modes here (shown by solid lines) do not match with those for  $\Gamma - Y$  direction at the  $\Gamma$  point. This is because (cell size)  $d = \sqrt{2}$  nm was used while simulating for the  $\Gamma - M$  direction as opposed to  $d = 1.5$  nm, which was used in the case of  $\Gamma - Y$  direction. Also, there are additional modes of lower amplitudes visible in the case of  $\Gamma - M$  direction. This is due to the fact that  $N(x)$  becomes a stepped approximation of the right hand side of (9.2) by the use of the FDM; thus compromising the effectiveness of the cut off at  $k_c = \pi/(\sqrt{2}a)$ , and exciting the second scattering centre to some extent (but not as well as  $k_c = \sqrt{2}\pi/a$ ).

In pursuit of our quest to close the gap in the  $\Gamma - M$  direction we eventually decided to simulate the SW dynamics in a large 2D MC with signal defined by Eq. (9.5) and perform a three-fold Fourier transform in contrast with the two-fold transforms done earlier. We transformed time to frequency domain and  $x$ - and  $y$ - dimensions to the 2D wavevector domain. The resulting dispersion relation as calculated from the numerical method is shown in Fig. 9.3 (a) using solid lines. Thus, we have obtained the magnonic band structure along all high the symmetry directions. The overall agreement with the PWM results (shown by dashed lines) although is poorer in comparison with Fig. 9.2 (a). This is due to the fact that cell size in the later attempt was increased from  $d = 1.5$  nm to  $d = 3$  nm. The complete and partial bandgaps width and center frequency, as seen from the dashed lines in Fig. 9.3 (a), are extracted in Tab. 9.1. Here, values for partial bandgaps depend upon the path, which has been used to plot the dispersion. Bandgap I is the only complete bandgap observed here with the maximum width of 15.37 GHz.

Most bands observed in Fig. 9.3 (a) increase or decrease almost monotonously along any high symmetry direction. Consequently, the width of bandgap I too, appears to decrease monotonously as we move either along  $\Gamma \rightarrow X \rightarrow M$  or  $\Gamma \rightarrow Y \rightarrow M$ . Both upper and lower limits of bandgap I are present at point M which suggests an anti-crossing of bands at that point. This can also be regarded as the cause of the gap formation. Narrower bandgap widths have been observed by different techniques before.<sup>60</sup> The relatively high width of 15.36 GHz of bandgap I here can be attributed to small lattice dimensions and edge pinning.<sup>213</sup> Bandgaps II to XI (Fig. 9.3 (a) and Tab. 9.1) are direction dependent partial bandgaps.

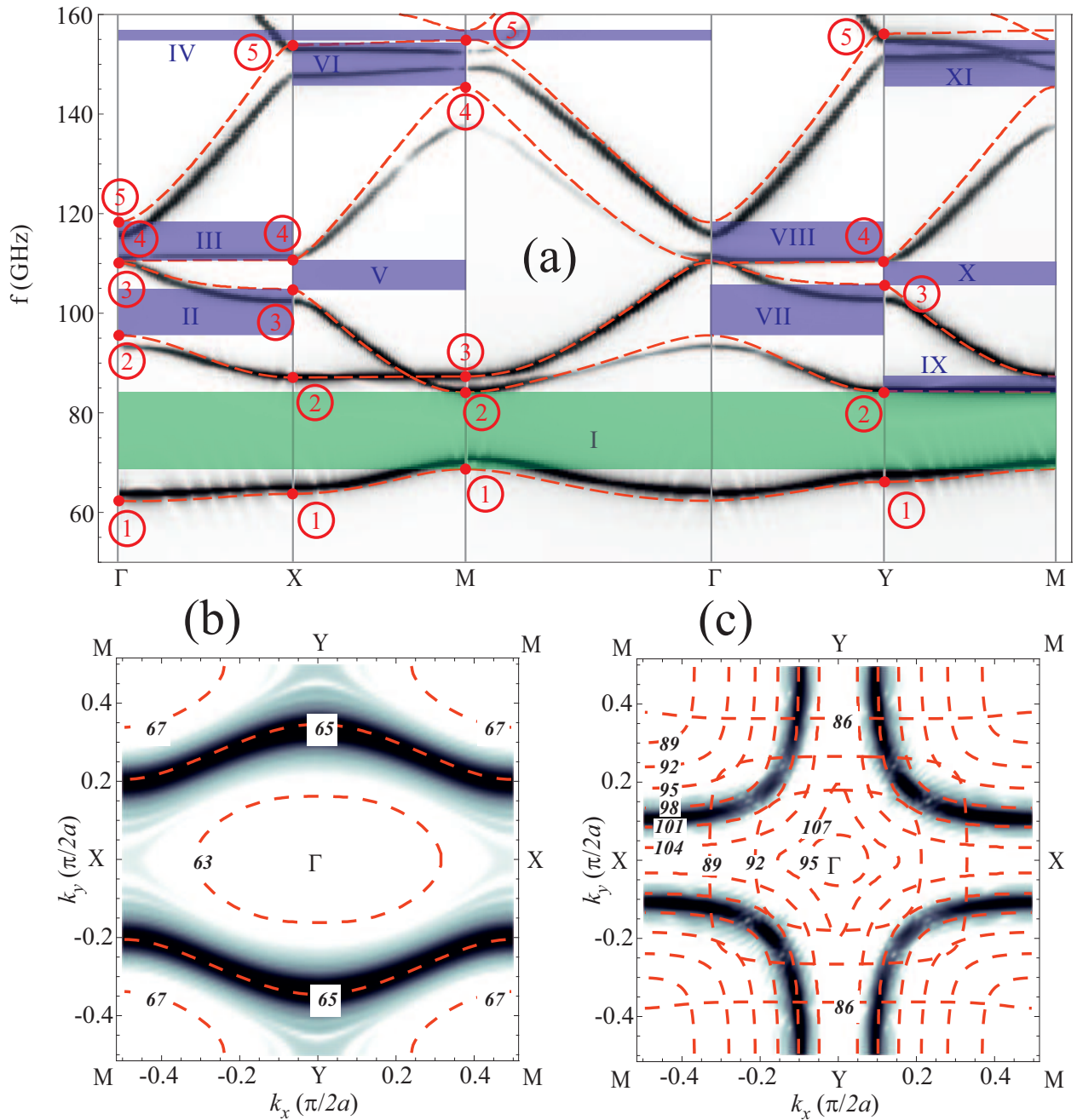


Figure 9.3.: (a) SW dispersion calculated using MS (solid line) and the PWM (dashed lines). The full and partial magnonic bandgaps are marked and numbered by Roman numerals. The circled Arabic numerals indicate the points on the dispersion for which the mode profiles are calculated in Fig. 9.4. Iso-frequency lines from (b) 63 GHz to 67 GHz (c) 86 GHz to 107 GHz (it is around the top and bottom of the first and second magnonic band, respectively) using the PWM is shown with dashed lines. Iso-frequency lines for (b)  $f \approx 67$  GHz and (c)  $f \approx 100$  GHz calculated by the numerical method is shown using solid lines.

Table 9.1.: Magnonic bandgap widths and center frequencies across different high symmetry directions as calculated by the PWM and labeled in Fig. 9.3 (a).

| Label | Extent                    | Center (GHz) | Gap Width (GHz) |
|-------|---------------------------|--------------|-----------------|
| I     | Complete Bandgap          | 76.39        | 15.36           |
| II    | $\Gamma - X$              | 100.18       | 9.24            |
| III   | $\Gamma - X$              | 114.45       | 7.7             |
| IV    | $\Gamma - X - M - \Gamma$ | 155.85       | 1.9             |
| V     | $X - M$                   | 107.75       | 5.9             |
| VI    | $X - M$                   | 149.6        | 8.4             |
| VII   | $\Gamma - Y$              | 100.68       | 10.24           |
| VIII  | $\Gamma - Y$              | 114.2        | 8.2             |
| IX    | $Y - M$                   | 85.80        | 3.01            |
| X     | $Y - M$                   | 108.1        | 4.6             |
| XI    | $Y - M$                   | 150.1        | 9.4             |

This is mainly because bands approaching point M from other high symmetry directions (with the exception of the band starting at  $\Gamma$ ⑤) tend to show greater slopes. As  $X$ ⑤ $\rightarrow Y$ ⑤ is a relatively flatter line, bandgap IV survives for three high symmetry directions. In a more isotropic forward volume arrangement,<sup>97,307</sup> bandgap IV might also have qualified as a complete bandgap if the dispersion in the  $X - M$  direction was also calculated. On the other hand, if wavevector dependent anisotropy is overlooked,<sup>5</sup> partial bandgaps (e.g. bandgap IV, or II and VII, or III and VIII) will appear as a complete bandgap. Partial bandgaps IV, V, VIII, X and XI are direct, while II, III, VI, VII and IX are indirect. Direct bandgaps are formed when the minimal and the maximal frequency of the magnonic bands surrounded the bandgap, from the top and bottom, respectively, are characterized by the same wavevector. While two different wavevectors are involved in the formation of indirect bandgap. In Fig. 9.3 (a) the minimal and maximal frequencies appear at high symmetry points. Occasionally, a bandgap may form between two high symmetry points due to anti-crossing of modes in a folded BZ,<sup>4</sup> but that is not observed here.

Now we calculate mode profiles ESD  $S_f$  and phase  $\theta$ , at the high symmetry points, using the PWM, for the first five modes as marked in Fig. 9.3 (a). The results are tabulated as Fig. 9.4 where  $S_f$  is represented by colour saturation and  $\theta$  is represented by hue. A general trend of higher frequency mode profiles limiting themselves to smaller regions in real space is observed. This trend has been seen for 1D systems as well.<sup>4</sup> Here, mode profiles

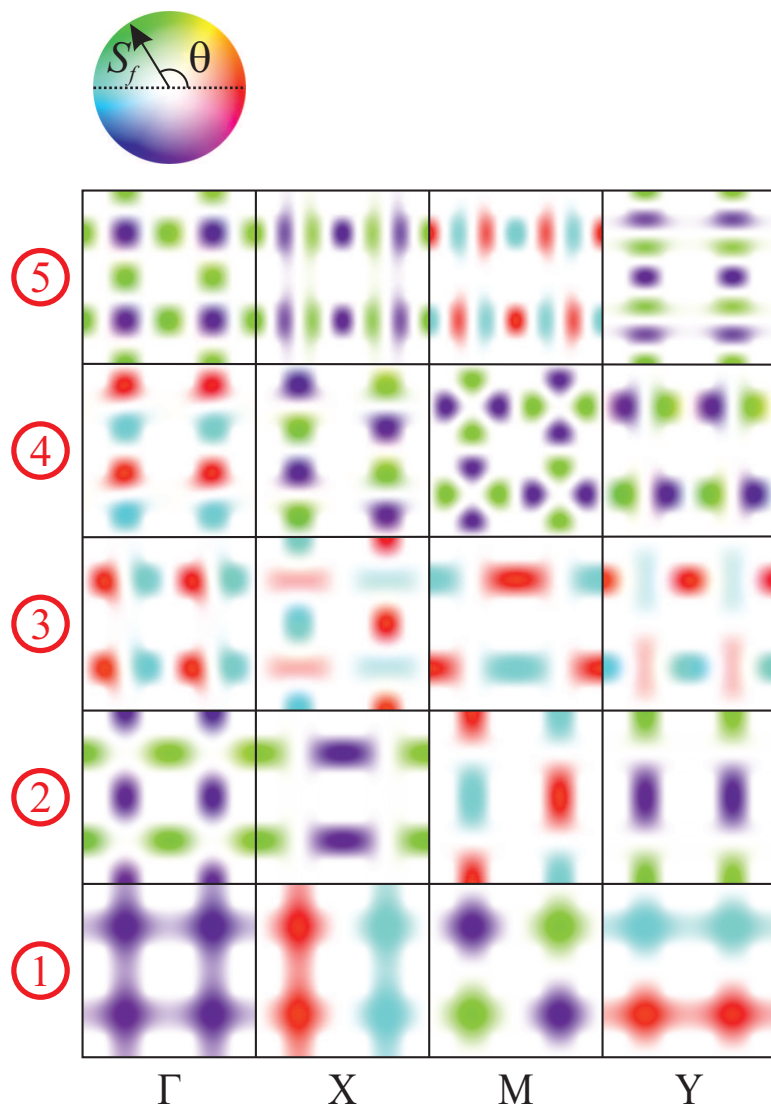


Figure 9.4.: (Color online) ESD  $S_f$ , and phase  $\theta$ , for high symmetry points  $\Gamma$ , X, M and Y at points ① through ⑤ marked on Fig. 9.3 (a).

appear similar in size at points  $X$ ⑤,  $M$ ⑤ and  $Y$ ⑤. Although, the distribution at  $Y$ ⑤ is vastly different due to a (nearby) mode-crossing in the  $Y - M$  direction (see Fig. 9.3 (a)). Mode profile at Y may be obtained by rotating the mode profiles at X by  $90^\circ$ . Modes with negligible group velocity are trapped and forbidden to move in specific high symmetry directions. Also, the number of nodal lines, which controls the spatial quantization of modes, generally increases with mode number ①:  $i \in \{1, 2, 3, 4, 5\}$ . No nodal lines are evident for  $\Gamma$ ①. Vertical and horizontal nodal lines are seen at  $X$ ① and  $Y$ ①, respectively; while  $M$ ① features both vertical and horizontal nodal lines. From Fig. 9.3 (a), we can see that points  $\Gamma$ ②,  $X$ ②,  $M$ ③ and  $Y$ ③ belong to the same mode and points  $\Gamma$ ③,  $X$ ③,  $M$ ② and  $Y$ ②

belong to a different mode. As the crossing between these modes occurs along the  $X - M$  direction, the mode profiles at  $X\textcircled{2}$  and  $M\textcircled{3}$  are comparable. Similarly, mode profiles at  $X\textcircled{3}$  and  $M\textcircled{2}$  are also comparable except,  $X\textcircled{3}$  has higher frequency and consequently, is more confined in space. In general, vertical and horizontal nodal lines dominate at points  $X$  and  $Y$ , respectively; while a more isotropic distribution is observed at point  $\Gamma$  and  $M$ . Modes  $\textcircled{1}$ ,  $\textcircled{2}$ , and  $\textcircled{5}$  are isotropic along  $x$ - and  $y$ -axes for the  $\Gamma$  point. However, modes  $\textcircled{3}$  and  $\textcircled{4}$  are disposed along rows and columns, respectively. Their local shape and size are comparable and accordingly, they are also degenerate as seen in Fig. 9.3 (a). Going from  $\Gamma$  to either  $X$  or  $Y$ ,  $\textcircled{4}$  maintains its size and frequency; except the  $DE^{309}$  geometry is evident in the later case. Similarly, the expanses of mode profiles at  $M\textcircled{2}$  and  $\textcircled{3}$  are comparable (as their frequencies are within 5 GHz of each other), and yet their orientations are mutually orthogonal.

Iso-frequency lines are shown in Figs. 9.3 (b) and (c), using both the PWM (dashed lines) and the MSs (solid lines). Iso-frequency contours calculated using the proposed method are thicker because small  $a$  yields a low wavevector resolution. The agreement between the results obtained from the two methods as 67 GHz line calculated using the MSs and the 65 GHz line calculated using the PWM is clear, but the 2 GHz difference in frequencies is due to the shift of the dispersion curves calculated with both methods shown in Fig. 9.3 (a). In contrast to Fig. 9.3 (b) the two methods appear to give identical results for the 100 GHz iso-frequency line, where the results of MS and PWM coincide. The shapes of iso-frequency lines control the direction of the propagating waves and consequently also alter the shapes of their wavefronts. Thus, although the dispersion along  $\Gamma - X$  and  $\Gamma - Y$  directions may appear comparable, the wavefronts of the propagating SWs from the first band will quickly uncover the underlying anisotropy, because of slightly different group velocity and curvature of different iso-frequency contours in two orthogonal directions, which is easily noticeable by the inspection of the contours for 63 and 65 GHz in Fig. 9.3 (b). This anisotropy is a manifestation of dipolar interactions hardly visible in this size and frequency regime in the magnonic band structure shown in Fig. 9.3 (a). Backward volume modes are characterized by negative group velocity in the case of dipole dominated or dipolar-exchange SW propagating in a ferromagnetic thin film.<sup>28</sup> This is not seen in Fig. 9.3 (a) as due to weakness of the dipolar

interactions the exchange field makes a significant contribution with increasing wavevector  $\mathbf{k}$  already near the BZ center.

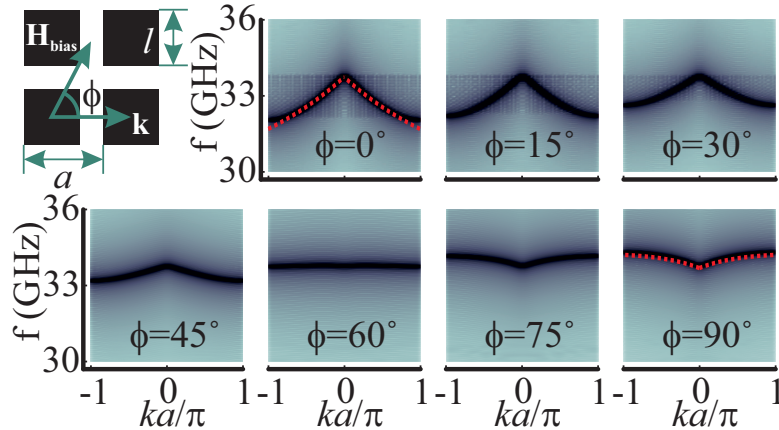


Figure 9.5.: First mode in a permalloy nano-dot array with varying angle  $\phi$ , between the bias field  $\mathbf{H}_{\text{bias}}$  ( $\mu_0 \mathbf{H}_{\text{bias}} = 1$  T), and wavevector  $\mathbf{k}$ , showing the transition from magnetostatic BV mode to DE configuration. The dashed lines are calculated using the analytic expressions for these two configuration with a reduced saturation magnetization. The structure considered here is given in the top left corner with  $a = 9$  nm,  $l = 6$  nm and thickness  $s = 3$  nm. Material parameters remain the same as before.

The developed method is not limited to the antidot lattices nor exchange dominated SWs. To prove this and better understand the properties of dipolar waves in MCs we take a look at the dispersion of SWs in the case of 2D MC composed of a square array (of lattice constant  $a = 9$  nm) of square dots (of edge  $l = 6$  nm and 3 nm thick). This structure is shown in the top left panel of Fig. 9.5 along with the dispersion relations of the first mode with increasing angle  $\phi$  (from  $\phi = 0$  to  $\phi = 90^\circ$ ), between  $\mathbf{H}_{\text{bias}}$  and  $\mathbf{k}$  in the subsequent panels. Here the wave propagation is mediated by the dipolar field only. We have found a strong anisotropy in the spectrum of the collective magnetostatic SW excitation, similar to already observed in the arrays of ferromagnetic dots of larger size in Ref. 47. We note here how the mode's group velocity gradually increases from negative (BV) to positive (DE) as  $\phi$  goes from  $0^\circ$  to  $90^\circ$ .<sup>47,301</sup> The transition appears to occur at a critical angle  $\phi = \phi_c \approx \pi/3$ . Note that here the direction of  $\mathbf{H}_{\text{bias}}$  is being changed as opposed to that of  $\mathbf{k}$  in the previous case. It is interesting to note that the dispersion relations obtained here for the array of nano-dots reminds us of the dispersion of magnetostatic waves in thin ferromagnetic film. To verify this hypothesis we calculate the dispersion

relation of magnetostatic waves in the thin ferromagnetic magnetic film (3 nm thick) with reduced magnetization, *i.e.* with the effective value of the saturation magnetization  $M_{s,\text{eff}}$ . The dashed lines overlaid in Fig. 9.5 are computed using the analytical expression for BV and DE configuration in the case of thin film<sup>28</sup> with a reduced saturation magnetization  $M_{s,\text{eff}} = M_s l^2 / a^2$ . A good agreement between the dispersion in the array and the effective thin film is found. A minor disagreement is introduced by the presence of the BZ boundaries but only near these boundaries. Further, the critical angle,  $\phi_c = \tan^{-1} \sqrt{H_{\text{bias}} / M_{s,\text{eff}}}$ <sup>310</sup> in the case of such thin film is also  $56.24^\circ \approx \pi/3$ . This implies that one should also be able to use the analytical expression to calculate the SW manifold between BV and DE geometries. This also shows, that a thin film MC composed of an array of saturated ferromagnetic nanodots can be used as a magnonic metamaterial, *i.e.*, an artificial crystal with tailored effective properties of spin wave dynamics.<sup>311–314</sup> Further studies are necessary to elucidate the limits of the effective saturation magnetization approach presented here. The influence of the dot–shape, their arrangement and inter–dot separation (mode–splitting has been experimentally demonstrated for nano–dot arrays<sup>315</sup>) need to further examined. However, these considerations are outside the scope of this work.

### 9.3. Conclusions

We have described a numerical algorithm to calculate the dispersion of plane propagating SWs in a 2D MC using multi-domain Fourier transform of results obtained from micromagnetic simulations. At the core of this technique is a new excitation signal, which is capable of generating SWs whose energy spectral density corresponds to the characteristic dispersion relation of the 2D MC. The lack of such signal has been discussed before in the case of 1D MCs.<sup>270,271</sup> The results obtained from this procedure were verified by the plane wave method when magnetization dynamics at antidot boundaries is pinned. We noted that both methods were in qualitative agreement with each other. The fact that better quantitative agreement was observed while using 2D PBC over 1D elements was due to lower cell size.<sup>4</sup>

Apart from a new numerical algorithm to compute the dispersion relation in any given direction of a two- or three-dimensional inverse lattice, this method will also allow for the

numerical computation of iso-frequency contours from micromagnetic simulations. Thus the numerical tool to study metamaterials properties of MCs was provided. It gives the possibility to design the properties of SWs relevant to technological applications and potentially exceeding these known from the homogeneous ferromagnetic thin films. The negative refraction, unidirectional media or caustic propagations are only some of the examples here.<sup>195,316,317</sup> Further, this method can be generalized to aid the numerical computation of dispersion or iso-frequency contours in the case of two- or three-dimensional phononic<sup>318</sup> and photonic<sup>319,320</sup> crystals as well.

The dispersion here appeared to be similar in  $\Gamma - X$  and  $\Gamma - Y$  directions. However, a noticeable anisotropy between the BV and DE geometries was very evident from the study of the mode profiles and the iso-frequency contours. As dipole field mediates the SW propagation in a 2D dot array we were able to obtain the negative group velocity associated with the first mode in the case of a BV magnetostatic configuration. We were also able to analyse the nature of bands and complete and partial bandgaps that were obtained from the dispersion calculations in the case of an MC. This can be useful in the design of attenuators,<sup>321</sup> phase-shifters,<sup>83</sup> filters<sup>85</sup> and logic gates.<sup>77</sup>

Low lattice constants were chosen in this article for both the antidot and the dot lattices to ensure a realistic computational time within the available computational resources. For larger lattice constants, larger cell sizes may be used with OOMMF. Cell sizes should not exceed the exchange length (about 5.6 nm in Py), if the exchange interaction is to be taken into account. In the case of 1D antidot waveguide, we noted<sup>66</sup> that a larger value of lattice constant  $a$ , brings the BZ boundaries closer and makes the modes less dispersive. Thus a smaller value of  $a = 9$  nm is used in the case of the nanodot array. In Ref. 47, some dispersion is observed (particularly in DE configuration), as nanodots are 30 nm thick. Simulating for a structure which is ten times thicker will similarly increase the required computational time. Recent advances in lithography techniques<sup>50,98–100</sup> have made it possible to fabricate dot and antidot lattices with a resolution below 10 nm. Thus, one can fabricate samples with dimensions comparable to the systems considered here. Experimental techniques similar to Brillouin light scattering spectroscopy<sup>111</sup> can be used to explore the SW dispersion relation.

# 10. Bandgaps in The Submillimetre Frequency Range in a Magnonic Antidot Waveguide

Even with all the improvements suggested so far to the numerical methods to compute SW dispersion, it is still difficult to confirm the existence of magnonic bandgaps – particularly in the submillimetre frequency range due to the aliasing which occurs during the Fourier transform of real valued magnetization data. As discussed in Chap. 4, the use of excitation signals in the form of sinc functions helps mitigate the aliasing. However, since the signal is applied only for a finite duration and only as a discrete approximation of the sinc signal, some aliasing is still seen. Close to the Nyquist frequency ( $\approx 500$  GHz in most cases), aliasing becomes well pronounced and obscures any bandgaps that may be existing there. Most of this work has been focused on magnetization dynamics in the microwave range; however, this chapter discusses an advancement made to the numerical method which nullifies aliasing in the entire SW spectrum and also raises the measured amplitude of the peaks.

## 10.1. Precessing Vector Fourier Transform (PVFT)

In order to avoid getting mirrored peaks (aliasing) from the Fourier transform of real valued data, we thought to generate complex valued data from the rotating components of the precessing magnetization vector. This has been shown in Fig. 10.1 where the projection,  $m_z$  of magnetization  $\mathbf{m}(t) = \mathbf{M}(t)/M_s$  along the bias field  $\mathbf{H}_{\text{bias}}$  (here we assume that the bias and the effective magnetic fields point almost in the same direction) does not change much

with time (Fig. 10.1 (a)) while the other two components,  $m_x$  &  $m_y$  do (Fig. 10.1 (b) & (c)). These three components are mutually orthogonal. This mapping was possible as one of the rotating components lead the other by a constant phase difference of  $\pi/2$  radians and they both have the same amplitude. As shown in Fig. 10.1 (c), these features can also be seen in a complex number  $z$  given by  $z = e^{i\omega t}$ .

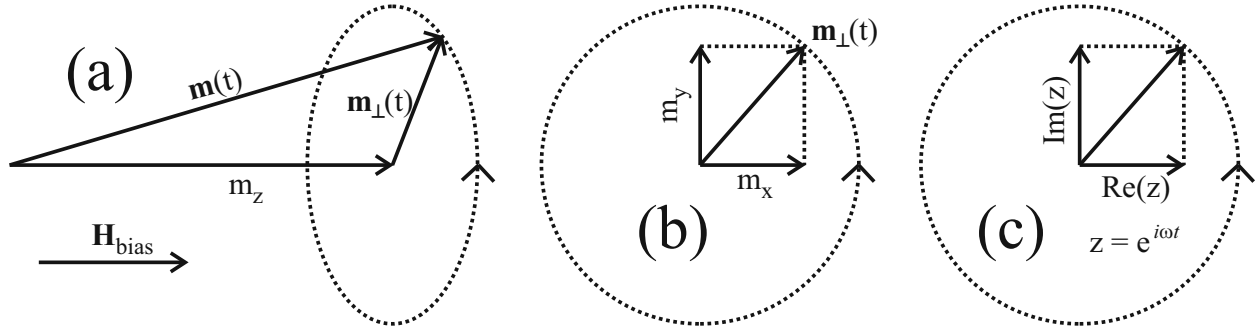


Figure 10.1.: A comparison between a precessing magnetization vector  $\mathbf{M}$  with a complex number of the form  $z = e^{i\omega t}$ . The bias field  $\mathbf{H}_{\text{bias}}$  points along the  $z$ -axis.

Consider the harmonic oscillator with the characteristic equation  $\ddot{r} = -\omega^2 r$ . Test functions  $r = z_+ = e^{i\omega t}$  and  $r = z_- = e^{-i\omega t}$  satisfy the equation. The real valued position variable  $r$  can then be expressed as

$$r = \frac{1}{2}(z_+ + z_-). \quad (10.1)$$

Fourier transforming,  $z_+$  or  $z_-$  w.r.t. time  $t$  will give a peak of unit amplitude at  $\omega$  or  $-\omega$ , respectively. On the other hand, Fourier transforming  $r$  (as given by Eq. (10.1)) will produce two peaks with half the amplitude: one at  $\omega$  and the other at  $-\omega$ . Thus, Fourier transforming  $z_+$  or  $z_-$  halves the number of peaks and doubles their amplitudes. This will improve the overall readability of the spectral data. So, instead of Fourier transforming any one component  $m_x$  or  $m_y$  (as marked in Fig. 10.1), we decide to transform  $m_i = m_x + im_y$ . It is assumed here that  $m_x$  leads  $m_y$ . Fourier transformation of  $m_i$  shall henceforth be referred to as *Precessing Vector Fourier Transform* (PVFT). Below, we will demonstrate the improvements achieved in the case of SW dispersion analysis as a result of this development.

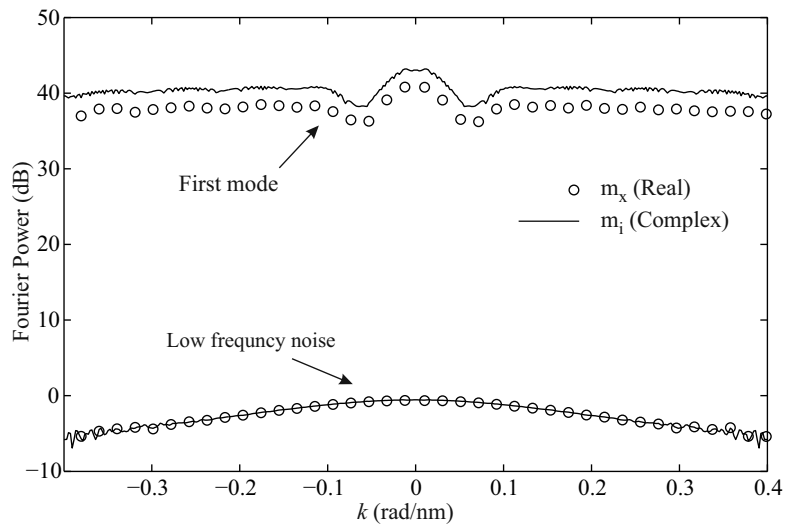


Figure 10.2.: A comparison between a precessing magnetization vector  $\mathbf{M}$  with a complex number of the form  $z = e^{i\omega t}$ . The bias field  $\mathbf{H}_{\text{bias}}$  points along the  $z$ -axis.

## 10.2. Increased Amplitude

To appreciate the increase in amplitude, one can compare the peaks corresponding to a SW dispersion mode with low frequency ( $f \approx 0$ ) noise level. Figure 10.2 shows power vs. wavevector profile of the first mode of a SW dispersion spectrum in a nano-wire with a cross section of  $3 \text{ nm} \times 3 \text{ nm}$ . Peaks at  $f \approx 0$  is also presented for comparison. The dynamics is simulated to have occurred in a bias of field  $\mu_0 \mathbf{H}_{\text{bias}} = 1.01 \text{ T}$  along the wire. Material parameters of Py were used during simulation. An uniform increase of power (about 2.4 dB) is observed across the wavevector range. A Hanning window after zero-padding (see Chap. 4) was used during both the conventional Fourier transform of  $m_x$  and the PVFT of  $m_i$ .

## 10.3. Reduced Aliasing

Consider the case of 2D ADL as shown in Fig. 9.1. In Fig. 10.3, we compare the result obtained by Fourier transform of real  $m_x$  and complex  $m_i$ . Here the lattice constants along  $x$ - and  $y$ - axes are  $a_x = 18 \text{ nm}$  and  $a_y = 24 \text{ nm}$ , respectively. The antidots are square holes (in a Py film) of edge  $l = 12 \text{ nm}$ . Film thickness  $u = 3 \text{ nm}$ . 2D PBC<sup>244</sup> is used to simulate an infinite lattice. We can clearly see that aliasing has reduced drastically in

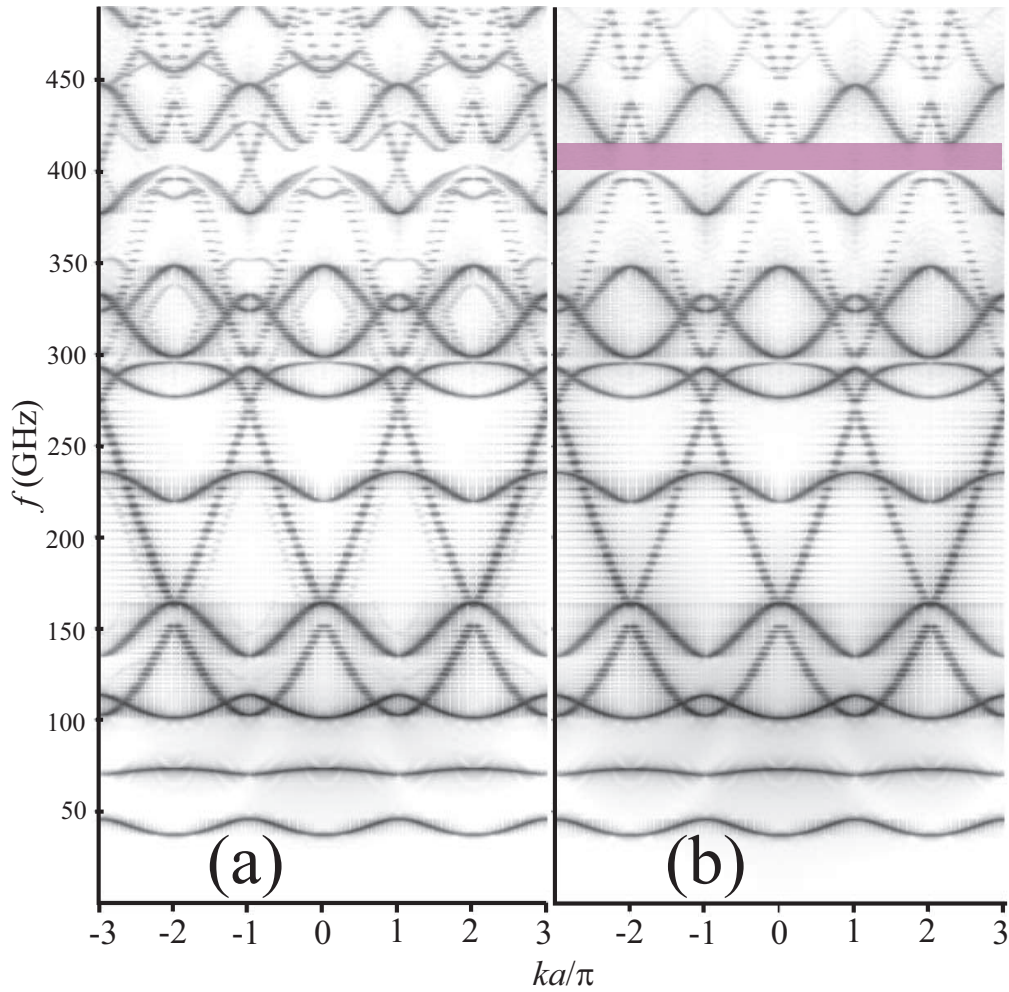


Figure 10.3.: SW dispersion in  $\Gamma - X$  direction in the case of a 2D ADL as shown in Fig. 9.1 without any edge pinning. Here lattice constants  $a_x = 18$  nm,  $a_y = 24$  nm, antidot edge  $l = 12$  nm and film thickness  $u = 3$  nm. A bias field  $\mu_0 \mathbf{H}_{\text{bias}} = 1.01$  T points along the  $x$ - axis. Material parameters of Py are assumed during simulations. (a)  $m_x$  and (b)  $m_i$  are used during Fourier transformations.

the submillimetre frequency range ( $> 300$  GHz) when we used PVFT in Fig. 10.3 (b). It is clearly observed that several aliased modes have disappeared in high frequency range (above 150 GHz). This demonstrates how the described technique has helped to improve the readability of the obtained results all the way up to the Nyquist frequency. As aliased modes get nullified, new bandgaps may appear. This has happened in the presented case where a 14.4 GHz wide bandgap (marked by a purple rectangle) appears above the 400 GHz mark. Thus, this new method has the potential to help reveal additional band gaps, which were previously unresolved and hence unavailable to any designer in a much higher frequency

range.

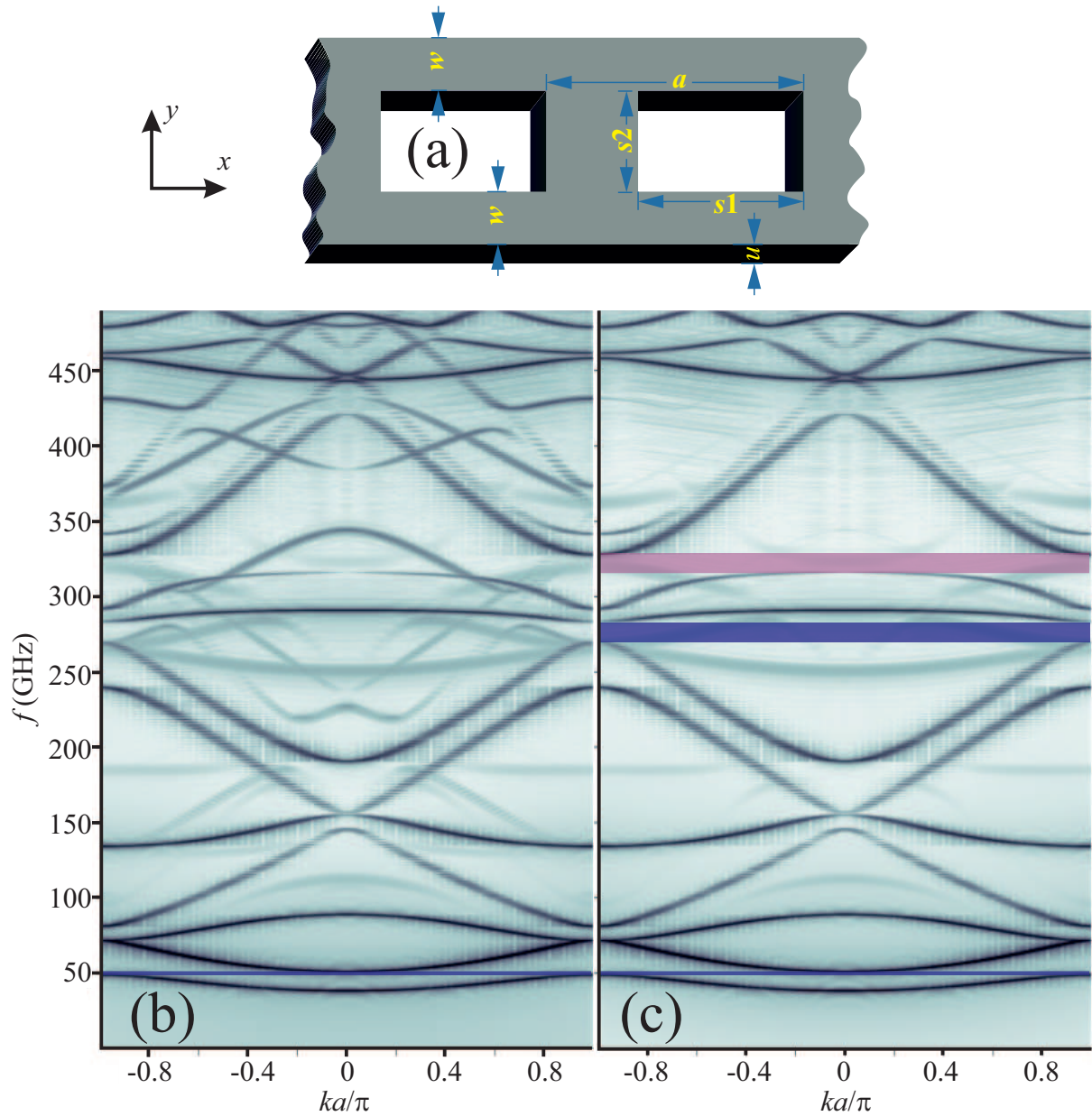


Figure 10.4.: SW dispersion in the case of a MAW as shown in (a) with  $w = 4.5$  nm,  $a = 18$  nm,  $s_1 = 12$  nm,  $s_2 = 9$  nm and  $u = 3$  nm under a bias field  $\mu_0 \mathbf{H}_{\text{bias}} = 1$  T pointing along the  $x$ - axis. Material parameters of Py are assumed during simulations. (a)  $m_x$  and (b)  $m_i$  are used during Fourier transformations.

Similar improvements were observed in the case of a MAW as shown in Fig. 10.4. Dispersion calculated using Fourier transformation of  $m_x$  and  $m_i$  are presented in Figs. 10.4 (a) and (b), respectively. A row of rectangular antidots of size  $(s_1, s_2) = (12, 9)$  nm is placed

centrally in  $2w + s2 = 18$  nm wide and  $u = 3$  thick Py waveguide. A bias field of  $\mu_0 \mathbf{H}_{\text{bias}} = 1$  T points along the length of the waveguide. During simulation, free boundary condition was used along with 1D PBC<sup>243</sup> (to mimic an ideal 1D magnonic crystal). A single 2.2 GHz wide bandgap marked by a blue rectangle is evident centred at 50.05 GHz in both cases. The new method, which yielded results shown in Fig. 10.4 (b) has successfully mitigated aliasing to verify the existence of two more bandgaps. Of these new bandgaps, the lower one of width 8.55 GHz (marked by a blue rectangle) is in the microwave frequency band (centred at 287.83 GHz) while the higher one (marked by a purple rectangle) is in the submillimetre frequency band (centred at 322.02 GHz).

Thus we established that the use of PVFT can increase the amplitude of peaks while also largely eliminating aliasing. This technique may be used in any problem where precessing vectors are encountered. In our case it enabled us to positively identify the existence of bandgaps in the submillimetre frequency band.

# 11. Experimentation Involving Magnonic Antidot Waveguides

In this chapter, we discuss some experimental results following the numerical works presented on one-dimensional (1D) magnonic antidot waveguides (MAWs). However, even with the recent advancements in nanofabrication, it is still not possible to fabricate large 1D or 2D periodic arrays of fine features with great precision. The samples presented here were fabricated using lithography techniques discussed in Sec. 3.5.

## 11.1. MAW Samples

The generic form of samples fabricated for this study is described in Fig. 11.1. The length and width of the waveguide was approximately  $60\ \mu\text{m}$  and  $5\ \mu\text{m}$ , respectively. Thickness was about  $20\ \text{nm}$ . Circular antidots of diameter  $d$  were milled in a  $6 \times 30$  array placed close to the middle of this waveguide. Their edge to edge separation was  $a_x$  along the length. The separation,  $a_{yi}$  between  $i^{\text{th}}$  and  $(i + 1)^{\text{th}}$  row is given as

$$a_{yi} = \begin{cases} a_{y1} & i \text{ is odd} \\ a_{y2} & i \text{ is even} \end{cases} . \quad (11.1)$$

Four such samples were studied experimentally using a time-resolved magneto-optic Kerr effect (TR-MOKE) setup. The approximate values of the parameters used for these samples are tabulated in Tab. 11.1. The exact values of antidots' diameters and their edge-to-edge separations ( $a_x$ ,  $a_{y1}$  and  $a_{y2}$ ) are within 10% of the tabulated values. Henceforth, the samples will be referred to by their Sample IDs as given in the table.

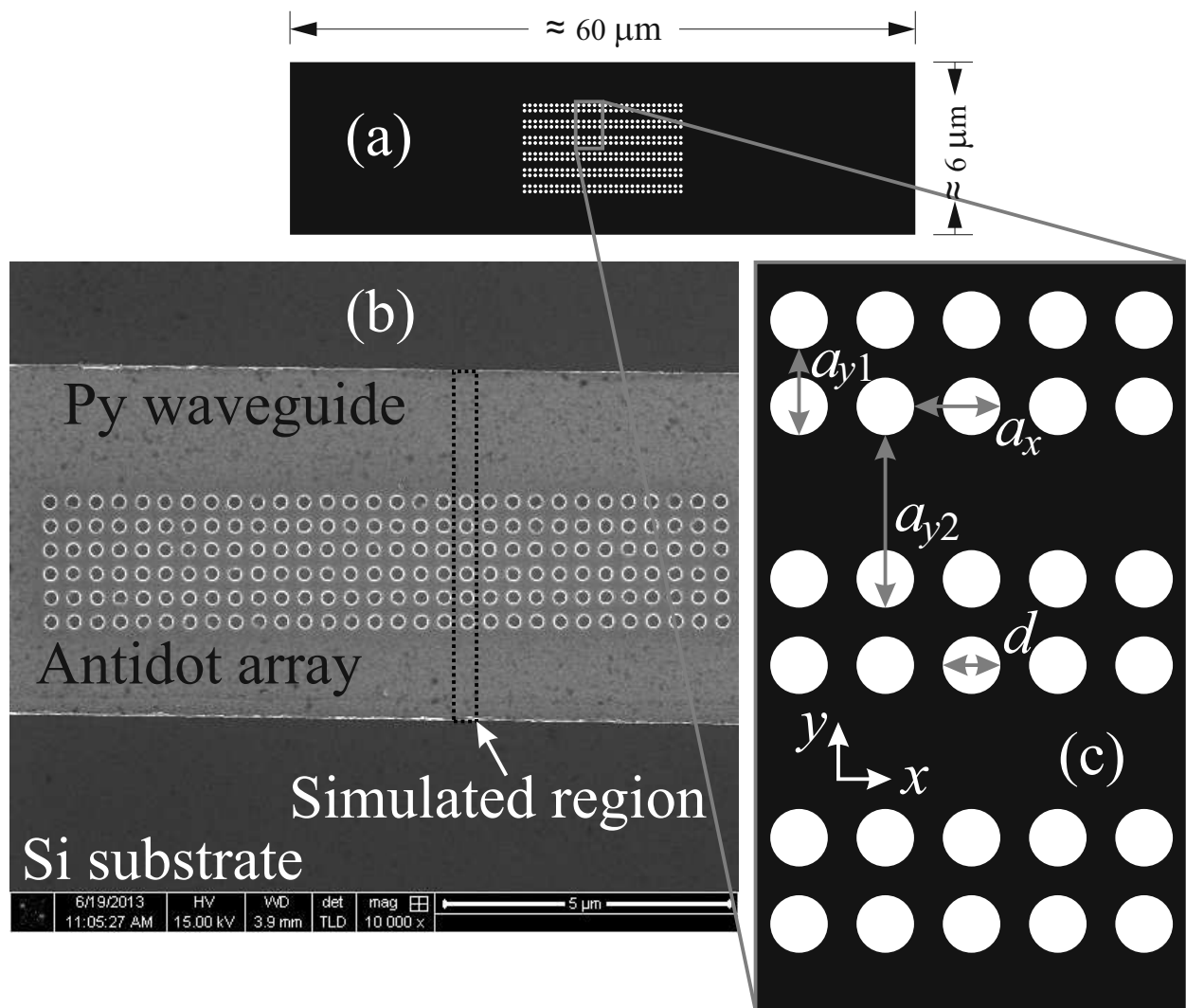


Figure 11.1.: (a) Dimension of the Py waveguide in which antidots were milled using focused ion beam lithography. (b) A scanning electron microscopy image produced during the inspection of the fabricated sample showing the 20 nm thick Py waveguide along with the antidot array, deposited over the Si substrate. (c) Dimensions within the antidot array.

Table 11.1.: Assignment of sample IDs to an instance of geometrical parameters as labelled in Fig. 11.1.

| Sample ID | $d$ (nm) | $a_x$ (nm) | $a_{y1}$ (nm) | $a_{y2}$ (nm) |
|-----------|----------|------------|---------------|---------------|
| ①         | 180      | 410        | 410           | 410           |
| ②         | 210      | 410        | 430           | 320           |
| ③         | 210      | 330        | 320           | 320           |
| ④         | 210      | 520        | 550           | 550           |

## 11.2. Magneto–Optic Kerr Effect (MOKE)

MOKE is a type of magneto–optic interaction associated with the change in polarization of light reflected from a magnetized surface. This effect was first observed by John Kerr in 1877.<sup>322</sup> The interaction of light with the applied magnetic field and magnetization of the material has been theorized to be the cause of this effect.<sup>6</sup> Upon reflection from a magnetized surface, a linearly polarized light transforms to an elliptically polarized light where the major axis of the ellipse is rotated from the plane of polarization of incident light by an angle proportional to the magnetization. This angular deviation can be measured to estimate the magnetization.

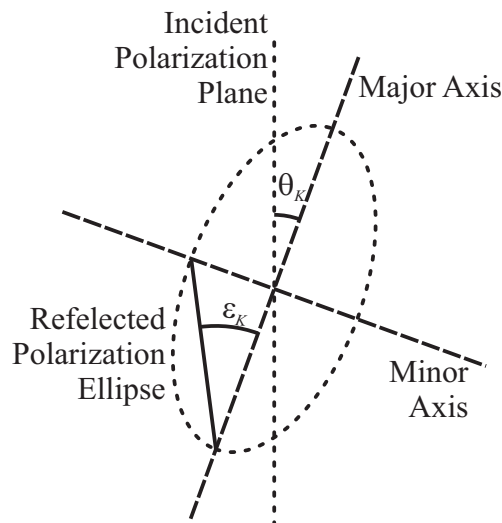


Figure 11.2.: Incident polarization plane and reflected polarization ellipse shown in dotted lines. Major and minor axes of the ellipse are shown in dashed lines. Kerr rotation and ellipticity are represented by angles  $\theta_K$  and  $\epsilon_K$ , respectively.

The angular distance between the major axis of the ellipse (of the elliptically polarized reflected light) and the plane of polarization (of the plane polarized incident light) is defined as *Kerr rotation*. This is marked as angle  $\theta_K$  in Fig. 11.2. *Kerr ellipticity* measures the flatness of the ellipse and is represented by angle  $\epsilon_K$  in Fig. 11.2. In our experiments we are interested in the Kerr rotation signal only.

### 11.2.1. Description of The Pump–Probe Optical Setup

A schematic of the TR–MOKE setup is presented in Fig. 11.3.<sup>6</sup> This setup is mounted on an optical table which is engineered to facilitate rapid attenuation of any acoustic vibrations. The table also features a very smooth surface covered with a square array of circular holes (25 mm grid) which facilitates the equipment setup process.

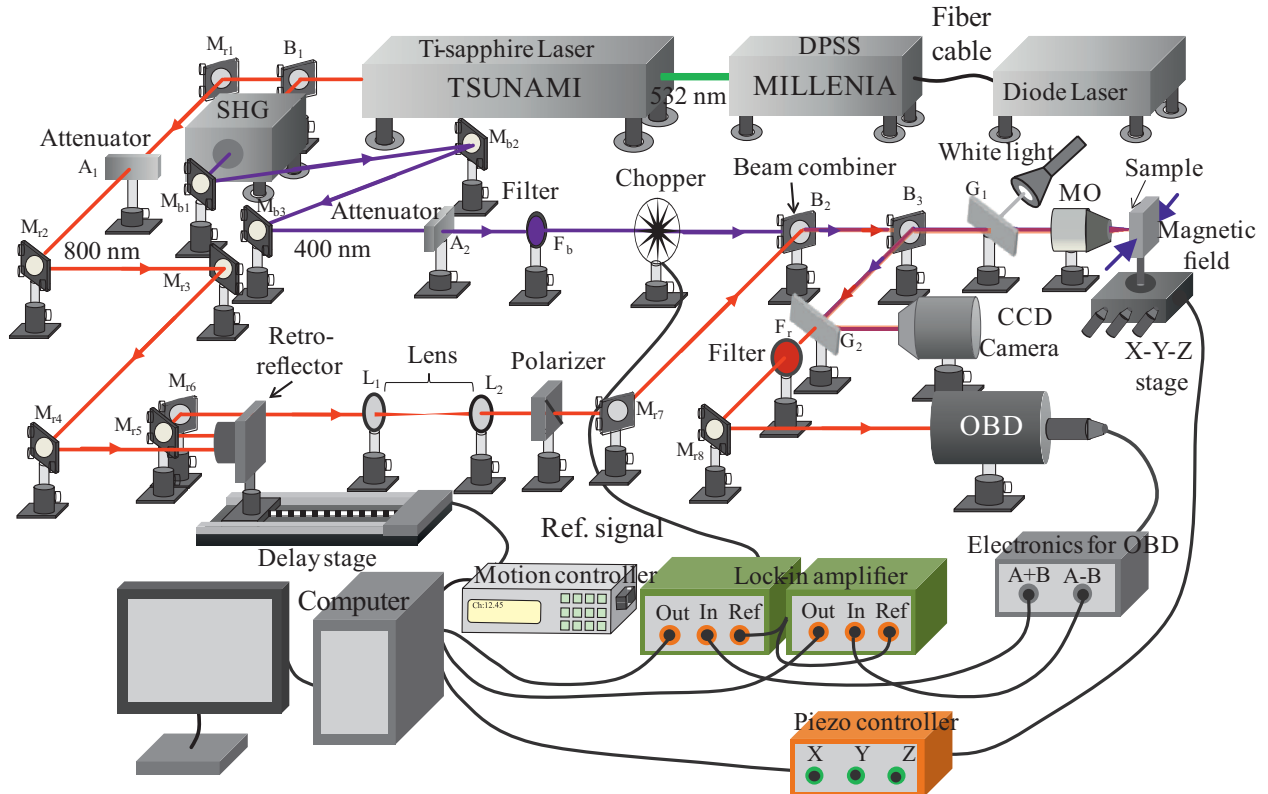


Figure 11.3.: A schematic diagram of an all optical TR–MOKE microscope with collinear pump–probe geometry as housed in the lab at the S. N. Bose National Centre for Basic Sciences. Source: Ref. 6.

As seen in Fig. 11.3, a diode laser is used to pump a solid state laser (Millenia), which in turn pumps the Ti–sapphire laser (Tsunami) with a maximum power of 10 W using a 532 nm light. Regenerative mode locking is used here to produce a train of laser pulses with  $\approx 70$  fs pulse width and average power of  $\approx 1.6$  W. The pulses come at a frequency of 80 MHz ( $\approx 20$  nJ/pulse). The output of a Ti–sapphire laser can be tuned from 690 nm to 1080 nm. However, here we keep the output wavelength at 800 nm. The Tsunami laser features control knobs which manipulate prisms in optical path to change the mean wavelength, pulse-width and power of the output beam. This output beam is vertically polarized with a spot size of

$\approx 2$  mm.

About 70% of the beam is directed towards a second harmonic generator (SHG) using the beam splitter  $B_1$  (see Fig. 11.3). An SHG uses non-linear methods<sup>323</sup> to halve the beam wavelength to 400 nm. This beam is used to excite the magnetization dynamics and is referred to as the *pump beam*. The Kerr rotation and thus the magnetization dynamics is probed using the 800 nm beam. This is referred to as the fundamental beam or the *probe beam*. The paths of the pump and probe beams are marked by blue and red lines, respectively in Fig. 11.3. A spectral filter  $F_b$  is used to ensure that no trace of the fundamental beam remains mixed with the probe beam. A sequence of mirrors ( $M_{b1}$ ,  $M_{b2}$  and  $M_{b3}$ ) is used to guide the pump beam on to the sample. An attenuator is used to control the intensity of the incident pump beam. A chopper modulates the intensity of the pump beam at 2 kHz. This modulation frequency also serves as a reference signal during the lock-in detection process of the probe beam. The path of the pump beam remains fixed.

The probe beam passes through a computer controlled variable delay stage, which uses a retro-reflector to turn the beam by  $180^\circ$  with some lateral off-set. Fixed mirrors ( $M_{r1}$ ,  $M_{r2}$ ,  $M_{r3}$  and  $M_{r4}$ ) are used to guide the probe beam on to the retro-reflector. An attenuator is also used here to control the intensity of the probe beam. Mirrors  $M_{r5}$ ,  $M_{r6}$  and  $M_{r7}$  are used to guide the retro-reflected probe beam on to the sample. A pair of collimating lenses  $L_1$  (focal length = 75 mm) and  $L_2$  (focal length = 200 mm) are used in telescopic arrangement to increase the probe beam's diameter to  $\approx 5$  mm, so the entire back-aperture of the microscope objective (MO) may be used. A Glan-Thompson polarizer (extinction coefficient 100,000 : 1) is used to refine the polarization state of the probe beam.

Both pump and probe beams are combined at beam combiner  $B_2$ , which is essentially a 50 : 50 non-polarized beam splitter set at  $45^\circ$  to the optical of the probe beam. Meticulous effort is required to ensure that both the pump and the probe beams remain collinear from this point.<sup>6</sup> The combined beam then passes through a MO (M-40X; N. A. = 0.65) at normal incidence which focuses the probe beam on the surface of sample to a diffraction limited spot size of about 800 nm. The pump beam is slightly defocused (spot size =  $1\mu\text{m}$ ) on the sample due to chromatic aberration. The sample is held by using a sample holder mounted on a computer controlled piezoelectric scanning  $x - y - z$  stage.

A white light source is used to illuminate the surface of the sample. This helps see micron size features on the sample using a charged coupled diode (CCD) camera and ascertain that the pump and probe beams are aligned on a desired spot on the sample. White light from the white light source is reflected into the MO by using a glass slide ( $G_1$ ). A beam-splitter  $B_3$  is used to turn the reflected pump, probe and white lights by  $90^\circ$  (see Fig. 11.3). The white light is guided into the CCD camera by using another glass slide ( $G_2$ ). The white light is turned off once the initial alignment has been verified. The probe is filtered out using a spectral filter  $F_r$ . Thus only the reflected probe beam, which contains the Kerr rotation signal is allowed to reach the optical bridge detector (OBD). Due to the conical symmetry of the beam focused using the MO, the effect of the in-plane (longitudinal and transverse) components of magnetization gets averaged out and only the out of plane, or *polar* component of magnetization contributes to the observed Kerr rotation.

Within the OBD, a polarized beam-splitter is used to split the elliptically polarized reflected probe beam into two mutually orthogonal plane polarized beams. The intensity of these plane polarized beams is converted into electronic signals,  $A$  and  $B$ , using Si-photodiodes. The sum ( $A + B$ ) and difference ( $A - B$ ) of these signals give total reflectivity and Kerr rotation. The polarized beam-splitter is kept at  $45^\circ$  to the initial plane of polarization to ensure the *balance* of the bridge:  $A - B = 0$ . Generally,  $A - B \propto M_z$ , where  $M_z$  is the  $z$ -component of the magnetization. The reflectivity signal ( $A + B$ ), contains information regarding carrier dynamics and phonon dynamics.

## 11.3. Results and Discussion

### 11.3.1. TR-MOKE Measurements from the $\text{Ni}_{80}\text{Fe}_{20}$ Antidot

#### Waveguide

Figure 11.4 shows the time-resolved Kerr rotation and the corresponding spin wave spectra and the simulation data corresponding to ① in (top panels) backward volume (BV) and (bottom panels) Damon-Eshbach (DE) configurations (see sub-Sec. 2.4.2). The Kerr rotation signals  $\theta_K \propto A - B \propto M_z$  as obtained from TR-MOKE microscopy for BV and DE configurations is given in Figs. 11.4 (a) and (b), respectively. Here the BV and DE configu-

rations refer to arrangements where the bias magnetic field is applied along  $x$ - and  $y$ - axes of the geometry described in Fig. 11.1 (c). In both cases, an ultrafast demagnetization followed by a fast re-magnetization and a slow re-magnetization and a precessional oscillation superposed on the relaxing magnetization is observed. A bi-exponential background (see sub-Sec. 2.3.4) is subtracted from the raw data to obtain  $\theta'_K$ :

$$\theta'_K(t) = \theta_K(t) - \theta_1 \exp(-t/\tau_1) - \theta_2 \exp(-t/\tau_2). \quad (11.2)$$

Here  $t$  is the time delay (controlled by the delay stage) in the arrival of the probe (beam) pulse w.r.t. to the pump (beam) pulse.  $\theta'_K(t)$  is shown for BV and DE configurations in Figs. 11.4 (c) and (d), respectively. The variables  $\theta_1$ ,  $\theta_2$ ,  $\tau_1$  and  $\tau_2$  are obtained using curve fitting techniques while minimizing the standard deviation of  $\theta'_K(t)$ .  $\tau_1$  and  $\tau_2$  are the relaxation times as discussed in sub-Sec. 2.3.4. The values of  $\tau_1$  and  $\tau_2$  obtained from curve fitting the experimental data presented in this chapter are of the order of 5 ps and 200 ps, respectively. Uniform waveguides registered a higher value of  $\tau_1$  ( $\approx 10$  ps). These results are in agreement with known values for permalloy.<sup>6</sup>

Energy spectral densities (ESDs) – squares of Fourier transforms of  $\theta'_K(t)$  for BV and DE configurations are plotted in Figs. 11.4 (e) and (f), respectively in arbitrary units using a non-logarithmic scale. Figs. 11.4 (g) and (h) are ESDs obtained using micromagnetic simulations for BV and DE configurations, respectively. The material parameters of Py were used during simulation with a cell size of 5 nm  $\times$  5 nm  $\times$  20 nm. A Gilbert damping constant of 0.008 was used for the dynamic simulation. A pulse excitation field was used to trigger the magnetization dynamics. Here the Fourier transforms are done directly on the spatially averaged  $z$ - component of magnetization. 1D periodic boundary condition (PBC) is used on a column of holes (as shown in Fig. 11.1) to mimic a large array. The same material parameters of Py, as used in the previous chapters (see page ‘xx’) were used during simulations in all cases examined in this chapter.

The experimental results differ from the simulated ones to some extent as the actual material parameters may differ to some degree from their ideal values due to fabrication defects. Also, some geometrical parameters vary from one column of antidots to another. On the other hand, while using the PBC all column are assumed to be identical. Further,

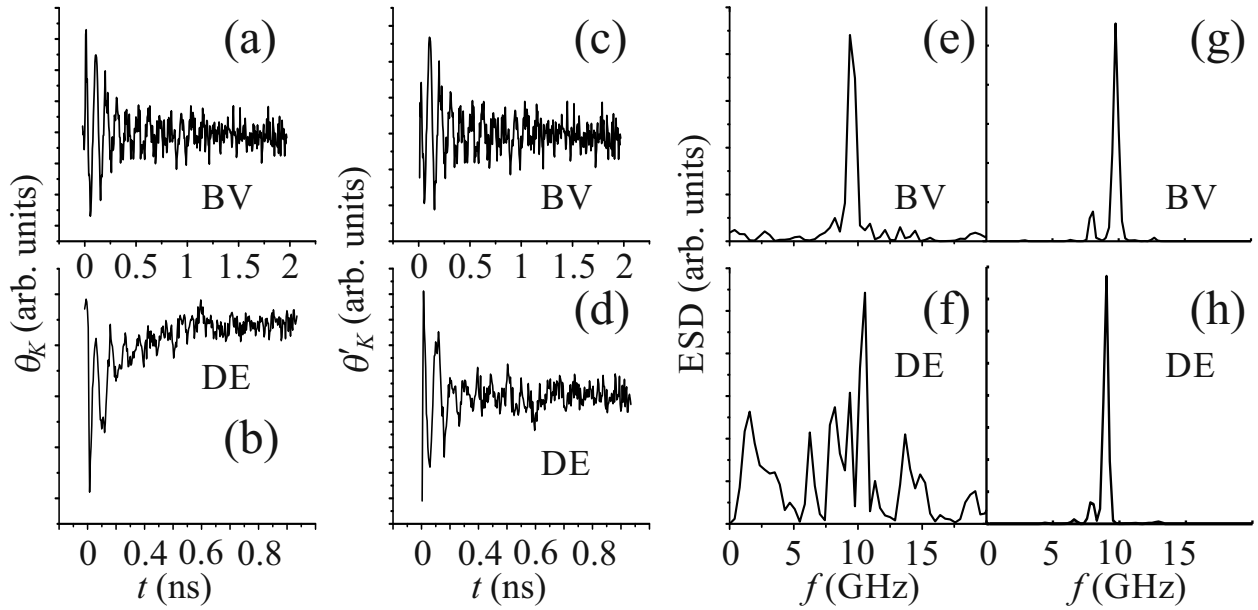


Figure 11.4.: TR-MOKE and simulation data for ① in (top row) BV and (bottom row) DE configurations. (a) and (b) show the time resolved Kerr rotation ( $\theta_K$ ) signal on a linear scale as obtained during experimentation. (c) and (d) represent the same signals with their bi-exponential backgrounds subtracted ( $\theta'_K$ ). (c) and (g) show the corresponding ESDs. ESDs are also calculated using micromagnetic simulations for (d) BV and (h) DE configurations. Bias field strength is 1 kOe in all cases.

the simulations are performed at an absolute zero temperature. Also, the use of PBC causes a reduction in observed number of modes.<sup>303</sup> PBC is used nonetheless, because simulation of the entire geometry would otherwise require forbiddingly vast computational resources. Thus, we generally expect a mode which is observed in simulation to be present in the experimental measurements, but not vice-versa. However, in few simulation results, artificial periodicity may produce a spurious mode or cause a mode to shift along the frequency axis. Henceforth, we represent the set of peaks observed during a simulation by  $\{f_S\} : f_S \in \{f_S\}$ . The set of experimentally observed peaks  $\{f_E\}$  can then be constructed such that the sum  $\sum (f_E - f_S)^2$  is minimized.

For a deeper understanding of the origin of SW band structure, one needs to consider the power and phase distribution of SWs as a function of position.<sup>4,49,50,64,65,68,117,262,324–326</sup> The same has been tabulated in Fig. 11.5 for different cases. The first and the third columns mark the case by declaring the sample ID, the peak frequency  $f_S$ , the magnetic bias field strength  $H_{\text{bias}}$  and the configuration (BV or DE). The second and the fifth columns depict the power

profiles and the third and the fourth columns depict the phase profiles. Six columns of holes are shown in each case by placing the simulated geometry nine times side-by-side (1D PBC has been used along the length of the waveguide).

In the simulated geometry, the presence of antidots divides the waveguide into two sub-waveguides. However, in reality this division is not complete as the rows of antidots are shorter than the waveguide itself. For the BV configuration corresponding to Fig. 11.4 (g), we have  $\{f_S\} = \{8.06, 9.77, 12.70\}$  GHz and  $\{f_E\} = \{8.20, 9.38, 10.94\}$  GHz. As seen in Fig. 11.5, the first two modes correspond to BV mode (located amidst the antidot lattice) and the ferromagnetic resonance mode (of the two sub-waveguides), respectively. The third mode is a highly quantized mode resonating in the antidot lattice itself. Since, during fabrication, the distance between any two column of antidots,  $a_x$ , can vary by  $\pm 10\%$ ,<sup>64</sup> we can see a number of modes around this region in Fig. 11.4 (e). For the DE configuration corresponding to Fig. 11.4 (h), we have  $\{f_S\} = \{6.59, 7.81, 9.03\}$  GHz and  $\{f_E\} = \{6.25, 8.20, 9.38\}$  GHz. As the bias field points along the width of the waveguide, demagnetized regions develop near the edges. Thus, the first mode here corresponds to the edge mode which is also confirmed by Fig. 11.5. The second mode is the DE mode, which corresponds to the demagnetized regions in the antidot lattice itself. Apart from the antidot lattice, this mode also resonates some distance away from the edges of the waveguide. Most of the power of the third mode is present in the two sub-waveguides. Another mode seen above 12.5 GHz possibly results due to highly quantized SW resonance as seen in the BV configuration as well. As the use of 1D PBC creates a stronger partition between the two sub-waveguides the resulting demagnetization becomes more pronounced leading to an overall negative shift in the SW frequency domain.

### 11.3.2. Dependence of SW Spectrum on the Lattice Parameters

The dependence of SW spectrum on the lattice parameters of the arrays (as given in Tab. 11.1) is shown in Fig. 11.6. The observed peaks have been analysed qualitatively to understand their nature. These peaks are also tabulated in Tab. 11.2 for a quantitative comparison. As the peaks move with changes in the lattice constants, a clear tunability transpires. Their power and phase distribution has also been presented in Fig. 11.5. A high

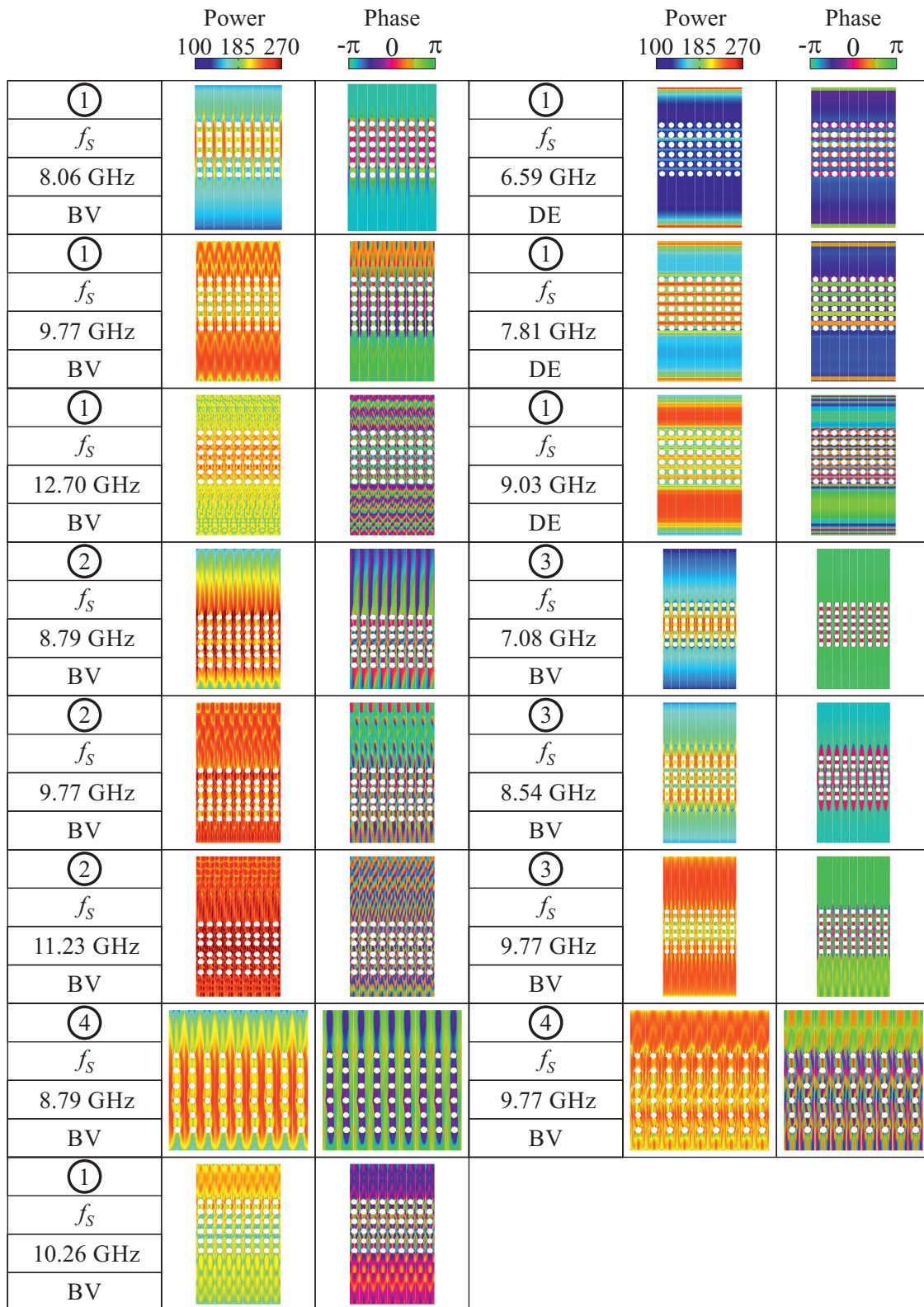


Figure 11.5.: SW power and phase calculated for different cases as marked in the first and the third columns. Bias magnetic field strength is at 1 kOe in all cases.

amplitude peaks is observed in all simulated cases at  $f_S = 9.77$  GHz. This corresponds to the ferromagnetic resonance in the sub-waveguides (see Fig. 11.5). As the sub-waveguides occupy a vast area, a peak of high amplitude can be expected. As  $a_{y1} + a_{y2}$  is the highest for ④, the area of sub-waveguides is minimized, resulting in a peak with lower amplitude. Thus we note that the average relative SW power of different modes can be controlled by changing the areas of the regions that they occupy. Depending upon the position of the array of antidots, the width of the sub-waveguides may be different. As seen in Fig. 11.5, this can lead to a small phase difference ( $\ll \pi$ ) between the sub-waveguides in a few cases.

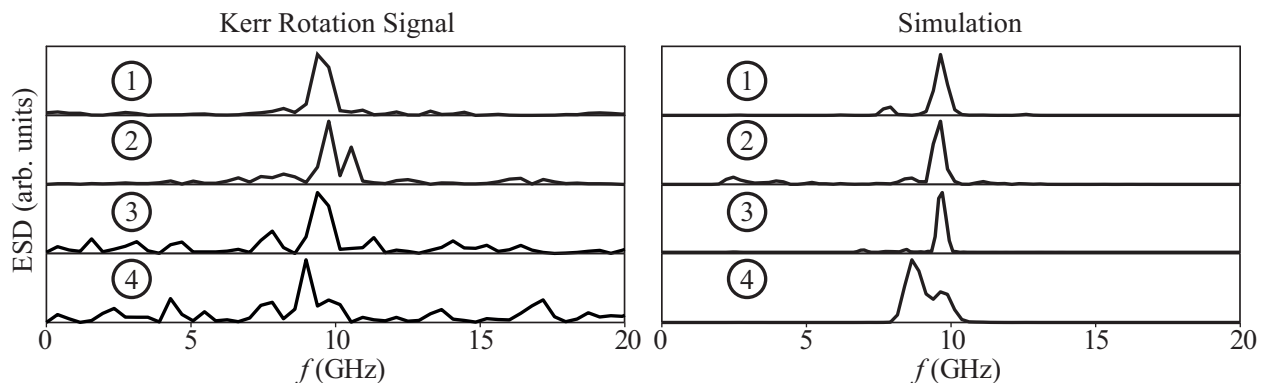


Figure 11.6.: SW ESD calculated using (left column) Kerr signal and (right column) simulations for ①, ②, ③ and ④ with a constant bias magnetic field strength  $H_{\text{bias}} = 1$  kOe along the length of the waveguide. A linear scale is being used to represent the peaks here.

Table 11.2.:  $\{f_S\}$  and  $\{f_E\}$  for results presented in Fig. 11.6.

| Sample ID | $\{f_S\}$ (GHz)     | $\{f_E\}$ (GHz)     |
|-----------|---------------------|---------------------|
| ①         | {8.06, 9.77, 12.70} | {8.20, 9.38, 10.94} |
| ②         | {8.79, 9.77, 11.23} | {8.20, 9.77, 10.55} |
| ③         | {7.08, 8.54, 9.77}  | {6.64, 7.81, 9.38}  |
| ④         | {8.79, 9.77}        | {8.98, 9.77}        |

The peaks attributed to the ferromagnetic resonance of the sub-waveguides appear to agree well with corresponding experimentally observed peaks. In all cases at least one BV mode, localized amidst the antidot array, is observed between 8 GHz and 8.8 GHz with little or no quantization. For ③ another BV mode is seen at 7.08 GHz. For ② as well, multiple BV modes are seen below 5 GHz, with relatively lower quantization (these modes are not shown in Fig. 11.5). As these modes are localized in the antidot lattice, their position (in the

frequency domain) is more sensitive to fabrication related fluctuations of lattice parameters  $d$ ,  $a_x$ ,  $a_{y1}$  and  $a_{y2}$ . Quantized modes in the antidot lattice is also seen for ① and ② above 10 GHz. When compared with the experimental results, these modes show more movement possibly because the quantization increases the sensitivity towards any variance in the lattice structure. These observations suggest that modes localized amidst the antidot array may be more sensitive to the precision of the fabrication processes.

### 11.3.3. Bias Field Dependence

We noticed that the peak associated with the ferromagnetic resonance of the sub-waveguides did not vary significantly with lattice constant in Fig. 11.6. This peak largely depends upon the magnitude of the applied bias field. In Fig. 11.7, we show the field dependence of SW band structure for a uniform waveguide and ① and ③. Bias field strengths of 1 kOe (maximum), 821 Oe, 692 Oe, 587 Oe and 492 Oe (minimum) were used for this experiment. A low frequency peak is visible in some experimental measurements. Typically it is associated with normal low frequency noise which occurs during TR-MOKE measurement and is filtered out during post processing by using a high pass filter. However, here the peaks, which appear systematically for certain bias magnetic field magnitudes — 821 Oe in all cases and 692 Oe for ③, have been presented as it is to allow for the readers to develop their interpretation independently.

A single peak which decreases monotonously with decreasing  $H_{\text{bias}}$  is seen in the case of the uniform waveguide. Experimentally observed peaks also appear to (qualitatively) agree with this Kittel mode (see sub-Sec. 2.3.3). This also helps to confirm that magnetic material parameters for simulations have been well chosen and the bias field values are well calibrated. Let us recall the Kittel formula (Eq. (2.52)):

$$\omega = |\bar{\gamma}| \sqrt{(H_{\text{bias}} + (N_{yy} - N_{xx}) M_s) (H_{\text{bias}} + (N_{zz} - N_{xx}) M_s)},$$

where the bias field points along the  $x$ -axis for the wide waveguides considered here. Thus, we can also assume  $N_{xx} \approx 0$  and  $N_{zz} \approx 1$  (normal to the plane of the waveguides). Hence,

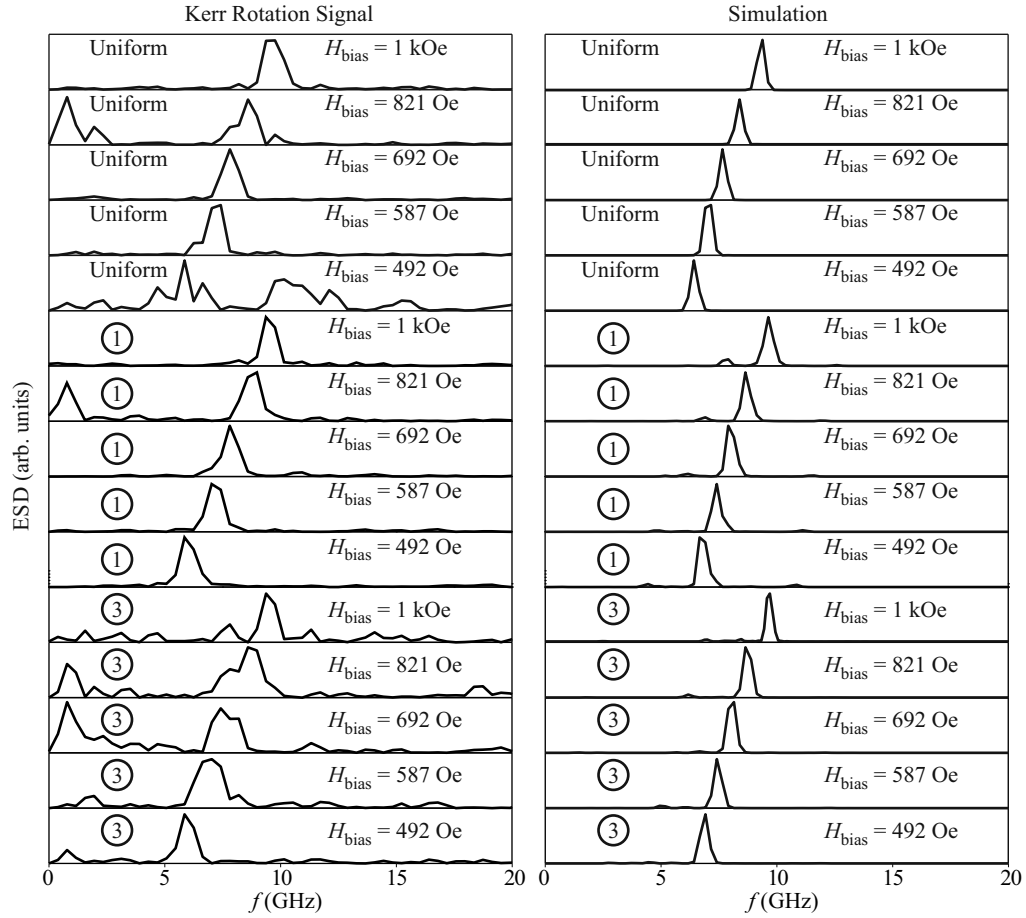


Figure 11.7.: SW spectra calculated using (left panel) Kerr signal and (right panel) simulations for a uniform waveguide and samples ① and ② with varying bias magnetic field strength  $H_{\text{bias}}$  along the length of the waveguide.

the Kittel formula reduces to:<sup>49</sup>

$$\omega = |\tilde{\gamma}| \sqrt{(H_{\text{bias}} + N_{yy}M_s)(H_{\text{bias}} + N_{zz}M_s)}. \quad (11.3)$$

Substituting  $N_{zz} = 1 - N_{yy}$  (see Eq. (2.49)) in the above equation, we get

$$\omega = |\tilde{\gamma}| \sqrt{(H_{\text{bias}} + N_{yy}M_s)(H_{\text{bias}} + (1 - N_{yy})M_s)}. \quad (11.4)$$

While using Eq. (11.4) to fit the simulated results, we get  $N_{yy}$  as 0.004378, 0.009288 and 0.01148 for uniform waveguide, ① and ③, respectively. Thus, we note that the presence of the antidot array close to the centre of a uniform waveguide can nearly double the demagnetizing factor  $N_{yy}$  — which can be further tuned by changing the lattice parameters

(from ① to ③). The plots of Eq. (11.4) corresponding to the aforementioned values of  $N_{yy}$  are shown in Fig. 11.8. Experimentally observed modes in different cases are represented by open symbols. For decreasing bias field strength, the modes in patterned waveguides (① and ③) appear to drop more rapidly than predicted. This may be the result of a change in the equilibrium magnetic configuration leading towards a more non-uniform magnetic state and a reduced effective magnetic field and precession frequency.

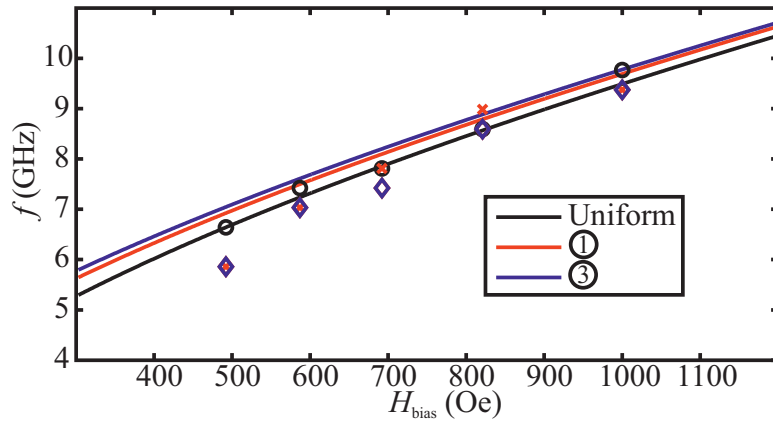


Figure 11.8.: (Solid lines) Curve fitting of simulated modes (shown in Fig. 11.7) using the Kittel formula (Eq. (11.4)). (Open symbols) Experimentally observed modes.

It can be noted that the experimentally observed peaks in Fig. 11.7 are always wider than the those seen in simulation. This can be corrected by using a higher Gilbert damping constant. However, doing so will compromise the resolution of simulated results. ④ is visibly asymmetrical (see Fig. 11.5). We know from Chap. 6<sup>4</sup> that the wider and the narrower sub-waveguides should resonate at different frequencies. However, here the difference is merely of about 0.5 GHz and the currently used Gilbert damping constant of 0.008 does not allow to resolve this phenomena. Also, since the wider sub-waveguide occupies a greater area, its peak is seen more prominently due to averaging. The evidence of this undetected splitting can be noticed by comparing the power and phase profiles at 9.77 GHz and 10.25 GHz in Fig. 11.5 for ① ( $H_{\text{bias}} = 1$  kOe). The peak seen in Fig. 11.7 for ① ( $H_{\text{bias}} = 1$  kOe) is at 9.77 GHz. In Fig. 11.5, this peak is seen to have greater power in the wider sub-waveguide. The narrower sub-waveguide shows more power at 10.25 GHz. This splitting is not resolvable in the experimental results as well probably due to the presence of an even higher damping.

From Fig. 11.5, we can see that the three modes which are evident at all bias field strengths

$H_{\text{bias}}$ , shift negatively along the frequency scale with reducing  $H_{\text{bias}}$ . The lowest and the highest modes are the BV and the quantized modes (with power distribution close to the antidot lattice) in all cases. The mode in the middle corresponds to the ferromagnetic resonance of the two sub-waveguides. As mentioned earlier, the two sub-waveguides resonate at slightly different frequencies, where that difference is lower than the mode width observed here. As seen in Fig. 11.5, ③ features two BV modes (with limited quantization) with power close to the antidot array for all cases except  $H_{\text{bias}} = 821$  Oe. As in the case of ①, the most powerful mode for ③ (as seen from Fig. 11.7), is again situated in the space of the two sub-waveguides. The entire band structure shifts negatively for ③ with decreasing values of  $H_{\text{bias}}$ .

## 11.4. Conclusions

In this chapter, we were able to demonstrate the tunability of magnonic spectra of MAWs based on their geometrical parameters and the bias magnetic field. All discussion here was limited to modes seen at the centre of the Brillouin zone. We showed that SW modes in the sub-waveguides were very stable towards any variance in the fabrication parameters. They were largely controlled by the orientation and magnitude of the bias magnetic field  $\mathbf{H}_{\text{bias}}$ . Edge mode of the MAW was clearly observed in the DE configuration. No edge mode was observed in the BV configuration due to the inherent shape anisotropy of the waveguide. Modes with power close to antidot lattice showed a greater dependence on the geometrical parameters as minor disagreement between simulation and experimental results was observed here. Quantized modes were also seen to have power close to the antidot lattice. The experimentally observed modes here showed greater disagreement hinting at higher sensitivity towards changes in the geometrical parameters from one column of antidots to another. We can thus conclude that some advances in the fabrication procedures relating to reducing variance in geometrical parameters of the fabricated samples need to happen in order to readily create reliable SW waveguides or filters.

# 12. Coupled Magnetic Vortices for All-Magnetic Transistor Operations

\*There has been a revolution in the study of inhomogeneous and non-trivial magnetic nano-structures such as magnetic vortices and antivortices due to their suggested applications in magnetic data storage, magnetic random access memory,<sup>128–131</sup> magnetic logic<sup>132</sup> and information processing devices.<sup>132</sup>

In our study we show that off-resonant signals<sup>327</sup> of lower amplitude can be used to design suitable transducers with isolated vortices, which will be required to convert other kinds of external signals (*e.g.* a rotating field) to vortex core gyration. In the case of a pair of magnetostatically coupled vortices, if a signal is applied to only one of them then the other one shows a greater core gyration *i.e.*, amplification when the core polarities are opposite. Antivortex solitons moving through the stray field are held responsible for this behaviour. We postulate some rules regarding their dynamics and use them to mimic transistor-like operations of switching and amplification with a chain of three vortices. Furthermore, we attempt to couple the output of this three vortex chain to two symmetrically placed daughter chains in an attempt to demonstrate a fan-out operation. However, the antivortices involved in the dynamics favoured one branch over the other resulting in a higher level of asymmetry – one of the branches received more power than the other.

---

\*This chapter is based upon Kumar *et al. Sci. Rep.* **4**, 4108 (2014).

## 12.1. Methods

Magnetic vortex dynamics was simulated using the finite difference method based Landau-Lifshitz-Gilbert (LLG) ordinary differential equation solver called Object Oriented Micro-magnetic Framework (OOMMF). Before the dynamics could be observed, a magnetic ground state has to be achieved with required vortex core polarity and chirality.<sup>128,129,148,230,328–332</sup> This was accomplished by using a pulse field  $H_t = H_0 \exp(-t'^2)$ . Here,  $\mu_0 H_0 = 1$  T and normalized time  $t' = (t - t_0)/(\sqrt{2}\sigma)$ .  $t_0 = 75$  ps and  $\sigma$  is the standard deviation of this Gaussian pulse in time whose full width at half maximum is 30 ps. Close to the centre of the circular geometries we apply  $H_z = \pm H_t/10$  along the  $Z$  axis where the sign controls the core's polarity. If the origin of co-ordinates is brought to the centre of the vortex then  $X$ – and  $Y$ –components of fields,  $H_x$  and  $H_y$  that would produce the desired chirality are given below

$$H_x = \mp H_t \sin(\theta);$$

$$H_y = \pm H_t \cos(\theta).$$

Here,  $\theta = \tan^{-1}(y/x)$  and the upper or lower signs were chosen for CCW or CW chiralities, respectively. It is to be noted that this pulse signal controlled by  $H_t$ , dies down quickly while the magnetic ground state is obtained by running the simulation for 40 ns under a high damping (Gilbert damping constant  $\alpha = 0.95$  is used in the LLG equation). We have used saturation magnetization,  $M_s = 0.8 \times 10^6$  A/m, exchange constant,  $A = 13 \times 10^{-12}$  J/m and zero magneto-crystalline anisotropy. During vortex dynamics simulations we reduce  $\alpha$  to a more realistic value of 0.008 for Py. Magnetization was observed every 10 ps for about 40 ns during dynamics. The cell size used during simulation was  $5 \text{ nm} \times 5 \text{ nm} \times 40 \text{ nm}$ .

Before we start to explore the dynamics of magnetic vortices, we first need to obtain the natural frequencies associated with a single isolated vortex. A broadband excitation signal was given to reveal these frequencies. The signal had only  $X$ -component,  $H_x^S$  which contained power up to  $f_{\text{cut}} = 45$  GHz and depended upon time  $t$  as given by:

$$H_x^S = H_x^0 \frac{\sin(2\pi f_{\text{cut}}(t - t_0))}{2\pi f_{\text{cut}}(t - t_0)}.$$

Here,  $\mu_0 H_x^0 = 0.05$  T and  $t_0 = 200$  ps.

Upon obtaining the magnetization data from OOMMF, we chose to analyse the results by looking at the time evolution of spatial average of normalized  $X$ -component of magnetization,  $\langle m_x \rangle$  for each vortex, and its corresponding ESD. Normalization is done by dividing the  $X$ -component of magnetization,  $M_x$  by  $M_s$ ; such that  $m_x = M_x/M_s$ . The Hanning window is used on  $\langle m_x \rangle$  to reduce spectral leakage. The windowed data is then zero padded and Fourier transformed to obtain the required ESD,  $|\bar{m}_x|^2$ .<sup>262</sup> This is plotted in figures on decibel scale as  $w_H \times 20 \log_{10} |\bar{m}_x|$ , where a window scaling factor of  $w_H = 2$  is used for the Hanning window. These ESDs were calculated after running the dynamics for over 40 ns, so that any transient vortex core dynamics are suppressed and steady state dynamic solutions appear to be more prominent in the spectrum. Power spectral density is considered to be more desirable in the case of persistent signals. However, here we run the simulations for finite amount of time. Also, natural damping ensures that net power input to the system becomes zero before the simulations finish. The stray field is also obtained from OOMMF during dynamics. The stray field plots were created using MATLAB. The contour colouring is based on the sum of squares of  $X$ - and  $Y$ -components of the stray field.

## 12.2. Results and Discussion

We use permalloy (Py: Ni<sub>80</sub>Fe<sub>20</sub>) with negligible magneto-crystalline anisotropy in the form of a 40 nm thin disk of diameter  $2R = 200$  nm to ensure a stable vortex structure.<sup>258</sup> The darker shade in Fig. 12.1 (a) represents such an isolated vortex. Figure 12.1 (b) shows a pair of coupled vortices whose centre to centre distance is  $a = 250$  nm. A chain of three vortices, with the same centre to centre distance  $a$ , has also been studied with different orientations of polarity. Spatially averaged  $X$ -component of magnetization  $\langle m_x \rangle$  has been used as an indicator of core displacement away from their equilibrium positions. The square of the amplitude of Fourier transform of  $\langle m_x \rangle(t)$  (with respect to  $t$ ) – also known as the energy spectral density (ESD) – shows the peaks in vortex core dynamics as a function of frequency.

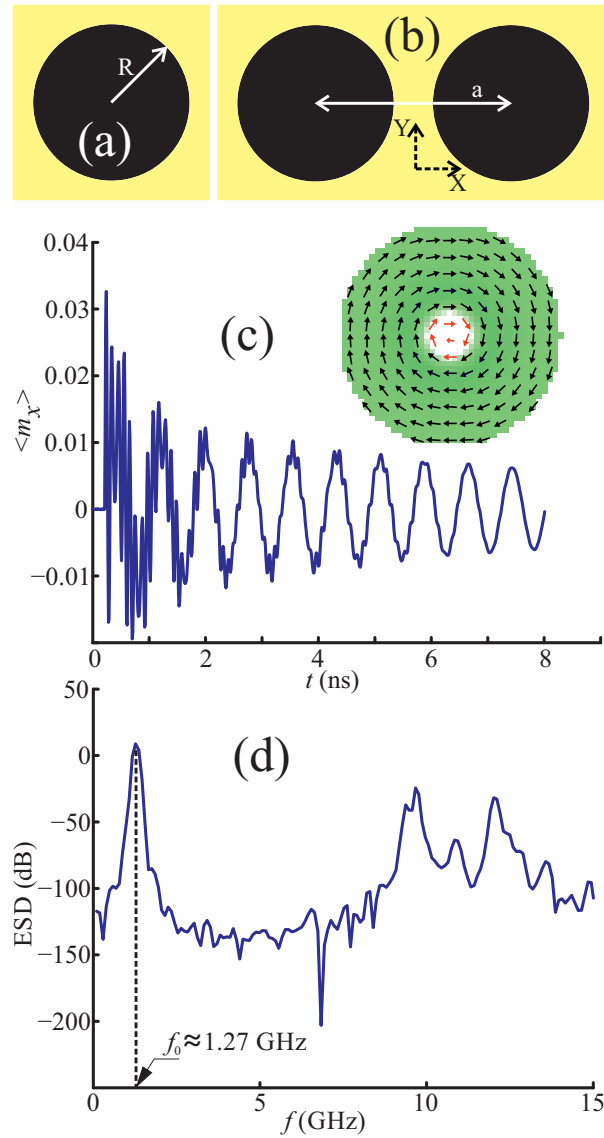


Figure 12.1.: Dark regions represent the 40 nm thick (a) isolated and (b) coupled pair of magnetic vortices each of diameter  $2R = 200$  nm. The centre to centre separation in the case of coupled vortices is set to  $a = 250$  nm. (c) Time evolution and (d) corresponding energy spectral density of  $\langle m_x \rangle$  in response to the signal  $H_x^S$ .

### 12.2.1. Isolated Magnetic Vortex

Figure 12.1 (c) shows a plot of  $\langle m_x \rangle$  vs. time and Fig. 12.1 (d) shows the associated ESD (in decibel) for the single vortex excited by a broadband signal. The gyrotropic mode is observed at frequency  $f = f_0 \approx 1.27$  GHz. Higher frequency modes associated with the generation of spin-waves<sup>333</sup> are also observed. Here, we concern ourselves with frequencies  $f \leq f_0$  while using signals that are rotating CW or CCW in the plane of the magnetic

vortices. With up polarity  $p = 1$ , CCW signals are known to produce greater gyration<sup>152</sup> which can lead to polarity switching. This can be useful in terms of data storage.<sup>327</sup> However, if the polarity switching is somehow avoided, one can use this to create a suitable transducer for appropriately rotating signals. To that end we can use signals with lower amplitude. Signals with off-resonant frequency  $f < f_0$ , should be used to reduce the convergence time. As shown in the Fig. A.1, anharmonicity of the gyration dynamics results in a beating frequency when off-resonant signals are used. A trade-off between convergence time and beating frequency needs to be further explored as a design consideration.

### 12.2.2. Coupled Magnetic Vortices Pair

We have examined the transfer of energy from one vortex to another in terms of their core gyration amplitude (measured in terms of  $\langle m_x \rangle$ ) when excitation is only given to one of them. Here,  $\langle m_x \rangle$  is computed for both the vortices separately. The dynamics was examined with all sixteen combinations of polarity and chirality of the two vortices. When a small external bias field is applied, the vortex cores may move up or down along the  $Y$ -axis. This changes their separation and causes magnetic surface charges to appear on the vortex boundaries; consequently affecting the strength of their magnetostatic coupling.<sup>9,137</sup> Hence, in the presence of a bias field, if both the vortices have the same chirality, their coupling will remain relatively unaffected, than when they have different chiralities. This phenomena can be used to affect a chirality dependent dynamics and signal transmission. However, in the absence of an external bias, we observed that chirality does not play any role towards enhancing the asymmetry in dynamics, as described below. Thus, henceforth all vortices in this work have CCW chirality. Furthermore, observable changes only appeared to occur between cases with similar and opposite polarities.<sup>156</sup> Mediated by several factors,<sup>150,334-337</sup> the resonant frequencies of a pair of vortices can differ from that of an isolated vortex. However, in this study, we used an excitation signal rotating at frequency  $f_0$ , which is applied only on the left disk (Fig. 12.1 (b)). Figures. 12.2 (a) and (c) show the results for the case when both polarities are up ( $p_1 p_2 = 1$ ) and Figs. 12.2 (b) and (d) show those when left core is up and right core is down ( $p_1 p_2 = -1$ ). Figures 12.2 (a) and (b) correspond to a signal amplitude of 0.5 mT and Figs. 12.2 (c) and (d) correspond to a signal amplitude of

1.5 mT. To ascertain that the results discussed here are independent of cell size, Fig. 12.2 was reproduced using a cell size of  $2.5 \text{ nm} \times 2.5 \text{ nm} \times 40 \text{ nm}$ . The same has been shared as Fig. A.2. Although the form of the peaks have changed to some extent, the relative gains at  $f = f_0$  remain largely unaffected.

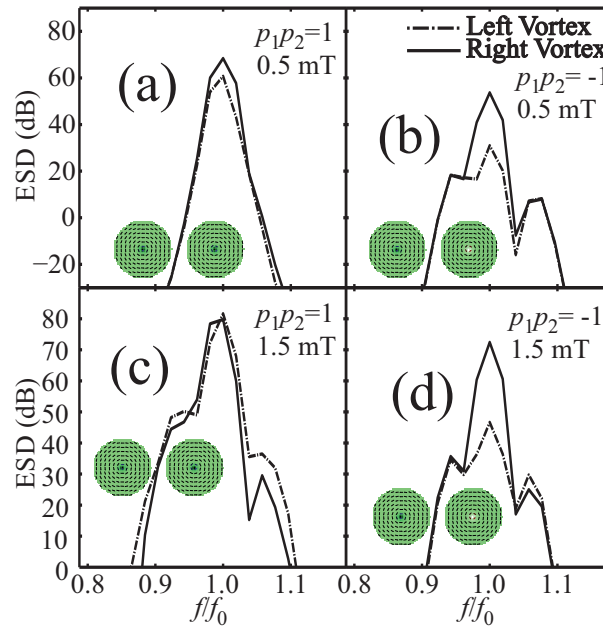


Figure 12.2.: ESDs of left and right magnetic vortices shown in the insets with ((a) and (c)) similar and ((b) and (d)) opposite polarities. (a) and (b) show the results for a signal amplitude of 0.5 mT while (c) and (d) show those for an amplitude of 1.5 mT, both rotating CCW at  $f = f_0$ .

With increase in the signal amplitude from 0.5 mT to 1.5 mT, we see a splitting<sup>338</sup> of the peak. Furthermore, when  $p_1 p_2 = -1$ , more energy is transmitted and stored in the right vortex. For signal amplitude of 0.5 mT and  $p_1 p_2 = 1$ , the left vortex, exhibits 60.72 dB of ESD at its gyrotropic mode while the right vortex exhibits 68.43 dB. While for  $p_1 p_2 = -1$ , these values become 30.99 dB and 53.69 dB, respectively. Thus, the difference in ESDs of gyrotropic modes of left and right vortices increases by about 15 dB. When signal amplitude is increased to 1.5 mT, these values become 81.66 dB (left vortex) and 79.76 dB (right vortex) for  $p_1 p_2 = 1$  and 46.67 dB (left vortex) and 72.45 dB (right vortex) for  $p_1 p_2 = -1$ . Here (for  $p_1 p_2 = -1$ ), the ESD (at  $f = f_0$ ) of the right vortex is 25.78 dB greater than that of the left vortex. This shows that opposite core polarity facilitates amplification of signal transfer, which is further enhanced by the input signal amplitude. An increase in about 9.5

dB in signal power (from 0.5 mT to 1.5 mT) has caused the difference in gain to increase by 12.69 dB. The dependence of this relative amplification on the strength of the input signal is essential to mimic the transistor operation where the base current controls the amplification.

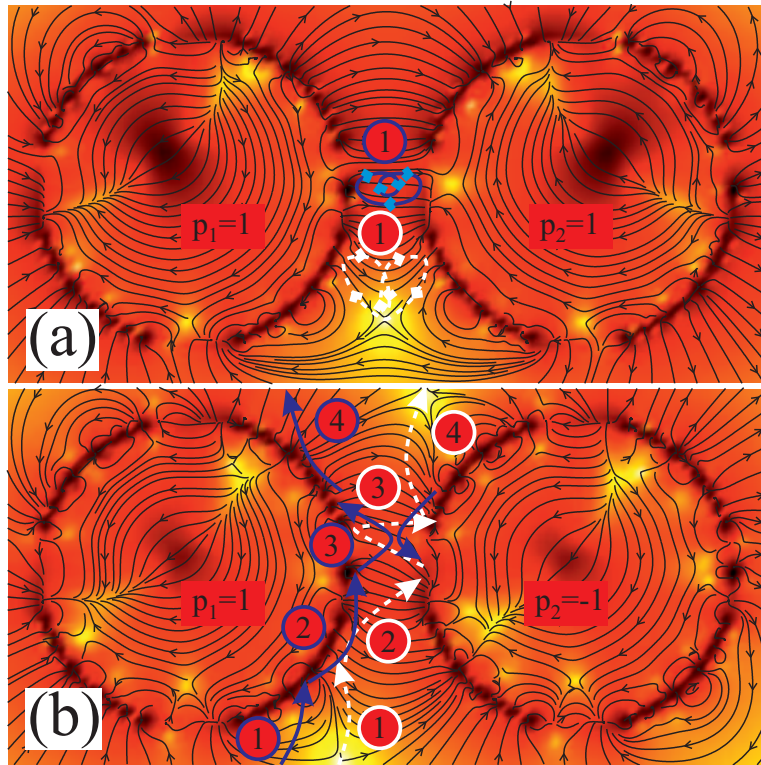


Figure 12.3.: Stray field distribution showing the path of travelling antivortex packets for  $p_1 p_2 = 1$  (a) and  $p_1 p_2 = -1$  (b). With time the packets shift their path from the dashed to the solid lines.

These observations, along with the ones made for an isolated vortex, testify to the existence of anharmonic and asymmetric dynamics present in the vortex core gyration, which cannot be explained by solutions of the Thiele's equation with linear approximations;<sup>146,233,339</sup> even if vortex core deformation<sup>221</sup> is taken into account. Although, the type of amplification described here has not been seen before, asymmetry based on polarity in terms of energy transfer rate and efficiency has been observed experimentally. Stronger or weaker stray field coupling can affect the rate of energy transmission,<sup>155</sup> but it does not guarantee the observed asymmetry in general and amplification in particular.

One may draw an analogy of this observation with a driven double pendulum made of identical pendulums. In this case, when the driving frequency is same as the eigenfrequency of the isolated pendulum then the top pendulum mass becomes stationary while the bottom

pendulum mass moves with an amplitude twice as that of the driving amplitude. This may be considered as an infinite amplification (although, the angular displacement of the top pendulum will still not be zero). However, for a coupled pendulum, where two pendulums are connected with a spring and dynamics is not pinned at any end (this system is closer to the coupled vortices presented here in terms of underlying equations of dynamics), no such amplification occurs when the driving frequency is the same as the eigenfrequency of the individual pendulum<sup>340</sup> (see Sec. A.1). Either way, a direct comparison of the energy transfer mechanism of coupled magnetic vortices with that of coupled mechanical oscillators is difficult due to the presence of additional parameters in the former case. The gyrovector, which serves as the inertia of the vortex core<sup>149</sup> can switch direction with core polarity resulting in the amplification observed here. Hypothetically, this will be comparable to obtaining an amplification in one of the coupled pendulums by changing its inertia from  $I$  to  $-I$ . An analytical model is yet to be developed to describe this phenomenon; but, this is outside the scope of this work (see Sec. A.1). Here, we considered a numerical approach and calculated the temporal evolution of the stray field and discovered that packets of antivortex structures travelling through the stray field mediate the transfer of energy between the two vortices. The path of these antivortices are shown in Fig. 12.3 for both polarity combinations when the excitation signal amplitude is at 1.5 mT. As time progresses the path shifts from dashed to solid lines.

As seen from Fig. 12.3 (a), a single antivortex packet moves in a closed path for  $p_1 p_2 = 1$ . This packet collides with other antivortex structures which originate at the boundaries of the nanodisks. We understand that the antivortex packets discussed here are not particles in the true sense and their apparent ‘collision’ is only a result of the interacting stray fields. This interaction (or collision) is also shown in the Supplementary Movie M1\*. It is only during this collision that these antivortex ‘solitons’ (‘soliton’ has been used loosely here to describe even those short-lived antivortex packets which do not possess consistent form for significant duration) are allowed to change their size (local field distribution) significantly.<sup>341</sup> When it collides with the left disk, which initially has more gyrotropic energy, it becomes smaller and when it collides with the right disk, it becomes larger. This indicates that there

---

\*Movie M1: <https://www.youtube.com/watch?v=RBLSFu8RHx0>

is an inverse relation between the size of the antivortex and the gyrotropic energy that it can transfer. As time progresses and the amplitudes of the gyrating vortex cores become comparable, the path of this bouncing soliton becomes smaller and it moves to a location shown by the solid line ① in Fig. 12.3 (a). The soliton itself does not change greatly in size after this point indicating no significant transfer of energy.

Figure 12.3 (b) shows that more than one antivortex solitons are involved in the energy transfer for the case when  $p_1 p_2 = -1$ . On a given vortex boundary, as one soliton gets terminated, another one is created. This creates a cascade of solitons, which vary in size (see Supplementary Movie M2\*). At first, the dashed lines mark the path of this cascade with the large arrowheads showing where a soliton gets localized. Branches are numbered from ① to ④, in an order such that the path of the new soliton is shown by the next branch. The path of this cascade changes gradually with time as well. Specifically, the number of rebounds between the boundaries of the vortices (the length of branch ③) may vary quite often. However, it is observed that as branch ① terminates, the remaining solitons, which follow branches ② and ③ are relatively smaller. When branch ③ terminates, a soliton of the same size as the first one (which traversed branch ①) emerges from the right vortex to trace the final branch ④. Thus the right vortex gains gyrotropic energy in the beginning of the dynamics. This cascade occurs twice every cycle, suggesting that signal transfer rate or efficiency can be controlled not only by the saturation magnetization<sup>155</sup> but also by the frequency of the signal and further optimization of signal transfer efficiency by tuning the dimensions of the coupled vortices is possible. As time progresses, the cascade starts to occur along the solid lines ① to ④, shown in Fig. 12.3 (b). When the gyration amplitude of the right vortex becomes a certain degree greater than that of the left one, we notice that the soliton, which was traversing the dashed branch ③ earlier, now starts from the boundary of the left vortex. However, it is deflected back by another soliton, which emerges from the right vortex – much like an electron or hole charge carrier being prohibited from crossing the depletion layer of a junction diode. We can turn this amplification ‘on’ or ‘off’ simply by switching the polarity  $p_2$ ; but it may be technologically more desirable to have this control via a third vortex.

---

\*Movie M2: <https://www.youtube.com/watch?v=CKTtnawFYU4>

### 12.2.3. Magnetic Vortex Transistor (MVT)

In order to examine this transistor-like behaviour, we now add another vortex towards the right of the vortex pair shown in Fig. 12.1 (b) to form a three vortex sequence with polarities (from left to right)  $p_1$ ,  $p_2$  and  $p_3$ , which take values of 1 or  $-1$  denoting up or down polarities. In the previous sub-section, we identified relative polarity as the source of the observed amplification. Hence, here we study only the four cases with  $p_1 = 1$  (up),  $p_2 = \pm 1$  and  $p_3 = \pm 1$ . Chirality in all cases is CCW. Signal is applied to the left vortex only. The ESDs for these cases around frequency  $f_0$  are shown in Fig. 12.4 (as shown in the insets, the excitation is given to shaded vortices only).

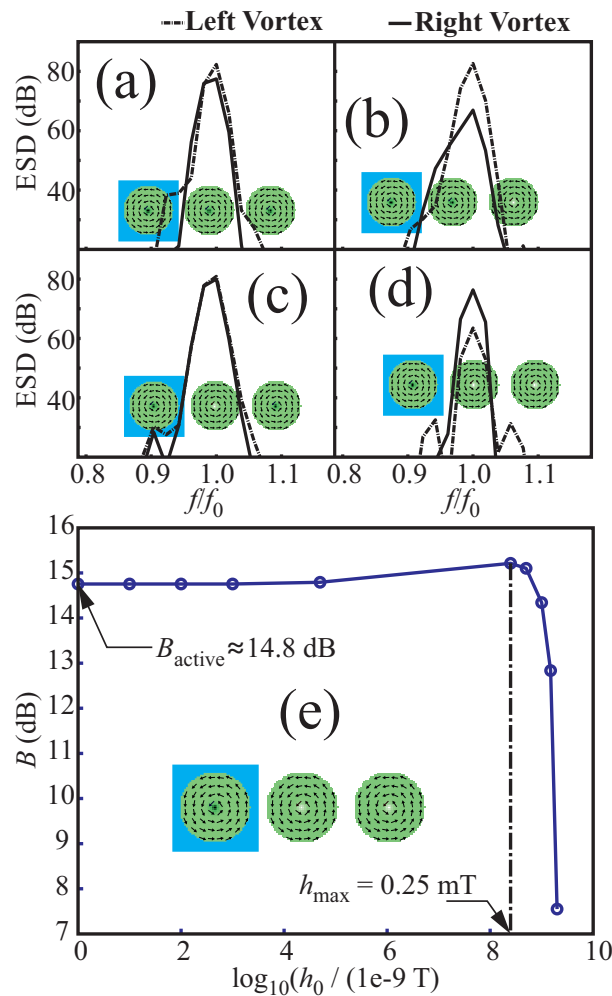


Figure 12.4.: ESDs of left and right magnetic vortices with  $(p_1, p_2, p_3)$  equalling (a) (1, 1, 1), (b) (1, 1, -1), (c) (1, -1, 1) and (d) (1, -1, -1) as shown in the respective insets. A 1.5 mT signal rotating CCW at frequency  $f_0$  is applied only to the left (shaded) vortex. (e) Gain  $B$ , versus logarithm of signal amplitude  $h_0$ .

Splitting can be observed in a few cases in Fig. 12.4. Unlike the splitting seen with increase in signal amplitude (see Fig. 12.2 (c)), which happens due to inherent non-linearities of the dynamics,<sup>338</sup> here it occurs for a different reason: an increase in the number of vortices leading to an increase in the number of permutations of couplings in the system.<sup>342</sup> Below, we consider any difference in ESD at the signal driving frequency of  $f = f_0$  only.

As seen in Figs. 12.4 (a) and (c), the transmission efficiency is equivalent for a persistent signal in both cases:  $(1, 1, 1)$  and  $(1, -1, 1)$ ; with the latter faring slightly better. Although, a third vortex was added in the chain, a gain of 12.84 dB (between right and left most vortices) is observed in Fig. 12.4 (d). Also, transistor like switching is observed clearly with the three vortex sequence considered here when changing from  $p_2 = -1$  (high base current) (Fig. 12.4 (d)) to  $p_2 = 1$  (low base current) (Fig. 12.4 (b)) changes the difference in signal levels of the right vortex (collector) from 12.84 dB to  $-15.71$  dB. We define the gain  $B$  in Eq. (12.1) as below:

$$B \equiv \text{ESD}_3(f_0) - \text{ESD}_1(f_0). \quad (12.1)$$

Here  $\text{ESD}_1(f_0)$  and  $\text{ESD}_3(f_0)$  are ESD at  $f = f_0$  for left and right vortices, respectively.

We further checked if this gain  $B$ , also depended upon the input signal amplitude  $h_0$ . Figure 12.4 (e) shows a plot of  $B$  versus  $h_0$  for  $h_0 = (1\text{e-}6, 1\text{e-}5, 1\text{e-}4, 1\text{e-}3, 5\text{e-}4, 0.25, 0.5, 1, 1.5, 2)$  mT. Left vortex's core reversed for  $h_0 = 3$  mT; and hence, we limit ourselves to 2 mT. For lower values of  $h_0$ , the gain appears to be constant at  $B = B_{\text{active}} \approx 14.8$  dB. This is reminiscent of a bipolar junction transistor (BJT) operating under small-signal conditions.<sup>343</sup> At higher signal strength, the gain  $B$ , no longer remains constant. This indicates that like other electronic transistors, our 'magnetic vortex transistor' is also susceptible to non-linear distortion. The maximum value of gain  $B = B_{\text{max}} \approx 15.21$  dB is seen for a signal strength of  $h_0 = h_{\text{max}} = 0.25$  mT.

We further investigate the roles of the stray field antivortex solitons on the transistor-like operations described above. We begin by analysing the temporal evolution of the stray field for cases where  $(p_1, p_2, p_3)$  equals  $(1, -1, 1)$  and  $(1, -1, -1)$ . The same is shown in

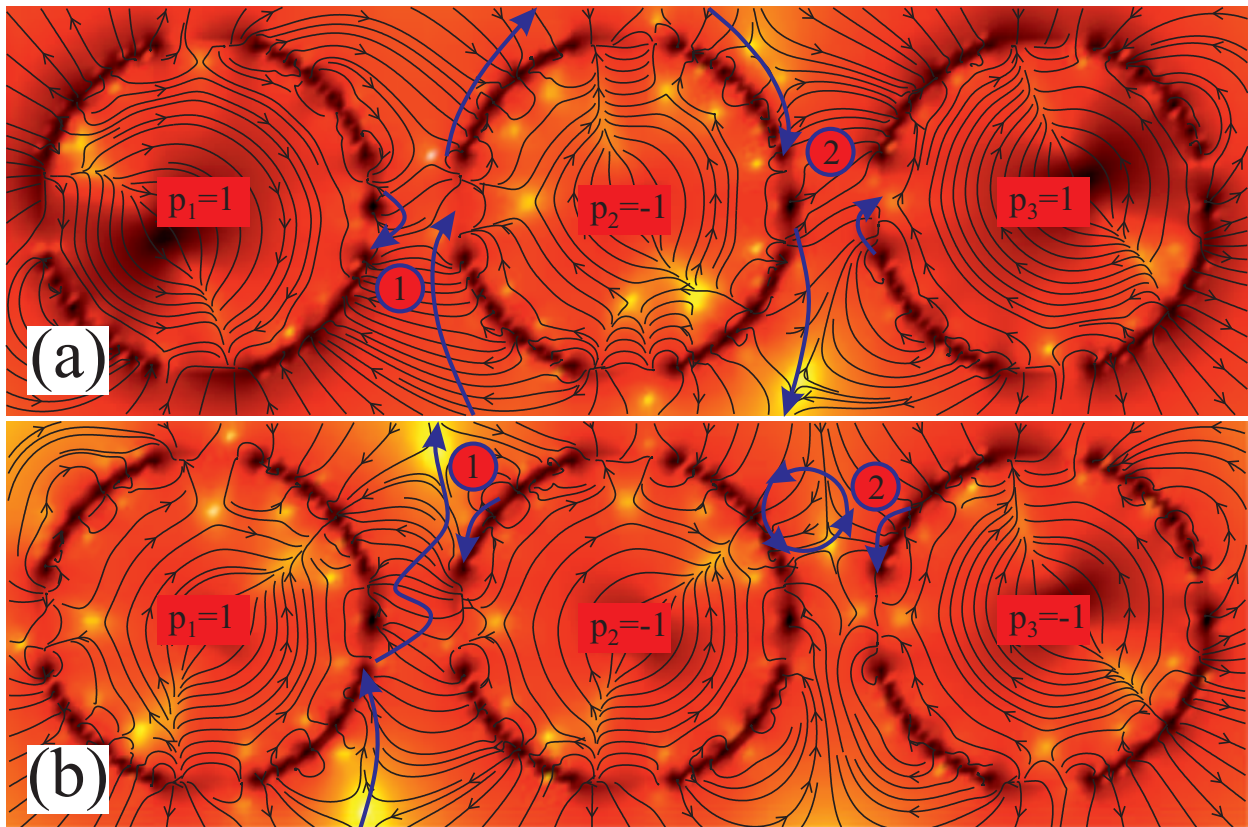


Figure 12.5.: Stray field distribution in the cases where  $(p_1, p_2, p_3)$  equals (a)  $(1, -1, 1)$  and (b)  $(1, -1, -1)$ . The path of antivortex packets after the dynamics has stabilized is marked with solid lines.

Supplementary Movies M3\* and M4†, respectively. Figures 12.5 (a) and (b) summarize the path of the solitons involved. Polarity dependent transient gyrotropic energy transfer between any two neighbouring vortices here too occur in the same manner as shown by the dashed lines in Fig. 12.3. These lines are omitted in Fig. 12.5 for clarity. Solid lines show the approximate paths the solitons follow after the dynamics had become relatively stabilized. For  $(p_1, p_2, p_3) = (1, -1, 1)$ , where no amplification ( $B < 0$  dB) is observed, the cascade of solitons form a large oval loop around the central vortex. Energy appears to be transferred during collisions at ① and ②. This creates a closed feedback loop directly between the left and the right vortices. The solitons skip along the boundary of the central vortex on several occasions in order to aid their own cascade. Most importantly, we note here as well that solitons in the bottom half of the loop (right to left vortex) appear larger (lesser energy)

\*Movie M3: <https://www.youtube.com/watch?v=PdfHQesec9k>

†Movie M4: <https://www.youtube.com/watch?v=b-cr5752DwE>

than those traversing the top half (left to right vortex). Thus the flow of energy still occurs from the left vortex, which is excited externally to the right one. However, an amplification ( $B > 0$  dB) is observed for  $(p_1, p_2, p_3) = (1, -1, -1)$  and Fig. 12.5 (b) sheds some light on this crucial finding. Here, the path of antivortex solitons between the left and the central vortex does not change greatly from its early transient stage. Here too, energy is transferred at the sites ① and ②, essentially from the left vortex to the right one. However, unlike in Fig. 12.5 (a), no feedback loop, and thus no energy rebalancing is present here. This leads to a unidirectional flow of energy as determined by the cascade of antivortex solitons. The right vortex core, thus builds up gyrotropic energy until its drag (or dissipation) matches the power influx. Thus an amplification of the gyrotropic mode of the right vortex is observed in this case. One can simplify the dynamics for the two cases analysed above by considering the central vortex as an efficient medium and taking it out of the picture. Then we can see that amplification was observed when  $p_1 p_3 = -1$ . However this amplification can be controlled by switching the polarity of the middle vortex ( $p_2$ ), similar to what is done by switching the base current in a BJT.

#### 12.2.4. Fan-Out

In an attempt to demonstrate a fan-out operation, which may support the development of more complex circuits, we placed two more MVTs symmetrically above and below the original MVT as shown in Fig. 12.6. Same material and structural parameters as before were used here. Power was given only to the left vortex of the original MVT. To our surprise, amplification was seen in only one of the branches. As in the inset of Fig. 12.6, the right vortex of upper branch in this network received about 15 dB more power than the lower branch. When all the core polarities in this network were reversed, the lower branch received the greater power by the same amount.

The cause of this asymmetry is the fact that the solitons do not split during a fan-out. Also, the antivortex seen between the first two vortices in Fig. 12.5 (b) goes on directly to hit the upper chain as marked in Fig. 12.6. Thus, further study regarding the implementation of a fan-out is warranted by looking at the path of these antivortices in different network configurations.

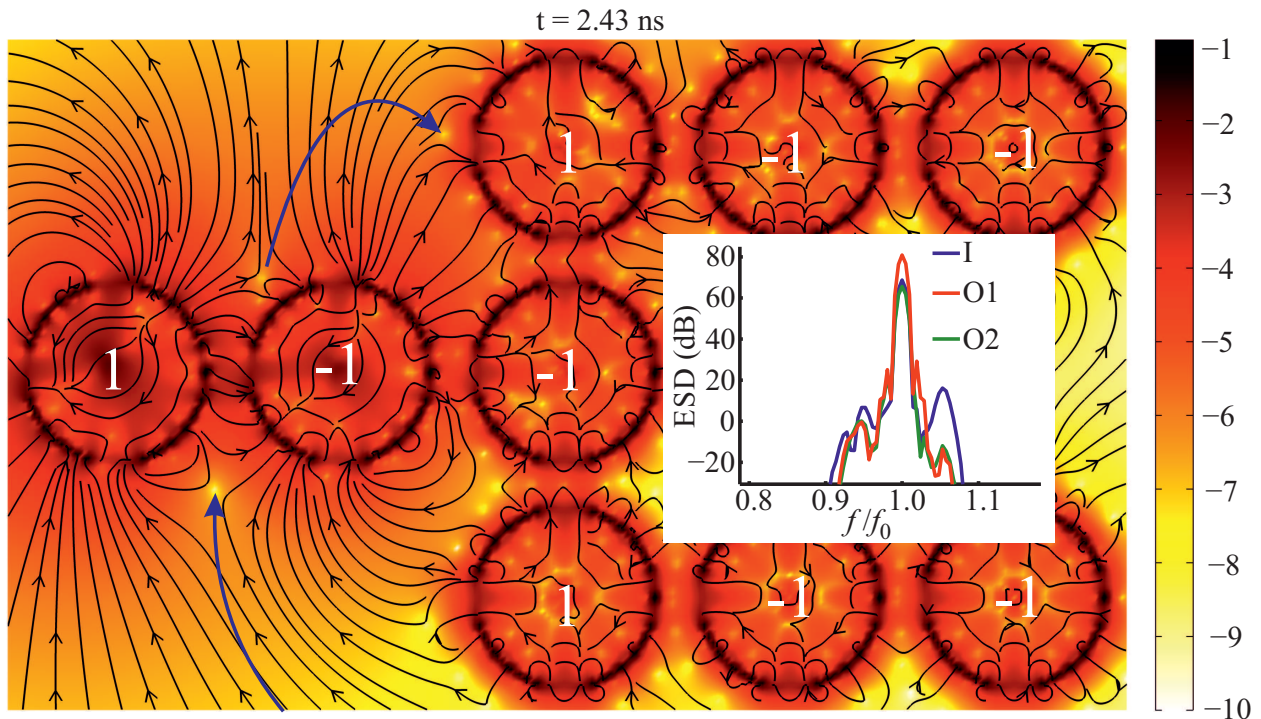


Figure 12.6.: Stray field distribution in a MVT network. Signal is given only to the left vortex in the middle row. Vortices are marked with their respective polarities. A path followed by antivortex packets taking energy from the left vortex in the middle chain to the left vortex of the top chain is marked. The ESDs of left and upper and lower rightmost vortices are given in the inset marked as ‘I’, ‘O1’ and ‘O2’ respectively.

### 12.3. Conclusions

We numerically examined the polarity dependent asymmetry and non-linearities in vortex dynamics. Cases presented in this chapter included isolated vortices and coupled two and three vortex sequences. We particularly examined the dynamics for gain in the transfer of gyrotropic mode power from one vortex to another. To start with, we describe the design considerations in creating a transducer which can convert power from an external rotating magnetic field signal to gyrotropic power. Best results were observed when the driving signal frequency was very slightly off-resonant w.r.t. the eigenfrequency of the transducer. In the case of coupled pair of vortices, when an excitation signal is applied to only one of the vortices then in certain situations, considerably more energy (a maximum gain of 27.68 dB) is transferred and stored in its neighbouring vortex if it has the opposite polarity. We further observed that this amplification of energy transfer can be extended over three vortices for a

particular case of  $(p_1, p_2, p_3) = (1, -1, -1)$ . We interpreted these remarkable observations using the temporal evolution of stray magnetic field and observed that antivortex packets moving through the stray field were accountable for the observed amplifications. The rules, which we postulated based upon the motion of the antivortex packets (or ‘solitons’) can also successfully explain the previous experimental observations in greater detail. We hope that further study of these solitons will aid the research community in creating a better analytical model which can predict such useful results as signal amplification without the need to do complete simulations.

Similar amplification may be observed in coupled mechanical oscillators. However, here the observed amplification in the energy transfer from left (input) to right (output) vortex for  $(p_1, p_2, p_3) = (1, -1, -1)$  can be controlled by switching the polarity  $p_2$  from 1 to  $-1$ , much like changing the states of a BJT between active and cut-off. This can be achieved by using a local magnetic field or a spin-polarized current; thus, making it a more suitable candidate for integration with current electronic technological ecosystem. Moreover the observed gain, while remaining constant at  $B_{\text{active}}$  for low signal strength  $h_0$ , drops dramatically for  $h_0 > 0.25$  mT. Thus the output will not increase over a certain upper limit (76.61 dB for the MVT described here). This is similar to the saturation state of an electronic transistor. Direct parallels to all three operational states of a BJT, namely active, cut-off and saturation have thus been demonstrated for the discussed MVT. Also, both classic transistor operations of signal switching and amplification have been described. The dependence of gain characteristic, in particular  $B_{\text{active}}$  and  $B_{\text{max}}$  should be further explored with different material and geometrical parameters of the MVT and the driving signal frequency (dynamic response).

Our attempt to demonstrate a fan-out operation uncovered that the solitons involved in the dynamics do not split easily. This resulted in a higher level of asymmetry between different branches of a symmetrical network. This asymmetry was unlikely if the dynamic stray field lacked any of the topologically stable antivortices and treated both the branches evenly. This helped us to further validate the importance of antivortex solitons in the energy transfer mechanism. More work will be needed to demonstrate a successful fan-out operation by considering the cascade of antivortices for different network parameters.

---

Pinning, which can occur due to fabrication related issues, is known to affect the natural frequency of an isolated vortex.<sup>344</sup> However, as the dynamics studied here was forced, the observed results are expected to remain unaffected unless the pinning potential is high enough to change the trajectory of the vortex core or the cascade of solitons. A stronger pinning may sometimes occur at the Py–air boundary.<sup>213</sup> We have not considered this type of pinning here as it can affect the generation and dynamics of the stray field which is responsible for some of the reported observations. Thus, a different soft–ferromagnet may have to be used if pinning becomes an issue.

While advancing the cause of nano–electronic devices,<sup>4</sup> we also hope that these findings will promote the continued search of new and improved transistors.<sup>345</sup> For the type of transistor proposed here to become technologically viable and competitive, further research towards miniaturization and reduction of energy consumption and response delay are highly desirable.

# 13. Conclusions

In this thesis, we studied magnetization dynamics in nanoscale magnetic systems. Two types of closely related phenomena of spin-wave (SW) propagation and magnetic vortex gyration were studied as they fall in the microwave frequency band. The propagation of SW propagation was studied in thin-films, waveguides, one-dimensional (1D) and two-dimensional (2D) magnonic crystals (MCs). Time-resolved magneto-optic Kerr effect (TR-MOKE) based microscopy was used to experimentally study SWs in nanoscale magnonic waveguides. The magnetic vortex core can be made to gyrate in a closed cyclic loop by using an in-plane rotating excitation field. The dependence of the steady state of this gyrotropic motion on relative core polarities of magnetostatically coupled magnetic vortex network was also studied.

## 13.1. Summary

We start with developing a numerical framework to visualize and analyse the SW dynamics in different types nanoscale magnetic systems. In order to represent the magnetization data in frequency or wavevector domains, we used multi-domain Fourier transforms. We enhance our numerical techniques to overcome some of the artefacts that are conventionally associated with the Fourier transforms. As a result, we begin to obtain high quality analysis data output which helped us uncover some new phenomena. In Chap. 4, we highlight the use of DFT windows and sinc functions to control the spectral leakage and aliasing, respectively. The efficacies of the numerical methods were established by comparing the results they produced with those obtained by using other techniques.<sup>79,213,315</sup> In Chap. 7, we improve the technique to compute SW power and phase profile to account for a specific wavevector while ignoring

the remainder of the wavevector domain. In Chap. 9, we ensure the framework is now able to compute SW dispersion relation for 2D MCs. This was done largely by designing a new excitation signal which was capable to exciting the entire SW spectrum without producing any spurious modes. Here, we also discussed how to numerically obtain the iso-frequency lines for a MC. In Chap. 10, we improve the framework further by mapping the magnetization data into the complex plane. This helped us uncover the existence of a magnonic bandgap in submillimetre wave band. While continuing to improve the framework on the one hand, we have also reported some remarkable observations on the other.

In Chap. 5, we compare the effects of pinned and free boundary conditions on the SW dispersion relations of a nanoscale magnonic antidot waveguide (MAW). Here we arrived at the conclusion that bandgaps can be opened more easily if magnetization dynamics at ferromagnet–air boundary is pinned. Pinning also shifted the SW band structure positively in the frequency domain. Thus, we learned that higher frequencies observed during experimental measurements may sometimes be related to this type of pinning.

In Chap. 6, we highlight the importance of the mirror symmetry of a magnonic antidot waveguide. First, we show that a small shift in the symmetrically placed row of antidots can cause the collapse of pre-existing magnonic bandgaps. Next, we demonstrate how similar collapse (of the magnonic bandgaps) can be engineered by employing an asymmetric bias magnetic field. Here, we observe that although, different bandgaps may have plural origins, their collapse can occur mainly due to a loss of degeneracy which was originally predicated upon the existence of mirror symmetry. We also show that intrinsic and extrinsic sources of asymmetry can be made to work against each other in order to selectively recover the pre-existing bandgaps. An analytical model to facilitate this procedure has also been developed. Thus, it can either be done consciously to alter the magnonic band structure of a MAW; or it can be used to rectify a systematic fabrication defect by calibrating the bias magnetic field of varying spatial profiles. The analytical model developed here was based on the discrete translational and the mirror symmetries of a crystal. Thus, the fundamentals behind the observations drawn here may be extended to other types of waves. The compensation effects should also be observable and usable in other systems outside the field of magnonics.<sup>287–289</sup>

It was known that the spectrum of dipole dominated SWs can be controlled by changing

the shape of the scattering centres on larger length scales.<sup>63</sup> In Chap. 7, we observe how the antidot's geometry can influence the SW dispersion in a MAW. Antidots in the shape of regular polygons are used for this analysis. We demonstrate that the band structure of exchange dominated SWs can be altered by changing the antidot shape. This change is seen to be effective only when the shape of the antidot actually changes the profile of the neighbouring exchange field. Power and phase distribution profiles were used to understand the origin of SW bands and bandgaps in different cases. As direct bandgaps are more desirable, this understanding can be used to improve the design of MAWs. Especially, since the direct bandgaps seen here can be opened at the same antidot filling fraction by simply changing the orientation of the holes.

After considering the effects of boundary conditions, mirror symmetry and antidot shape, in Chap. 8, we consider the effects of other geometrical parameters on SW dispersion in a MAW. The parameters considered here are antidot's size and MAW's lattice constant and scale. We also revisited the effect of antidot shape while considering MAWs on a different scale. The results obtained here can allow us to further characterize and control the magnonic band structure in a MAW. While examining the effect of MAW's scale we gained additional insight into the influence that exchange and dipolar interactions wield in the formation of the magnonic band structure. Using the PWM, it was found that an increase in the scale of the MAW can reveal backward volume magnetostatic bands in the spectrum. These bands are characterized by anti-parallel phase and group velocities close to the BZ centre. Although, a stronger splitting of degenerate modes was observed here the formation of SW band structure occurred in a manner which was qualitatively comparable to the case of exchange dominated SWs.

This study was conducted under the pinned boundary conditions. It was noticed that the effect of pinning becomes more pronounced with increase in the size of the antidots. This can allow one to control the crosstalk between the two halves of the waveguide (sub-waveguides) to increase or reduce the splitting of the degenerate modes. When the antidots' size is small in comparison the lattice constant of the waveguide, lower SW modes were localized amidst the row of the antidots. We also noticed that as a MAW's lattice constant was increased it started to resemble a uniform waveguide. However, unlike in the case of a uniform waveguide,

where the SW dispersion modes are parabolic, here they became flatter. This was due to the fact that an increase in the lattice constant caused the BZ boundaries to come closer. Thus, the anticrossing of modes at the BZ boundaries starts to occur more frequently resulting in a flattening of the SW dispersion modes.

As magnonic analogues of the electronic Fermi surfaces, iso-frequency lines can help us explore the SW dynamics in the wavevector space. In Chap. 9, the use of iso-frequency lines helped us underscore the anisotropy that existed between two mutually orthogonal SW propagation directions. We also explored the band structure of 2D MCs in more detail by analysing the mode profile of SWs using the power and phase analysis of the SW. In this chapter, we also noticed that SW dispersion in a square dot array was largely mediated by the dipole field even though the edge of the square dots and the lattice constant were only 6 nm and 9 nm, respectively. A negative group velocity associated with the first mode in the case of a backward volume magnetostatic configuration was observed here, and unlike the case described in Fig. 8.5, the upward curve associated with exchange dominated SWs was never registered.

In Chap. 11, we experimentally explore the tunability of SW band structure of MAWs based on their geometry and the bias magnetic field. As pump-probe based time-resolved Kerr effect (TR-MOKE) microscopy was used to observe the dynamics, the discussion here is limited to a very low wavevector regime. Thus, instead of obtaining an entire band structure, we get a few peaks associated with  $k \rightarrow 0$ . Based on the agreements (or the lack thereof) while comparing experimental and simulated results, we showed that SW modes, particularly the quantized modes, localized amidst the antidot array were more sensitive to any variance in the fabrication parameters. In contrast, the SW modes in the sub-waveguides were very stable and only manipulable by magnetic bias field's strength or direction. Edge mode of the waveguide was observed only in the Damon-Eshbach configuration and not in the backward volume configuration as the lateral edges were much farther away.

We also investigated magnetic vortex core gyration. It has a characteristic frequency in the low gigahertz and sub-gigahertz frequency bands. We first demonstrated that isolated magnetic vortices can transduce energy from rotating magnetic field to vortex core gyration. We also noted that core-switching here can be avoided if off-resonance signals of lower

amplitudes are used. Although, one also needs to consider a trade-off between the time taken to achieve the steady state and an anharmonic beating that is observed here. Next, we uncovered gyration mode amplification in magnetostatically coupled magnetic vortices. As inertia in the case of magnetic vortex cores is a vector (gyrovector) – as opposed to a scalar in the case of a conventional coupled oscillator, we demonstrated that this amplification can be switched on or off (by switching vortex core polarities). Based on this finding we also demonstrate transistor like operational states using a three vortex sequence.

Since these observations could not be explained by the current analytical model, we started to examine the temporal evolution of the stray field. We then discovered that antivortex packets moving through the stray field could account for these observations. Consequently our attempt to demonstrate a conventional fan-out operation was unsuccessful as the involved antivortices were topologically stable and would not split to divide the power equally in the daughter branches. We note this higher level of asymmetry was unlikely if the dynamic stray field did not possess these antivortices. This successfully validated the importance of antivortex solitons in the energy transfer mechanism.

## 13.2. Future Scope

If some of the techniques described here are to indeed become useful in creating new technology, the first thing that needs to be addressed is the resolution of the fabrication processes. There is a clear and wide divide between the length-scales of magnetic systems which are fabricable and those that can be handled using finite element or finite difference based numerical methods that exist today. Even with the recent advances in fabrication techniques which can allow one to pattern with resolutions below 10 nm,<sup>50,98–100,346</sup> it is still not possible to fabricate very accurately. For example, as seen in Chap. 11 the patterned dimensions may vary by  $\pm 10\%$ . This was clearly seen to alter the spectrum of SW modes localized amidst the antidot array.

In Chap. 5, we pointed out that pinning (at the edges of a geometry) can cause bandgaps to appear even if the filling fraction of antidots is as low as 5%. However, pinning cannot be achieved reliably. The results presented in Chap. 11 appear to agree with results simulated

without the pinned boundary condition. Pinning largely depends upon the surface magnetic anisotropy which can get accidentally altered<sup>282</sup> during the fabrication processes. Thus, further study is required with the aim to control the surface anisotropy during the fabrication techniques that are involved here.

In Chap. 6, we noticed how important the mirror symmetry of a waveguide is, as far as the band structure of exchange-dominated SWs are concerned. Similar investigation can be done for dipole-dominated SWs, after taking the inhomogeneity and anisotropy of the demagnetizing field<sup>286</sup> and the multi-mode character of waveguides<sup>201</sup> into account. This necessitates further research on this subject. Also, since the process of development of the analytical model presented here was dependent solely on the mirror and discrete translational symmetries of the MAW — a 1D MC, future research may be undertaken to develop similar models for photonic or phononic analogues.

MCs were studied in some detail in this work. Useful devices, such as an add-drop filter can be envisioned by using magnonic quasicrystals. Thus more work needs to be conducted with crystals which do not feature perfect discrete translational symmetry.

While discussing the observed amplifications of the gyrotropic modes in Chap. 12, we mention (see Sec. A.1) that the present analytical model does not predict these results. We think that further study, guided by the analysis of the dynamic stray field, can help with the development of an analytical model capable of predicting these useful results. We also need to optimize the gain  $B$ , as defined in Eq. (12.1), by examining its dependence on various geometrical and material parameters and the nature of excitation frequency. In the absence of a more complete analytical model, one will presently need to rely on extensive simulations to accomplish this task.

More work will also be required in the future in order to miniaturize the single transistor. The ‘magnetic vortex transistor’ (MVT) described in Chap. 12, spans an area of about  $750 \text{ nm} \times 250 \text{ nm}$  with a thickness of  $40 \text{ nm}$ . These dimensions will have to be reduced by an order of magnitude in order to make the MVT as a more attractive substitute to the kinds of transistors used today. As the diameter of an isolated nanodisk, which can support a magnetic vortex cannot be reduced indefinitely, more fundamental research is required here. We also need to study the power consumption and efficiency of a MVT to minimize the

losses during transistor operations.

Fan-out is required to facilitate the design of more complex circuits. Since the topologically stable antivortices, which appear to be responsible for the observed amplification, do not treat different branches of the circuit symmetrically, more work is required here. Perhaps a successful fan-out can be obtained by observing the cascade of the involved antivortices and rearranging the branches of the circuit accordingly.

# A. Appendix

## A.1. Supplementary Note for Chap. 12

For a pair of coupled harmonic oscillators featuring the same inertia, stiffness and damping, it is not possible to get an increased oscillation in one of the oscillators while the other one is being driven with a frequency close to the eigenfrequency of individual oscillators. Some close parallels can be drawn between such mechanical coupled oscillators and a pair of magnetostatically coupled vortices as shown in Fig. 12.1 (b). We write the following Thiele's equation for both the vortices identifying them with subscripts  $i = 1$  (left vortex) or  $i = 2$  (right vortex):

$$-\kappa \mathbf{r}_i + \mathbf{G}_i \times \mathbf{v}_i + \overleftrightarrow{\mathbf{D}} \cdot \mathbf{v}_i - \frac{\partial W_{\text{int}}(\mathbf{r}_1, \mathbf{r}_2)}{\partial \mathbf{r}_i} + \mathbf{T}_{\text{sig},i} = 0.$$

Here,  $\kappa$  is a stiffness factor which seeks to restore the displaced vortex core functioning much like the stiffness of a spring.<sup>163</sup>  $\mathbf{G}_i = -Gp_i\hat{\mathbf{z}}$  ( $G > 0$ ),<sup>163</sup> is the inertia associated with  $i^{\text{th}}$  vortex core. Polarity  $p_1 = 1$  and  $p_2 = \pm 1$  depending upon the case under consideration. Although,  $\mathbf{G}_i$  depends upon polarity, the term  $\mathbf{G}_i \times \mathbf{v}_i$  does not. This is because, if the polarity  $p_i$  is switched, both  $\mathbf{G}_i$  and  $\mathbf{v}_i$  change to  $-\mathbf{G}_i$  and  $-\mathbf{v}_i$ , respectively; thus, preserving the original cross product. In the case of isotropic damping, the term  $\overleftrightarrow{\mathbf{D}} \cdot \mathbf{v}_i$  can be replaced with  $D\mathbf{v}_i$ , where  $D$  is a scalar independent of polarity.<sup>163</sup> Also,<sup>151</sup>

$$\mathbf{T}_{\text{sig},i} = \begin{cases} \mu(\hat{\mathbf{z}} \times \mathbf{H}_{\text{sig}}) & i = 1 \\ 0 & i = 2 \end{cases},$$

where,  $\mu$  is a chirality dependent coupling constant and  $\mathbf{H}_{\text{sig}}$  is an in plane excitation field rotating at frequency  $\kappa/G$ . It is important to consider this eigenfrequency because a transducer which is converting a magnetic field signal to vortex core gyration signal is likely to show significant peaks around it (see Fig. A.1 (e)).  $W_{\text{int}}$  is the interaction energy between the two vortices, which according to Ref. 149 is given as

$$W_{\text{int}} = c_1 c_2 (\eta_x x_1 x_2 - \eta_y y_1 y_2),$$

where,  $c_1 = c_2 = 1$  for the CCW chiralities considered here and  $\eta_{x,y}$  is the interaction coefficients depending upon certain geometrical and material parameters, but independent of relative polarity.

It has now been established that all the terms in the Thiele's equation, with the exception of the dissipation term, are independent of relative polarity  $p_2$  of the vortices. The dependence of the dissipation term upon the direction of velocity does not affect the absolute value of gain  $r_2/r_1$ . Thus, according to this model, the gain  $r_2/r_1$  should not depend upon polarity  $p_2$ . This deviates from the polarity dependent amplification presented here. In the case of analogous mechanical coupled oscillators, it would be possible to show such gain while driving at a frequency  $f$  ( $\leq f_0$ ), if the inertia of the oscillator (which is not being driven directly) was changed from  $I$  to  $-I$ . However, that is a purely hypothetical consideration.

## A.2. Supplementary Figures for Chap. 12

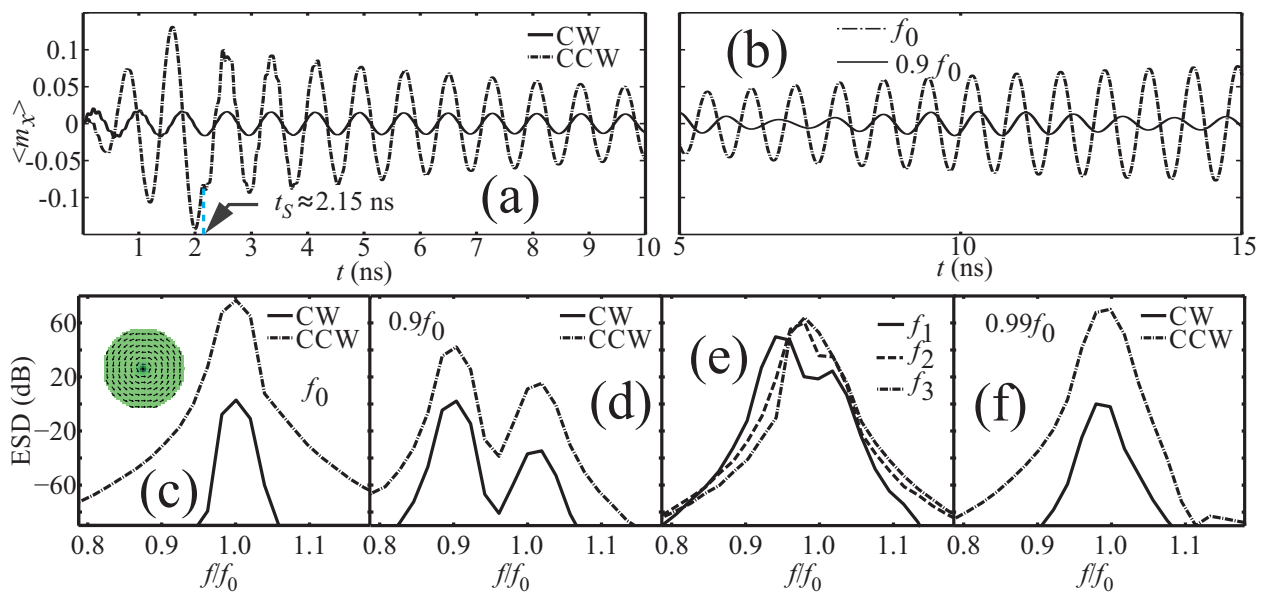


Figure A.1.: (a) Plots of  $\langle m_x \rangle$  vs. time for signals rotating CW and CCW with a frequency  $f_0$  and amplitude 1.5 mT. Polarity switching is seen with CCW signal at  $t_s \approx 2.15$  ns. (b) Plots of  $\langle m_x \rangle$  vs. time for signals rotating CCW with frequencies  $f_0$  and  $0.9f_0$  and amplitude 0.5 mT. No polarity switching is observed. Convergence for  $f_0$  is taking more time. ESDs of vortex dynamics with excitation signal rotating CW and CCW with amplitude 0.5 mT and frequencies (c)  $f_0$ , (d)  $0.9f_0$  and (f)  $0.99f_0$ . Beating is observed. Beating frequency decreases systematically with increasing signal frequency. (e) ESDs of vortex dynamics with excitation signal rotating CCW with amplitude 0.5 mT and frequencies  $f_1 = 0.95f_0$ ,  $f_1 = 0.975f_0$  and  $f_1 = 0.98f_0$ . As seen in the inset of (c), the core polarity is up and chirality is CCW.

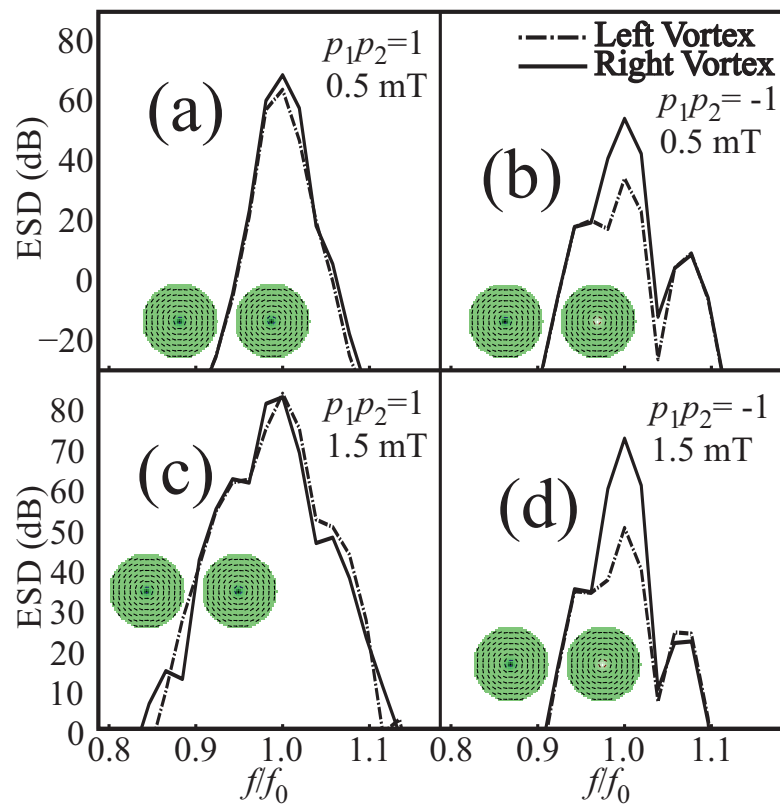


Figure A.2.: ESDs of left and right magnetic vortices shown in the insets with ((a) and (c)) similar and ((b) and (d)) opposite polarities while using a cell size of  $2.5 \text{ nm} \times 2.5 \text{ nm} \times 40 \text{ nm}$ . (a) and (b) show the results for a signal amplitude of  $0.5 \text{ mT}$  while (c) and (d) show those for an amplitude of  $1.5 \text{ mT}$ , both rotating CCW at  $f = f_0$ .



# Bibliography

- [1] F. Bloch, Z. Physik **61**, 206 (1930).
- [2] F. J. Dyson, Phys. Rev. **102**, 1217 (1956).
- [3] A. V. Chumak, V. S. Tiberkevich, A. D. Karenowska, A. A. Serga, J. F. Gregg, A. N. Slavin, and B. Hillebrands, Nat. Commun. **1**, 141 (2010).
- [4] J. W. Kłos, D. Kumar, M. Krawczyk, and A. Barman, Sci. Rep. **3**, 2444 (2013).
- [5] S.-K. Kim, J. Phys. D: Appl. Phys. **43**, 264004 (2010).
- [6] B. Rana, *Quasistatic and Ultrafast Magnetization Dynamics in Magnetic Nanostructures*, Ph.D. thesis, University of Calcutta (2013).
- [7] L. D. Landau and E. M. Lifshitz, Phys. Zeitsch. der Sow. **8**, 153 (1935).
- [8] T. Gilbert, IEEE Trans. Mag. **40**, 3443 (2004).
- [9] A. Barman, S. Barman, T. Kimura, Y. Fukuma, and Y. Otani, J. Phys. D: Appl. Phys. **43**, 422001 (2010).
- [10] M. N. Baibich, J. M. Broto, A. Fert, F. N. Van Dau, F. Petroff, P. Etienne, G. Creuzet, A. Friederich, and J. Chazelas, Phys. Rev. Lett. **61**, 2472 (1988).
- [11] G. Binasch, P. Grünberg, F. Saurenbach, and W. Zinn, Phys. Rev. B **39**, 4828 (1989).
- [12] M. Inoue, K. Arai, T. Fujii, and M. Abe, J. Appl. Phys. **85**, 5768 (1999).
- [13] P. F. Carcia, A. D. Meinhaldt, and A. Suna, Appl. Phys. Lett. **47**, 178 (1985).
- [14] P. F. Carcia, J. Appl. Phys. **63**, 5066 (1988).
- [15] S. Choi, K.-S. Lee, K. Y. Guslienko, and S.-K. Kim, Phys. Rev. Lett. **98**, 087205 (2007).
- [16] S. Gliga, *Ultrafast Vortex Core Dynamics Investigated by Finite-element Micromagnetic Simulations*, Schriften des Forschungszentrums Jülich / Reihe Energie & Umwelt: Reihe Energie & Umwelt (Forschungszentrum Jülich, Zentralbibliothek, 2010).
- [17] J. Bland and B. Heinrich, eds., *Ultrathin Magnetic Structures II*, Ultrathin Magnetic Structures (Springer, 2005).

- [18] S. Iida, *J. Phys. Chem. Solids* **24**, 625 (1963).
- [19] R. Arias and D. L. Mills, *Phys. Rev. B* **60**, 7395 (1999).
- [20] J. Lindner, K. Lenz, E. Kosubek, K. Baberschke, D. Spoddig, R. Meckenstock, J. Pelzl, Z. Frait, and D. L. Mills, *Phys. Rev. B* **68**, 060102 (2003).
- [21] J. Xiao, A. Zangwill, and M. D. Stiles, *Phys. Rev. B* **70**, 172405 (2004).
- [22] T. Sebastian, Y. Ohdaira, T. Kubota, P. Pirro, T. Brächer, K. Vogt, A. A. Serga, H. Naganuma, M. Oogane, Y. Ando, and B. Hillebrands, *Appl. Phys. Lett.* **100**, 112402 (2012).
- [23] A. Conca, J. Greser, T. Sebastian, S. Klingler, B. Obry, B. Leven, and B. Hillebrands, *J. Appl. Phys.* **113**, 213909 (2013).
- [24] L. Zhang, J. Ren, J.-S. Wang, and B. Li, *Phys. Rev. B* **87**, 144101 (2013).
- [25] R. Shindou, R. Matsumoto, S. Murakami, and J.-i. Ohe, *Phys. Rev. B* **87**, 174427 (2013).
- [26] A. I. Akhiezer, V. G. Bar'yakhtar, and S. V. Peletminskii, *Spin Waves* (North-Holland, 1968).
- [27] A. Gurevich and G. Melkov, *Magnetization Oscillations and Waves* (Taylor & Francis, 1996).
- [28] D. Stancil and A. Prabhakar, *Spin Waves: Theory and Applications* (Springer, 2009).
- [29] K.-J. Lee, A. Deac, O. Redon, J.-P. Nozieres, and B. Dieny, *Nat. Mater.* **3**, 877 (2004).
- [30] T. Holstein and H. Primakoff, *Phys. Rev.* **58**, 1098 (1940).
- [31] C. Rüegg, A. Furrer, D. Sheptyakov, T. Strässle, K. W. Krämer, H.-U. Güdel, and L. Mélési, *Phys. Rev. Lett.* **93**, 257201 (2004).
- [32] S. O. Demokritov, V. E. Demidov, O. Dzyapko, G. A. Melkov, A. A. Serga, B. Hillebrands, and A. N. Slavin, *Nature* **443**, 430 (2006).
- [33] P. Nowik-Boltyk, O. Dzyapko, V. E. Demidov, N. G. Berloff, and S. O. Demokritov, *Sci. Rep.* **2**, 482 (2012).
- [34] G. Srivastava, *The Physics of Phonons* (Taylor & Francis, 1990).
- [35] S. Nikitov, P. Tailhades, and C. Tsai, *J. Magn. Magn. Mater.* **236**, 320 (2001).
- [36] H. Puzkarski and M. Krawczyk, *Solid State Phenom.* **94**, 125 (2003).
- [37] S. Neusser and D. Grundler, *Adv. Mater.* **21**, 2927 (2009).

- 
- [38] B. Lenk, H. Ulrichs, F. Garbs, and M. Munzenberg, *Physics Reports* **507**, 107 (2011).
- [39] L. J. Heyderman and R. L. Stamps, *J. Phys.: Condens. Matter* **25**, 363201 (2013).
- [40] C. G. Sykes, J. D. Adam, and J. H. Collins, *Appl. Phys. Lett.* **29**, 388 (1976).
- [41] C. Bayer, M. P. Kostylev, and B. Hillebrands, *Appl. Phys. Lett.* **88**, 112504 (2006).
- [42] V. V. Kruglyak, R. J. Hicken, A. N. Kuchko, and V. Y. Gorobets, *J. Appl. Phys.* **98**, 014304 (2005).
- [43] A. V. Chumak, A. A. Serga, B. Hillebrands, and M. P. Kostylev, *Appl. Phys. Lett.* **93**, 022508 (2008).
- [44] Z. K. Wang, V. L. Zhang, H. S. Lim, S. C. Ng, M. H. Kuok, S. Jain, and A. O. Adeyeye, *Appl. Phys. Lett.* **94**, 083112 (2009).
- [45] S. Mamica, M. Krawczyk, and J. W. Kłos, *Adv. Cond. Matt. Phys.* **2012**, 161387 (2012).
- [46] S. Vysotskii, S. Nikitov, E. Pavlov, and Y. Filimonov, *J. Commun. Technol. Electron.* **55**, 800 (2010).
- [47] S. Tacchi, M. Madami, G. Gubbiotti, G. Carlotti, H. Tanigawa, T. Ono, and M. P. Kostylev, *Phys. Rev. B* **82**, 024401 (2010).
- [48] S. Tacchi, F. Montoncello, M. Madami, G. Gubbiotti, G. Carlotti, L. Giovannini, R. Zivieri, F. Nizzoli, S. Jain, A. O. Adeyeye, and N. Singh, *Phys. Rev. Lett.* **107**, 127204 (2011).
- [49] S. Saha, S. Barman, J. Ding, A. O. Adeyeye, and A. Barman, *Appl. Phys. Lett.* **102**, 242409 (2013).
- [50] R. Mandal, S. Saha, D. Kumar, S. Barman, S. Pal, K. Das, A. K. Raychaudhuri, Y. Fukuma, Y. Otani, and A. Barman, *ACS Nano* **6**, 3397 (2012).
- [51] M. Krawczyk and H. Puzskarski, *Phys. Rev. B* **77**, 054437 (2008).
- [52] S. Mamica, M. Krawczyk, M. L. Sokolovskyy, and J. Romero-Vivas, *Phys. Rev. B* **86**, 144402 (2012).
- [53] M. J. Pechan, C. Yu, R. L. Compton, J. P. Park, and P. A. Crowell, *J. Appl. Phys.* **97**, 10J903 (2005).
- [54] S. Neusser, B. Botters, and D. Grundler, *Phys. Rev. B* **78**, 054406 (2008).
- [55] S. Neusser, G. Duerr, H. G. Bauer, S. Tacchi, M. Madami, G. Woltersdorf, G. Gubbiotti, C. H. Back, and D. Grundler, *Phys. Rev. Lett.* **105**, 067208 (2010).

- [56] S. Tacchi, M. Madami, G. Gubbiotti, G. Carlotti, A. Adeyeye, S. Neusser, B. Botters, and D. Grundler, *IEEE Trans. Magn.* **46**, 1440 (2010).
- [57] S. Neusser, H. G. Bauer, G. Duerr, R. Huber, S. Mamica, G. Woltersdorf, M. Krawczyk, C. H. Back, and D. Grundler, *Phys. Rev. B* **84**, 184411 (2011).
- [58] S. Tacchi, B. Botters, M. Madami, J. W. Kłos, M. L. Sokolovskyy, M. Krawczyk, G. Gubbiotti, G. Carlotti, A. O. Adeyeye, S. Neusser, and D. Grundler, *Phys. Rev. B* **86**, 014417 (2012).
- [59] C.-L. Hu, R. Magaraggia, H.-Y. Yuan, C. S. Chang, M. Kostylev, D. Tripathy, A. O. Adeyeye, and R. L. Stamps, *Appl. Phys. Lett.* **98**, 262508 (2011).
- [60] Z. K. Wang, V. L. Zhang, H. S. Lim, S. C. Ng, M. H. Kuok, S. Jain, and A. O. Adeyeye, *ACS Nano* **4**, 643 (2010).
- [61] G. Duerr, M. Madami, S. Neusser, S. Tacchi, G. Gubbiotti, G. Carlotti, and D. Grundler, *Appl. Phys. Lett.* **99**, 202502 (2011).
- [62] S. Tacchi, G. Duerr, J. W. Kłos, M. Madami, S. Neusser, G. Gubbiotti, G. Carlotti, M. Krawczyk, and D. Grundler, *Phys. Rev. Lett.* **109**, 137202 (2012).
- [63] J. W. Kłos, M. L. Sokolovskyy, S. Mamica, and M. Krawczyk, *J. Appl. Phys.* **111**, 123910 (2012).
- [64] S. Saha, R. Mandal, S. Barman, D. Kumar, B. Rana, Y. Fukuma, S. Sugimoto, Y. Otani, and A. Barman, *Adv. Funct. Mater.* **23**, 2378 (2013).
- [65] R. Mandal, P. Laha, K. Das, S. Saha, S. Barman, A. K. Raychaudhuri, and A. Barman, *Appl. Phys. Lett.* **103**, 262410 (2013).
- [66] J. W. Kłos, D. Kumar, M. Krawczyk, and A. Barman, *Phys. Rev. B* **89**, 014406 (2014).
- [67] R. Zivieri, S. Tacchi, F. Montoncello, L. Giovannini, F. Nizzoli, M. Madami, G. Gubbiotti, G. Carlotti, S. Neusser, G. Duerr, and D. Grundler, *Phys. Rev. B* **85**, 012403 (2012).
- [68] D. Kumar, P. Sabareesan, W. Wang, H. Fangohr, and A. Barman, *J. Appl. Phys.* **114**, 023910 (2013).
- [69] V. V. Kruglyak, S. O. Demokritov, and D. Grundler, *J. Phys. D: Appl. Phys.* **43**, 264001 (2010).
- [70] A. A. Serga, A. V. Chumak, and B. Hillebrands, *J. Phys. D: Appl. Phys.* **43**, 264002 (2010).
- [71] S. O. Demokritov and A. N. Slavin, *Magnonics: From Fundamentals to Applications* (Springer, 2013).

- [72] T. Schneider, A. Serga, B. Hillebrands, and M. Kostylev, *J. Nanoelectr. Optoelectr.* **3**, 69 (2008).
- [73] F. Macià, A. D. Kent, and F. C. Hoppensteadt, *Nanotechnology* **22**, 095301 (2011).
- [74] A. Khitun, M. Bao, and K. L. Wang, *J. Phys. D: Appl. Phys.* **43**, 264005 (2010).
- [75] R. V. Mikhaylovskiy, E. Hendry, and V. V. Kruglyak, *Phys. Rev. B* **82**, 195446 (2010).
- [76] H. Rong, S. Xu, O. Cohen, O. Raday, M. Lee, V. Sih, and M. Paniccia, *Nat. Photon.* **2**, 170 (2008).
- [77] A. Khitun, M. Bao, and K. Wang, *IEEE Trans. Mag.* **44**, 2141 (2008).
- [78] H. Yu, G. Duerr, R. Huber, M. Bahr, T. Schwarze, F. Brandl, and D. Grundler, *Nat. Commun.* **4**, 2702 (2013).
- [79] G. Venkat, D. Kumar, M. Franchin, O. Dmytriiev, M. Mruczkiewicz, H. Fangohr, A. Barman, M. Krawczyk, and A. Prabhakar, *IEEE Trans. Mag.* **49**, 524 (2013).
- [80] S. Choi, K.-S. Lee, and S.-K. Kim, *Appl. Phys. Lett.* **89**, 062501 (2006).
- [81] J. Podbielski, F. Giesen, and D. Grundler, *Phys. Rev. Lett.* **96**, 167207 (2006).
- [82] T. Schneider, A. A. Serga, B. Leven, B. Hillebrands, R. L. Stamps, and M. P. Kostylev, *Appl. Phys. Lett.* **92**, 022505 (2008).
- [83] Y. Au, M. Dvornik, O. Dmytriiev, and V. V. Kruglyak, *Appl. Phys. Lett.* **100**, 172408 (2012).
- [84] K.-S. Lee, D.-S. Han, and S.-K. Kim, *Phys. Rev. Lett.* **102**, 127202 (2009).
- [85] S.-K. Kim, K.-S. Lee, and D.-S. Han, *Appl. Phys. Lett.* **95**, 082507 (2009).
- [86] F. Ciubotaru, A. V. Chumak, N. Y. Grigoryeva, A. A. Serga, and B. Hillebrands, *J. Phys. D: Appl. Phys.* **45**, 255002 (2012).
- [87] A. Khitun, *J. Appl. Phys.* **111**, 054307 (2012).
- [88] S. Bonetti, P. Muduli, F. Mancoff, and J. Åkerman, *Appl. Phys. Lett.* **94**, 102507 (2009).
- [89] O. Prokopenko, E. Bankowski, T. Meitzler, V. Tiberkevich, and A. Slavin, *IEEE Magn. Lett.* **2**, 3000104 (2011).
- [90] M. Madami, S. Bonetti, G. Consolo, S. Tacchi, G. Carlotti, G. Gubbiotti, F. B., Mancoff, M. A. Yar, and J. Åkerman, *Nat. Nanotechnol.* **6**, 635 (2011).
- [91] T. Satoh, Y. Terui, R. Moriya, B. A. Ivanov, K. Ando, E. Saitoh, T. Shimura, and K. Kuroda, *Nat. Photon.* **6**, 662 (2012).

- [92] A. Kozhanov, D. Ouellette, Z. Griffith, M. Rodwell, A. Jacob, D. Lee, S. Wang, and S. Allen, *Appl. Phys. Lett.* **94**, 012505 (2009).
- [93] V. E. Demidov, M. P. Kostylev, K. Rott, J. Munchenberger, G. Reiss, and S. O. Demokritov, *Appl. Phys. Lett.* **99**, 082507 (2011).
- [94] L. Bai, M. Kohda, and J. Nitta, *Appl. Phys. Lett.* **98**, 172508 (2011).
- [95] P. Clausen, K. Vogt, H. Schultheiss, S. Schafer, B. Obry, G. Wolf, P. Pirro, B. Leven, and B. Hillebrands, *Appl. Phys. Lett.* **99**, 162505 (2011).
- [96] G. Duerr, K. Thurner, J. Topp, R. Huber, and D. Grundler, *Phys. Rev. Lett.* **108**, 227202 (2012).
- [97] T. Schwarze, R. Huber, G. Duerr, and D. Grundler, *Phys. Rev. B* **85**, 134448 (2012).
- [98] F. H. M. Rahman, S. McVey, L. Farkas, J. A. Notte, S. Tan, and R. H. Livengood, *Scanning* **34**, 129 (2012).
- [99] V. Sidorkin, E. van Veldhoven, E. van der Drift, P. Alkemade, H. Salemink, and D. Maas, *J. Vac. Sci. Technol. B* **27**, L18 (2009).
- [100] T. G. Siegfried, Y. Ekinici, H. H. Solak, O. J. F. Martin, and H. Sigg, *Appl. Phys. Lett.* **99**, 263302 (2011).
- [101] T. Silva and W. Rippard, *J. Magn. Magn. Mater.* **320**, 1260 (2008).
- [102] R. E. Camley and R. L. Stamps, eds., *Chapter Four - Spin-Torque Oscillators*, *Solid State Physics*, Vol. 63 (Academic Press, 2012) pp. 217 – 294.
- [103] S. I. Kiselev, J. C. Sankey, I. N. Krivorotov, N. C. Emley, R. J. Schoelkopf, R. A. Buhrman, and D. C. Ralph, *Nature* **425**, 380 (2003).
- [104] J. E. Hirsch, *Phys. Rev. Lett.* **83**, 1834 (1999).
- [105] K. Uchida, S. Takahashi, K. Harii, J. Ieda, W. Koshibae, K. Ando, S. Maekawa, and E. Saitoh, *Nature* **455**, 778 (2008).
- [106] C. M. Jaworski, J. Yang, S. Mack, D. D. Awschalom, J. P. Heremans, and R. C. Myers, *Nat. Mater.* **9**, 898 (2010).
- [107] H. Adachi, K. ichi Uchida, E. Saitoh, and S. Maekawa, *Rep. on Prog. in Phys.* **76**, 036501 (2013).
- [108] M. Agrawal, V. I. Vasyuchka, A. A. Serga, A. D. Karenowska, G. A. Melkov, and B. Hillebrands, *Phys. Rev. Lett.* **111**, 107204 (2013).
- [109] B. F. Miao, S. Y. Huang, D. Qu, and C. L. Chien, *Phys. Rev. Lett.* **111**, 066602 (2013).

- 
- [110] A. V. Kimel, A. Kirilyuk, A. Tsvetkov, R. V. Pisarev, and T. Rasing, *Nature* **429**, 850 (2004).
- [111] K. Perzlmaier, M. Buess, C. H. Back, V. E. Demidov, B. Hillebrands, and S. O. Demokritov, *Phys. Rev. Lett.* **94**, 057202 (2005).
- [112] A. V. Kimel, A. Kirilyuk, F. Hansteen, R. V. Pisarev, and T. Rasing, *J. Phys.: Condens. Matter* **19**, 043201 (2007).
- [113] J.-Y. Bigot, M. Vomir, and E. Beaurepaire, *Nat. Phys.* **5**, 515 (2009).
- [114] Y. Gong, A. R. Kutayiah, X. H. Zhang, J. H. Zhao, and Y. H. Ren, *J. Appl. Phys.* **111**, 07D505 (2012).
- [115] W. K. Hiebert, A. Stankiewicz, and M. R. Freeman, *Phys. Rev. Lett.* **79**, 1134 (1997).
- [116] A. Barman, V. V. Kruglyak, R. J. Hicken, A. Kundrotaite, and M. Rahman, *Appl. Phys. Lett.* **82**, 3065 (2003).
- [117] B. Rana and A. Barman, *SPIN* **03**, 1330001 (2013).
- [118] Y. Zhang, T.-H. Chuang, K. Zakeri, and J. Kirschner, *Phys. Rev. Lett.* **109**, 087203 (2012).
- [119] D. Polley, A. Ganguly, A. Barman, and R. K. Mitra, *Opt. Lett.* **38**, 2754 (2013).
- [120] T. Kampfrath, A. Sell, G. Klatt, A. Pashkin, S. Mahrlein, T. Dekorsy, M. Wolf, M. Fiebig, A. Leitenstorfer, and R. Huber, *Nat. Photon.* **5**, 31 (2011).
- [121] J. Nishitani, T. Nagashima, and M. Hangyo, *Phys. Rev. B* **85**, 174439 (2012).
- [122] T. J. Silva, C. S. Lee, T. M. Crawford, and C. T. Rogers, *J. Appl. Phys.* **85**, 7849 (1999).
- [123] G. Counil, J.-V. Kim, T. Devolder, C. Chappert, K. Shigeto, and Y. Otani, *J. Appl. Phys.* **95**, 5646 (2004).
- [124] S. Demokritov, B. Hillebrands, and A. Slavin, *Phys. Rep.* **348**, 441 (2001).
- [125] C. L. Ordóñez Romero, M. A. Cherkasskii, N. Qureshi, B. A. Kalinikos, and C. E. Patton, *Phys. Rev. B* **87**, 174430 (2013).
- [126] R. Antos, Y. Otani, and J. Shibata, *J. Phys. Soc. Jpn.* **77**, 031004 (2008).
- [127] K. Y. Guslienko, K.-S. Lee, and S.-K. Kim, *Phys. Rev. Lett.* **100**, 027203 (2008).
- [128] B. Van Waeyenberge, A. Puzic, H. Stoll, K. W. Chou, T. Tyliczszak, R. Hertel, M. Fahnle, H. Bruckl, K. Rott, G. Reiss, I. Neudecker, D. Weiss, C. H. Back, and G. Schutz, *Nature* **444**, 461 (2006).

- [129] K. Yamada, S. Kasai, Y. Nakatani, K. Kobayashi, H. Kohno, A. Thiaville, and T. Ono, *Nat. Mater.* **6**, 270 (2007).
- [130] R. P. Cowburn, *Nat. Mater.* **6**, 255 (2007).
- [131] J. Thomas, *Nat. Nanotechnol.* **2**, 206 (2007).
- [132] R. Cowburn, *J. Magn. Magn. Mater.* **242–245**, 505 (2002).
- [133] J. A. J. Burgess, A. E. Fraser, F. F. Sani, D. Vick, B. D. Hauer, J. P. Davis, and M. R. Freeman, *Science* **339**, 1051 (2013).
- [134] A. Wachowiak, J. Wiebe, M. Bode, O. Pietzsch, M. Morgenstern, and R. Wiesendanger, *Science* **298**, 577 (2002).
- [135] T. Shinjo, T. Okuno, R. Hassdorf, K. Shigeto, and T. Ono, *Science* **289**, 930 (2000).
- [136] M. R. Pufall, W. H. Rippard, S. E. Russek, S. Kaka, and J. A. Katine, *Phys. Rev. Lett.* **97**, 087206 (2006).
- [137] K. Y. Guslienko, B. A. Ivanov, V. Novosad, Y. Otani, H. Shima, and K. Fukamichi, *J. Appl. Phys.* **91**, 8037 (2002).
- [138] S.-B. Choe, Y. Acremann, A. Scholl, A. Bauer, A. Doran, J. StÅhr, and H. A. Padmore, *Science* **304**, 420 (2004).
- [139] S. Sugimoto, Y. Fukuma, S. Kasai, T. Kimura, A. Barman, and Y. Otani, *Phys. Rev. Lett.* **106**, 197203 (2011).
- [140] A. Vansteenkiste, K. W. Chou, M. Weigand, M. Curcic, V. Sackmann, H. Stoll, T. Tyliczszak, G. Woltersdorf, C. H. Back, G. Schutz, and B. Van Waeyenberge, *Nat. Phys.* **5**, 332 (2009).
- [141] M. Curcic, B. Van Waeyenberge, A. Vansteenkiste, M. Weigand, V. Sackmann, H. Stoll, M. FÅhnle, T. Tyliczszak, G. Woltersdorf, C. H. Back, and G. Schütz, *Phys. Rev. Lett.* **101**, 197204 (2008).
- [142] M. Weigand, B. Van Waeyenberge, A. Vansteenkiste, M. Curcic, V. Sackmann, H. Stoll, T. Tyliczszak, K. Kaznatcheev, D. Bertwistle, G. Woltersdorf, C. H. Back, and G. Schütz, *Phys. Rev. Lett.* **102**, 077201 (2009).
- [143] M. Bolte, G. Meier, B. KrÅger, A. Drews, R. Eiselt, L. Bocklage, S. Bohlens, T. Tyliczszak, A. Vansteenkiste, B. Van Waeyenberge, K. W. Chou, A. Puzic, and H. Stoll, *Phys. Rev. Lett.* **100**, 176601 (2008).
- [144] B. L. Mesler, K. S. Buchanan, M.-Y. Im, and P. Fischer, *J. Appl. Phys.* **111**, 07D311 (2012).
- [145] K.-S. Lee and S.-K. Kim, *Appl. Phys. Lett.* **91**, 132511 (2007).
- [146] A. A. Thiele, *Phys. Rev. Lett.* **30**, 230 (1973).

- [147] V. Novosad, F. Y. Fradin, P. E. Roy, K. S. Buchanan, K. Y. Guslienko, and S. D. Bader, *Phys. Rev. B* **72**, 024455 (2005).
- [148] Y. Liu, S. Gliga, R. Hertel, and C. M. Schneider, *Appl. Phys. Lett.* **91**, 112501 (2007).
- [149] J. Shibata, K. Shigeto, and Y. Otani, *Phys. Rev. B* **67**, 224404 (2003).
- [150] J. Shibata and Y. Otani, *Phys. Rev. B* **70**, 012404 (2004).
- [151] K. Y. Guslienko, *Appl. Phys. Lett.* **89**, 022510 (2006).
- [152] K.-S. Lee and S.-K. Kim, *Phys. Rev. B* **78**, 014405 (2008).
- [153] K. L. Metlov and K. Y. Guslienko, *J. Magn. Magn. Mater.* **242–245**, 1015 (2002), proceedings of the Joint European Magnetic Symposia (JEMS'01).
- [154] K.-S. Lee, H. Jung, D.-S. Han, and S.-K. Kim, *J. Appl. Phys.* **110**, 113903 (2011).
- [155] H. Jung, K.-S. Lee, D.-E. Jeong, Y.-S. Choi, Y.-S. Yu, D.-S. Han, A. Vogel, L. Bocklage, G. Meier, M.-Y. Im, P. Fischer, and S.-K. Kim, *Sci. Rep.* **1**, (2011).
- [156] A. Vogel, T. Kamionka, M. Martens, A. Drews, K. W. Chou, T. Tylliszczak, H. Stoll, B. Van Waeyenberge, and G. Meier, *Phys. Rev. Lett.* **106**, 137201 (2011).
- [157] A. Vogel, A. Drews, M. Weigand, and G. Meier, *AIP Advances* **2**, 042180 (2012).
- [158] L. Landau and E. Lifshits, *Ukr. J. Phys.* **53**, 14 (2008).
- [159] B. Krüger, A. Drews, M. Bolte, U. Merkt, D. Pfannkuche, and G. Meier, *Phys. Rev. B* **76**, 224426 (2007).
- [160] S. Barman, A. Barman, and Y. Otani, *IEEE Trans. Magn.* **46**, 1342 (2010).
- [161] S. Barman, A. Barman, and Y. Otani, *J. Phys. D: Appl. Phys.* **43**, 335001 (2010).
- [162] H. Jung, Y.-S. Choi, K.-S. Lee, D.-S. Han, Y.-S. Yu, M.-Y. Im, P. Fischer, and S.-K. Kim, *ACS Nano* **6**, 3712 (2012).
- [163] J.-H. Kim, K.-S. Lee, H. Jung, D.-S. Han, and S.-K. Kim, *Appl. Phys. Lett.* **101**, 092403 (2012).
- [164] A. Morrish, *The Physical Principles of Magnetism*, An IEEE Press classic reissue (Wiley, 2001).
- [165] R. O'Handley, *Modern Magnetic Materials: Principles and Applications*, A Wiley-Interscience publication (Wiley, 1999).
- [166] G. Bordignon, *Simulations of ferromagnetic nano-structures*, Ph.D. thesis, University of Southampton (2008).

- [167] A. Aharoni, *Introduction to the Theory of Ferromagnetism*, International Series of Monographs on Physics (Clarendon Press, 2000).
- [168] M. Oogane, T. Wakitani, S. Yakata, R. Yilgin, Y. Ando, A. Sakuma, and T. Miyazaki, *Jpn. J. Appl. Phys.* **45**, 3889 (2006).
- [169] S. Trudel, O. Gaier, J. Hamrle, and B. Hillebrands, *J. Phys. D: Appl. Phys.* **43**, 193001 (2010).
- [170] C. Scheck, L. Cheng, and W. E. Bailey, *Appl. Phys. Lett.* **88**, 252510 (2006).
- [171] A. Knittel, *Micromagnetic simulations of three dimensional core-shell nanostructures*, Ph.D. thesis, University of Southampton (2011).
- [172] J. H. E. Griffiths, *Nature* **158**, 670 (1946).
- [173] C. Kittel, *Phys. Rev.* **73**, 155 (1948).
- [174] A. Hubert and R. Schäfer, *Magnetic Domains: The Analysis of Magnetic Microstructures* (Springer, 1998).
- [175] E. Beaurepaire, J.-C. Merle, A. Daunois, and J.-Y. Bigot, *Phys. Rev. Lett.* **76**, 4250 (1996).
- [176] B. Koopmans, *Nat. Mater.* **6**, 715 (2007).
- [177] E. Carpena, E. Mancini, C. Dallera, M. Brenna, E. Puppini, and S. De Silvestri, *Phys. Rev. B* **78**, 174422 (2008).
- [178] J.-Y. Bigot, M. Vomir, L. Andrade, and E. Beaurepaire, *Chemical Physics* **318**, 137 (2005).
- [179] L. Guidoni, E. Beaurepaire, and J.-Y. Bigot, *Phys. Rev. Lett.* **89**, 017401 (2002).
- [180] P. M. Oppeneer and A. Liebsch, *J. Phys. Condens. Matter* **16**, 5519 (2004).
- [181] G. P. Zhang and W. Hübner, *Phys. Rev. Lett.* **85**, 3025 (2000).
- [182] E. Beaurepaire, G. M. Turner, S. M. Harrel, M. C. Beard, J.-Y. Bigot, and C. A. Schmuttenmaer, *Appl. Phys. Lett.* **84**, 3465 (2004).
- [183] M. Battiato, K. Carva, and P. M. Oppeneer, *Phys. Rev. Lett.* **105**, 027203 (2010).
- [184] A. Eschenlohr, M. Battiato, P. Maldonado, N. Pontius, T. Kachel, K. Holldack, R. Mitzner, A. Föhlisch, P. M. Oppeneer, and C. Stamm, *Nat. Mater.* **12**, 332 (2013).
- [185] B. Koopmans, J. J. M. Ruigrok, F. D. Longa, and W. J. M. de Jonge, *Phys. Rev. Lett.* **95**, 267207 (2005).
- [186] M. Krauß, T. Roth, S. Alebrand, D. Steil, M. Cinchetti, M. Aeschlimann, and H. C. Schneider, *Phys. Rev. B* **80**, 180407 (2009).

- [187] G. P. Zhang, W. Hubner, G. Lefkidis, Y. Bai, and T. F. George, *Nat. Phys.* **5**, 499 (2009).
- [188] B. Koopmans, G. Malinowski, F. Dalla Longa, D. Steiauf, M. Fahnle, T. Roth, M. Cinchetti, and M. Aeschlimann, *Nat. Mater.* **9**, 259 (2010).
- [189] A. Laraoui, V. Halté, M. Vomir, J. Vénuat, M. Albrecht, E. Beaurepaire, and J.-Y. Bigot, *The European Physical Journal D* **43**, 251 (2007).
- [190] A. Laraoui, J. Vénuat, V. Halté, M. Albrecht, E. Beaurepaire, and J.-Y. Bigot, *Journal of Applied Physics* **101**, 09C105 (2007).
- [191] F. Goedsche, *Phys. Status Solidi B* **39**, K29 (1970).
- [192] J. Gouzerh, A. A. Stashkevich, N. G. Kovshikov, V. V. Matyushev, and J. M. Desvignes, *Journal of Magnetism and Magnetic Materials* **101**, 189 (1991).
- [193] Y. I. Gorobets and S. A. Reshetnyak, *Tech. Phys.* **43**, 188 (1998).
- [194] A. V. Vashkovskii and E. H. Lokk, *Phys.-Usp.* **47**, 601 (2004).
- [195] S.-K. Kim, S. Choi, K.-S. Lee, D.-S. Han, D.-E. Jung, and Y.-S. Choi, *Appl. Phys. Lett.* **92**, 212501 (2008).
- [196] V. E. Demidov, S. O. Demokritov, D. Birt, B. O’Gorman, M. Tsoi, and X. Li, *Phys. Rev. B* **80**, 014429 (2009).
- [197] P. A. Fleury, S. P. S. Porto, L. E. Cheesman, and H. J. Guggenheim, *Phys. Rev. Lett.* **17**, 84 (1966).
- [198] V. K. Dugaev, P. Bruno, B. Canals, and C. Lacroix, *Phys. Rev. B* **72**, 024456 (2005).
- [199] S. Yang, Z. Song, and C. P. Sun, *Eur. Phys. J. B* **52**, 377 (2006).
- [200] K. Perzlmaier, G. Woltersdorf, and C. H. Back, *Phys. Rev. B* **77**, 054425 (2008).
- [201] D. R. Birt, B. O’Gorman, M. Tsoi, X. Li, V. E. Demidov, and S. O. Demokritov, *Appl. Phys. Lett.* **95**, 122510 (2009).
- [202] S. O. Demokritov, A. A. Serga, A. André, V. E. Demidov, M. P. Kostylev, B. Hillebrands, and A. N. Slavin, *Phys. Rev. Lett.* **93**, 047201 (2004).
- [203] A. Kozhanov, D. Ouellette, M. Rodwell, S. J. Allen, A. P. Jacob, D. W. Lee, and S. X. Wang, *J. Appl. Phys.* **105**, 07D311 (2009).
- [204] E. Vilkov, *Phys. Solid State* **48**, 1754 (2006).
- [205] D. D. Stancil, B. E. Henty, A. G. Cepni, and J. P. Van’t Hof, *Phys. Rev. B* **74**, 060404 (2006).
- [206] V. Vlaminck and M. Bailleul, *Science* **322**, 410 (2008).

- [207] A. M. Kosevich, B. A. Ivanov, and A. S. Kovalev, Phys. Rep. **194**, 117 (1990).
- [208] Y. K. Fetisov, C. E. Patton, and V. T. Synogach, JETP Lett. **83**, 488 (2006).
- [209] M. Wu, P. Krivosik, B. A. Kalinikos, and C. E. Patton, Phys. Rev. Lett. **96**, 227202 (2006).
- [210] Y. M. Bunkov and G. E. Volovik, J. Low Temp. Phys. **150**, 135 (2008).
- [211] C. Kittel, *Introduction to solid state physics* (Wiley, 1976).
- [212] H. Kronmüller and S. Parkin, *Handbook of magnetism and advanced magnetic materials: Micromagnetism*, Handbook of Magnetism and Advanced Magnetic Materials (John Wiley & Sons, 2007).
- [213] J. W. Kłos, D. Kumar, J. Romero-Vivas, H. Fangohr, M. Franchin, M. Krawczyk, and A. Barman, Phys. Rev. B **86**, 184433 (2012).
- [214] B. A. Kalinikos and A. N. Slavin, J. Phys. C: Solid State Phys. **19**, 7013 (1986).
- [215] K. Y. Guslienko, S. O. Demokritov, B. Hillebrands, and A. N. Slavin, Phys. Rev. B **66**, 132402 (2002).
- [216] F. Morgenthaler, Proc. IEEE **76**, 138 (1988).
- [217] J. O. Vasseur, L. Dobrzynski, B. Djafari-Rouhani, and H. Puszkarski, Phys. Rev. B **54**, 1043 (1996).
- [218] E. Feldtkeller and H. Thomas, Phys. Kondens. Materie **4**, 8 (1965).
- [219] N. Usov and S. Peschany, J. Magn. Magn. Mater. **118**, L290 (1993).
- [220] J. Bland and B. Heinrich, *Ultrathin Magnetic Structures IV: Applications of Nanomagnetism*, Ultrathin Magnetic Structures (Springer, 2005).
- [221] J. K. Ha, R. Hertel, and J. Kirschner, Phys. Rev. B **67**, 224432 (2003).
- [222] S. Parkin, Appl. Phys. Lett. **61**, 1358 (1992).
- [223] E. Shuryak, *The QCD Vacuum, Hadrons and Superdense Matter*, Lecture Notes in Physics Series (World Scientific, 2004).
- [224] G.-W. Chern, H. Youk, and O. Tchernyshyov, J. Appl. Phys. **99**, 08Q505 (2006).
- [225] A. A. Belavin and A. M. Polyakov, JETP Lett. **22**, 245 (1975).
- [226] T. Senthil, A. Vishwanath, L. Balents, S. Sachdev, and M. P. A. Fisher, Science **303**, 1490 (2004).
- [227] F. Bloch, Phys. Rev. **70**, 460 (1946).
- [228] K.-S. Lee, S. Choi, and S.-K. Kim, Appl. Phys. Lett. **87**, 192502 (2005).

- [229] R. Hertel, S. Gliga, M. Fähnle, and C. M. Schneider, *Phys. Rev. Lett.* **98**, 117201 (2007).
- [230] N. Kikuchi, S. Okamoto, O. Kitakami, Y. Shimada, S. G. Kim, Y. Otani, and K. Fukamichi, *J. Appl. Phys.* **90**, 6548 (2001).
- [231] A. Malozemoff and J. Slonczewski, *Magnetic domain walls in bubble materials*, Applied solid state science: Supplement (Academic Press, 1979).
- [232] D. L. Huber, *J. Appl. Phys.* **53**, 1899 (1982).
- [233] D. L. Huber, *Phys. Rev. B* **26**, 3758 (1982).
- [234] K. Y. Guslienko, V. Novosad, Y. Otani, H. Shima, and K. Fukamichi, *Appl. Phys. Lett.* **78**, 3848 (2001).
- [235] K. Y. Guslienko, X. F. Han, D. J. Keavney, R. Divan, and S. D. Bader, *Phys. Rev. Lett.* **96**, 067205 (2006).
- [236] M. Kläui, C. A. F. Vaz, J. A. C. Bland, W. Wernsdorfer, G. Faini, E. Cambril, and L. J. Heyderman, *Applied Physics Letters* **83**, 105 (2003).
- [237] J. Shibata, Y. Nakatani, G. Tatara, H. Kohno, and Y. Otani, *Phys. Rev. B* **73**, 020403 (2006).
- [238] L. Berger, *Phys. Rev. B* **33**, 1572 (1986).
- [239] J. Shibata, Y. Nakatani, G. Tatara, H. Kohno, and Y. Otani, *J. Magn. Magn. Mater.* **310**, 2041 (2007), proceedings of the 17<sup>th</sup> International Conference on Magnetism.
- [240] Y. Gaididei, D. D. Sheka, and F. G. Mertens, *Appl. Phys. Lett.* **92**, 012503 (2008).
- [241] B. C. Choi, J. Rudge, E. Girgis, J. Kolthammer, Y. K. Hong, and A. Lyle, *Appl. Phys. Lett.* **91**, 022501 (2007).
- [242] A. Barman, *J. Phys. D: Appl. Phys.* **43**, 195002 (2010).
- [243] K. M. Lebecki, M. J. Donahue, and M. W. Gutowski, *J. Phys. D: Appl. Phys.* **41**, 175005 (2008).
- [244] W. Wang, C. Mu, B. Zhang, Q. Liu, J. Wang, and D. Xue, *Comput. Mater. Sci.* **49**, 84 (2010).
- [245] M. Grimsditch, L. Giovannini, F. Montoncello, F. Nizzoli, G. K. Leaf, and H. G. Kaper, *Phys. Rev. B* **70**, 054409 (2004).
- [246] J. Fidler and T. Schrefl, *J. Phys. D: Appl. Phys.* **33**, R135 (2000).
- [247] M. Donahue and R. McMichael, *IEEE Trans. Magn.* **43**, 2878 (2007).

- [248] J. Miltat and M. Donahue, “Handbook of magnetism and advanced magnetic materials,” (Wiley-Interscience, Chichester, 2007) Chap. Numerical Micromagnetics: Finite Difference Methods, pp. 742–764.
- [249] W. Brown, *Micromagnetics* (Interscience Publishers, 1963).
- [250] M. Donahue and D. G. Porter, *OOMMF User’s Guide, Version 1.0* (Tech. Rep. NIS–TIR 6376, National Institute of Standards and Technology, Gaithersburg, MD, 1999) <http://math.nist.gov/oommf/doc/userguide12a3/userguide/> .
- [251] M. J. Donahue, D. G. Porter, R. D. McMichael, and J. Eicke, *J. Appl. Phys.* **87**, 5520 (2000).
- [252] M. J. Donahue, *J. Appl. Phys.* **83**, 6491 (1998).
- [253] M. J. Donahue and R. D. McMichael, *Physica B: Cond. Matter* **233**, 272 (1997).
- [254] T. G. Stockham, Jr., in *Proceedings of the April 26-28, 1966, Spring Joint Computer Conference, AFIPS ’66* (Spring) (ACM, New York, NY, USA, 1966) pp. 229–233.
- [255] K. Y. Guslienko and A. N. Slavin, *Phys. Rev. B* **72**, 014463 (2005).
- [256] G. Rado and J. Weertman, *Journal of Physics and Chemistry of Solids* **11**, 315 (1959).
- [257] B. Delaunay, *Bull. Acad. Sci. USSR, Classe Sci. Mat. Nat.* **7**, 793 (1934).
- [258] W. Scholz, *Scalable Parallel Micromagnetic Solvers for Magnetic Nanostructures*, Ph.D. thesis, Institut für Festkörperphysik (2003).
- [259] V. Kruglyak and R. Hicken, *J. Magn. Magn. Mater.* **306**, 191 (2006).
- [260] M. Dvornik and V. V. Kruglyak, *Phys. Rev. B* **84**, 140405 (2011).
- [261] A. V. Oppenheim and R. W. Schaffer, *Discrete-Time Signal Processing* (Pearson Education, 2006).
- [262] D. Kumar, O. Dmytriiev, S. Ponraj, and A. Barman, *J. Phys. D: Appl. Phys.* **45**, 015001 (2012).
- [263] R. Lyons, *Understanding Digital Signal Processing*, Prentice-Hall accounting series (Pearson Education, 2010).
- [264] F. Harris, *Multirate signal processing for communication systems* (Prentice Hall PTR, 2004).
- [265] J. W. Cooley and J. W. Tukey, *Math. Comp.* **19**, 297 (1965).
- [266] S. Neusser, B. Botters, M. Becherer, D. Schmitt-Landsiedel, and D. Grundler, *Appl. Phys. Lett.* **93**, 122501 (2008).

- [267] F. S. Ma, H. S. Lim, Z. K. Wang, S. N. Piramanayagam, S. C. Ng, and M. H. Kuok, *Appl. Phys. Lett.* **98**, 153107 (2011).
- [268] D. Stancil, *Theory of Magnetostatic Waves* (Springer-Verlag, 1993).
- [269] R. Damon and J. Eshbach, *J. Phys. Chem. Solids* **19**, 308 (1961).
- [270] K. Di, H. S. Lim, V. L. Zhang, M. H. Kuok, S. C. Ng, M. G. Cottam, and H. T. Nguyen, *Phys. Rev. Lett.* **111**, 149701 (2013).
- [271] K.-S. Lee, D.-S. Han, and S.-K. Kim, *Phys. Rev. Lett.* **111**, 149702 (2013).
- [272] H. Puzskarski, *Surf. Sci. Rep.* **20**, 45 (1994).
- [273] S. Mamica, H. Puzskarski, and J. C. S. Lévy, *Phys. Status Solidi B* **218**, 561 (2000).
- [274] C. Yu, M. J. Pechan, W. A. Burgei, and G. J. Mankey, *J. Appl. Phys.* **95**, 6648 (2004).
- [275] R. D. McMichael and B. B. Maranville, *Phys. Rev. B* **74**, 024424 (2006).
- [276] T. Fischbacher, M. Franchin, G. Bordignon, and H. Fangohr, *IEEE Trans. Mag.* **43**, 2896 (2007).
- [277] J. W. Kłos, M. Krawczyk, and M. Sokolovskyy, *J. Appl. Phys.* **109**, 07D311 (2011).
- [278] C. Costa, P. Barbosa, F. B. Filho, M. Vasconcelos, and E. Albuquerque, *Solid State Commun.* **150**, 2325 (2010).
- [279] J. Kaczér and L. Murtinová, *Phys. Status Solidi A* **23**, 79 (1974).
- [280] M. Sokolovskyy and M. Krawczyk, *J. Nanopart. Res.* **13**, 6085 (2011).
- [281] T. Wolfram and R. E. De Wames, *Phys. Rev. B* **4**, 3125 (1971).
- [282] C. A. F. Vaz, J. A. C. Bland, and G. Lauhoff, *Rep. Prog. Phys.* **71**, 056501 (2008).
- [283] V. Vlaminck and M. Bailleul, *Phys. Rev. B* **81**, 014425 (2010).
- [284] A. Christ, O. J. F. Martin, Y. Ekinici, N. A. Gippius, and S. G. Tikhodeev, *Nano Lett.* **8**, 2171 (2008), pMID: 18578551.
- [285] Z. H. Cho and J. H. Yi, *Concepts Magn. Reson.* **7**, 95 (1995).
- [286] R. Gieniusz, H. Ulrichs, V. D. Bessonov, U. Guzowska, A. I. Stognii, and A. Maziewski, *Appl. Phys. Lett.* **102**, 102409 (2013).
- [287] T. G. Pedersen, C. Flindt, J. Pedersen, N. A. Mortensen, A.-P. Jauho, and K. Pedersen, *Phys. Rev. Lett.* **100**, 136804 (2008).
- [288] J. Bai, X. Zhong, S. Jiang, Y. Huang, and X. Duan, *Nat. Nanotechnol.* **5**, 190 (2010).

- [289] W. Oswald and Z. Wu, Phys. Rev. B **85**, 115431 (2012).
- [290] H. Al-Wahsh, A. Akjouj, B. Djafari-Rouhani, and L. Dobrzynski, Surf. Sci. Rep. **66**, 29 (2011).
- [291] B. Obry, P. Pirro, T. Brächer, A. V. Chumak, J. Osten, F. Ciubotaru, A. A. Serga, J. Fassbender, and B. Hillebrands, Appl. Phys. Lett. **102**, 202403 (2013).
- [292] V. S. Tkachenko, A. N. Kuchko, M. Dvornik, and V. V. Kruglyak, Appl. Phys. Lett. **101**, 152402 (2012).
- [293] Q. Wang, Z. Zhong, L. Jin, X. Tang, F. Bai, H. Zhang, and G. S. Beach, J. Magn. Magn. Mater. **340**, 23 (2013).
- [294] J. Li, L. Zhou, C. T. Chan, and P. Sheng, Phys. Rev. Lett. **90**, 083901 (2003).
- [295] C. Croënne, E. J. S. Lee, H. Hu, and J. H. Page, AIP Advances **1**, 041401 (2011).
- [296] N. I. Polushkin, J. Appl. Phys. **114**, 033908 (2013).
- [297] B. Hillebrands and K. Ounadjela, *Spin Dynamics in Confined Magnetic Structures I*, Anglistische Forschungen (Springer, 2002).
- [298] H. Yang, G. Yun, and Y. Cao, J. Phys. D: Appl. Phys. **44**, 455001 (2011).
- [299] J. Ding, M. Kostylev, and A. O. Adeyeye, Appl. Phys. Lett. **100**, 073114 (2012).
- [300] G. Gubbiotti, S. Tacchi, M. Madami, G. Carlotti, S. Jain, A. O. Adeyeye, and M. P. Kostylev, Appl. Phys. Lett. **100**, 162407 (2012).
- [301] M. Dvornik, Y. Au, and V. Kruglyak, in *Magnonics*, Topics in Applied Physics, Vol. 125, edited by S. O. Demokritov and A. N. Slavin (Springer Berlin Heidelberg, 2013) p. 101.
- [302] A. Jafarpour, C. Reinke, A. Adibi, Y. Xu, and R. K. Lee, IEEE J. Quant. Electron. **40**, 1060 (2004).
- [303] V. V. Kruglyak, P. S. Keatley, A. Neudert, R. J. Hicken, J. R. Childress, and J. A. Katine, Phys. Rev. Lett. **104**, 027201 (2010).
- [304] C. Luo, S. G. Johnson, J. D. Joannopoulos, and J. B. Pendry, Phys. Rev. B **65**, 201104 (2002).
- [305] S. Enoch, G. Tayeb, and B. Gralak, IEEE Trans. Antennas. Propag. **51**, 2659 (2003).
- [306] X.-F. Li, X. Ni, L. Feng, M.-H. Lu, C. He, and Y.-F. Chen, Phys. Rev. Lett. **106**, 084301 (2011).
- [307] R. Bali, M. Kostylev, D. Tripathy, A. O. Adeyeye, and S. Samarin, Phys. Rev. B **85**, 104414 (2012).

- [308] S. Neusser, G. Duerr, S. Tacchi, M. Madami, M. L. Sokolovskyy, G. Gubbiotti, M. Krawczyk, and D. Grundler, *Phys. Rev. B* **84**, 094454 (2011).
- [309] R. Leite and R. C. Filho, *J. Magn. Magn. Mater.* **226-230**, 482 (2001).
- [310] M. Hurben and C. Patton, *J. Magn. Magn. Mater.* **139**, 263 (1995).
- [311] X.-Y. Jiang, ed., “Metamaterial,” (Intech, 2012) Chap. Magnonic Metamaterials, pp. 341–371.
- [312] M. Mruczkiewicz, M. Krawczyk, R. V. Mikhaylovskiy, and V. V. Kruglyak, *Phys. Rev. B* **86**, 024425 (2012).
- [313] R. Zivieri and L. Giovannini, *Metamaterials* **6**, e127 (2012).
- [314] O. Dmytriiev, M. Dvornik, R. V. Mikhaylovskiy, M. Franchin, H. Fangohr, L. Giovannini, F. Montoncello, D. V. Berkov, E. K. Semenova, N. L. Gorn, A. Prabhakar, and V. V. Kruglyak, *Phys. Rev. B* **86**, 104405 (2012).
- [315] B. Rana, D. Kumar, S. Barman, S. Pal, Y. Fukuma, Y. Otani, and A. Barman, *ACS Nano* **5**, 9559 (2011).
- [316] V. Veerakumar and R. E. Camley, *Phys. Rev. B* **74**, 214401 (2006).
- [317] M. P. Kostylev, A. A. Serga, and B. Hillebrands, *Phys. Rev. Lett.* **106**, 134101 (2011).
- [318] D. Alleyne and P. Cawley, *J. Acoust. Soc. Am.* **89**, 1159 (1991).
- [319] G. Burt, S. V. Samsonov, K. Ronald, G. G. Denisov, A. R. Young, V. L. Bratman, A. D. R. Phelps, A. W. Cross, I. V. Konoplev, W. He, J. Thomson, and C. G. Whyte, *Phys. Rev. E* **70**, 046402 (2004).
- [320] H. Gersen, T. J. Karle, R. J. P. Engelen, W. Bogaerts, J. P. Korterik, N. F. van Hulst, T. F. Krauss, and L. Kuipers, *Phys. Rev. Lett.* **94**, 073903 (2005).
- [321] K. Sekiguchi, T. N. Vader, K. Yamada, S. Fukami, N. Ishiwata, S. M. Seo, S. W. Lee, K. J. Lee, and T. Ono, *Appl. Phys. Lett.* **100**, 132411 (2012).
- [322] E. Lewis, M. Faraday, J. Kerr, and P. Zeeman, *The Effects of a Magnetic Field on Radiation: Memoirs by Faraday, Kerr, and Zeeman*, Scientific memoirs, VIII (American Book Company, 1900).
- [323] Spectra-Physics, *Model 3980: Frequency Doubler and Pulse Selector* (Spectra-Physics, California, 2002).
- [324] B. Rana, D. Kumar, S. Barman, S. Pal, R. Mandal, Y. Fukuma, Y. Otani, S. Sugimoto, and A. Barman, *J. Appl. Phys.* **111**, 07D503 (2012).
- [325] B. K. Mahato, B. Rana, R. Mandal, D. Kumar, S. Barman, Y. Fukuma, Y. Otani, and A. Barman, *Appl. Phys. Lett.* **102**, 192402 (2013).

- [326] D. Kumar, J. W. Kłos, M. Krawczyk, and A. Barman, *J. Appl. Phys.* **115**, 043917 (2014).
- [327] M. Kammerer, M. Weigand, M. Curcic, M. Noske, M. Sproll, A. Vansteenkiste, B. Van Waeyenberge, H. Stoll, G. Woltersdorf, C. H. Back, and G. Schuetz, *Nat. Commun.* **2**, 279 (2011).
- [328] S. Yakata, M. Miyata, S. Honda, H. Itoh, H. Wada, and T. Kimura, *Appl. Phys. Lett.* **99**, 242507 (2011).
- [329] M. Jaafar, R. Yanes, D. Perez de Lara, O. Chubykalo-Fesenko, A. Asenjo, E. M. Gonzalez, J. V. Anguita, M. Vazquez, and J. L. Vicent, *Phys. Rev. B* **81**, 054439 (2010).
- [330] B. Pigeau, G. de Loubens, O. Klein, A. Riegler, F. Lochner, G. Schmidt, and L. W. Molenkamp, *Nat. Phys.* **7**, 26 (2011).
- [331] M. Curcic, H. Stoll, M. Weigand, V. Sackmann, P. Juellig, M. Kammerer, M. Noske, M. Sproll, B. Van Waeyenberge, A. Vansteenkiste, G. Woltersdorf, T. Tyliczszak, and G. Schütz, *Phys. Status Solidi B* **248**, 2317 (2011).
- [332] S. Jain, V. Novosad, F. Fradin, J. Pearson, V. Tiberkevich, A. Slavin, and S. Bader, *Nat. Commun.* **3**, 1330 (2012).
- [333] X. Zhu, Z. Liu, V. Metlushko, P. Grütter, and M. R. Freeman, *Phys. Rev. B* **71**, 180408 (2005).
- [334] K. S. Buchanan, P. E. Roy, M. Grimsditch, F. Y. Fradin, K. Y. Guslienko, S. D. Bader, and V. Novosad, *Nat. Phys.* **1**, 172 (2005).
- [335] A. D. Belanovsky, N. Locatelli, P. N. Skirdkov, F. A. Araujo, J. Grollier, K. A. Zvezdin, V. Cros, and A. K. Zvezdin, *Phys. Rev. B* **85**, 100409 (2012).
- [336] C. E. Zaspel, *Appl. Phys. Lett.* **102**, 052403 (2013).
- [337] K. Y. Guslienko, K. S. Buchanan, S. D. Bader, and V. Novosad, *Appl. Phys. Lett.* **86**, 223112 (2005).
- [338] K. S. Buchanan, M. Grimsditch, F. Y. Fradin, S. D. Bader, and V. Novosad, *Phys. Rev. Lett.* **99**, 267201 (2007).
- [339] A. A. Thiele, *J. Appl. Phys.* **45**, 377 (1974).
- [340] N. K. Bajaj, *The Physics of Waves and Oscillations* (Tata McGraw - Hill, 1988).
- [341] T. Kanna and M. Lakshmanan, *Phys. Rev. Lett.* **86**, 5043 (2001).
- [342] D.-S. Han, A. Vogel, H. Jung, K.-S. Lee, M. Weigand, H. Stoll, G. Schutz, P. Fischer, G. Meier, and S.-K. Kim, *Sci. Rep.* **3**, 2262 (2013).

- 
- [343] T. F. Bogart, “Electronic devices and circuits,” (Universal Book Stall, New Delhi, New Delhi, 2000) Chap. 5, pp. 134 – 195.
- [344] R. L. Compton and P. A. Crowell, *Phys. Rev. Lett.* **97**, 137202 (2006).
- [345] J. Volz and A. Rauschenbeutel, *Science* **341**, 725 (2013).
- [346] A. J. Bourdillon, G. P. Williams, Y. Vladimirovsky, and C. B. Boothroyd, *Proc. SPIE* **5374**, 546 (2004).